Rapid, Electrostatic Self-Assembly of Nanoparticles with Kelvin Probe Characterisation



Benjamin Francis Porter
St. Catherine's College
University of Oxford

A THESIS SUBMITTED FOR THE DEGREE OF
DOCTOR OF PHILOSOPHY

TRINITY TERM 2015

This thesis is dedicated to Francis, Sonny and Jean.

Acknowledgements

Although I may have been able to achieve this thesis by myself, it would not have been anywhere near as stylish without the encouragement and support of those around me.

I am indebted to my research supervisor, Dr Harish Bhaskaran, whose experience and guidance has been invaluable to my work. I am also grateful to Dr Krisztian Kohary of Exeter University for his guidance during the initial stage of my doctoral work in Exeter. The support and encouragement of many friends and colleagues would also have been extremely difficult to replace. In praise I'd like to name Peiman, Mercè, Daniel, Gerardo, Madhav, Carlos and Dominique. To my friends who I haven't named here, frankly, I'm surprised you bothered to read this.

I also acknowledge the financial support of the EPSRC, as well as Marie Curie Actions and the John Fell Fund, without which none of this would have been possible.

Special thanks go to my girlfriend Stella, who has supported me past the point of reason, and my parents for their constant encouragement to push beyond my limits. And a final thanks to 55% of Scotland for not breaking the union whilst I was away from home.

Abstract

The pick-and-place of components to build up complex working machines, such as the robotic arms on automotive assembly lines, has been integral to the enormous success and complexity of modern heavy industry. Modern nanomanufacturing stands in stark contrast to this strategy, reliant instead on the two-dimensional patterning of radiation-sensitive resists to build high-density machines of relative simplicity. The driving goal of our research has thus been to develop a new method of manipulation that would allow the pick-and-place of nanoscale components to mirror that of the assembly lines. A manipulator that could reliably perform this process would open the door to a new age of complex nanomachines.

After analysing the current state-of-the-art in nano-object manipulation, we decided to utilise a combination of voltage-driven electric fields with chemically functional monolayers to achieve this goal. The mechanism was intended to be highly compatible with a Scanning Probe Microscope-style tip that could act as the manipulator tool on such an assembly line. This led to the design of several devices that were intended to capture single nanoparticles from a colloidal suspension, which had a negative surface charge in solution. We used numerical simulations using the Guoy-Chapman model of ionic solutions to determine what electrical and geometrical parameters would create the best devices single particle selectivity. We then describe the fabrication of devices using nanolithography techniques including electron-beam lithography, thin-film deposition and etching. Scanning electron microscopy of these devices after voltage-driven assembly showed that the mechanism had very limited success with few incidences of nanoparticle funnelling. This led through several different

troubleshooting analyses of the mechanism that identified a myriad of issues affecting these devices. Ultimately we successfully created a radical new approach that incorporated hydrophobic monolayers with polar surfaces. This method exploited the hydrophobic interaction to overcome the hydrostatic barrier and resulted in repeatable single-particle assembly onto devices in sub 5-minute timeframes.

Another aspect identified in this work was that the electronic state of nano-objects and monolayers on device surfaces is very important, but is difficult to pinpoint even when data sheets are available. We developed an emerging method of open-loop Dual-Harmonic Kelvin Probe Microscopy to identify these materials by their electronic surface potentials, successfully performing measurements in electrolytes where nanomanipulation would take place. This line of research led to novel considerations of how the size of the nanoparticles fundamentally distorts KPM measurements. We identify this as an important and often ignored effect that must be considered when using probes to differentiate between different materials at the nanoscale.

Table of Contents

Acknowledgements iii

Abstract v

Table of Contents vii

Abbreviations xi

Chapter 1 1

Introduction 1

1.1 Single Particle Placement 2

1.1.1 Building Atom-by-Atom 4

1.1.2 Nanoparticle Manipulation 4

1.1.3 Electrokinetic Nanomanipulation 8

1.1.4 Optical Nanomanipulation 10

1.1.5 Self-assembly 13

1.2 Probe-based nanomanufacturing techniques 17

1.2.1 Ablation 17

1.2.2 Thermochemical lithography (TCL) 19

1.2.3 Local anodic oxidation (LAO) 21

1.2.4 Pen lithography 24

1.2.5 Direct Laser Writing and Resist Based Nanomanufacturing 24

1.3 Thesis Goals and Summary 28

Chapter 2 31

Modeling electrostatically-driven placement in colloids 31

2.1 Colloidal dispersions 32

2.2 Physics at charged interfaces in solution 33

2.2.1 Guoy-Chapman Theory of the diffuse electric double-layer 33

2.2.2 Total interaction energy: DLVO Theory 37

2.3 Simulation of Single Nanoparticle Placement Devices 42

2.3.1 Simulations of *Gate* Devices 44

2.3.2 Simulations of Pedestal Devices 53

2.3.3 Simulations of Interdigitated Electrode Devices 55

2.4 Chapter Summary 57

Chapter 3 59

Voltage-driven devices for single-particle placement 59

3.1 Fabrication process 59

3.1.1 Electron-beam lithography 59

3.1.2 Positive and negative-tone electron-beam resists 60

3.1.4 Device schematic design 63

3.1.5 Monolayer self-assembly 65

3.2 Voltage-Driven Assembly in *Gate* Devices 66

3.2.1 Gate Device Fabrication 66

3.2.2 Gate Device Testing 68

3.3 Assembly in Pedestal Devices 81

3.3.1 Pedestal Device Fabrication 81

3.3.2 Pedestal Device Testing 81

3.4 Assembly in Interdigitated Electrode Devices 88

3.4.1 Interdigitated Electrode Fabrication 88

3.4.2 Interdigitated Electrode Testing 91

3.5 Troubleshooting 100

3.5.1 Colloid stability 100

3.5.2 Coverage of Molecular Monolayers 102

3.6 Chapter Summary 107

Chapter 4 107

Nanoparticle Assembly onto Molecular Monolayers 107

4.1 Self-Assembly of Nanoparticles 107

4.1.1 Planar surfaces 108

4.1.2 Single-nanoparticle self-assembly mechanism 109

4.1.3 Alternative nanoparticle self-assembly 116

4.2 Devices Modified by Non-Polar Monolayers 120

4.3 Chapter Summary 128

Chapter 5 131

Surface Identification by Dual-Harmonic Kelvin Probe Microscopy 131

5.1 Conventional Kelvin Probe Microscopy 132

5.2 Dual-Harmonic Kelvin Probe Microscopy 136

5.3 Kelvin Probe Measurements of Nanoparticles 140

5.3.1 Influence of capacitance gradient 141

5.3.2 DHKPM in air 144

5.3.3 DHKPM in water 149

5.4 Chapter Summary 152

Chapter 6 153

Conclusions 153

Appendix A 157

Poisson-Nernst-Planck Model 157

List of Tables and Figures 163

Bibliography 167

Abbreviations

SPM: Scanning Probe Microscopy

AFM: Atomic Force Microscopy

SEM: Scanning Electron Microscopy

STM: Scanning Tunneling Microscopy

KPM: Kelvin Probe Microscopy

DHKPM: Dual-Harmonic Kelvin Probe Microscopy

XPS: X-ray Photoelectron Spectroscopy

DLS: Dynamic Light Scattering

LDE: Laser Doppler Electrophoresis

MHA: 16-mercaptohexadecanoic acid

APTES: 3-(aminopropyl)triethoxysilane

TMODS: triethoxy(octadecyl)silane

Chapter 1

Introduction

The first wave of the nanotechnology revolution would not have been possible without 2D lithography techniques[1], enabling the high density integration of simple devices into industrial-scale production. Unfortunately, more complex devices[2], of various applications and scope, are either beyond the limits of this methodology or require excessive investments of resources. In order to integrate 3D devices with the 2D nature of lithography, the placement and manipulation of nanoscale components to form complex 3D nanostructures has been a long term objective of nanoscale engineering[1],[3]–[5]. Direct pick-and-place of building blocks has been an inspiration to scientists since it was first demonstrated using single atoms by Eigler and Schweizer[6], and research continues to push towards improving the functionality of atomic[7],[8], molecular[9] and nanoparticle[10],[11] manipulations. However, even the ability to directly control the placement of nanoparticles at room temperature into arbitrary 3-D configurations remains an ongoing objective. This is in spite of important advances in self-assembly of nanoparticles into structures[12]–[14] that recently resulted in an entire circuit[15].

Many of the leading approaches in this field are run from the piezoelectric stages of AFMs with cantilever probes. These probes scan surfaces directly with a sharp probe

tip (typically 10 nm or less in diameter) attached to a cantilever arm and the topology tracked by laser beam deflection from the cantilever's top side onto a position-sensitive photodetector[1]. When compared to electron gun technologies, this technique is relatively simple in operation whilst still remarkably efficient, producing images in excess of 1000 fps with nanoscale resolution[16] and capturing molecular processes in real-time[17]. Its relative simplicity gives probe-based techniques many advantages, such as being able to operate in a wide range of environments at both extreme and ambient temperatures, with tips performing multiple functions that can be applied to nanofabrication[18]. With this in mind, this review will offer a comprehensive look at the different means by which nanoparticles can be manipulated using existing technologies. We will place a particular focus on probe-based methods as well as the most competitive alternatives available to scientists today.

Extracts of this chapter were published in the *Journal of Materials Research* as part of a literature review on the state of the art in additive nanomanufacturing [19].

1.1 Single Particle Placement

Single particle placement covers both the ability to create structures atom-by-atom and positioning pre-prepared nanoscale objects within an existing framework. We will cover electrical, mechanical and optical methods to attract, retain, and position particles enabling fabrication of the smallest human-made structures. We will focus on the possibilities afforded by SPM technologies, electrokinetics, and optical confinement. Finally we will briefly cover some of the possibilities self-assembly offers

including the prospect of combining self-assembly with other single particle placement methods.

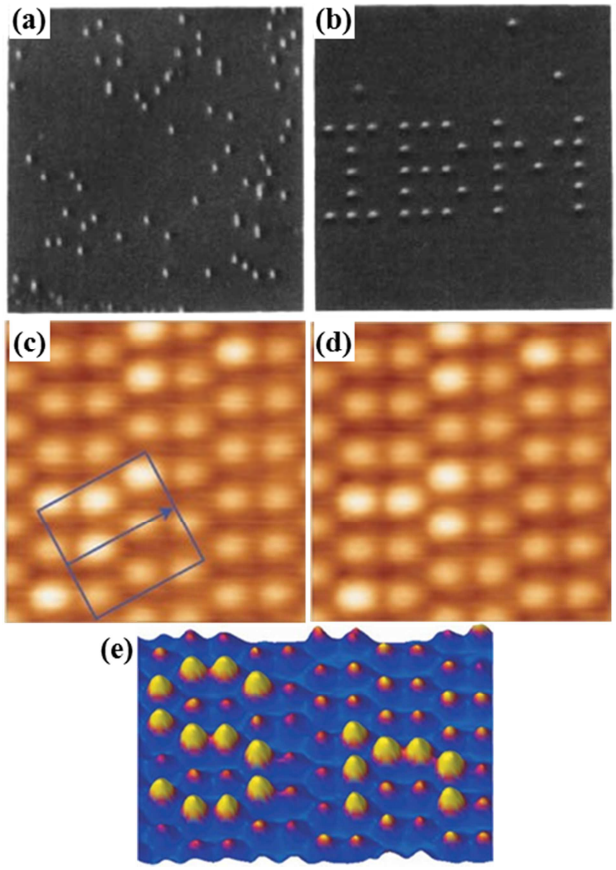

FIG. 1.1 Atomic manipulation with probes.

(a, b) STM images of the arrangement of Xe atoms on a Ni surface (a) before and (b) after manipulation with the STM probe. Reproduced from[6]. Each letter is 5 nm from top to bottom. (c-e) A sequence of AFM images showing the lateral manipulation of substitutional Sn adatoms in a Ge surface by inducing adatom exchange at room temperature with an AFM probe tip. Reproduced from[7]. One of these manipulation steps is presented (c) before and (d) after adatom exchange of the brighter Sn atoms and (c) shows the final AFM image of the Sn atoms rearranged to give the atomic symbol Sn. (c) and (d) are 4.6 x 4.6 nm and (e) is 7.7 x 7.7 nm.

1.1.1 Building Atom-by-Atom

Building devices from individual atoms remains the ultimate long-term goal for researchers in nanotechnology. As of yet, the only machines proven capable of such manipulations are SPM technologies: the STM and the AFM.

In arguably the most well-known use of a STM, researchers at IBM Corporation pioneered atomic manipulation by rearranging Xe atoms on a Ni substrate to spell out "IBM" (FIG. 1(a) and (b)).[6] AFM manipulation of atoms have advanced the technology up to room temperatures, achieving the atomic switching of adatoms[7] (FIG. 1(c)-(e)) or the more unconventional vertical interchange of atoms between the surface and the tip.[8] These approaches demonstrate the impressive atomic limit of the current technology and are used frequently in fundamental research to position and characterise atoms and molecules.[20]–[22] Although STM probes do not offer high throughput, it is the most precise nanomanufacturing tool available and is being used to fabricate some of the first single atom transistors for quantum computing.[23] The process, known as STM lithography, involves selectively driving the electrical desorption of hydrogen atoms from the surface of hydrogen passivated silicon and letting a phosphorus atom diffuse through the window formed by the missing hydrogen atom.

1.1.2 Nanoparticle Manipulation

The mental picture provoked when talking about manufacturing is often that of assembly lines of robotic arms manipulating component parts and assembling them into more complex machines. This literal understanding of manufacturing has been miniaturized and microscale, electrothermally actuated robotic hands have been used

to break off vertically aligned carbon nanotubes and place them onto surfaces, such as on the tip of an AFM probe.[24],[25] With hands like these, even nanotubes tens of nanometres in diameter can be gripped and moved.[26] Although this is a process that struggles to manipulate smaller nano-objects and operates at temperatures too high for many applications, microgrippers challenged the idea that some objects are just too small to pick up and place in a desired location.

The AFM offers more flexibility to researchers; it is capable of manoeuvring a diverse range of materials from nanoparticles[10],[11] and atoms[7],[8] to biological cells[27], be it under vacuum or immersed in liquid. The rudimentary method of nanoparticle manipulation with an AFM uses the probe tip to push, pull and slide nanoparticles around on a substrate, positioning them into desired configurations[28]. By moving the probe on a vector through the centre of the targeted particle in the desired direction, the nanoparticle can be moved across the surface by the interaction forces between the nanoparticle and tip apex. Unfortunately these methods have very low throughput and require the operator to constantly image the surface to track the particle's progress. The accuracy of each iterative process has a high uncertainty, since the particle will be likely skewed to one side or the other of the intended path if not pushed *precisely* in the centre, which becomes more likely for smaller particles. Recognising these flaws, Kim *et al* pioneered a novel method of manipulating nanoparticles whilst simultaneously imaging the surface[10]. They relied on the principle that static friction is time-dependant and will increase if two surfaces are left inert. They studied 15 nm Au nanoparticles on planar quartz surfaces. One nanoparticle was initially "kicked" to reduce the standing friction, before the surface was scanned at a sufficiently high rate (~7Hz) with the AFM in tapping mode. The

kicked particle moved across the surface in a direction perpendicular to the scanning axis, with motion ceasing abruptly and precisely when the scan speed was dropped below the threshold. This phenomenon resulted from the mechanical force the probe tip exerts on the nanoparticle on each pass pushing it along the surface, which also created ghost images of the particle giving an intuitive picture of its path. Critically, this result was only observed for the nanoparticle that was initially kicked, validating

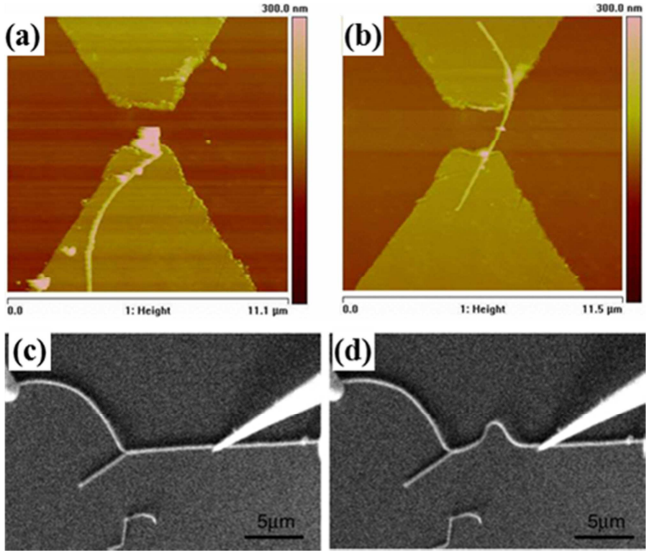

FIG. 1.2 Nano-object manipulation with probes.

(a, b) An AFM probe with a haptic force feedback is used to move a carbon nanotube on the surface between two electrodes to create an infrared sensor. Reproduced from[31]. AFM images (a) before and (b) after the nanomanipulation show the successful transfer. (c, d) SEM images of the bending of a carbon nanofiber with an STM probe in a 4-probe STM system. Reproduced from[32].

the hypothesis regarding the importance of the change in friction. To demonstrate how effective this technique was, they ran comparison studies with the existing manipulation method, reporting that efficiency was improved by a factor of 5 to 10 whilst achieving at least parity of precision. Using this method of nanomanipulation, the same group have managed to characterise the coupling between a gold

nanoparticle in a hybrid nanostructure with a semiconductor quantum dot,[12] demonstrating the usefulness of this technique to more efficient mechanical manipulation. Testing with other particles *and nanoscale objects will be needed to see how transferrable the method can be.

In an alternative approach to circumventing the unreliable manipulation of objects with the AFM, Li *et al* have developed a system that generates real-time force feedback to the operator through a haptic joystick[29], that is also used to update AFM scans of the surface[30]. The development of this technology[3] has culminated in a corrective fabrication technique, wherein carbon nanotubes (CNTs) are assembled near electrodes by dielectrophoresis before being repositioned to bridge the electrode gap[31] (see FIG. 1.2 (a) and (b)). Using this technique of nanorobotic manipulation, they were able to build and test single-walled, multi-walled and bundles of CNTs onto electrodes to operate as functional infrared sensors.

In many cases, visualisation is realised by building the manipulators into an SEM setup to give operators real-time visualisation of the objects they are controlling. This is a common combination for microgrippers, but has also been employed with SPM probes. For example, in work by Qin et al., carbon fibres that are pushed, bent, burnt and broken under the real-time observations of the SEM[32] (see FIG. 1.2(c) and (d)). The combination of these machines could prove useful to researchers, who can take measurements and images of their devices during processes driven by the probe tips.

The need for active engagement of a human operator with these different mechanisms to ensure successful manipulation of nano-objects makes industrial adaptation impractical at present, with the best applications available in pure research. This problem may be solved if recognition and positioning of components

can be automated by software. Additionally, mechanical manipulations are primarily limited to the 2D rearrangement of existing nano-objects, which limits the scope for 3D manufacturing, but may be good for quality control if the human element is removed.

1.1.3 Electrokinetic Nanomanipulation

A force can be exerted on charged objects in solution when in a DC electric field, an effect known as electrophoresis, which allows for straightforward manipulation of particles towards charged surfaces. These charged surfaces are easily created by the application of a DC voltage between electrodes[33], although alternative methods of charge patterning down to hundreds of nanometres can also be used to direct the 2D assembly of components[34]–[36]. Electrophoresis has been criticised for being limited to the manipulation of charged objects. However, the ability to functionalise nanoparticles with surface monolayers[37] enables a wide variety of nanoparticles to be manipulated. It should be noted, though, that some researchers have encountered problems when attempting to assemble films with DC or AC fields alone[38].

Analogously, dielectrophoresis refers to the force generated on a neutral particle when it is in an AC electric field: the electric field polarizes the particle, which in the non-uniform field results in a non-zero Coulomb force acting on the particle. Although two electrodes are usually required for dielectrophoresis[39], the use of a triaxial probe to generate a dielectrophoresis field that acts as a non-contact trap for dielectric nanoparticles has been recently demonstrated[40],[41] (see FIG. 13). This method is proposed to work for particles as small as 5 nm[40] and has been verified for the isolation of 100 nm polystyrene beads[41]. The non-contact manipulation of

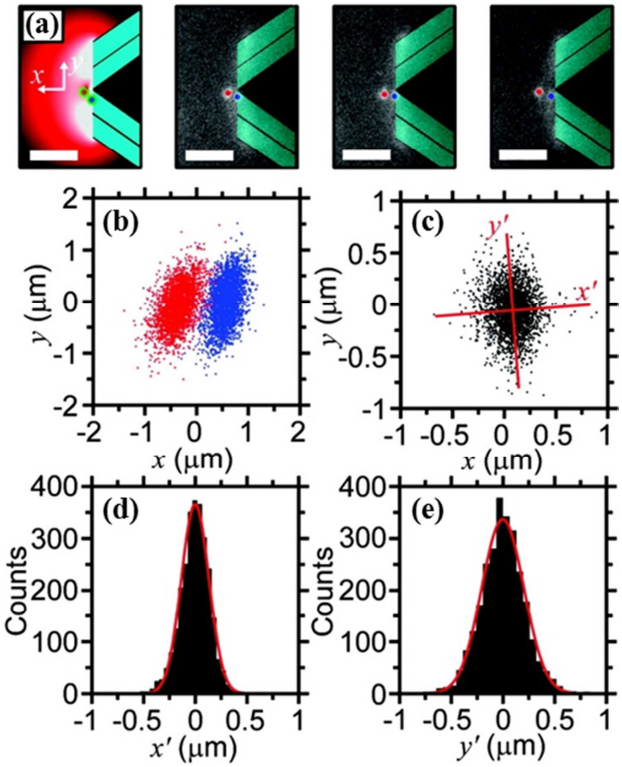

FIG. 1.3 Non-contact capture of 200 nm polystyrene beads by dielectrophoretic probes.

(a) Schematic and three representative fluorescence images of a 100 nm radius bead trapped in the negative-dielectrophoresis trap. (b) Scatter plots of the position of the bead in the trap (red dot) and the tip inferred from the position of an attached bead (blue dot). (c) Scatter plot of the separation between the trapped bead and the triaxial tip given by the separation of trapped bead/adhered bead pairs. The axes of tightest and loosest trapping are determined with principle component analysis and are shown on the plot as the x-axis and y-axis respectively. (d) Histogram of the spread of the trapped bead about the x-axis. (e) Histogram of the spread of the trapped bead about the y-axis. Reproduced from[41].

nanoparticles in 3D can thus be achieved, with the probe moving the particle through the solution and releasing it on command. However, the strength of the trap limits the positioning accuracy of the particles in the solution, with the polystyrene beads having standard deviations of 133 nm and 204 nm in the x and y axes from the intended location. The increasingly strong influence of Brownian forces will only exacerbate this problem as the manipulated particles become smaller. However, if the electric field

confining the particle could be amplified, then its position might be more easily confined, and the accuracy improved. Despite the initial problems, this method represents one of the most impressive results within nanoparticle manipulation.

1.1.4 Optical Nanomanipulation

The energy profile of a laser can be used as an optical trap for metallic and dielectric nanoparticles, capable of 3D manipulation. The forces exerted by these *optical tweezers* are only of the order of piconewtons, generally making it useful only for objects immersed in liquid media, which has seen it used primarily for manipulating biological entities[42]. Recent advances are now allowing the manipulation of nanoscale objects[43]–[46], such as gold nanoparticles[43] and silver nanowires[44] arbitrarily positioned onto surfaces. The error in the positioning of these particles, however, is currently untenably high for reliable fabrication practices e.g. 40 nm particles with deposition errors on the order of hundreds of nanometres[43]. This limitation to the tweezers is unfortunate, given the flexibility of manipulation it offers such as using the polarisation of the light to orient and align the objects[44],[46].

The precision of this placement can be improved though: for instance by coupling the laser with cavities in an optical resonator, it has been demonstrated that even 22 nm polymer particles can be immobilised in the cavities[47] (see FIG. 1.4). Because these cavities increase the electric field density within them when the laser is on, with positioning error typically within 25 nm achieved. This is comparable to the accuracy of the self-assembly approach to single-particle placement[48]. The use of these nanoapertures also benefits from a low increase in temperature of approximately 0.3 K, which helps limit the attraction of multiple particles to the aperture by

thermophoresis and avoids damaging biological entities during manipulation. Following a similar design practice 50 nm polystyrene beads have recently been trapped in a nanoaperture on an optical fibre and manipulated in suspension over several microns[49] (See FIG. 1.5). This near-field optical nanotweezer is able to both

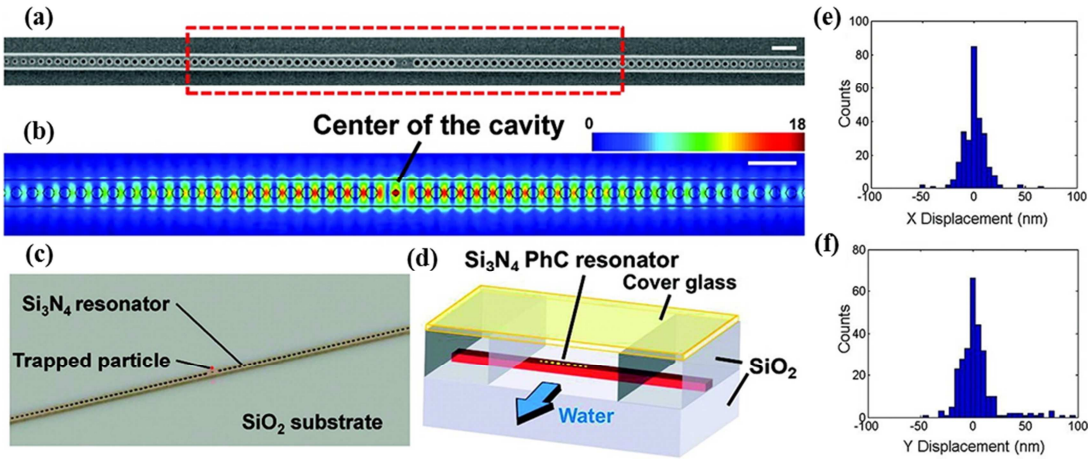

FIG. 1.4 Capture of 22 nm polymer nanoparticles in a photonic crystal (PhC) resonator.

(a) Scanning electron microscope image of a silicon nitride PhC resonator. (b) FDTD simulation showing the electric field distribution near the resonator cavity (indicated by the red dashed lines in panel (a). The colours indicate the relative field intensity (arbitrary unit). Strong field enhancement can be seen within the small hole at the centre of the cavity. Scale bars in (a) and (b), 1 µm. (c) Schematic showing trapping of a nanoparticle on a silicon nitride PhC resonator. (d) Schematic showing the relative locations of the resonator and the flow chamber. The resonator and the waveguides connected to the resonator are on the top of a silicon dioxide layer. The upper part of the resonator is exposed to the aqueous solution in the flow chamber, while the waveguides connected to the resonator are surrounded by silicon dioxide. (e, f) Histograms of the displacement of the trapped particle from the trap centre in the X and Y direction. Reproduced from[47].

manipulate and track the particle in 3D through the same fibre, allowing a facile means of manipulating dielectric nano-objects, even though the wavelength of the laser used was more than 21 times the diameter of the bead. Additionally, the

reflected signal collected by the fibre was able to make a distinction as to whether or not a particle was currently trapped at the tip. This represents an important leap forward into the nanoscale world for optical tweezers, almost certainly establishing the use of similar apertures for future mechanisms.

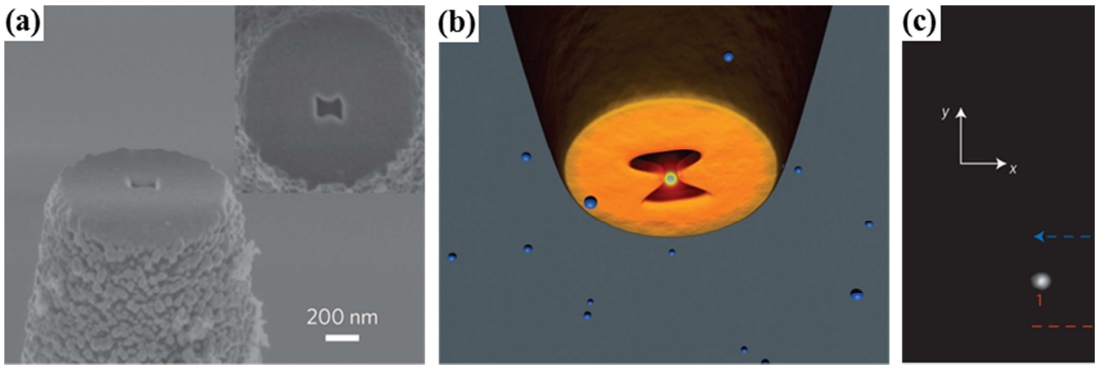

FIG. 1.5 Manipulation of 50 nm polystyrene beads with near-field optical tweezers.

(a) SEM image of an 85-nm-gap bowtie nanoaperture patterned at the extremity of a tapered optical fibre. (b) Schematic of experimental configuration. The 1,064 nm trapping laser is directly coupled into the fibre to excite the transverse mode of the bowtie nanoaperture. (c) Composite image reproducing the displacement of the trapped object. This displacement takes place over a 30 s time period with numbers 1–12 represent the successive steps of the tip and particle movement. Reproduced from[49].

The plasmonic heating effect can nevertheless be put to good use: by exposing a gold nanoparticle embedded in a layer of PDMS to laser light, the localised heating cures the PDMS in proximity to the particle[50]. The laser also acted as an optical tweezer, which was able to move the particle around to draw 2D features into the PDMS, with no curing of the PDMS observed due to laser exposure alone, and producing PDMS nanowires several microns in length and 120-130 nm in diameter. It remains to be seen if these features could then be used as a mask for further processing. There is also a difficulty that arises from continuously write with a nanoparticle without retracing previous paths used by the particle to prevent over-cured and thus over-

sized features, to build full nanostructures. Any large scale patterning with multiple particles would also need to initially locate particles in the PDMS, and write structures whilst presumably not coming into proximity of other particles causing unintended curing. However, the potential to write 3D features in this manner is an exciting future area of research.

1.1.5 Self-assembly

By exploiting chemical processes through which materials bond to each other, it is possible to self-assemble features from the bottom-up with molecules and particles as the building block. The assembly of these components can be directed by a variety of interparticle forces[51], which are commonly used to create molecular monolayers on surfaces, which is extremely useful for thin film applications[12], and ordered arrays of nanoparticles[52]. This has proven to be an extremely useful tool for nanofabrication, with an extensive body of research investigating the various methods and applications of self-assembly[52]–[54].

Combining multiple methods of self-assembly has even succeeded in the creation of an operational 3D motor from a single polymer crystal[55]. Successive self-assembly processes allowed a crystal of R-hydroxyl-ω-thiol-terminated polycaprolactone to be coated in three different types of nanoparticles: gold nanoparticles to facilitate optical visualisation; platinum nanoparticles to drive the motor by catalysing the decomposition of the surrounding hydrogen peroxide solution; and iron oxide nanoparticles to allow for remote magnetic guidance of the motor. The functioning motor is shown to perform all of these functions simultaneously, with attempts at moving around magnetic polystyrene microparticles proven partly successful. This

type of study shows just how useful nanoparticles and self-assembly are to expanding the functionality of complex devices.

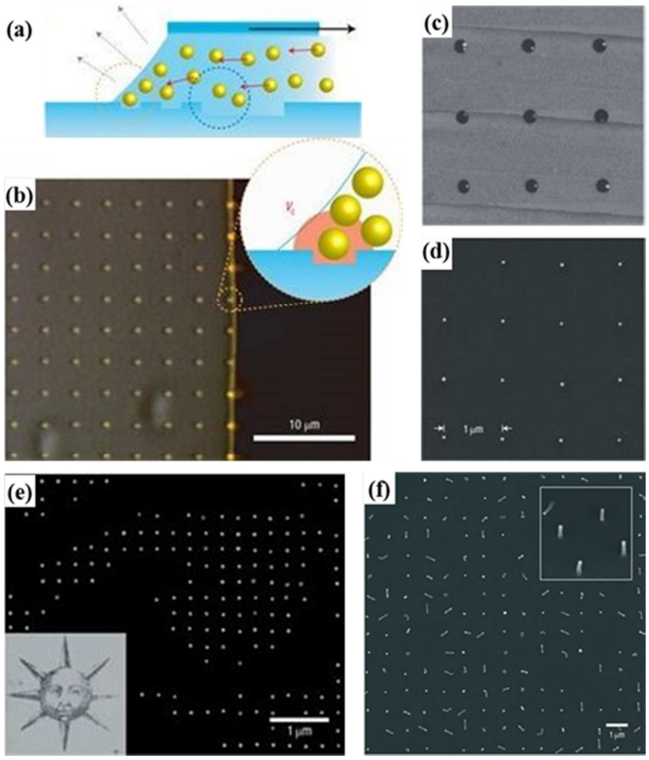

FIG. 1.6 Single nanoparticle printing using self-assembly.

(a) Schematic of the nanoparticle capture process: a colloid meniscus containing 60 nm Au nanoparticles is drawn across an indented PDMS surface. (b) A bright-field optical micrograph of the assembly in action; the bright line indicates the accumulation zone of nanoparticles in the colloid. (c, d) AFM topography scans of 60 nm Au nanoparticles (c) captured on the PDMS stamp and (d) printed onto a silicon substrate. (e) SEM image of detail (left eye) from a printed array of Au nanoparticles. (f) SEM image of silicon nanowires grown from a printed array of Au nanoparticles (inset is tilted). Reproduced from[56].

However, the exact positions the molecules bond to in self-assembly requires careful engineering of the devices; lithography methods are vital to ensuring that the assembly occurs in the right locations. Self-assembly is therefore not available as a standalone fabrication method that can build completely arbitrary assemblies, but it

does allow for existing surfaces and objects to be functionalised to perform other useful tasks,[12]–[14],[56] including large-scale growth of features like carbon nanotubes for circuits[15].

Patterning areas of a surface for self-assembly, although limited to the resolution of the preceding lithography steps, can even direct the very precise manipulation of nanoparticles individually. For instance, 60 nm gold nanoparticles were shown to be isolated onto a PDMS stamp by drawing a meniscus of gold colloid across the indented surface[56] (see FIG. 1.6). As the nanoparticles that accumulated at the edge of the meniscus pass over the surface indents, individual nanoparticles are drawn into each dent by capillary forces while the Stokes drag of the meniscus pulls additional particles away. Transfer printing was then used to attach these gold particles to a separate PMMA coated substrate, transferring the majority of the pattern and allowing the PDMS stamp to be reused. Once hydrogen plasma cleaning has removed the PMMA film, the nanoparticles were shown to have retained their functionality for nanowire growth. Similar approaches to capillary driven assembly have also reported the capture of Au nanoparticles down to 2 nm in diameter[57]. Since this technique can be extended to other types of nanoparticles, provided very good accuracy during transfer (reportedly within 100 nm of their captured locations) and a positioning error rate of less than 20 p.p.m., this approach to nanoparticle printing could be extremely useful in nanomanufacturing. It may also benefit from an update with some of the latest transfer printing techniques being developed[58].

Unfortunately capillary assembly makes it hard to control the exact location that nanoparticles will adhere to, which is very important to positioning particles in desired configurations. A more accurate method of isolating nanoparticles may instead be

achieved by electrostatic interactions between a colloid and self-assembled

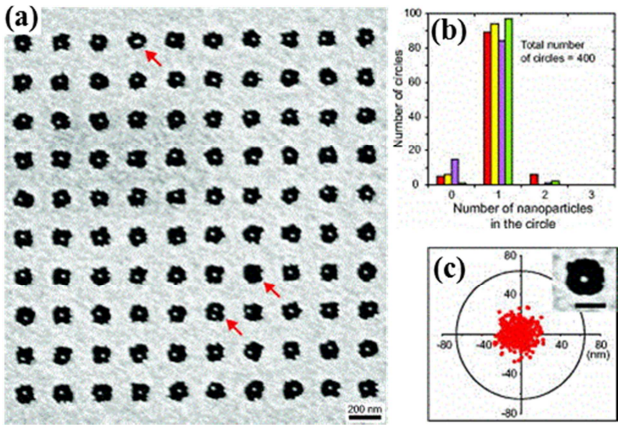

FIG. 1.7 Single nanoparticle capture in an array by self-assembly.

SEM images of 20 nm Au particles self-assembled onto a surface patterned with gates. (b) Histogram of the number of nanoparticles captured on each of 400 tested gates. (c) Superimposed plot for the positions of single nanoparticles. Inset: SEM image of a gate containing one Au nanoparticle. Reproduced from[48].

monolayers[48] (See FIG. 1.7). The proof-of-concept device worked by employing patterned circular areas of a substrate with a self-assembled monolayer (SAM) terminated by amino groups, and the surrounding area with a carboxyl terminated SAM: these two surfaces had a static surface charge in solution (relative to the pH level) as a result of protonation and deprotonation respectively, such that the area inside the circle was positively charged and the area outside was negatively charged. Immersion of this *gate* in 20 nm colloidal gold nanoparticles capped with citrate ions that carry a negative surface charge in solution, resulted in the attraction of the gold towards the *gates*' positively charged area, with the surrounding negative charge funnelling the gold nanoparticles to the centre of the *gates*. Once one of these particles was bound to a gate, the negative surface charge of the gold nanoparticle opposed the approach of additional particles, which insured only single particle placement. This is an extremely impressive result considering that the diameter of the

gate is almost 7 times larger than that of the particle it isolated and could have been even better if the lithographic definition of the *gates* were more accurate. It is entirely likely that a combination of the techniques of the gating mechanism[48] and transfer printing[58],[59] can be combined for electrically directed assembly[60]; incorporated into a probe configuration, this may be useful for the 3D printing of individual nanoparticles.

In conclusion, single particle placement is able to build structures ranging from individual atoms up to hundreds of nanometres, but so far the throughput is very low and only useful for basic research and proof of concept designs. However, once commercially viable technologies have been discovered, increased automation will be able to increase the throughput. The possibility to combine self-assembly with one or more of the technologies described in this review is especially promising.

1.2 Probe-based nanomanufacturing techniques

1.2.1 Ablation

The simplest method of modifying surface features with an AFM is to scratch material away using a hardened tip, causing direct and localised deformation of the substrate[18]. The effectiveness of nanoscratching, as this is known, is highly dependent on the characteristics of the tip. If the tip is too soft or is pressed into the substrate with excessive force, then the atoms of the tip apex will erode very quickly. This will increase the width of created features and greatly reduce the probe's lifetime. Harder tips are thus the favoured choice for building nanoscratching probes, such as diamond or diamond-like-carbon (DLC). Reducing the force applied will also reduce tip

wear rates, but this necessitates multiple scratching passes to form equivalently deep patterns. Unfortunately waste material from the scratching process is not entirely removed and instead forms ridges bordering the new features, limiting the resolution that can be achieved by this technique.

The most promising variation on this technique applies the familiar method of milling to the nanoscale. Termed nanomilling, this process uses an AFM probe tip attached directly to 3D piezoelectric actuators that rotate the probe in elliptical patterns to mechanically remove material from solid substrates, enabling the top-down fabrication of precise three-dimensional nano-scale structures. Established by Gozen and Ozdoganlar in 2010[61], this technique was intended as an improvement on the limited capabilities of typical nanoscratching procedures. Rotating a hardened AFM tip at high speeds in an elliptical pattern, they show that material is sheared from the surface. By directly affixing the tip to the piezoelectric actuator, the forces applied to the surface are more direct, bypassing the high compliance of the cantilever incorporated with the majority of probe nanofabrication systems. Analysis of this method shows that the 3d specifications of the volume targeted can be controlled with less than 5 nm average error in each dimension[62]. During his doctoral work, Gozen was able to characterise nanomilling and show its successful sculpting of PMMA, SU-8 and copper surfaces[63]. This promises to be a simple method capable of complete ablation, which could be extremely advantageous to a manufacturing industry that will always consider cheaper alternatives to current etching processes. Research into analysing the full functionality of the nanomilling system, specifically the erosion of the milling tip[63], is on-going, but this process could fabricate arbitrary 3D

surface structures from a standing structure without the need for masking at all and with a very high level of accuracy.

1.2.2 Thermochemical lithography (TCL)

The tips of AFM probes can also be heated to hundreds of degrees Celsius, which allow the localised heating of a substrate. This is done with thermochemical lithography (TCL), where a heated element is scanned across a polymer surface with carefully selected properties to cause rapid chemical changes[64]–[69]. This is such an effective process, that early research even showed that resistive heating of a 5 µm diameter wire was able to create 2D polymer wires down to just 28 nm in width[70]. Although the size of these wires was consistent enough for compact lithography, it was a remarkable achievement considering the method's simplicity. By instead using a heated AFM probe, TCL has seen particular development at IBM Zurich, where local desorption of a glassy resist in proximity to the tip was used to create a 25 nm tall Matterhorn with a lateral pixel size of 29 nm[69]. The throughput for this process was in the range of 5×10^4 μm^2/hour, which is not far from e-beam processing times. The Matterhorn model is impressively detailed vertically, although the starkly different scale factors used for the x and y axes compared to the z axis point to the limited depth their lithography was capable of was limited by the probe's shape, preventing deeper etching without destroying surrounding features.

The probe approach at IBM Zurich, now established with the spin-off company SwissLitho, has since focused on attempting to couple their methods of TCL with RIE to create deeper patterns[64]. In this case, the probe etched the mask features into a 20 nm PPA organic resist top layer. Multiple RIE etching steps ultimately transfer this

top pattern into an underlying carbon rich polymer HM8006 on a silicon wafer, which can be used for industrial level etching. Using this process they created nested L lines, notoriously difficult to create due to difficulties with overlapping features. The characterisation of the RIE process for etching the HM8006 layer seems to have been key to the quality achieved, with line roughness of a mere 2.7 nm achieved – something which may also improve the output of the LAO approach. In parallel to this research, SwissLitho have also made great headway, testing multiple applications for the technology including: a means of stitching multiple writing fields together on a large scale by mapping surface roughness measured by the AFM[71]; creating templates for the guiding the assembly of nanorods onto underlying substrates[72]; and exploiting the 3D patterning capability to record information with 3 bits per 20 nm pixel[73].

Other uses of TCL have sought to use the chemical change to write the devices directly. Of particular interest is the ability to pattern graphene circuitry onto devices by surface modification, most recently by the reduction of graphene fluoride on a surface[65]. This method successfully created graphene nanoribbons down to 40 nm in width and with a measured resistance ten times that of pristine graphene, indicating not all fluorine has been removed; notably this measurement was of larger 120 nm features, implying lower quality/higher fluorine concentrations for smaller lines. This was generated as an alternative to the reduction of graphene oxide, which fails to produce a useful graphene surface for good circuitry[74].

1.2.3 Local anodic oxidation (LAO)

One of the most common uses of an AFM for nanomanufacturing is local anodic oxidation (LAO) of substrates, which can form robust masks for subsequent deposition or etching processes or to create nanoscale oxide elements[18]. The process is performed within a controlled environment with high humidity, typically in the 40-70% range, which causes a substantial water meniscus to form between the probe tip and the surface when in close proximity. By applying a strong electrical bias between tip and substrate (negative and positive polarity respectively) the water molecules ionise, causing oxyanions to accumulate on the surface within the meniscus contact area. This causes the growth of oxide features with size dependent on the meniscus size, applied bias and the AFM operating mode employed.

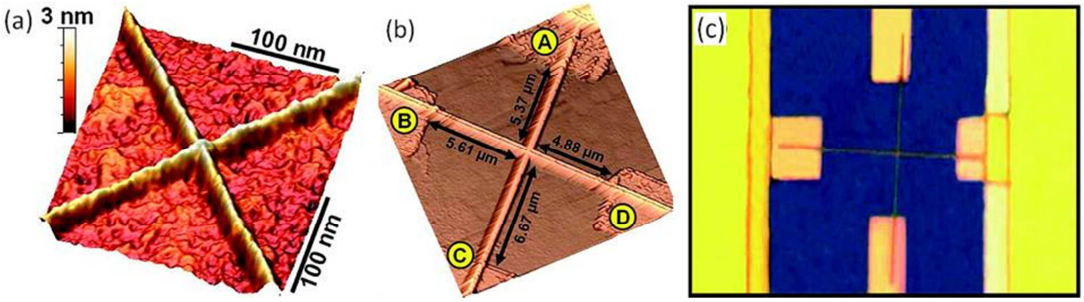

FIG. 1.8 Local anodic oxidation lithography of Si nanowires.

(a) AFM topography image of two oxidised lines masking a Si on insulator substrate. (b) AFM topography of two perpendicular Si nanowires after KOH etching of unmasked Si. (c) Optical image of the complete four-arm Si nanowire transistor. Reproduced from [75].

One of the principal uses of this technique has been to create Si nanowire (SiNW) circuits, which have great potential as ultrasensitive sensors. Such SiNW must be fabricated to high and consistent sub-10 nm precision to have reliable output signals; LAO with an AFM can provide such precision, besting the high costs and proximity effects of electron beam lithography (EBL). For instance, SiNW transistors were

fabricated with nanoscale channel widths by researchers in Madrid by using LAO to define a specific SiO_2 mask (FIG. 1.8)[75]. N-type doped silicon cantilevers were oscillated under dynamic mode over the target regions of a silicon-on-insulator (SOI) substrate, applying a sequence of 3 V pulses every 100 μs to create an oxide layer approximately 2.5 nm thick. Wet etching of the unmasked Si with KOH, and subsequent removal of the oxide mask by HF successfully fabricated a four arm SiNW transistor between pre-patterned electrical contacts. As an alternative to chemical etching, they also fabricated a SiNW transistor by etching of the Si by reactive ion etching (RIE) instead; this produced SiNWs with near vertical walls (top and bottom widths of 4 and 10 nm and 37.5 nm height) compared to the relatively trapezoidal cross-section of the KOH etch. The RIE process is further used to write "NANO" with SiNWs, demonstrating the ability to flexibly fabricate linear and circular NWs of consistent size. Furthermore, electrical testing of these transistors shows good agreement with theory, indicating that this method of fabrication leaves the SiNW properties unaltered.

Having established their processes for successful AFM-LAO, the same research group have proceeded to design and fabricate a wide variety of SiNW circuitry[76]. With consistent channel width of sub-10 nm established, sub-100 nm placement of adjacent NWs and feature height controlled primarily by initial Si thickness and RIE etching time, they were able to control the electrical response of a SiNW transistor of any geometry by tailoring its size and dopant concentration. These transistors were measured to be highly sensitive, with an on/off current ratio of 10^5 giving excellent contrast. As a demonstration of their sensing capability, the transistor was used to detect the presence of bovine serum albumin (BSA) antigens and antibodies in solution

(immunology processes). The resulting sub nA changes in channel current compared to pure water were successfully detected, with the change attributed to the formation of an analyte-ligand complex; this importantly showed that the high sensitivity of SiNW sensors built by bottom-up nanofabrication processes was not affected by the LAO method. The sensing capability has also been demonstrated for other processes, such as detecting and differentiating between the different biomolecular processes of recombinational DNA repair by RecA Protein in a microfluidic cell[77]. In this case, the SiNW successfully differentiate between the measured current for six different environments, with reversibility and reusability results for the device showing promise, demonstrating how useful AFM-LAO can be for fabricating ultrasensitive sensors.

The capability of AFM-LAO to pattern oxide surface elements also has great potential for modifying the functionality of a substrate. For instance, the use of LAO on a graphene surface has been shown to infuse the monolayer material with oxygen-containing functional groups[78]. Furthermore, they demonstrate that the magnitude of the bias applied to the tip to cause oxidation directly affects the level of oxidation in the graphene oxide (GO) layer, so that the resistivity of the GO increases and decreases with the voltage supplied (no observable changes in the size of the GO were observed until a -5V bias, but down to at least -10V it progressively increased from about 20 to 90 nm). This meant the graphene surface to be tailored with multi-level Schottky barriers between graphene and GO regions from 4eV to 2meV, dependent on the voltage used to oxidise it; thus, LAO can fine tune the electronic resistivity of a graphene substrate by oxidising local elements.

1.2.4 Pen lithography

Material can also be deposited directly onto a substrate by an AFM probe heads that incorporate a nano-sized pipette into the probe head, which allows for the delivery of material to a surface directly. This style of dip-pen or fountain-pen nanolithography (DPN, FPN) allows the localised deposition of liquid mediated matter to surfaces, which has spawned dedicated companies like NanoInk, Inc. Among the most recent developments for this technique, thermal-DPN has been able to mask graphene sheets with a protective layer of polystyrene, which has been used to create standalone graphene features by plasma etching[79],[80] or chemical isolation by fluorinating unmasked graphene[79]. The chemical isolation proved somewhat successful, preserving the electrical properties of the masked graphene, which is excellent for its use for writing circuitry. However, the polystyrene mask has proved difficult to remove under sonication without damaging the device, which will damage the mechanical and optical uses of graphene.

Another development in this field of great relevance to other probe-based nanomanufacturing strategies is hard-tip soft-spring lithography[81]. This demonstrated that many probes can work in parallel for nanolithography by using a flexible support base of PDMS underneath the probe array.

1.2.5 Direct Laser Writing and Resist Based Nanomanufacturing

Direct laser writing (DLW) of nanoscale features is capable of building 3D structures from the ground up in a rapid and facile manner (see FIG. 1.9). Although DLW is a resist based fabrication method and therefor requires an additional development step, it very similar in nature to additive fabrication method because the fabricated

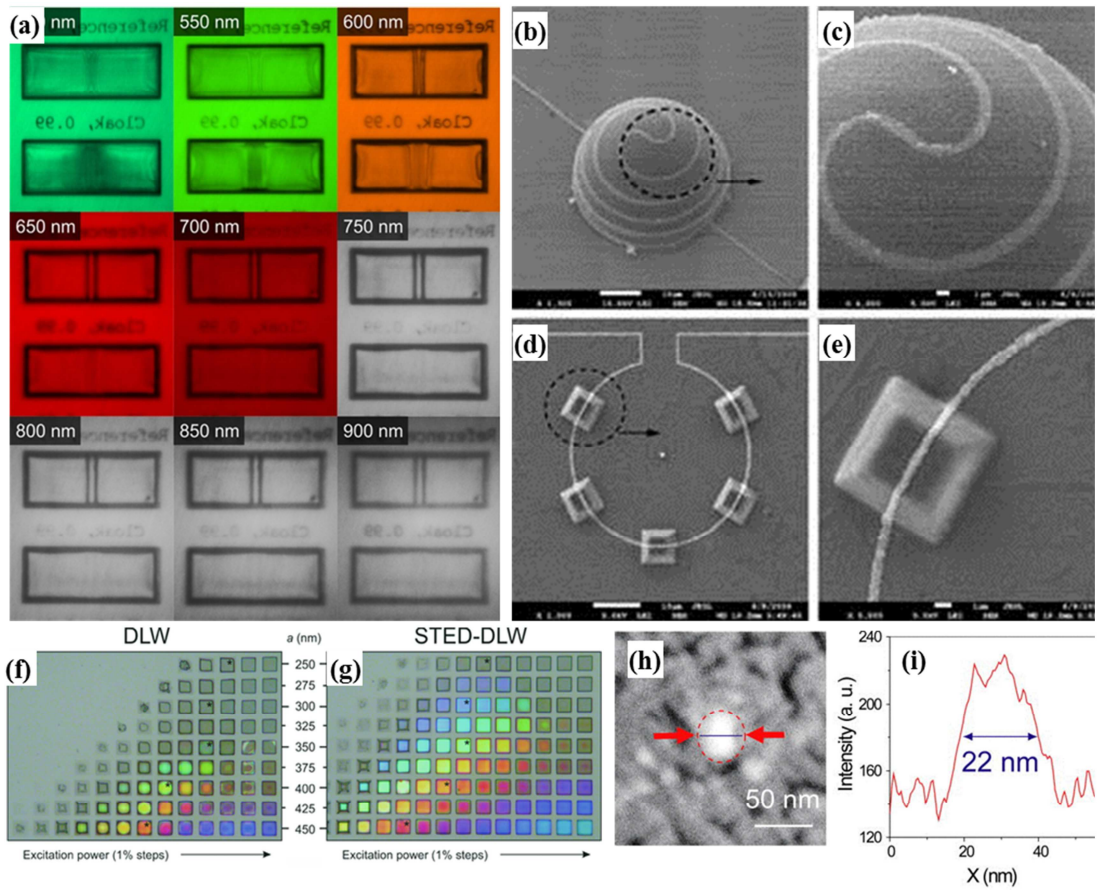

FIG. 1.9 Features and devices created by Direct Laser Writing.

(a) True colour images of carpet invisibility cloak for unpolarised light, ranging in wavelength from 500 to 900 nm, with both reference and cloak structures. Reproduced from[85]. (b-e) SEM images of silver microscale lines drawn arbitrarily onto 3D structures. Reproduced from[102]. (f, g) True-colour reflection-mode optical micrographs of woodpile photonic crystals 20 x 20 μm^2 fabricated by (f) regular DLW (MPP) and (g) STED-DLW. Reproduced from[96]. (h) SEM image of a 22 nm silver dot grown by laser driven nucleation and growth, with (i) the corresponding intensity profile as indicated in the micrograph. Reproduced from[89].

structures have their final shape without following deposition or etch steps. Laser driven three-dimensional (3D) nanofabrication is best achieved by multi-photon polymerisation (MPP)[82],[83]. In MPP, the concentration of photons in the neck of a femtosecond pulse of a laser beam allows for the controlled photopolymerisation of a targeted volume (or voxel) in a photoresist. Development of this resin allows 3D

features to be written at typically 10 to 500 µm/s with nanoscale resolution. This is particularly useful for fabricating 3D photonic structures[83]–[85] that would otherwise be extremely expensive and difficult to manufacture with the alignment of sequential 2D layers via traditional lithography. The successful commercialisation of this technology by companies like Nanoscribe GmbH has enabled photonics researchers to investigate new applications in 3D with invisibility cloaks[84],[85], Gecko-mimicking surfaces[86] and 3D data storage[87] among other impressive achievements in recent years.

The range of materials that can be polymerised for MPP nanofabrication is a significant challenge for materials science to explore. For solid structures advanced composites or solutions that respond to MPP have been demonstrated, resulting in structures of vanadium[88] and silver[89]. The simplest approach to avoiding this is to use the surfaces of 3D polymer structures as scaffolds for the deposition of other materials. Metallisation of such scaffolds by atomic layer deposition or electroless plating has been shown to work for metallic photonic crystals[90] and metamaterials[91]. The polymer structures written can also be used for casting of 3D structures from other materials like titania[92].

Maximising the resolution of MPP is of course an important goal, with Abbe's diffraction limit representing the typical limit. A recent review[93] summarised the advances in sub-diffraction limit DLW. As an example Cao *et al* achieved the highest resolution of this technique to date with 40 nm dots in a highly sensitive photoresin[94] and 22 nm silver dots by laser activated nanoparticle growth[89]. These results are extremely impressive, but the high resolution was only achievable for individual dots. When continuous structures were attempted, a larger line width of

130 nm was achieved at a comparatively low scanning speed of 3 μm/s[94]. Stimulated emission depletion (STED), which has achieved 5.8 ±0.8 nm resolution in microscopy[95], is also being put forward as a promising route to sub-diffraction MPP. It has been effective in building 3D nanoscale structures over a large area[85],[92] and shows significant improvement over regular MPP for 175 nm parallel structures[96] achieving 65 nm line widths[97] whilst scanning at 100 μm/s.

DLW is also able to create a wider range of features in 2D by initiating reactions locally with the input of energy from the laser. This includes reducing graphite oxide to draw supercapacitors[98], the laser-induced chemical vapour deposition of graphene on Ni[99], the growth of carbon nanotubes[100],[101], and the electroless plating of silver[102]. Integrating these technologies could enable the entirely laser driven fabrication of carbon nanotechnologies. Other methods of laser writing like sintering of a silver nanoparticle ink[103] could work well for large scale patterning of electrodes. In these cases higher scan speeds up to 1000 mm/s have been shown to reduce the features line width and height to below 5 μm and 50 nm respectively, with an increasingly high surface roughness an unfortunate consequence.

Although technically not an additive manufacturing method, scanning near-field photolithography provides a cheap alternative traditional nanoscale photolithography. By utilizing the evanescent field from an illuminated nanoscale aperture in close proximity to the photoresist direct writing of sub-diffraction limited structures with resolution down to 70 nm can be achieved[102]–[104]. Vast improvements to this technology has been achieved by utilizing flying plasmonic lenses thereby potentially outperforming electron beam lithography in terms of cost and speed[105]. The

inventors envisage this technology to be able to pattern a 12 inch wafer in 2 min with sub-100 nm resolution in the future.

1.3 Thesis Goals and Summary

The majority of present day nanomanufacturing strategies for assembling nanoparticles using AFM-based tools are limited to 2D manipulation coupled with active visual guidance of a human operator. An ideal robotic manipulator would mirror automotive assembly, taking individual components from a bulk media and removing them to a different environment where they can be placed into arbitrary 3D configurations. Of particular importance is the need for a fully automatable manufacturing process, where hundreds of probes working in parallel follow the same work routine to build a whole chip of devices simultaneously. This type of parallel processing with probes is only possible at present through methods that focus on 3D top-down lithography methods rather than the 3D bottom-up assembly of nanoscale objects.

The throughput and accuracy of all these lithography techniques is all but incomparable to the state-of-the-art uses of electron beam lithography, which has achieved sub-5 nm features and can operate thousands of beams in parallel[104]. Although this appears ideal for achieving the best 2D features, the resource cost of making circuitry in industry by e-beam lithography today is already deplorably high and would be exacerbated by pursuit of these dimensions. The practical search for higher density electronics is thus being pursued in three dimensions, which again highlights the usefulness of a 3D nanomanipulator.

Accurate and exclusive immobilisation of individual particles has only been shown to be highly accurate by a self-limited gating mechanism that self-assembles single nanoparticles from colloidal gold with excellent precision[48]. Since the key driving force behind this assembly appears to have been static surface charges of the monolayers, with effective electric potentials at the surface on the order of 100 mV, we propose that the use of a low applied voltage instead to exert an electrophoretic force on the nanoparticles would control their directed assembly[60]. This force attracts a nanoparticle to a specific location where its opposing electrostatic charge will discourage additional particles from attaching to the same location. Once a particle is attached, an electrostatic force of opposite polarity would then repel the particle and drive the removal of the particle at the desired location; such techniques of detachment have been successfully demonstrated[59] and can be directly applied to the system described here. This self-limiting method would allow the consistent, accurate and controlled picking and placing of *single* nanoparticles from a colloidal suspension. We foresee that by integrating this method with an AFM style probe, an effective means to pick-and-place various charged nanoparticles would create an accurate and scalable 3D nanomanufacturing technique.

In this thesis, we examine devices we designed to accurately, repeatedly and rapidly control the assembly of individual nanoparticles with the use of controlled applied voltages. The intended long-term goal of this research is to enable pick-and-place manufacturing techniques, isolating, manipulating and depositing simple components to create complex nanostructures, where the mechanism in this research would act as the capture process. A mechanism to achieve this for nano-objects does not currently exist; the best results have been achieved through self-assembly, meeting the criteria

of accuracy and exclusivity, but requiring hours to guarantee assembly. The key to using a voltage-driven, rather than a voltage-inhibited approach, was to provide an option of using higher voltage pulses to speed up the single-particle assembly process. However, when tested the devices encountered several issues that we had not foreseen when considering the concept for this project. Following several troubleshooting analyses we are confident that we isolated the issues that prevented the devices from operating properly, which will inform future research in this area.

In the next chapter we will examine the physics behind the nanoparticle-capture mechanism and use this to build simulations for devices to achieve this process. In chapter 3 we will then present the methods we used to fabricate and test these devices including subsequent troubleshooting, which concluded that the driving voltage destabilised the colloid in the devices proposed in chapter 2. In chapter 4 we will then present the approaches that were taken to increase the efficiency of single-particle capture mediated by molecular monolayers. This was ultimately achieved through a combination of polar and non-polar surfaces to introduce funnelled-dewetting of particles onto surfaces in short time scales. Finally, Chapter 5 will examine work on developing an open-loop Kelvin Probe Microscopy (KPM) method, which was required to identify many of the functional components of these devices in their native environment. **The key contributions of this work were:**

1) The invention, testing and analysis of simulations and experiments with novel voltage-controllable single nanoparticle capture devices;

2) Development of a new, rapid method for single-particle assembly that combines electrostatic funnelling with hydrophobic dewetting of a non-polar monolayer, which accelerates the particle manipulation to practical timescales for applications;

3) The innovative use of open-loop Dual-Harmonic Kelvin Probe Microscopy measurements to characterise the assembly of nanoparticles in solution and identifying a clear trend in the convolution of these measurements with the geometry of the surface.

Chapter 2

Modeling electrostatically-driven placement in colloids

An important first step to creating successful nanoparticle pick-and-place devices was to create simulations of how different designs might operate. The primary objective of this work was to create a precise and rapid capture mechanism, isolating specific components from a bulk. Our review has shown that the most precise nanoparticle control is achieved through electrostatic interactions; a simple end product with few moving parts and excellent selectivity based on previous research with self-assembly[48],[105] Colloidal dispersions of nanoparticles contain a high density of nanoparticles (e.g. 10^8 to 10^{14} particles per mL) and the particles in many of these colloids carry an innate surface charge, which stabilises the colloid and prevents agglomeration. This surface charge should also enable the particles to be manipulated by electric fields exerted by the devices and enable single-particle selectivity. Understanding how these particles interact is vital if they are to be successfully manipulated, so in this chapter we investigate the significant surface forces and other media that need to be understood in colloidal dispersions. We then use this understanding to simulate the behaviour of voltage-driven capture devices to determine the ideal parameters for consistent single-nanoparticle capture.

2.1 Colloidal dispersions

Gold nanoparticles have been used since ancient times for the staining of glass, but their optical, chemical and electronic properties make them strong candidates for a diverse range of applications. These properties are highly dependent on the exact size and shape of the particles, which makes producing consistent batches with low size-distributions a high priority. This has led to the development of several aggregation strategies for producing these nanoparticles[106], most commonly by the chemical reduction of gold salts in aqueous or non-aqueous media.

The precise chemical mix used to prepare these colloidal dispersions is dependent on the desired size of the gold nanoparticles. For the preparation of gold nanoparticles on the order of 10-20 nm in diameter, the Turkevich method is the most common synthesis route and follows a typical nucleation process. Originally devised by Turkevich et al. in 1951[107] and later refined by Frens in the 1970s[108], the colloid is created by the reduction of chloroauric acid in aqueous solution by sodium citrate, followed by the capping of nucleated gold aggregates with citrate ions. In this case, the sodium citrate thus plays the role of both reducing and capping agent in the synthesis, which is not universally true for this process. The reaction requires the solution to be heated and stirred continuously over several hours and is very sensitive to the proportions of the reactants; small reductions in the concentration of citrate ions can allow larger gold nanoparticles to aggregate, although the range of particle size is less homogeneous than with the 10-20 nm particles. The citrate ligands that stabilise these molecules are strongly bound to the surface so much so that even thiol ligands have difficulty in displacing them[109].

In the interests of developing more environmentally friendly preparation methods, other research has focused on the use of alternative methods of green synthesis, which have been shown to successfully produce gold nanoparticles tens of nanometres in size[110]. This approach tends to result in comparatively less homogeneous nanoparticle sizes and shapes, but avoids the use of the toxic chemicals typically required for aggregation of nanoparticles and could yet be refined in the future.

Synthesis can also be achieved without chemical reduction by using an external energy source, such as photo-, electro-, and sono-chemical processes, but the process for auric ion aggregation is approximately the same with all these strategies. From the top-down, colloids can also be created by the ablation and dispersion of bulk material with a colloid mill, but these result in much larger particles above the nanoscale range.

For use in these experiments, gold nanoparticles in the size range of 20 to 80 nm in diameter were purchased from BBI Solutions. These nanoparticles were synthesised using the Turkevich method described above, so were capped and stabilised by citrate ions, which confer a negative surface charge in solution allowing them to be manipulated by DC electric fields.

2.2 Physics at charged interfaces in solution

2.2.1 Guoy-Chapman Theory of the diffuse electric double-layer

When solid surfaces are in solution they usually carry a small surface charge. This can arise as a result of ionisable surface molecules, such as carboxyl or amine groups, provided that pH of the solution favours protonation or deprotonation as appropriate.

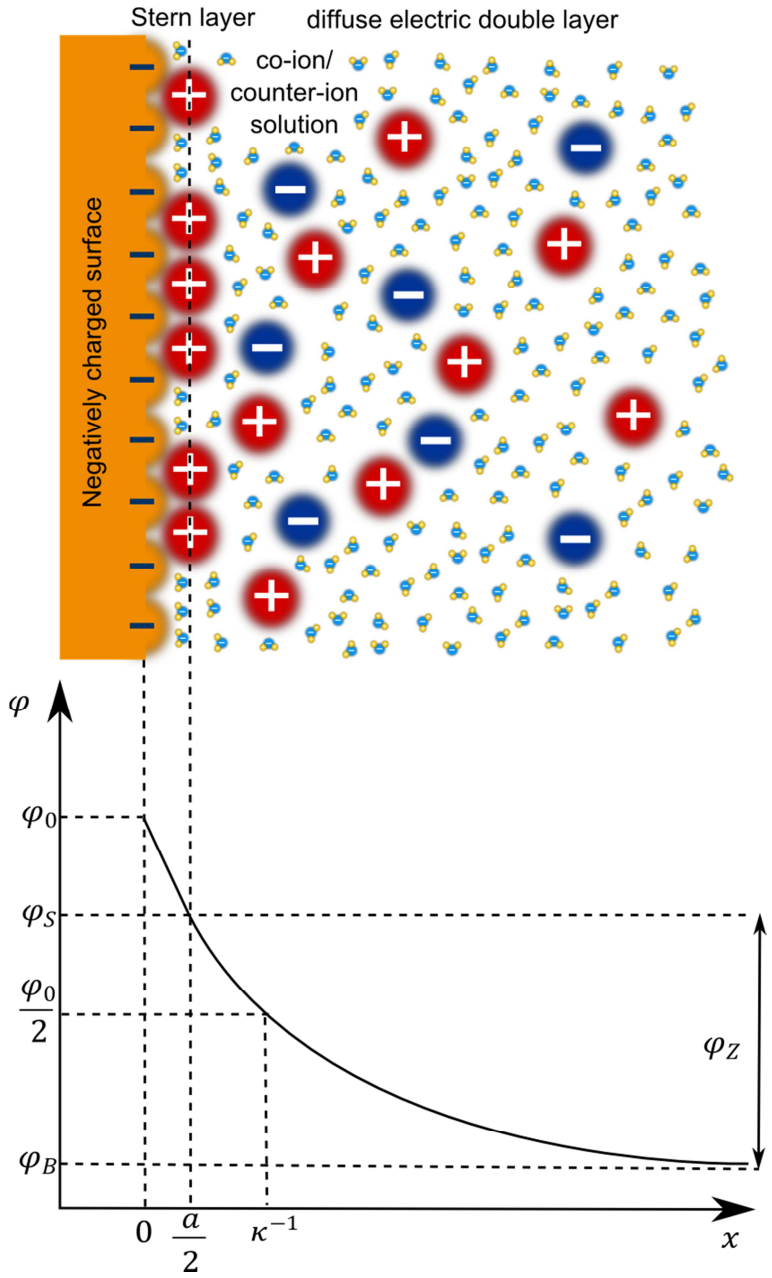

FIG. 2.1 Electric potential distribution at the solid-liquid interface.

A schematic of the distribution of ions and molecules at the interface between a charged surface and an electrolyte. The highly orientated and ordered nature of ions and polar water molecules adjacent to the surface in the Stern layer is also represented. The electric potential φ has various values of φ_0 at the solid surface, $\varphi_S$at the centre of the Stern/Helmholtz layer (half the ionic radius, a), and the bulk potential φ_B. The zeta potential φ_Z is equal to the difference between φ_S and φ_B. The inverse Debye length κ^{-1} marks the distance from the surface where $\varphi = \frac{\varphi_0}{2}$.

A similar pH dependency can result in metal oxide surfaces becoming charged as well, forming O^- or OH_2^+ surfaces for acidic and basic solutions respectively. Any ions in the solution are affected by these fixed surface charges and as a result become distributed in a region close to the surface known as the diffuse double layer.

The *Helmholtz model*[111],[112] for this layer assumes that counter-ions completely neutralise the electric field of these fixed charges by absorbing evenly across the surface. However, this oversimplifies the nature of the double layer, which is really a highly diffuse region of counterions and polar molecules in constant, rapid thermal motion around the surface. The more realistic *Gouy-Chapman model*[111],[112] instead considers the distribution of ions around the charged interface to form a Boltzmann distribution[111]:

$$N_i = N_{i0}\exp(\frac{-Z_i e\varphi}{k_B T}) \tag{2.1}$$

Here N_i and N_{i0} are the number of ionic species i per unit volume near the charged interface and in the bulk of the solution respectively, Z_i is the valency of ionic species i, φ is the electronic potential, k_B is Boltzmann's constant and T is the temperature. The overall charge density is then the sum of all the charge contribution of these ions:

$$\rho = \sum_i Z_i e\, N_i = \sum_i Z_i e N_{i0}\exp(\frac{-Z_i e\varphi}{k_B T}) \tag{2.2}$$

Combining Eq. (2.2) with Poisson's equation for electrostatics[111],[113],

$$\boldsymbol{\nabla}^2\varphi = \frac{\rho}{\varepsilon_0\varepsilon_r} \tag{2.3}$$

where $\boldsymbol{\nabla^2}$ is the *Laplacian* operator, defined for this three-dimensional system,

$$\boldsymbol{\nabla}^2 = \frac{\partial^2}{\partial x^2} + \frac{\partial^2}{\partial y^2} + \frac{\partial^2}{\partial z^2} \tag{2.4}$$

results in the Poisson-Boltzmann equation[111],[113]:

$$\nabla^2\varphi = -\sum_i \frac{Z_i e N_{i0}}{\varepsilon_0 \varepsilon_r} \exp\left(\frac{-Z_i e \varphi}{k_B T}\right) \tag{2.5}$$

*w*here ε_0 and ε_r are the permittivity of free space and the relative permittivity of the liquid media respectively. This nonlinear second-order differential equation can be solved for the distribution of the electric potential in the solution, given that the electronic surface potential and concentration of ions present in the solution are known. The thickness of the diffuse electric double layer can be characterised by the Debye length, κ^{-1}, where[111]:

$$\kappa^{-1} = \left(e^2 \sum_i \frac{\rho_{\infty i} {z_i}^2}{\varepsilon_0 \varepsilon_r k T}\right)^{-\frac{1}{2}} \tag{2.6}$$

Here κ is the inverse Debye length, the distance from the surface at which the surface potential of the Poisson-Boltzmann has been reduced to half of its initial value (FIG. 2.1). It should be noted that this thickness is primarily dependent on the concentration of ions in the solution and not on the magnitude of the surface potential.

A weakness in this model is the treatment of ions as point charges; under conditions of high surface potential or high ion concentration, the density of ions adjacent to the interface becomes unrealistic. The *Stern model*[111],[112] provides a fix to this problem, by assuming that the ions in the first layer of surface adjacent ions from the solution at the solid-liquid interface have finite size. Thus there is a linear drop in the electric potential across this first layer, known as the *Stern* (or *Helmholtz) layer*. This layer is considered to be valid up to the charge centre of the first layer of ions, outside of which a Guoy-Chapman model of a diffuse double layer can be applied (see FIG. 2.1). The potential difference between the *Stern potential,* φ_S (at the boundary of the

Stern layer) and the potential of the electrolyte bulk, φ_B is defined as the zeta potential, φ_z[112]. Assuming electroneutrality of the bulk solution, φ_B should tend towards zero away from charged surfaces, so when calculating the electric potential distribution with Eq (2.5), it is reasonable to use the zeta potential of solid-liquid interfaces as the boundary condition. The *zeta* potential (or *Electrokinetic* potential) is also defined in literature as the electric potential at another boundary in the double layer called the *slipping plane*. This plane exists in the middle of the diffuse double layer outside of the *Stern* layer, within which the electrolyte moves with the nanoparticle during phoresis. This situation generally reflects a situation where the electrolyte has a very high ionic strength, where ions form a denser layer on the surface than the single layer of ions accounted for in the Stern layer. At low ionic strength, the *Stern* layer and the *slipping plane* become indistinguishable, allowing the previous equivalence of the Stern potential and the zeta potential to hold (assuming bulk electroneutrality) – as the majority of these measurements consider weak electrolytes, we used this assumption.

2.2.2 Total interaction energy: DLVO Theory

When two solid surfaces approach each other, there are two principal energy potentials that need to be considered: the van der Waals potential and the double-layer interaction energies. The van der Waals potential V_W is largely independent of the properties of the electrolyte between the surfaces[111]. In the case of colloidal nanoparticles, as discussed in section 2.1, two spherical particles of equal radius r whose surfaces are separated by distance s have a van der Waals potential, V, of[111]:

$$V_W = \frac{-Hr}{12s} \tag{2.7}$$

where H is the Hamaker constant. When interacting across a fluid, H is replaced by an effective Hamaker constant, H_e:

$$H_e = \left(\sqrt{H_p} - \sqrt{H_m}\right)^2 \tag{2.8}$$

Here H_p and H_m are the Hamaker constants of the particles and the electrolyte medium respectively[114]. Particles from the same colloidal dispersion should also have the same surface charge, causing a repulsive force between them. This force on

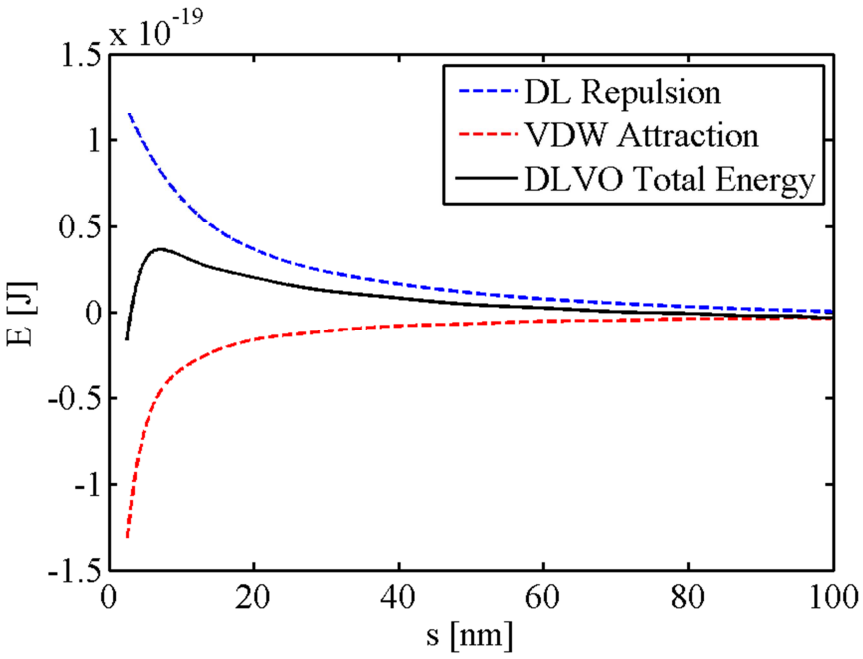

FIG. 2.2 DLVO potential energy barrier between two colloidal nanoparticles

The van der Waals potential energy (VDW Attraction/Eq. (2.6)) and the electrical double layer potential energy (DL Repulsion/Eq. (2.10)) are combined in DLVO theory to produce a metastable energy barrier between two gold 20 nm diameter particles with separation, s in water. V_W was determined with an experimental value for H_e of 4x10^{-19}J.[111],[135] V_E was determined by simulation of the *Poisson-Boltzmann* equation with the finite element method for an electrolyte containing an equal number of single valency anions and cations with concentrations of 1 µM each and an electric surface potential of –100 mV.

these particles can then be calculated by integrating the Maxwell Stress Tensor over the nanoparticle's surface[113]:

$$\vec{F} = \oiint \left\{ \varepsilon_0 \varepsilon_r \vec{E}\vec{E} - \frac{1}{2}\varepsilon_0 \varepsilon_r \vec{E}.\vec{E}\bar{\bar{I}} \right\}.\vec{n}dS \tag{2.9}$$

where $\vec{F}$ is the electric force calculated for all the following results, $\bar{\bar{I}}$ is the unit tensor, $\vec{n}$ is the normal vector to the surface and the electric field $\vec{E} = -\nabla\psi(\vec{r})$. The interaction energy of this repulsion V_E can then be obtained by integrating this force with respect to the separation $\vec{s}$ between the surfaces[115]:

$$V_E = \int_s^\infty \vec{F} d\vec{s} \tag{2.10}$$

The combined contribution of these attractive and repulsive potential energy contributions $V_T = V_W + V_E$ forms the basis of DLVO theory, named for the collective contributions of Derjaguin and Landau[116] and Verwey and Overbeek[117]. The energy barrier created between two colloid particles by the double-layer repulsion prevents the agglomeration of particles that would otherwise occur due to van der Waals forces. This permits the metastable state of a colloidal dispersion, which would otherwise agglomerate to the lower entropy state of a large bulk (FIG. 2.2).

The stability of this energy barrier can be affected by several factors. If the electrolyte the colloidal particles are dispersed in have a higher ionic strength, then the diffuse electric double layer shrinks in size as the surface charge of the particles is neutralised by counter-ions more efficiently. This is represented by the inverse Debye length (Eq. (2.6)): for an electrolyte with anion and cation concentrations of 1 μM the double layer reduces the boundary potential to half its initial value at a distance of κ^{-1} = 305 nm, but this is reduced to just 13.6 nm for a higher concentration of 500 μM. This reduces the effectiveness of the electrical repulsion between particles in a colloid, so

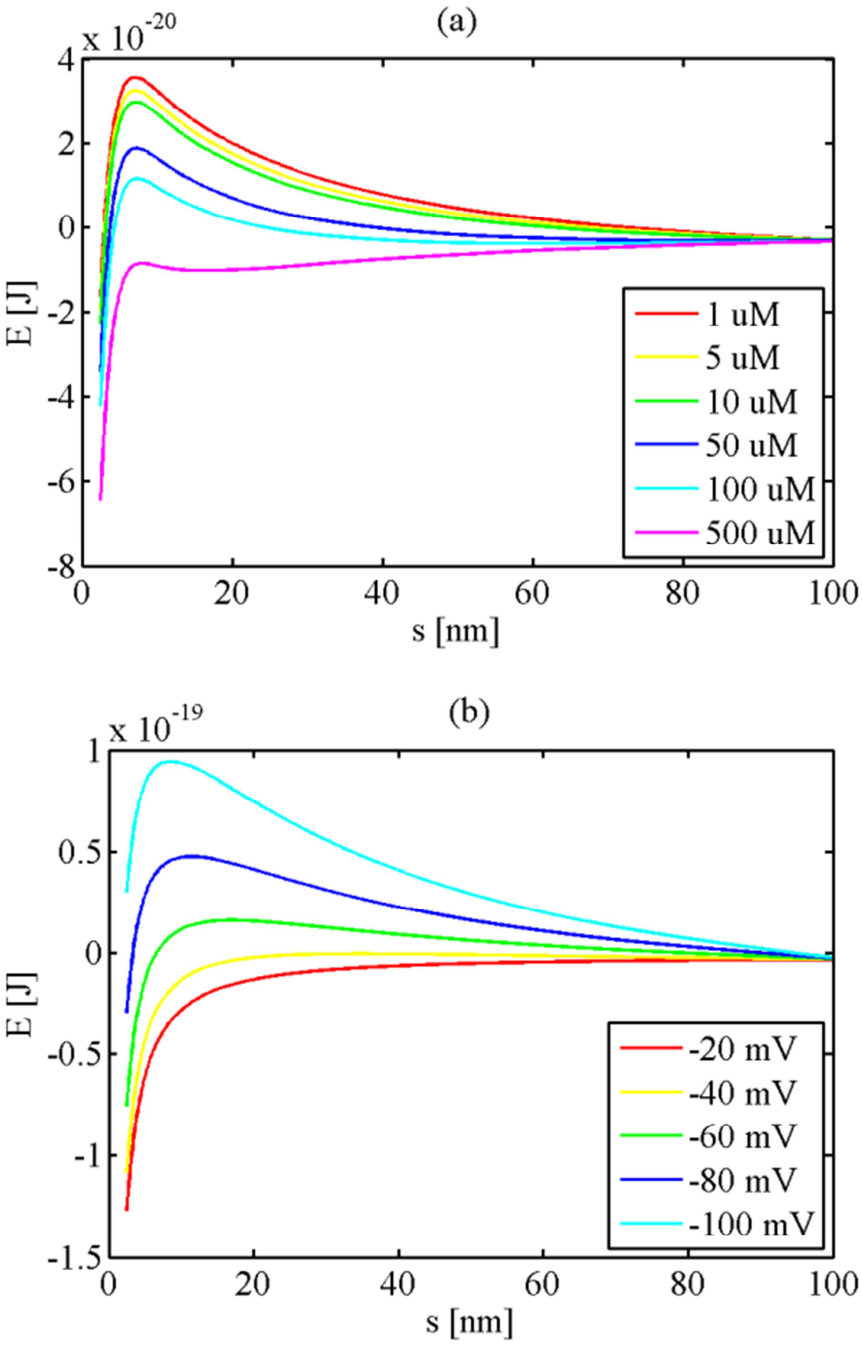

FIG. 2.3 Dependence of colloid stability on ion concentration and surface potential.

The above graph shows the total potential energy barrier between two gold 20 nm diameter particles with separation, s in water. V_W was determined with an experimental value for H_e of $4x10^{-19}$J.[111],[135] V_E was determined by simulation of the *Poisson-Boltzmann* equation with the finite element method for an electrolyte. In (a), the electrolyte containing an equal number of single valency anions and cations with concentrations ranging from 1 µM to 500 µM each and a surface potential of -100 mV. In (b), the electrolyte concentration is held at 1 µM and the surface potential is swept from -20 mV to -100 mV.

that the van der Waals attraction becomes the strongest interaction (FIG. 2.3a). This makes the colloid unstable, so particles agglomerate to form larger masses. Colloid stability is also highly dependent on the magnitude of the particles' zeta potential. If the surface potential is too low, then electric repulsion is insufficient to create an energy barrier to prevent particle agglomeration (FIG. 2.3b). In practice, these considerations of colloid stability oversimplify the system as it is difficult to separate the effect of changes in ionic strength and zeta potential. In the formation of a colloid (Section 2.1), low electrical repulsion could be the result of a low concentration of capping agent: the particles will continue to agglomerate matter until stable state is reached at a larger size. However, the zeta potential is nominally independent of the particle size once alike colloids have stabilised and the choice of capping agent is the biggest factor to creating smaller nanoparticles.

An additional repulsive force arises from the mutual repulsion between counter-ions and water molecules as two surfaces are brought close together. The contribution of this force was included in the calculations of Huang et al. when they explained their process for nanoparticle self-assembly[48]. However, the effective range of this osmotic pressure does not extend to more than a few nanometres[111]. This prevents the hydration forces from having any meaningful contribution to the funnelling effects that arise from the self-assembly of nanoparticles, where interparticle separation is several times that of the particle size[105].

2.3 Simulation of Single Nanoparticle Placement Devices

The pioneering experiments for single nanoparticle capture utilised a self-assembly approach, to assemble negatively charged 20 nm diameter gold particles onto tailored surfaces. This self-assembly, which was discussed in the Introduction, was achieved by

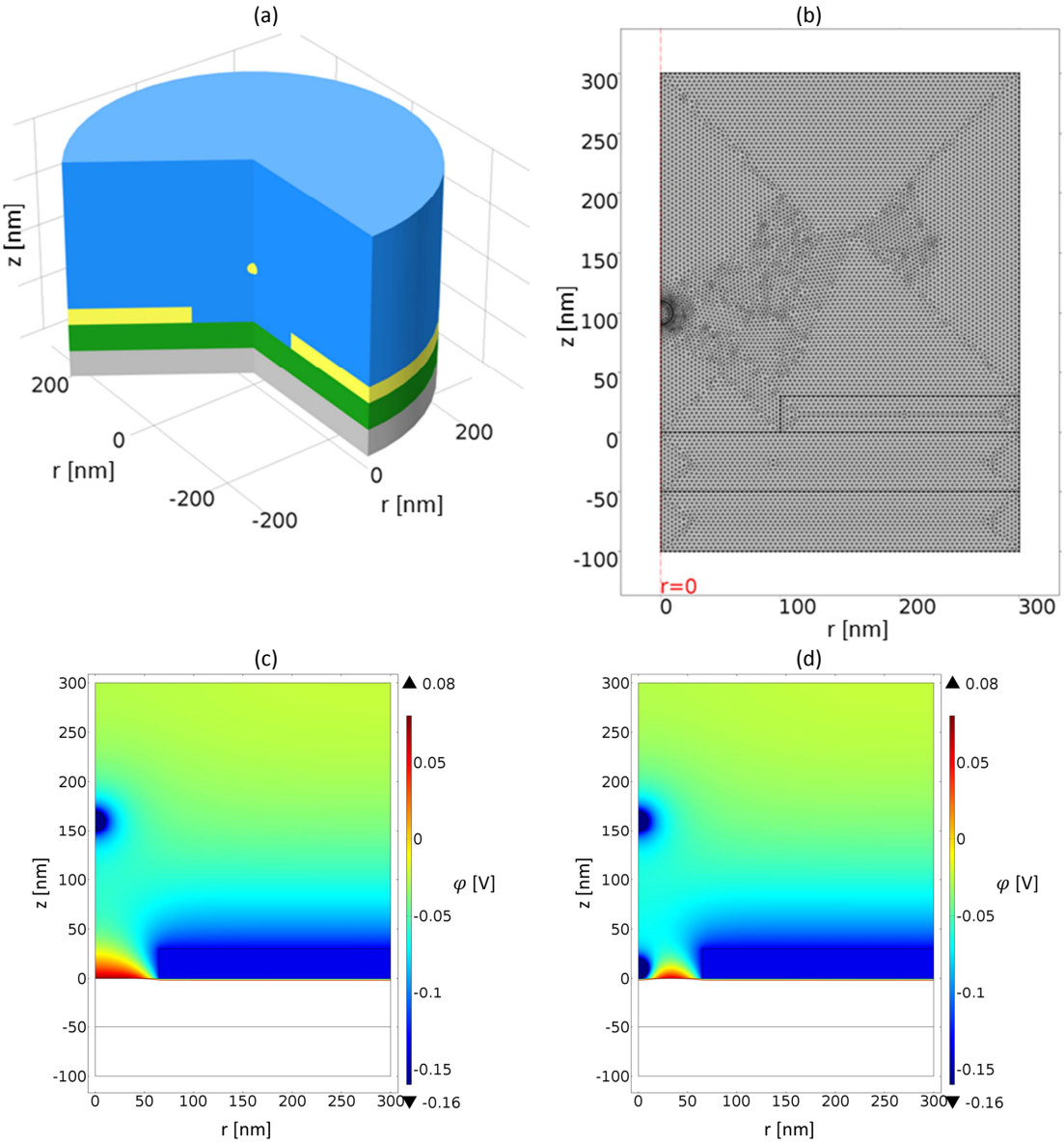

FIG. 2.4 Finite Element Analysis.

The finite element model created using COMSOL Multiphysics. (a) 3D rendering of 2D axially symmetric model rotated around the z-axis. (b) The triangular mesh generated on the 2D plane, with a maximum dimension of 2 nm. (c, d) The electric potential produced above a Gate device (c) with and (d) without a second nanoparticle occupying the centre of the target area.

patterning a surface of SiO_2 with Au and coating these surfaces with amino-terminated silane and carboxyl-terminated thiol monolayers respectively. In aqueous solution of a fairly neutral pH, the amino surface undergoes protonation to become positively charged and the carboxyl surface undergoes deprotonation to become negatively charged. When brought into contact with a colloid dispersion of negatively charged 20 nm gold nanoparticles, they demonstrated that these particles can be funnelled onto the positively charged surfaces[105], with Coulombic repulsion excluding other nanoparticles and achieving single-nanoparticle capture with a high success rate[48]. To enable us to achieve this feat of self-assembly using voltage-controlled electric fields, we sought to reproduce the simulations they used to explain this process[48]. With these results, we reasoned that the force profile for this approach would provide a benchmark of what electric field conditions would achieve single-nanoparticle capture.

We performed finite element analysis of each strategy we considered for particle capture using COMSOL Multiphysics, a finite element analysis software package. We used the Guoy-Chapman Theory in COMSOL to calculate the electric potential in a 20 nm Au colloidal dispersion. An example of the geometry and calculated electric potential for these devices is presented in FIG. 2.4. The simulations used the same values for surface potentials and ionic concentrations as calculated in the original paper on nanoparticle funnelling by Ma et al.[105]. In order to maintain the zeta potentials required for manipulation with electric fields for controlling the nanoparticles, they should be kept in an aqueous solution of roughly neutral pH. The colloidal gold examined contained 20 nm Au nanoparticles with bulk ion concentrations of $[Na^+] = 4.2\text{x}10^{-6}$M, $[C_6O_7H_7^-] = 9.7\text{x}10^{-9}$M, $[C_6O_7H_6^{2-}] = 6.5\text{x}10^{-7}$M,

$[C_6O_7H_5^{3-}]$ = 1.0x10^{-6}M, $[H_3O^+]$ = 2.5x10^{-7}M and $[OH^-]$ = 4.0x10^{-8}M and the surface potentials for the self-assembled monolayer of 16-mercaptohexadecanoic acid (MHA) and the Au nanoparticles were taken as -134 mV and -159 mV respectively, as previously determined[48],[105].

Calculations were also performed using the time-dependent Poisson-Nernst-Planck system (Appendix A), which more accurately simulated the distribution of ions but was computationally slow and produced similar results to the Poisson-Boltzmann equation.

2.3.1 Simulations of *Gate* Devices

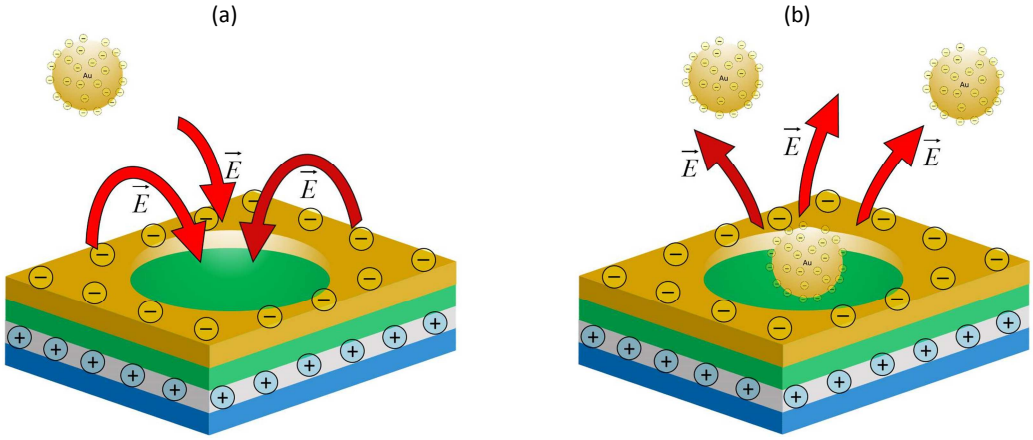

FIG. 2.5 Gate Device Concept.

An electric bias is applied to a Ti layer (light grey), insulated from the colloid by Si_3N_4 (green) and patterned with Au (gold), functionalized with a self-assembled monolayer of MHA for a negatively charged surface in solution. (a) The electric field attracts negatively charged 20 nm Au particles in the solution towards the holes (gates) in the Au layer, whilst the negative surface potential results in funnelling towards the centre of each gate. (b) Once one particle is attached to the surface of the gate, it provides a negative screening charge, with the resulting electric field preventing deposition of further nanoparticles.

To enable capture of single nanoparticles by voltage-driven electric fields, we developed a device design referred to as gates, which is illustrated in FIG. 2.5. An

example of the resulting force profiles for unplugged and plugged gates in this colloid

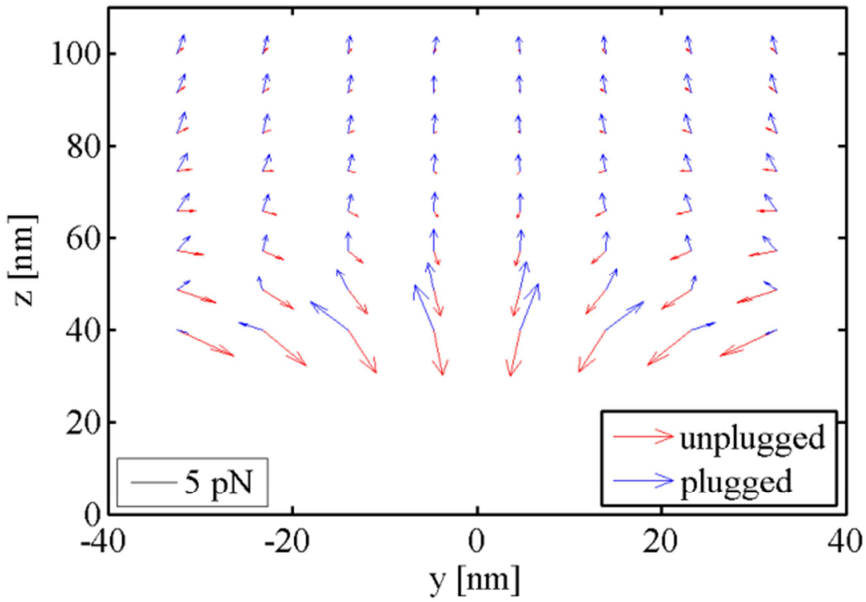

FIG. 2.6 Voltage Driven Placement: Force Vectors in Liquid.

An arrow field plot of the forces acting on a nanoparticle at a range of locations above a gate for unplugged and plugged gates. The length of the vector indicates the magnitude of the force relative to the arrow in the key. The variables z and y denote the height of a particle above the gate and the radial position of the particle respectively.

is illustrated in FIG. 2.6, where the arrow field represents the resulting force vectors for the unplugged (red) and plugged (blue) regimes of the gate. This profile shows a clear change in the force profile once the gate is plugged, with repulsive forces replacing the attractive forces of an unplugged gate. The lateral forces also guide particles towards the centre of the gate, resulting in the central placement of the particle. Thus when comparing the different designs we have focused on the vertical forces above the centre of the gate. The following section details the results of these simulations and a discussion on the optimal parameters required for single particle placement.

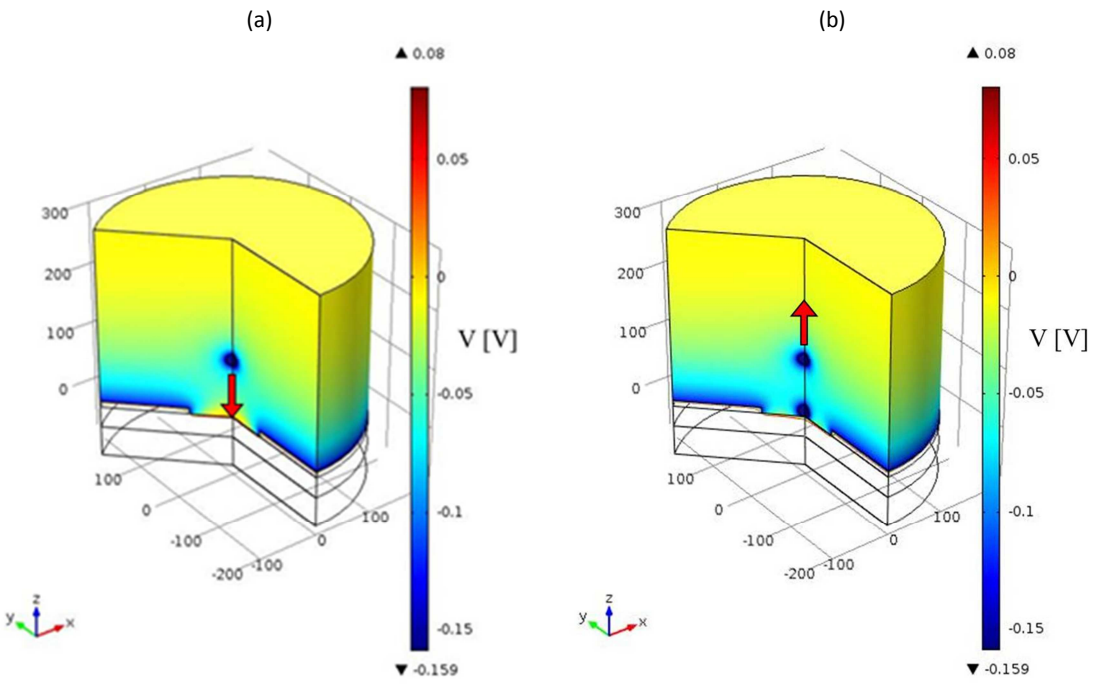

FIG. 2.7 Rendering of gate device simulated electric potential.

(a) & (b) The volume electric potential of an (c) unplugged and (d) plugged gate with a 20 nm Au nanoparticle in close proximity above the gate. In these models the gate is 130 nm in diameter, the Si_3N_4 insulation layer is 50 nm thick, a 1 V bias is applied through the Ti underlay and the zeta potentials of the patterned Au and nanoparticles are -135 mV and -159 mV respectively. The red arrows represent the force acting on the particle above the gate.

Alongside these results, the equivalent forces for the static charge method established by Huang et al.[48] were also modelled (designated as “static” in the results) to offer a direct comparison for our proposed directed assembly system. As a measure of the significance of the forces exerted on particles in this colloid, we considered the characteristic Brownian force acting on these 20 nm particles as being on the order of *kT/a*: this is approximately 0.4 pN for this system, where *a* is the radius of the gold nanoparticles. To comprehensively describe the gate, we varied the diameter of the gate, the voltage applied and the thickness of the Si_3N_4 insulation, and the effects on the performance of the gate were analysed. (These values were typically held at

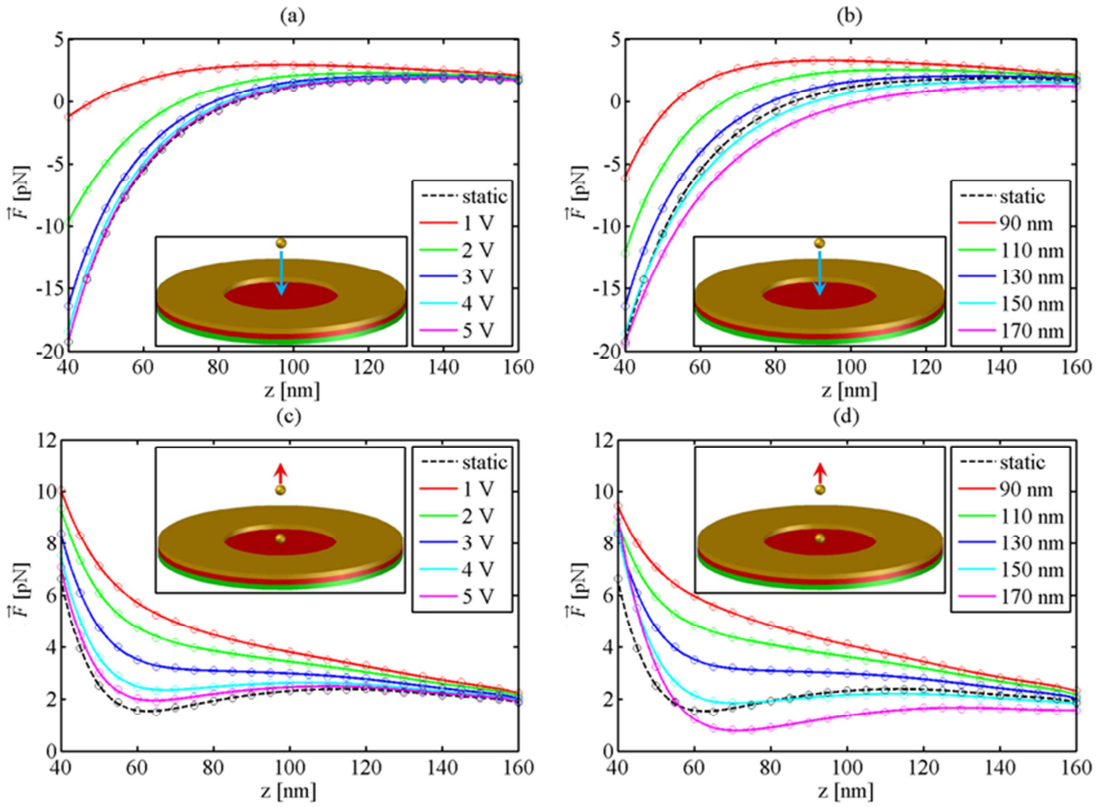

FIG. 2.8 Voltage Driven Placement: Effect of Applied Voltage and Gate Diameter.

The force $\vec{F}$ acting on a nanoparticle at varying height z above the centre of a gate simulated with 50 nm of Si_3N_4 insulation for different voltages and gate diameters (a positive force points upwards and away from the gate and vice versa for a negative force). The target location on the gate was vacant for (a) and (b) and occupied by another nanoparticle in (c) and (d). (a) and (c) show the effects of varied voltage for a 130 nm diameter gate; (b) and (d) show the effects varied diameter for a 3 V applied bias. Static indicates the equivalent force profile for the statically charged device that Huang et al. pioneered[48].

130 nm, 3 V and 50 nm respectively when other values were altered.) The principal objective of these tests was to ascertain the ideal conditions for single nanoparticle capture; the largest geometrical dimensions that could reliably capture nanoparticles of much smaller diameter would enable better reproducibility in fabrication.

When no nanoparticle is captured (an unplugged gate) a 5 V bias is sufficient to create attractive forces that are strong enough to match the forces obtained by the static

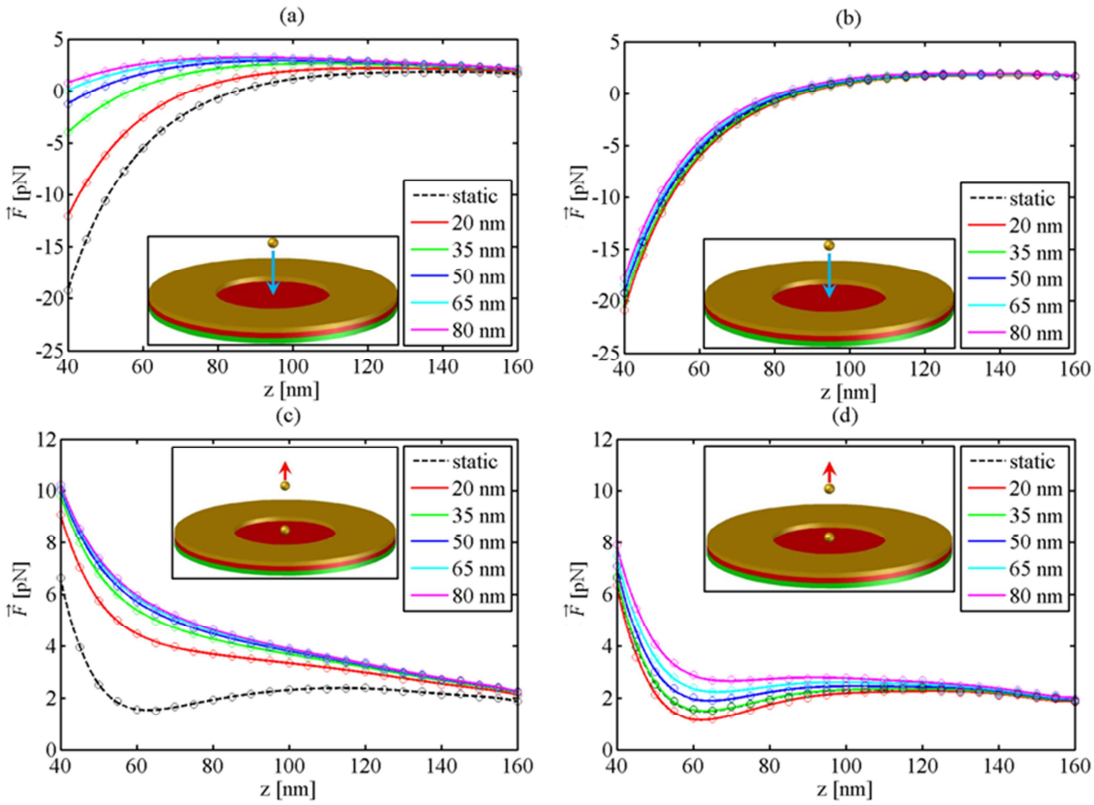

FIG. 2.9 Voltage Driven Placement: Effect of Insulator Thickness.

The force $\vec{F}$ acting on a nanoparticle at varying height z above the centre of a gate simulated with varied applied voltage (a negative F is vertically down towards the gate, positive is upwards away from it). The insulation thickness was varied in all cases (see inset key), with an applied bias of 1 V in (a) and (c) and 5 V in (b) and (d). The target location on the gate was vacant for (a) and (b) and occupied by another nanoparticle in (c) and (d). Static indicates the equivalent force profile for the statically charged device that Huang et al. pioneered[48].

charge method[48] (FIG. 2.8a). Higher voltages for this typical geometry do not lead to substantially stronger attractive forces in the gate region. When the diameter is varied (FIG. 2.8b), we find that, as expected, larger diameters result in higher attractive forces, indicating that they are likely to attract multiple nanoparticles. Encouragingly, when a nanoparticle is captured in a gate (now a plugged gate) the resulting repulsive profile is relatively strong (

FIG. 2.8c), which would prevent the approach of additional nanoparticles thus ensuring selectivity. Conversely, smaller-diameter gates are less likely to capture a nanoparticle, given the smaller magnitude of the attractive force and the lower probability of a nanoparticle being captured by the attractive force funneling vectors (FIG. 2.8d). Thus the optimum design is a balance between these two competing interests with the goal being to use the largest possible diameter that can result in single particle sensitivity.

The sensitivity of the gate to changes in the voltage may also be tailored by alterations to the thickness of the insulation layer (FIG. 2.9). For instance, with a thinner Si_3N_4 insulation of 20 nm, a 1 V bias (FIG. 2.9a and FIG. 2.9c) achieves a substantially stronger attractive profile than for thicker insulations. This difference is markedly reduced when the bias is increased to 5 V (FIG. 2.9b and FIG. 2.9d), although the repulsive profile is still much weaker at this magnitude. From this a gate with thinner insulation and relatively low voltage (1-2 V) can be deemed the best choice. However, quality of very thick insulating layers can be highly variable, leading to imprecision in the particle placement within the gate. Optimizing this accuracy will be especially vital for the future functionality of nanomanufacturing.

Modifying the applied voltage is the most important feature in this design as it allows us to adjust the force exerted on the nanoparticle, depending principally upon its surface potential. This dependency is illustrated in FIG. 2.10, where the value of the surface potential is given a hypothetical 50% uncertainty and the resulting force profiles of plugged and unplugged gates are plotted. From this we see that for nanoparticles with higher surface potentials the same placement effect appears to be more effective, with stronger attractive and repulsive forces for unplugged and

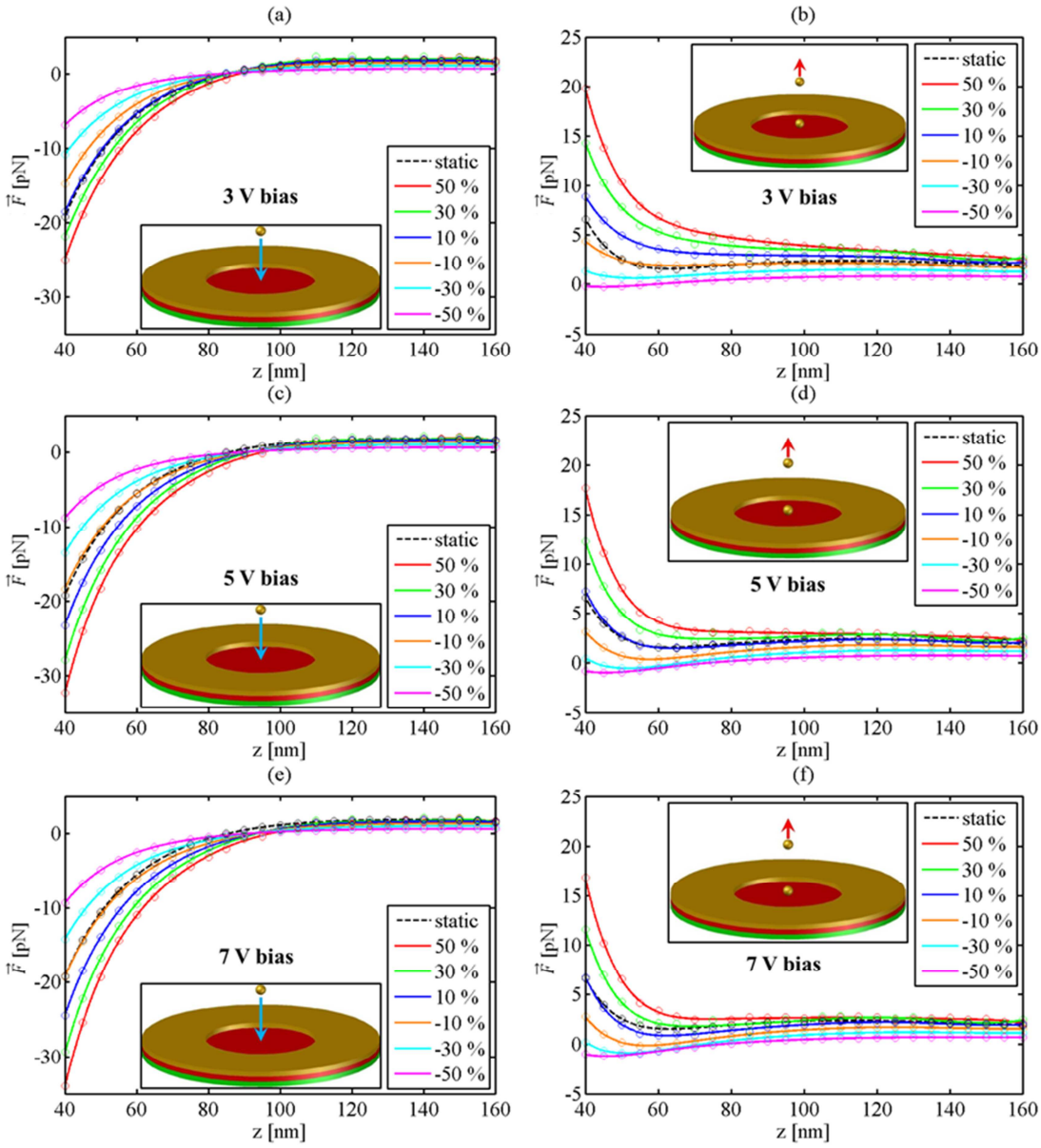

FIG. 2.10 Voltage Driven Placement: Effect of particle surface potential.

The force $\vec{F}$ acting on a nanoparticle at varying height z above the centre of a gate simulated with a hypothetical 50% uncertainty in the magnitude of the Au nanoparticle's surface potential (a negative F is vertically down towards the gate, positive is upwards away from it). The applied bias was set at 3 V in (a) and (b), 5 V in (c) and (d); and 7 V in (e) and (f). The target location on the gate was vacant for (a), (c) and (e) and occupied by another nanoparticle in (b), (d) and (f). Static indicates the equivalent force profile for the statically charged device that Huang et al. pioneered[48].

plugged gates respectively. Although relatively weak attractive forces are also experienced for lower surface potentials, the repulsive forces of plugged gates appear compromised by the reduced screening potential of the nanoparticle protecting the gate. Therefore, it appears that there could be a lower limit to the potential a nanoparticle would need for a specific gate to isolate it from suspension. Lower surface potential would likely result from a smaller particle size, so it would benefit from reduced gate dimensions requiring lower voltage; larger particles could also be inhibited by gates that are too small.

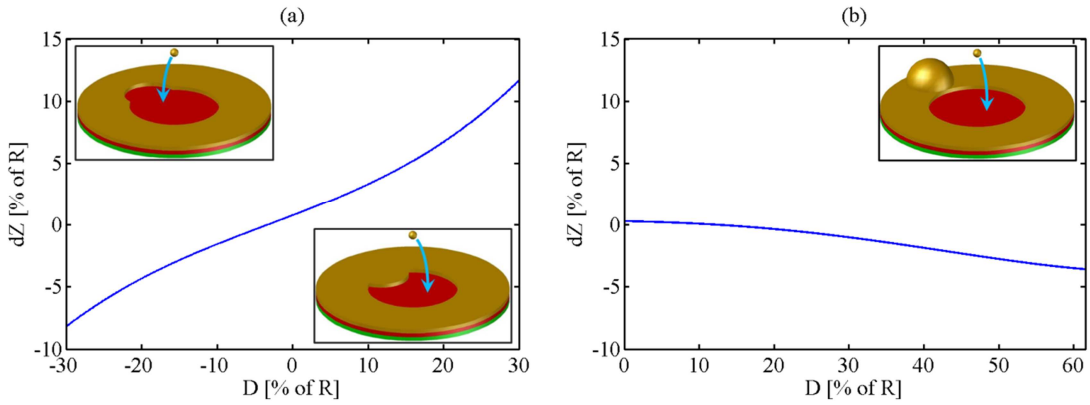

FIG. 2.11 Voltage Driven Placement: Effect of Geometrical Imperfections.

Testing the robustness of a gate 130 nm in diameter to fabrication defects. (a) The results of possible lithographic edge defects of size D on the placement of nanoparticles dZ, presented as percentages of the original gate radius R. (b) The results of possible Au deposition defects of size D on the placement of nanoparticles dZ as percentages of the gate radius R.

The robustness of the design can also be demonstrated by simulating the effect of defects in the gate fabrication process on the placement of nanoparticles. These defects would represent the worst-case fabrication abnormalities, assuming processes that are completely out-of-spec. For example, in the first instance, we consider defects accrued by lithographic processes in the Au top layer could produce a deformed shape of the gate, as illustrated in the plan views of FIG. 2.11a. The results indicate that up to

a 30% deformation of the gate geometry in either direction (relative to the intended gate radius) would have a limited effect on the equilibrium point nanoparticles will be drawn to, with inset defects causing the greater displacement. This is because the dielectric in contact with the solution is reduced, weakening the electric field that attracts the nanoparticles and making the lateral forces of the SAM relatively stronger than with offset defects. This demonstrates that the system is very tolerant to patterning defects; for example a 10% deformation would cause a 3.3% particle placement error for the design.

Another type of defect that is not uncommon in patterning and lift-off processes is surface flatness variations. Such defects could also be caused during the Au deposition, potentially causing bulges in the layer that make the influence of the SAM electric potential on any nearby particle more prominent in that region. We model such a defect for the worst case scenario, i.e. a single defect in the metal layer near the edge of the surface. The results in FIG. 2.11 show that even if these defects were to reach unrealistic levels of 40 nm in size (which is four times the thickness of the Au layer), they would still only affect the nanoparticle placement by 3.6%. This indicates that deposition defects would have around 4 times less impact on the placement than patterning defects. This robustness is a result of the gates being essentially 3-dimensional; thus surface defects near the edges have a smaller effect in the plane.

Among the exciting possibilities of this design, this work could lead on to implementing such “gates” on AFM probes, which could then be used for controlled transfer of individual nanoparticles. The limit to the maximum gate dimensions will need to be examined under experimental testing to validate the effectiveness of these designs for single nanoparticle capture. The voltage required to trap these particles is

shown to be lower with a larger gate diameter, but this could compromise the central positioning of captured particles and result in multiple particle capture.

2.3.2 Simulations of Pedestal Devices

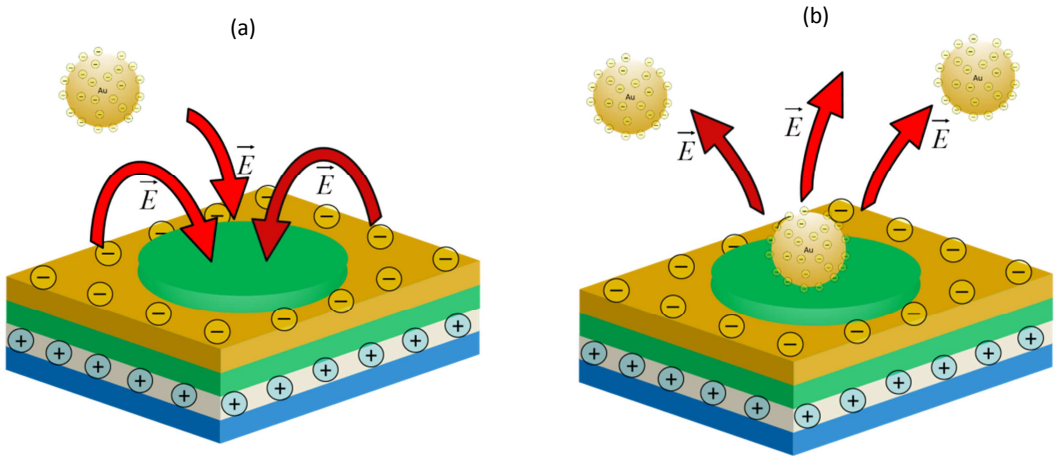

FIG. 2.12 Pedestal Device Concept.

This concept is very similar to the Gate Device Concept (FIG. 2.5), with the alteration that the SiO_2 target area is raised up above the surrounding Au surface like a pedestal. In this way when an electric bias is applied to the lower electrode, nanoparticles are funnelled on top of the pedestal, blocking the approach of additional particles afterwards (b).

The pedestal device design operates by the same principles as the gate device, with the addition that the target area is raised up above the surface of the device (FIG. 2.12). This design requires additional steps for fabrication, but if successful captured particles will be proud of the surface and thus in a better location to be transferred to another surface they are brought into contact with. This configuration is also more akin to a probe.

The results from simulations with pedestal devices are presented in FIG. 2.13, with a plot for an equivalent gate device included. With an increasing height of pedestal the attractive force in an unplugged pedestal becomes increasingly weak, due to the

greater separation between the electrode and the particle. In the case of a 5 V driving voltage (FIG. 2.13a), only a pedestal height of 25 nm can achieve a consistently

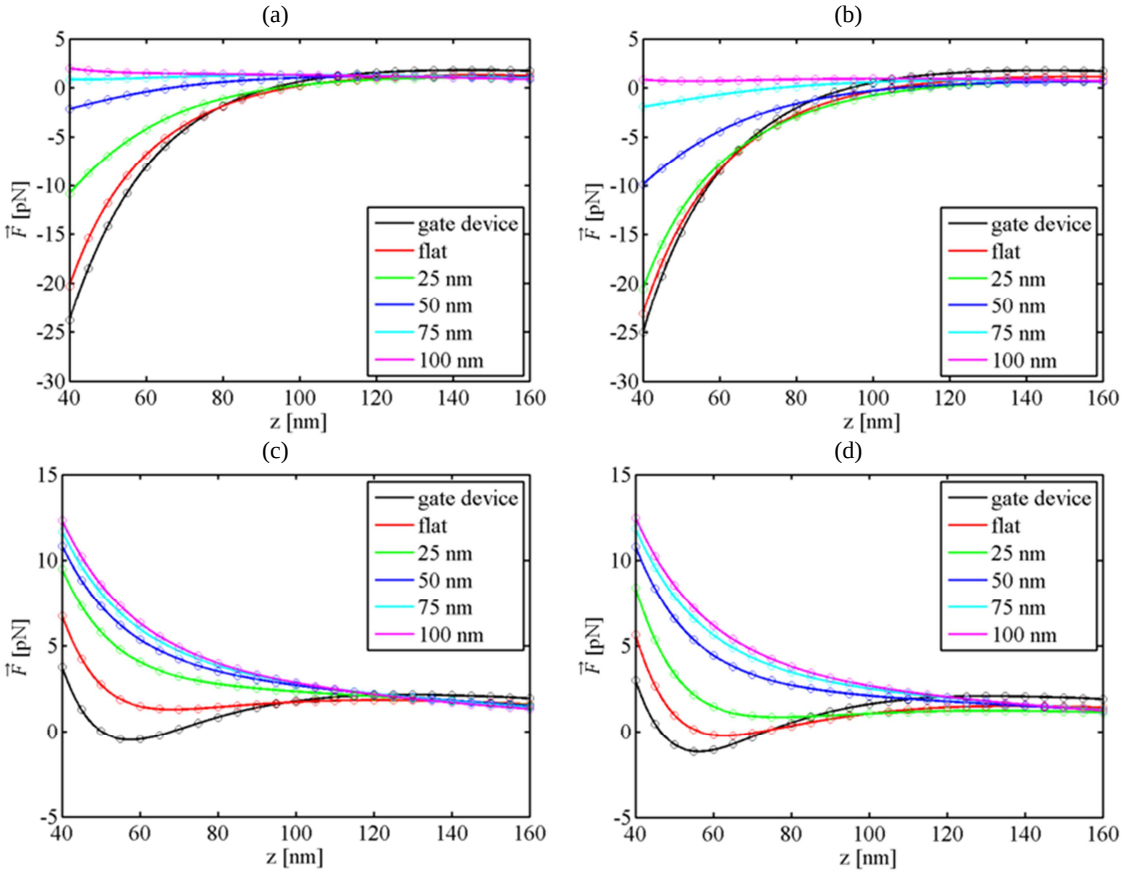

FIG. 2.13 Effect of Pedestal Height and Voltage.

The force $\vec{F}$ acting on a nanoparticle at varying height z above the centre of a gate simulated with varied applied voltage (a negative F is vertically down towards the gate, positive is upwards away from it). In all simulations the pedestal height was varied, with (a, c) a 5 V bias or (b, d) a 10 V bias applied to the lower electrode and the pedestal-target area had a diameter of 130 nm. 50 nm of SiO_2 insulation separated the electrode and the base of the surrounding 30 nm thick Au area. The target area was vacant in (a, b) and occupied by another nanoparticle in (c, d). Gate device and flat indicate the force response for the gate device configuration described above and when the target area is level with the surrounding functionalised-Au respectively.

attractive force profile and an adequate repulsive profile when a particle has been captured (FIG. 2.13c). Increasing the driving voltage to 10 V (FIG. 2.13b) allows a taller pedestal of around 50 nm to achieve a moderate attractive force profile, whilst

maintaining a sufficient repulsive force to inhibit the approach of additional nanoparticles (FIG. 2.13d). This higher driving voltage is more likely to result in damage to the device, so whilst these results indicate that a pedestal device could feasibly achieve single-nanoparticle placement the mechanism is more likely to be successful with the gate device described above.

2.3.3 Simulations of Interdigitated Electrode Devices

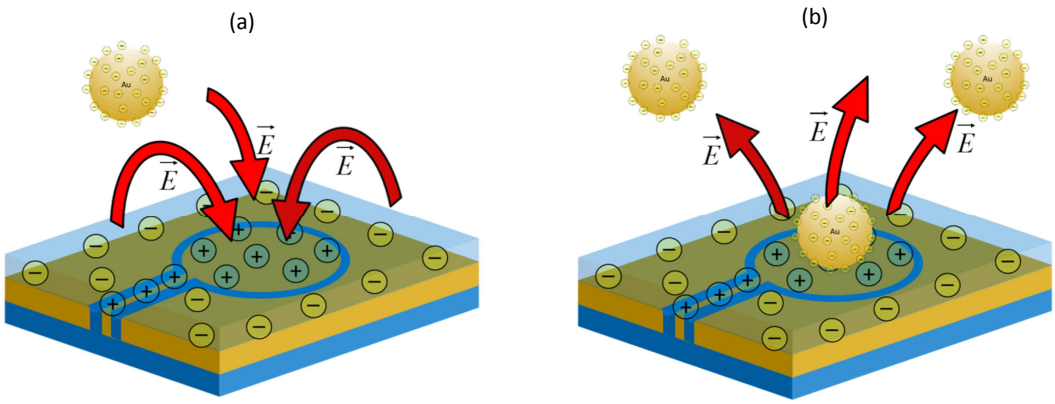

FIG. 2.14 Interdigitated Electrode Device Concept.

In this concept the anode and cathode of a capacitor are interdigitated in a design that should generate a funnelling electric field similar to that of the other devices (FIG. 2.5, FIG. 2.12). These electrodes were encapsulated in a layer of SiO_2 insulation (semi-transparent top layer) to prevent the discharge of particles upon capture. The resulting electric field should then (a) funnel nanoparticles onto the SiO_2 above the anode, (b) where it should prevent the approach of additional nanoparticles.

An alternative to the functionalisation of surfaces could be to drive single nanoparticle placement entirely through the use of an applied bias on interdigitated electrodes (FIG. 2.14). In this case the positive and negative terminals are connected to the inner and outer electrodes respectively to provide the driving electric field for single-nanoparticle placement. The results of simulations for these electrodes for varied

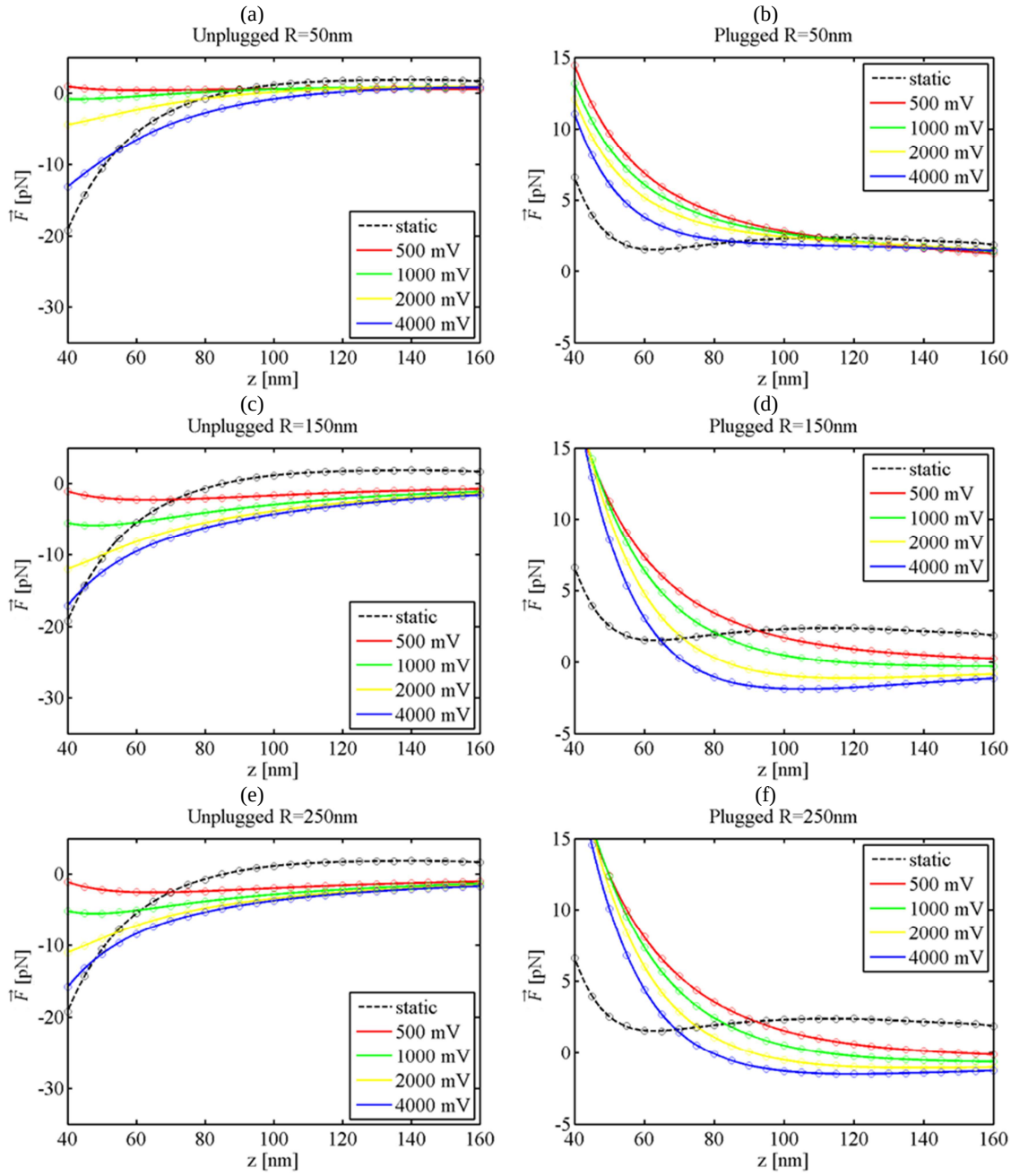

FIG. 2.15 Interdigitated Electrode Placement: Effect of Voltage and Anode Radius.

The force $\vec{F}$ acting on a nanoparticle at varying height z above the centre of an interdigitated electrode setup, simulated with varied applied voltage (a negative F is vertically down towards the gate, positive is upwards away from it). The applied voltage between the electrodes was varied for all these devices, with the radius of the cathode changed from 50 nm (a, b) to 150 nm (c, d) and 250 nm (e, f). The target location on the electrode was vacant for (a, c, e) and occupied by another nanoparticle in (b, d, f). Static indicates the equivalent force profile for the statically charged device that Huang et al. pioneered[48].

applied bias and diameters of the inner electrode (FIG. 2.15); the covering layer of SiO_2 insulation was fixed at 50 nm and the electrodes were separated by 100 nm. As with the Gate and Pedestal devices, a stronger applied voltage and a larger drain diameter increase the force drawing nanoparticles towards the central anode. However, it is only with a relatively small anode diameter of 50 nm that the repulsive force for a plugged device is sufficient to prevent the approach of additional nanoparticles (FIG. 2.15b). For larger anode diameters (FIG. 2.15d, f) the force acting on the nanoparticles was attractive over long range, particularly at the higher voltages required to attract the first particle. This is primarily due to the large gap between the electrodes, necessary to keep them insulated. Reducing the spacing between these electrodes should reduce this effect but will make devices of this type more difficult to fabricate. This indicates that the interdigitate electrode devices could achieve the same successful single-particle placement of the gate devices discussed above, but would require smaller critical dimensions.

2.4 Chapter Summary

We have proposed an innovative voltage-driven, self-limiting single nanoparticle capture process for colloidal dispersions. By numerical analysis we modeled the electric potential profile exerted by all these designs, with DLVO theory of electric potential at charged interfaces used for the solution the nanoparticles were dispersed in. Simulations with this system compared to successful self-assembly experiments demonstrate that these designs will selectively capture single nanoparticles by repelling other particles once a particle is captured. A larger gate will lead to a greater force, but increases the chance of capturing multiple particles in any one gate,

although we speculate that there is a range of particle sizes and surface potentials that can be isolated by any one gate – we show that up to a 50 % increase in the surface potential of the Au nanoparticle would improve the particle selectivity. we have also shown that this design would be very resilient to fabrication defects, with lithography defects of 10% and deposition defects of 400% only effecting particle placement by 3.3% and 3.6% respectively, which indicates a very highly robust methodology. This novel system could in essence be used for robust single nanoparticle capture with an applied voltage, and once the captured nanoparticles are placed on a target substrate, will be able to repeat this process of capture repeatedly. In the next chapter we use these parameters to fabricate proof-of-concept devices, which we tested to see if single-nanoparticle placement could be achieved by this method. If successful, then this method could be applied to our ultimate goal of capturing and placing particles with a probe tip for pick-and-place nanomanufacturing.

Chapter 3

Voltage-driven devices for single-particle placement

Simulations in chapter 2 showed that single-nanoparticle capture can be achieved using voltage-driven devices. These devices combine controlled electrical biases with molecularly functionalised surfaces to create new adjustable capture mechanisms. In this chapter we present our efforts to build and test the ability of these devices to capture nanoparticles from colloidal dispersions of Au nanoparticles. We detail the nanolithography methods we employed to build these devices, based on standard electron-beam lithography with thin-film deposition and monolayer self-assembly. Finally, the results of these tests are analysed based on scanning electron microscope images of the resulting nanoparticle deposits to determine the effectiveness of the devices at achieving single-particle placement.

3.1 Fabrication process

3.1.1 Electron-beam lithography

The fabrication process for all the devices built during this project was based upon standard electron-beam nanolithography. The specific system we used to do this was a Jeol 5500FS, which is based in the Denys Wilkinson building's class 10,000 cleanroom.

Electrons are accelerated to energies of 50 keV and concentrated into a focused beam through an electron gun column. For nanolithography, a sample coated with an electron-sensitive film is exposed to this beam, which changes the solubility of this "resist" in the exposed area. This enables 2D nanometric features to be written into the resist. When the sample is removed, immersion in an appropriate developer causes the solvation of exposed (or unexposed) areas of the resist, creating a 2D mask corresponding to the pattern written by the electron-gun with features down to a few nanometres in size. Thin-film deposition and etching processes and subsequent removal of this resist allow transfer of these features into final devices.

3.1.2 Positive and negative-tone electron-beam resists

The choice of resist in this process is very important. The most commonly used e-beam resist in our cleanroom was poly(methylmethacrylate) (PMMA). This resist is dissolved to a 2-8 % solution in anisole, which is spin-coated onto a clean substrate at speeds of 1000-6000 rpm. Once coated, the substrate is baked on a hot plate typically at 180°C for 90 seconds, which evaporates the acetate solvent, leaving behind a film of PMMA 100 – 400 nm in thickness (depending on spin-coating speed). During e-beam lithography, the electron irradiation breaks the bonds between the polymer chains, making the exposed areas more prone to solvation. The developer often used for the PMMA after exposure is methyl isobutyl ketone (MIBK), usually diluted in isopropanol (IPA) to prevent damage to the unexposed resist. For instance, a dilution of MIBK:IPA 1:3 had a development time of 30 seconds for an exposure dose of 300 $\mu C/cm^2$.

Resists that break down under electron-beam exposure this way are called positive e-beam resists. However, there also many types of negative e-beam resist, which have

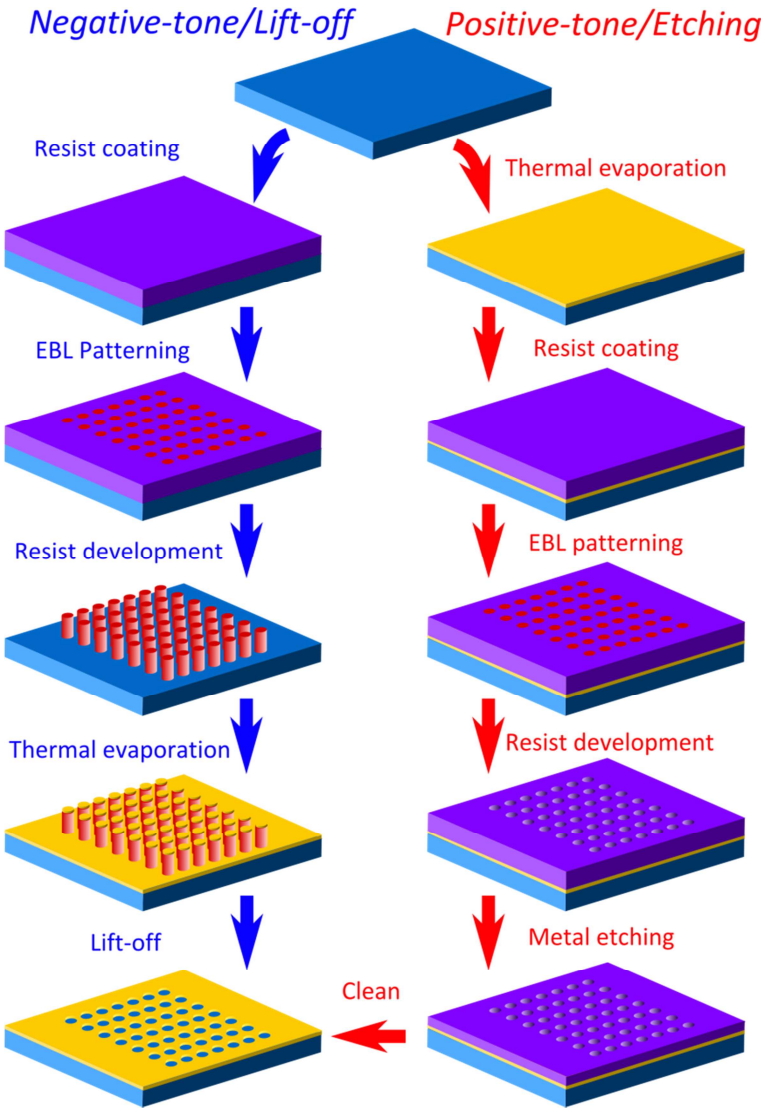

FIG. 3.1 Electron Beam Lithography (EBL) process with positive and negative-tone resists.

Above are two of the fabrication workflows we used to create arrays of holes in Au for *Gate* and *Pedestal* devices is presented. When using the negative e-beam resist Ma-N 2405, a dielectric-coated wafer was spin-coated with the resist and then patterned by EBL. Development left the exposed areas intact creating pillars of resist that masked the area underneath them from subsequent thermal evaporation of approximately 30 nm of Au (with 5 nm Cr adhesion layer), which left arrays of holes in the Au after resist lift-off. With the positive e-beam resist PMMA, the wafer was first coated with Cr/Au before spin coating of the resist and subsequent EBL patterning. Development removed the exposed resist, leaving the underlying metal layer exposed to dry or wet etching processes, which left arrays of holes in the Au after resist lift-off.

the reciprocal response of strengthening under electron beam exposure. The negative-tone resist we used during fabrication, Ma-N 2405 produced and distributed by Micro Resist Technology GmbH, consists of two components: a polymeric bonding agent, a novolak based resin, and a photoactive compound, an aromatic bisazide[118]. During electron irradiation, cationic polymerisation occurs wherein the photoactive compound becomes charged and reactive, consequently binding together the surrounding polymer agent. This results in the exposed areas of resist remaining intact when the resist is developed in Ma-D 525 – an alkali based solvent produced by Micro Resist technology GmbH for development of Ma-N 2400 series resists.

The selection of a positive or negative tone e-beam resist is primarily driven by the requirements of the specific fabrication process, as illustrated in FIG. 3.1. In this case, negative-tone Ma-N 2405 was initially selected when the subsequent metal layer was deposited by thermal evaporation of Cr and Au, as this provided the most efficient e-beam writing process. The steeper side walls of this resist also made removal (or "lift-off") of the metal-coated resist areas simpler in principle. However, another fabrication route we used involved the etching of an existing metal layer beneath a patterned resist. We also tried reversing the written areas of the resist with PMMA, so as to expose the areas surrounding the remaining pillars in a similar manner to the negative-tone process, which had a much higher writing time. Ma-N 2405 also suffered from inconsistency due to the age of the available solution, other adhesion issues and sometimes features collapsed because the resist could not be made thinner. These issues were later reduced by the acquisition of the thinner Ma-N 2403 resist.

It is also possible in the PMMA process to coat the substrate with two layers of different molecular weights; for e-beam lithography, PMMA chains with relative molecular masses of 495 kg/mol and 950 kg/mol are the most commonly used (commonly designated PMMA 495K and 950K respectively). The shorter PMMA molecule with lower molecular weight PMMA resist is more sensitive to post-exposure development, so when a 950K film is coated on top of 495K film, the development removes more from the lower layer than the top, creating an overcut in the PMMA mask at the edge of the features - this can enable a cleaner lift-off process after metal deposition. This process worked well when exposing nanometric area for etching, but when we used this approach for masking nanometric areas the increased height of resist due to the bi-layer made the aspect ratio of resist remaining on the surface more prone to collapse.

3.1.4 Device schematic design

In order to fabricate the devices we had designed for voltage driven capture of nanoparticles (section 2.3), the Jeol 5500FS e-beam converted device layouts produced in external programs to calculate the exposure pattern. For the Gate and Pedestal Devices, resist needed to protect circular areas of the surface, with various diameters, and a large number of circles of each size were required to perform statistical analysis after nanoparticle capture. We used AutoCAD software, an Autodesk Inc. product, to create these patterns. The masks designed for *Gate* and *Pedestal* devices are shown in FIG. 3.2a and FIG. 3.2c, where each column contains four 10 x 10 arrays of these circles, with column map markers indicating the intended

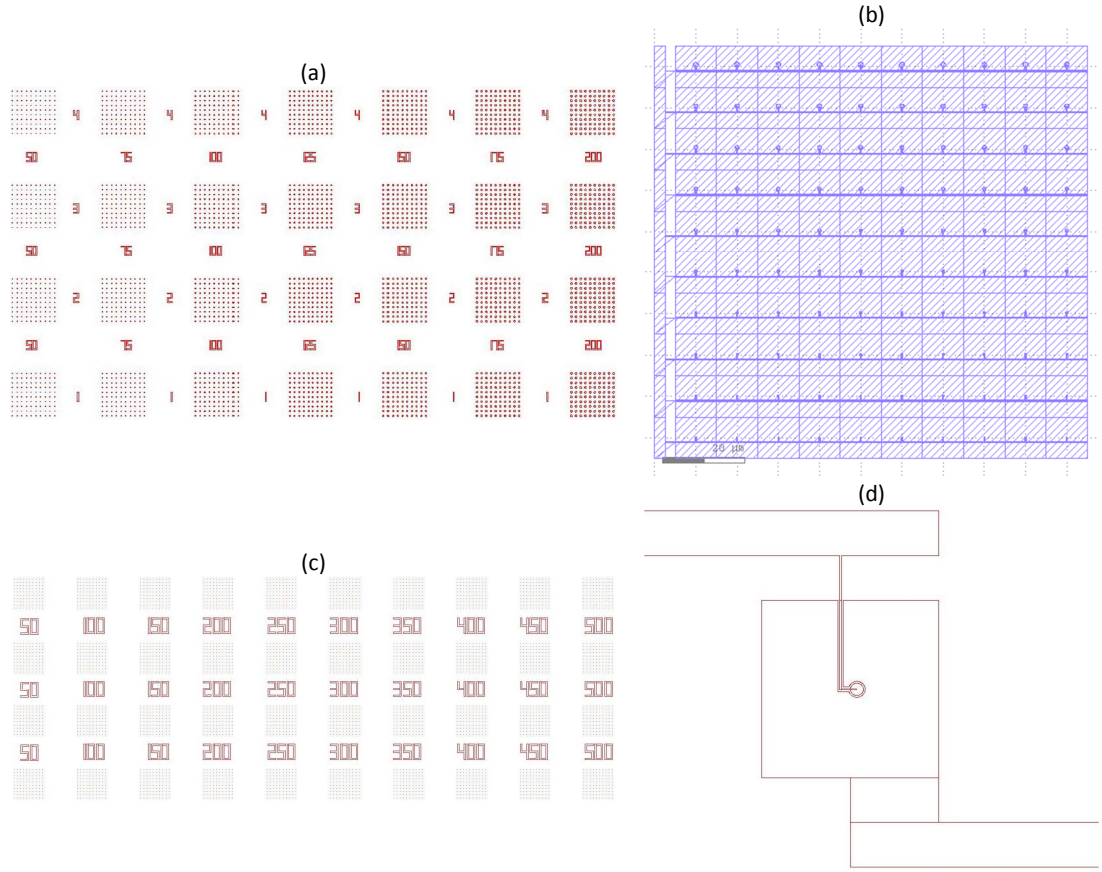

FIG. 3.2 Schematic designs for Electron Beam Lithography of features.

Schematics used to generate masks for electron beam lithography of (a, c) *Gate* and *Pedestal* devices and (b, d) *Interdigitated Electrodes* devices.

circle diameter and row numbers to designate each array for the smaller mask .

The masks designed for *Interdigitated Electrode* devices are shown in FIG. 3.2b and FIG. 3.2d. The masks defined the areas to be metalised for electrodes, seperated by a minimum 50 nm gap and the circular areas in the centre of varying diameter intended as the target areas. Cadence, a design software from Cadence Design Systems Inc., was used in preference to AutoCAD for this design, because it offered more flexibility for changing device dimensions but had not previously been available during the design of the other masks. The original plan of using arrays of these electrodes (FIG. 3.2b) encountered several fabrication issues, so *Interdigitated Electrode* testing was performed on individual electrode configurations (FIG. 3.2d).

These mask designs were then converted into Jeol EBL files, where the system would take the requested exposure dose and physical step size (2 nm typical) between exposed areas to determine the necessary writing speed. At the conversion stage, either mask could be converted into the inverse of the designed mask to accommodate a change in the tone of resist used.

3.1.5 Monolayer self-assembly

The designs for the Gate and Pedestal devices examined in section 2.3 rely on the negative surface charge created by the carboxylic acid ligands of the molecule, 16-mercaptohexadecanoic acid (MHA) with structure $HS(CH_2)_{15}COOH$. After electron-beam lithography and thermal evaporation have created a patterned Au surface on the device, the final fabrication step requires this molecule to be self-assembled onto the Au. This assembly occurs through the formation of Au-S covalent bonds that anchor each molecule to the surface and creates a well-ordered molecular monolayer across the surface terminating in the carboxylic acid ligand.

For these samples, surfaces of Au were prepared by thermal evaporation of 5 nm of Cr and 30 nm of Au onto Si/SiO_2 wafers in a bell jar pumped down to $4x10^{-7}$ mbar, with the Cr acting as an adhesion layer to the surface. The solution is prepared by dissolving MHA powder (Sigma Aldrich, 99%) to a 1 mM solution in ethanol. These Au coated surfaces are then immersed in this solution for a minimum of 12 hours, which gives time for a well-ordered monolayer of the MHA to bond to the Au surface. Finally, the sample is removed from the solution for three rounds of sonication in ethanol, for 10 minutes per round, before drying under compressed nitrogen.

3.2 Voltage-Driven Assembly in *Gate* Devices

Having thoroughly simulated the voltage directed assembly of nanoparticles into a *Gate* device design in section 2.3.1, we then sought to fabricate and test these devices using the methods discussed above. We concluded from the simulations that the device configuration was very flexible and several applied biases would achieve single-particle selectivity, with increasing voltage achieving capture in smaller diameter capture areas and increasing the number of captured particles.

3.2.1 Gate Device Fabrication

Initially Ma-N 2405 electron-beam resist was used to fabricate Gate Devices, which follows the negative-tone/lift-off fabrication process outlined in FIG. 3.1. Electron-beam lithography of the arrays of circles, outlined in FIG. 3.2a, were intended to create pillars of resist on the surface. However, this resist was prone to collapse as a result of the spin-coated film being too thick, with the pillars of resist frequently collapsing on the surface. An example of this is presented in FIG. 3.3(b, c), where the resist had collapsed and fallen over on the surface, due to the relatively high aspect ratio of the pillars (470 nm x 200 nm). This was achieved with a spin coating of resist at 6000 rpm and this thickness of the film could not be reduced further. Attempts were made to counter this issue by diluting the Ma-N 2405 resist with anisole, but this reduced the effectiveness of the resist. We used Ti-prime, an adhesion promoter, to prevent the detachment of Ma-N 2405 from the surface in further experiments, but the pillars continued to collapse.

The lift-off approach to device fabrication was also achieved using PMMA 495K and 950K electron-beam resists (section 3.1.2) by swapping the exposed and unexposed

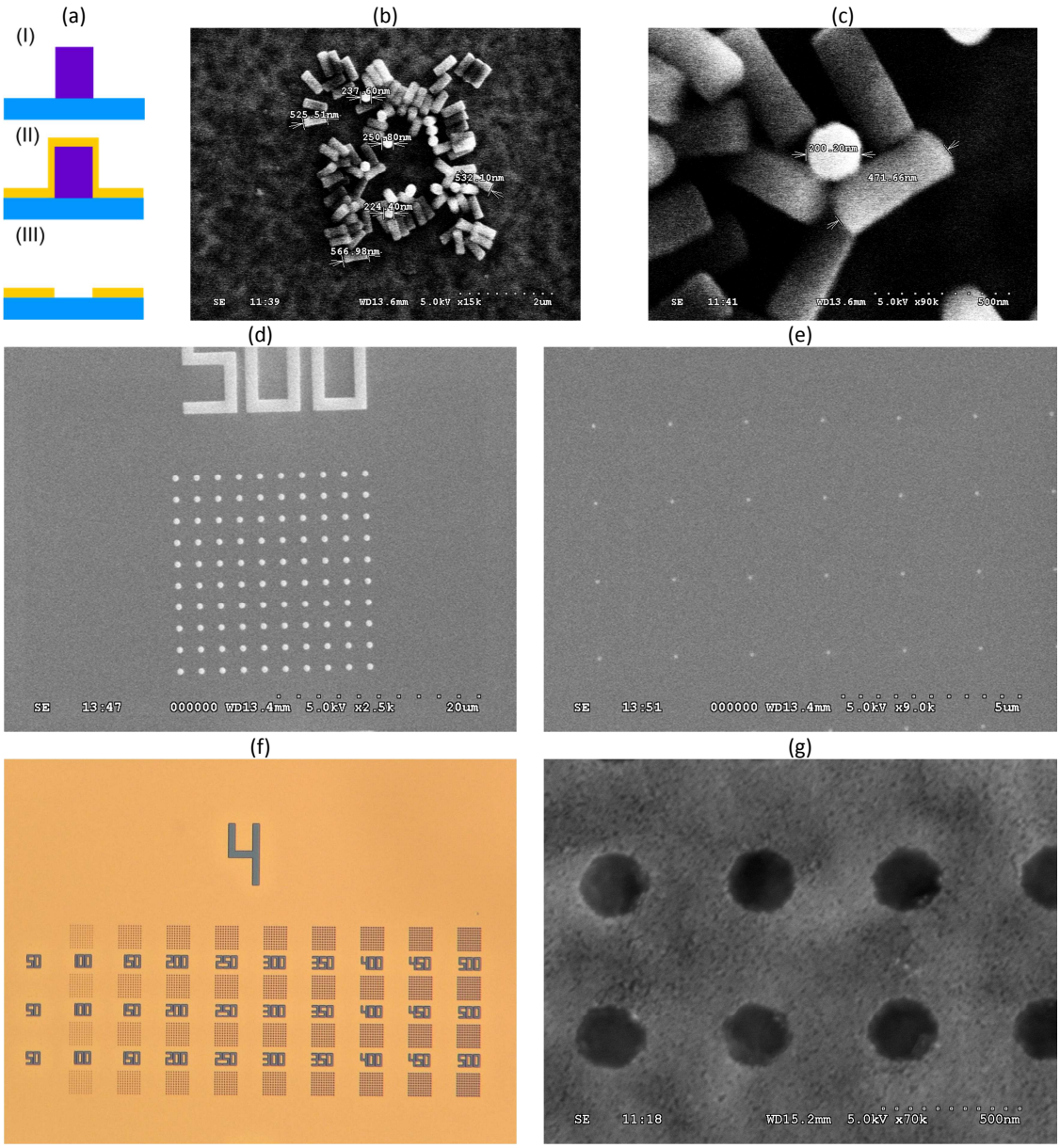

FIG. 3.3 Fabrication of Gate devices with different electron-beam resists.

(a) Elevation schematic of the lift-off process (FIG. 3.1) used for fabrication of Gate devices: (I) a masking resist (purple) is patterned into pillars on a substrate; (II) the sample and resist are coated with Cr (5 nm) and Au (30 nm); (III) the final lift-off stage cleans away the resist and the metal layer covering it. (b, c) Representative SEM images of Ma-N 2405 resist collapsed on the surface after development. (d, e) PMMA resist after development for pillars of (d) 500 nm and (e) 50 nm diameter pillars of resist. (f, g) Images of gate devices taken with (e) an optical microscope and (f) an SEM.

resist areas, leaving resist pillars on the substrate as with negative-tone resist. However, this increased the writing time and these resists suffered from lift-off issues

where the removed resist did not also lift-off the metal covering it. For many of the smallest resist pillars (sub-300 nm), even using a bi-layer resist did not alleviate this issue.

These problems prompted a shift to the use of the positive-tone/etching process (FIG. 3.1) to write holes into a PMMA resist (FIG. 3.3(d, e)) and etch the underlying metal layer to provide cleaner features (FIG. 3.3(f, g)). The disadvantage with this approach was that the Au and Cr layers could be over-etched to lose the resolution of the resist. However, this did not inhibit testing and was eventually refined to limit this disadvantage. The 30 nm Au layer was etched in a potassium iodide 5 mM solution in distilled water under sonication for 70 seconds. The remaining 5 nm Cr layer was etched by a standard Cr etchant (Sigma Aldrich, 651826) comprised of diammonium hexanitratocerate and nitric acid, diluted to a 0.1 M solution in distilled water under sonication for 60 seconds.

3.2.2 Gate Device Testing

My first tests were with the extensively modeled *Gate* device (section 2.3.1), which was built into the Au surface of a wafer. A schematic for each of these chips is shown in FIG. 3.4a. An electrical contact is made to a lower doped-Si^+ electrode, which is insulated from the surface of the device by a layer of SiO_2. Nanolithography of an electron beam resist, as described above, and shadow masking to isolate the upper and lower conductive surfaces was followed by thermal evaporation of 5 nm of Cr and 30 nm of Au and lift-off of the resist created holes in the Au layer through to the SiO_2 surface (FIG. 3.3f, g). A monolayer of MHA was then grown onto the remaining Au

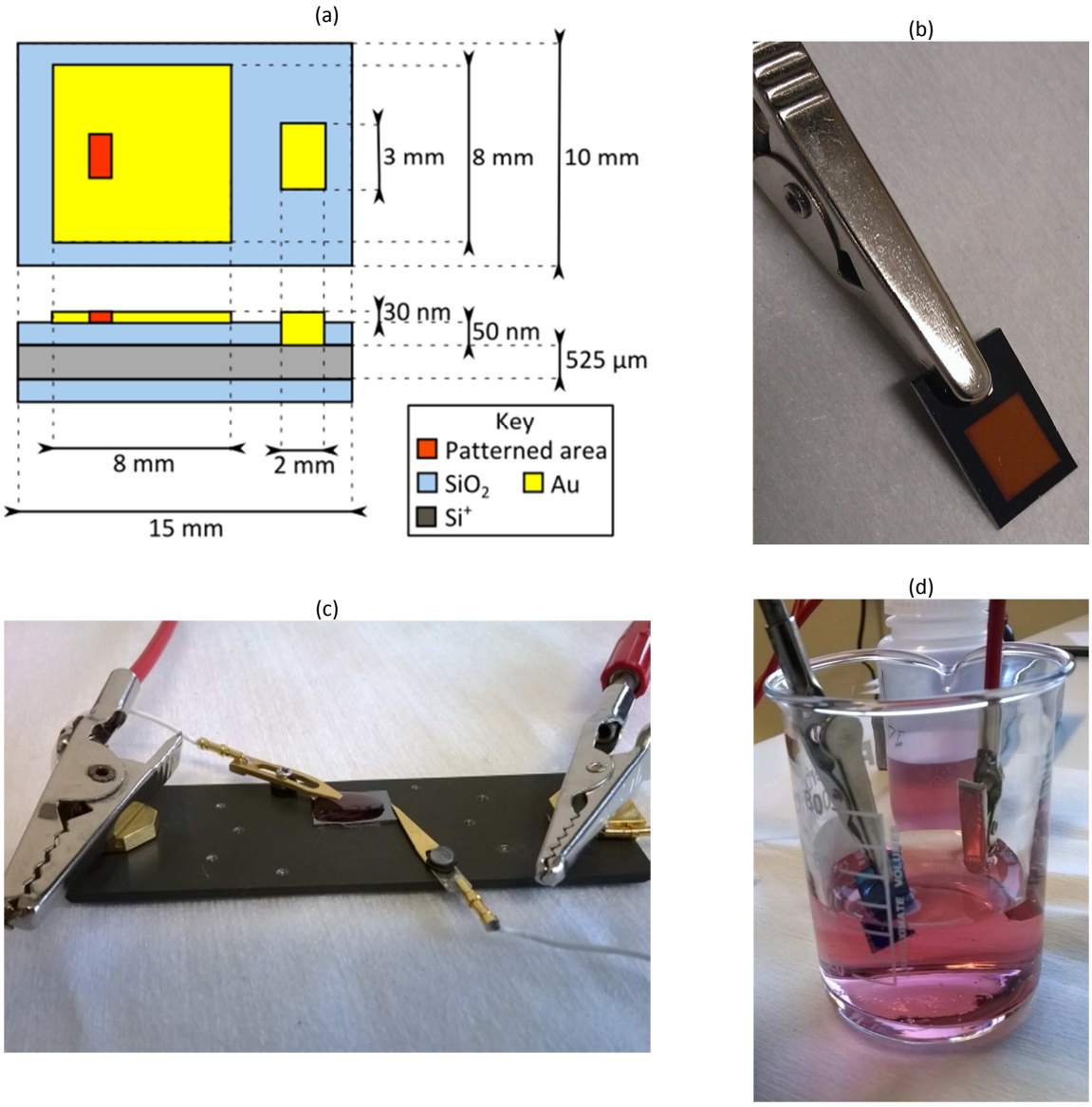

FIG. 3.4 Gate device testing setup.

(a) A schematic of a gate device chip as prepared for testing. A metal contact is made through the SiO_2 to the lower doped Si electrode, which is intended to provide the driving force for particle capture. The Au surface is coated with a monolayer of MHA. The red patterned area has holes through the Au to the SiO_2 surface as defined by nanolithography (FIG. 3.2a, FIG. 3.3g). (b) One gate device chip with electrical contact to the lower electrode. (c, d) Two different configurations for gate device testing. In (c) the negative terminal is contacted to the top of the colloid droplet 1.2 mm above the surface of the chip. In (d) the negative terminal is held on the opposite side of a 100 mL beaker filled with the colloid. In both (c) and (d) the colloid is brought into contact with the patterned Au surface whilst the contact to the lower electrode is kept dry.

surface to (section 3.1.5) to provide the negative surface charge that should funnel the particles to the centre of the target areas.

In testing, the lower electrode of the device was biased by the positive terminal of a 9 V battery, as a low-noise power source, with the output controlled by a potentiometer and measured with a voltmeter. The negative terminal of the battery was connected to top of the Au colloid droplet placed on top of the area where the gate devices were patterned (FIG. 3.4c). After an allotted time for deposition had elapsed, the voltage was turned off the device was rinsed first in distilled water and then in isopropanol before drying under a stream of compressed N_2 gas. The results were then analysed using a field-emission SEM, to image nanoparticles in and around the devices. These images have predominantly been produced as large half-page images to ensure that the nanoparticles are visible to the reader.

Initially *Gate* devices used Si_3N_4 as a dielectric instead of SiO_2 to insulate the electrodes, deposited onto a Ti electrode by plasma-enhanced chemical vapour deposition. This was the dielectric we had used during modeling of these devices in section 2.3.1, but we were forced to change strategy as the composition of the deposited films consistently failed to isolate the two electrodes. We switched to using thermally grown SiO_2 on doped-Si to separate the Si^+ and Au electrodes to provide the simplest solution to this problem. With this dielectric, there were fewer incidences of insulation failure. Prior to testing, this insulation failure was signified by a low resistance between the upper and lower electrodes. If this was the case then testing frequently resulted in the top Au surface peeling off the chip both during testing with the colloid and during rinsing in distilled water. An example of a chip with peeled Au can be seen in the inset picture of FIG. 3.5a. In these cases particles were deposited

(a)

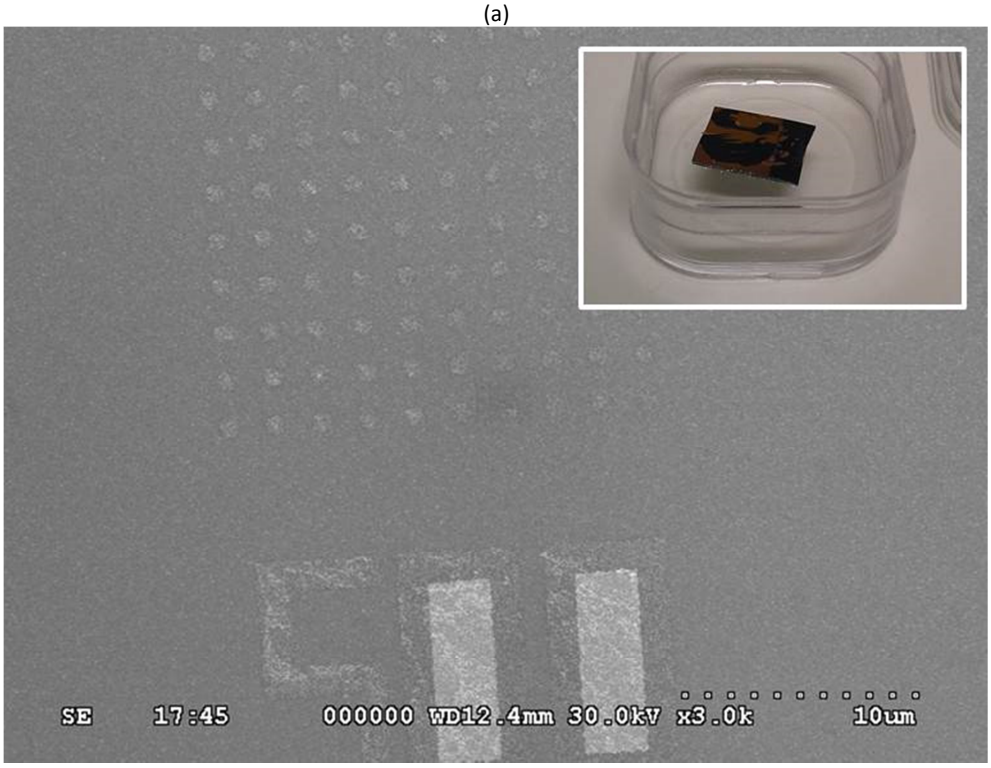

(b)

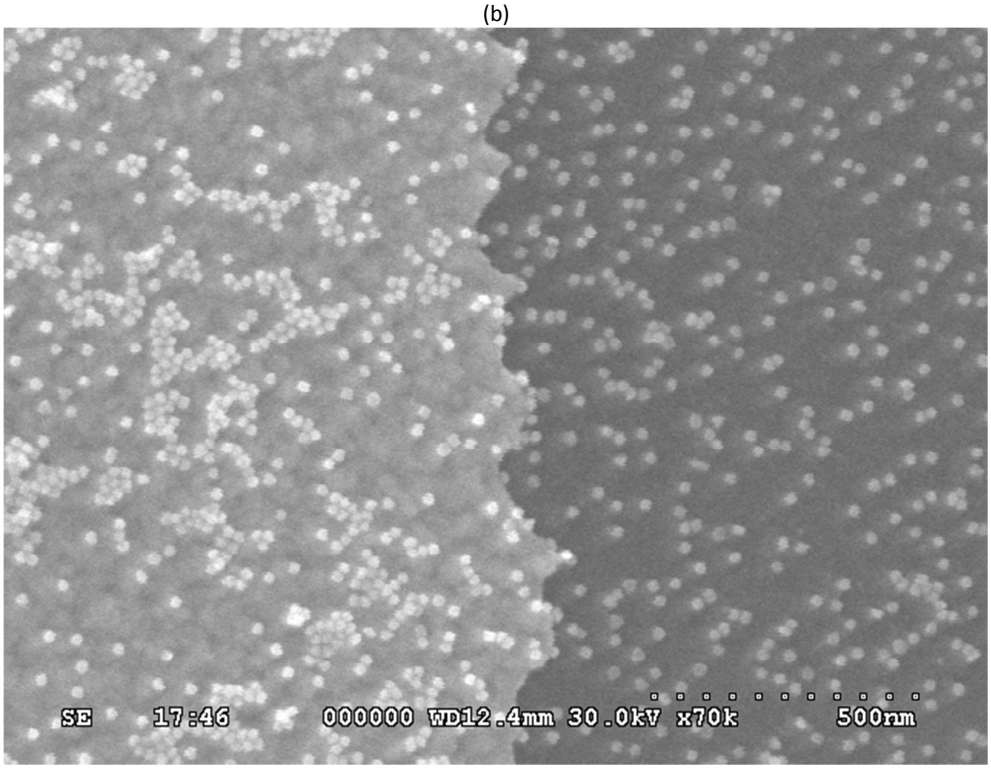

FIG. 3.5 Gate devices with short-circuited insulation (1/2).

Representative SEM images of *Gate* devices where the insulation short-circuited. (a) *Gates* and marker for a 500 nm diameter array, with an inset image of the chip with peeled Au layer following testing. (b) Zoomed in scan of Au (bright) and SiO_2 (dark) areas of 500 nm marker in (a). Particles have assembled onto both SiO_2 and Au surfaces, with more clusters on the Au.

(a)

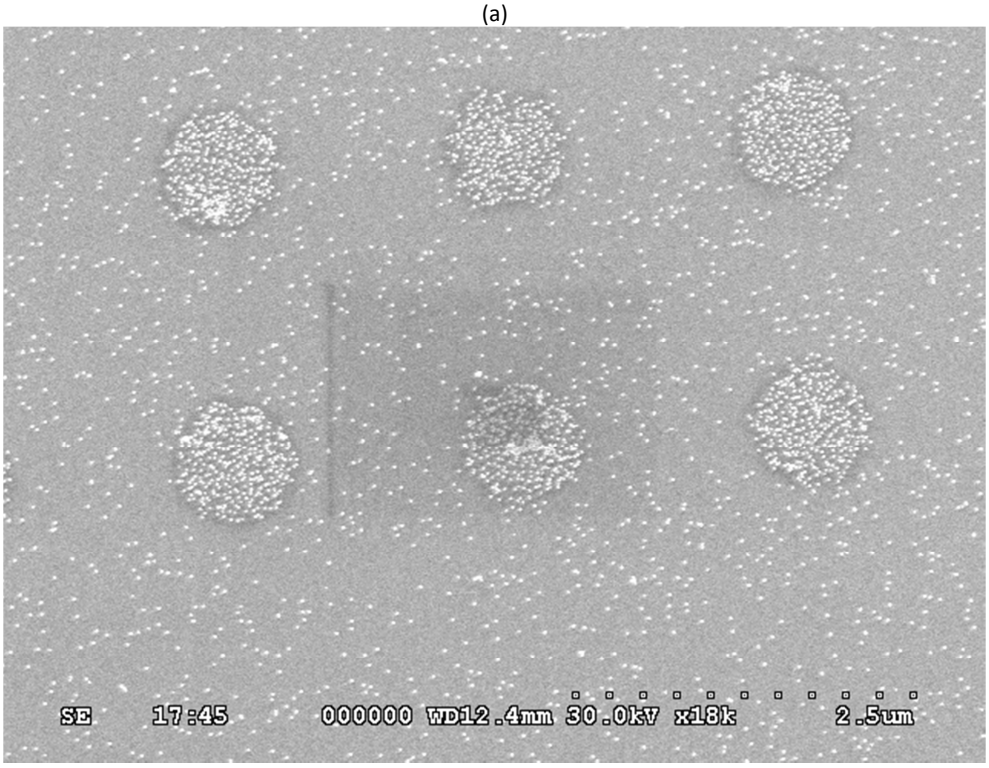

(b)

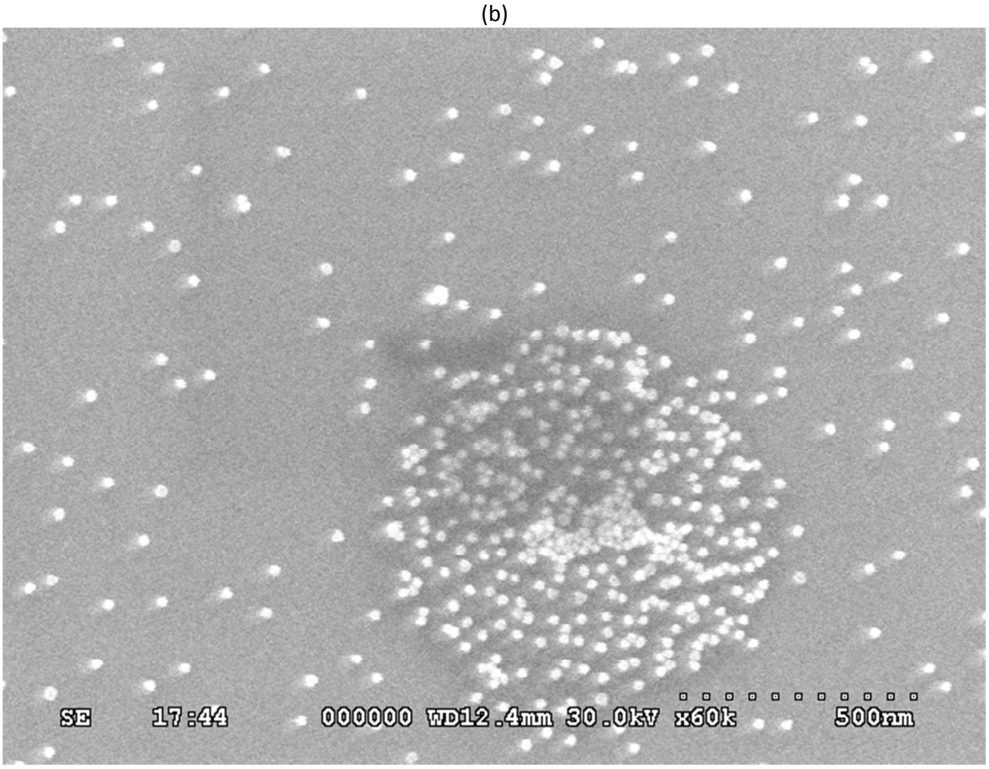

FIG. 3.6 Gate devices with short-circuited insulation (2/2).

Representative SEM images of Gate devices where the insulation short-circuited. (a) six 500 nm diameter *Gates* and (b) one zoomed in image. Particles primarily assembled on the SiO_2 but also on the surrounding surface – because the Au peeled off, this is likely the adhesive Cr layer that was underneath.

across the remaining surfaces, with uneven interparticle separation. The SEM images in FIG. 3.5 present an unusual case where some Au remained on the surface, isolated from the rest of the film within markers. Closer scrutiny (FIG. 3.5b) showed that the particles on this Au had formed larger clusters, indicative of the discharge of particles on the electrode surface. On the *Gate* devices themselves (FIG. 3.6), particles formed clusters on the SiO_2 with less dense deposits of particles on the remaining Cr, which would have been exposed to the colloid only once the Au had detached.

Other devices had issues with the quality of the formation of MHA monolayers on the Au surfaces (FIG. 3.7, FIG. 3.8). Although particles were visibly deposited onto the targeted SiO_2 they were also dispersed across the MHA coated Au, which should have provided a negative surface charge to repel nanoparticles from the Au surface. Other contaminants were also visible on these surfaces, which after further investigation appeared to originate following the MHA self-assembly step in device fabrication. Following more thorough cleaning procedures before and after assembly reduced the occurrence of this contamination.

With a cleaner fabrication process in place, some *Gate* devices did manage to achieve successful particle capture in the intended target areas of the devices. For instance, FIG. 3.9 shows 10 x 10 arrays of 1 µm diameter *Gate* devices, with results representative of deposition after 60 seconds with a 3 V driving voltage through 100 nm of SiO_2. In several incidences particles were captured in the *Gates*, with FIG. 3.10 showed close-up images of many of the particles in these *Gates*. Extending the deposition time resulted in further agglomeration of particles on the surface of devices. Results after 10 minutes deposition under the same conditions resulted in the formation of larger clusters in some areas (FIG. 3.11a). More particles were also

(a)

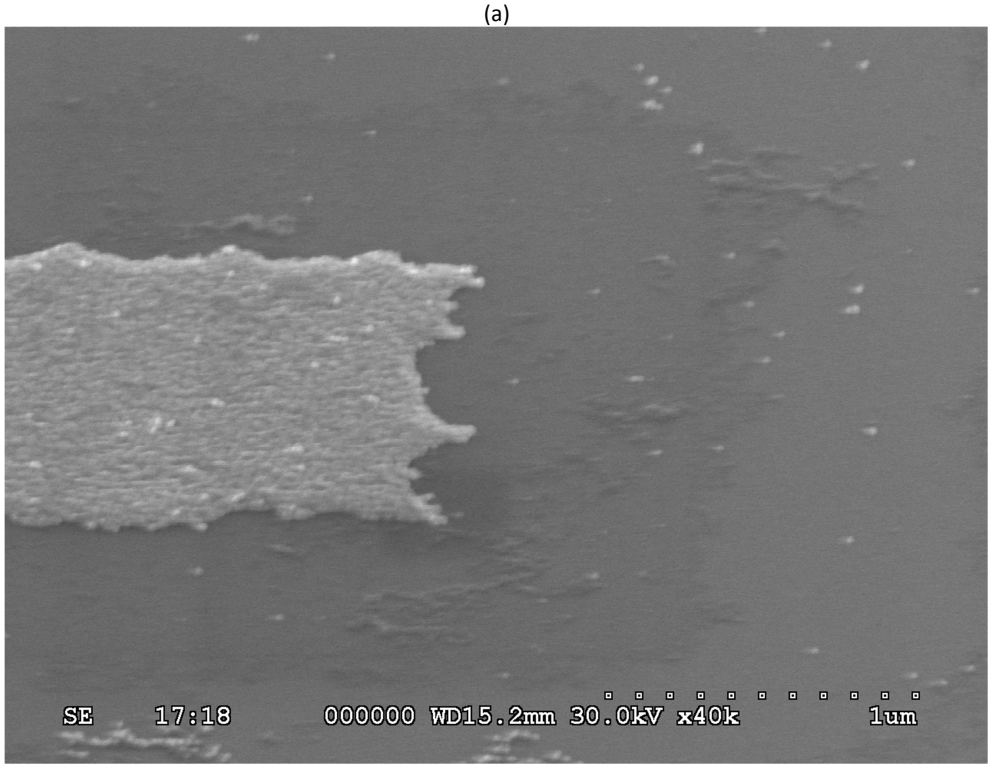

(b)

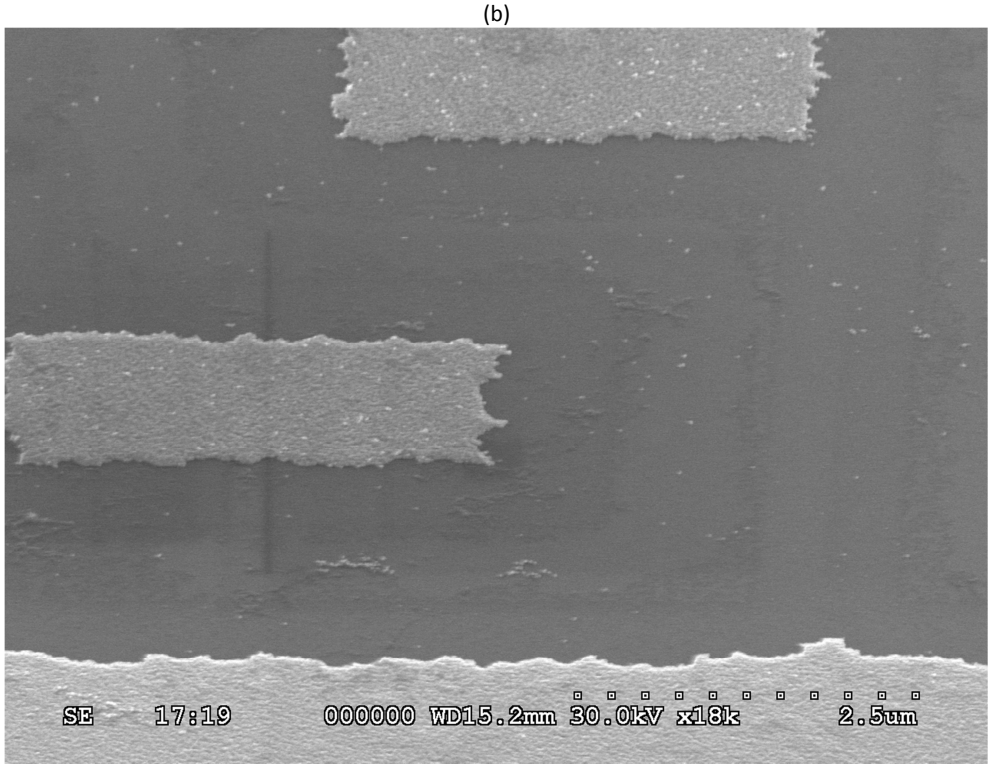

FIG. 3.7 Gate Devices with poor MHA assembly (1/2).

Representative SEM images of *Gate* devices after deposition with other contaminants visible. Particles are dispersed with no long range order on both the Au and SiO_2 surfaces of these devices. Other contaminants, which were later found to be residual MHA, are visible alongside the particles.

(a)

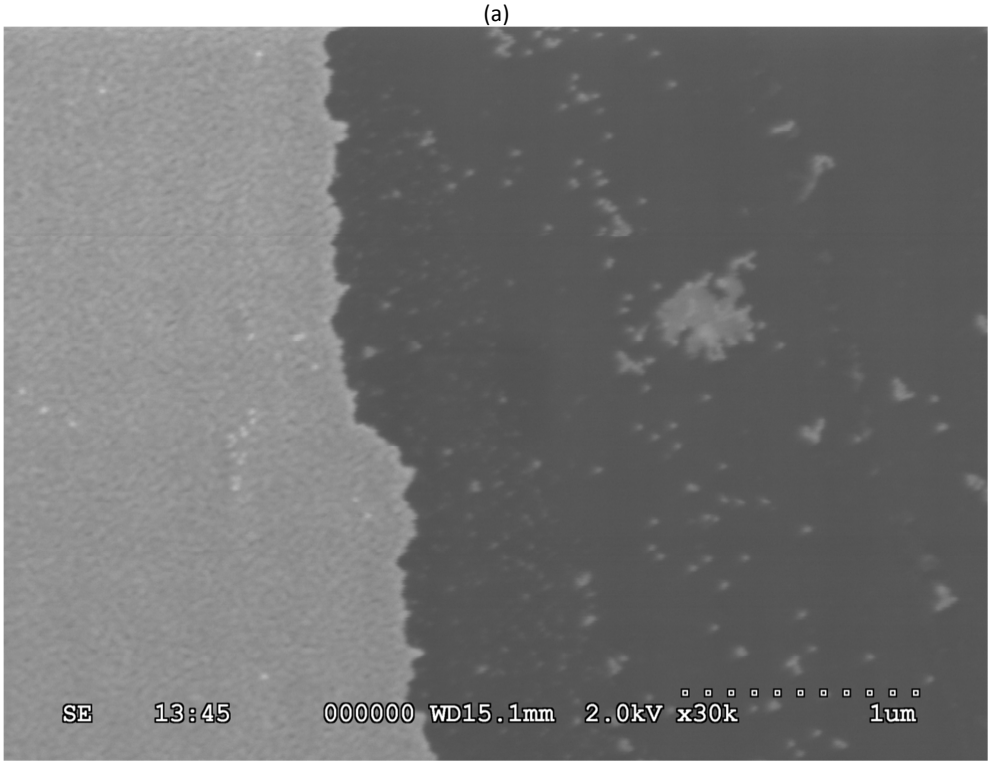

(b)

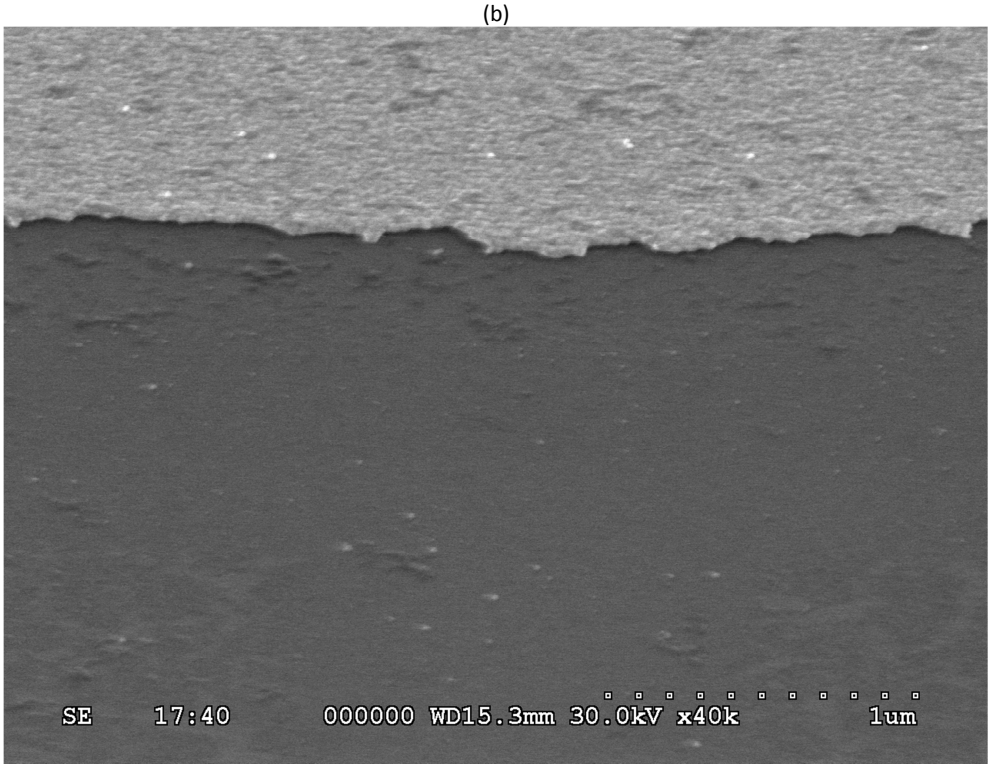

FIG. 3.8 Gate Devices with poor MHA assembly (2/2).

Representative SEM images of *Gate* devices after deposition with other contaminants visible. Particles are dispersed with no long range order on both the Au and SiO_2 surfaces of these devices. Other contaminants, which were later found to be residual MHA, are visible alongside the particles.

deposited onto the SiO_2 as expected. Deposition times of up to an hour (FIG. 3.18), the type of time-scales required for monolayer mediated self-assembly, resulted in widespread instability with particles deposited across all surfaces and undergoing agglomeration. The choice of testing setup did not affect these results (FIG. 3.4c, d).

Overall, tests with *Gate* devices indicated that there were several problems with the voltage-driven mechanism we were trying to achieve. The frequent adhesion of nanoparticles to the MHA coated Au surfaces indicated that this surface was not performing its primary function of repelling nanoparticles. This failure may be due to inadequacies of the MHA monolayer, failing to coat the surface, or instabilities induced by the applied voltage of the devices. Additionally, particles were not adhering as rapidly as was anticipated. It was expected that particles may require long time periods to form well-ordered distributions on the targeted areas, but the trend over long-term appears to be the formation of nanoparticle clusters on all surfaces. This indicates instability either innate to the colloid or induced by the applied bias that was driving assembly, which will need to be assessed. There could also be weaknesses in the model failing to anticipate changes to the local ionic concentration, pH and hydrostatic barrier that inhibit the deposition of particles in these voltage-driven *Gates*. These issues will be addressed in greater detail in section 3.5.

(a)

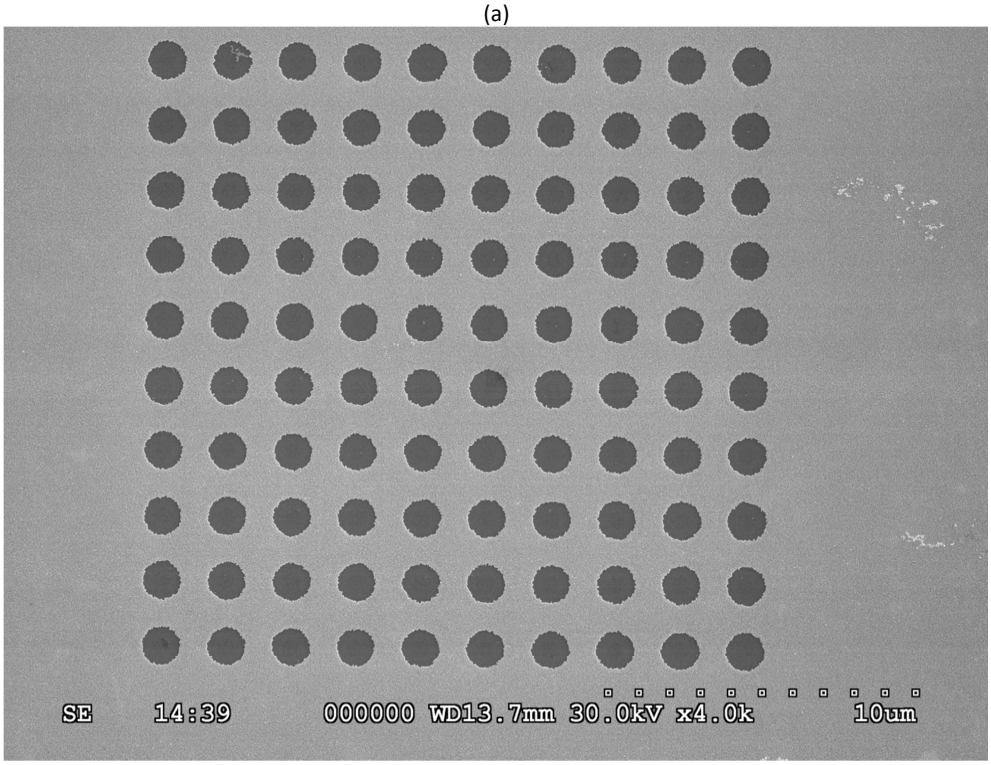

(b)

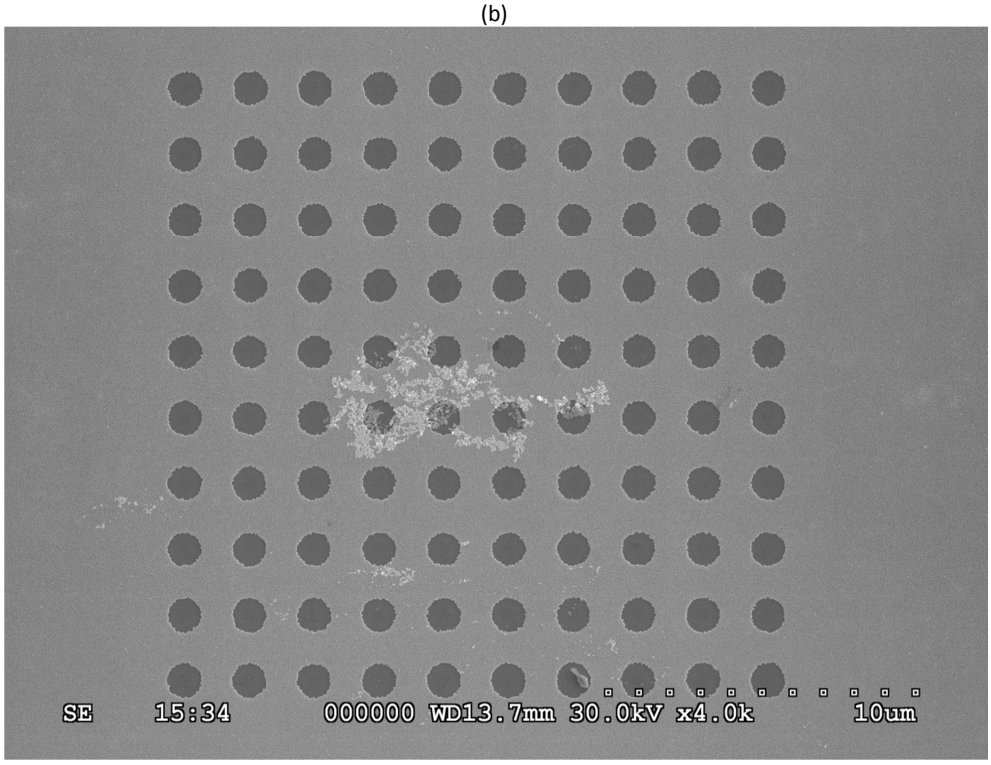

FIG. 3.9 Gate Devices after testing (1/4).

Representative SEM images of *Gate* devices after 1 minute of deposition with a driving voltage of 3 V in 1 µm diameter devices. In (a) and (b) particles are visible on the targeted SiO_2 surfaces with some evidence of funnelling towards the centre. Many particles have deposited on the MHA coated Au as well, with large clusters created on the array in (b).

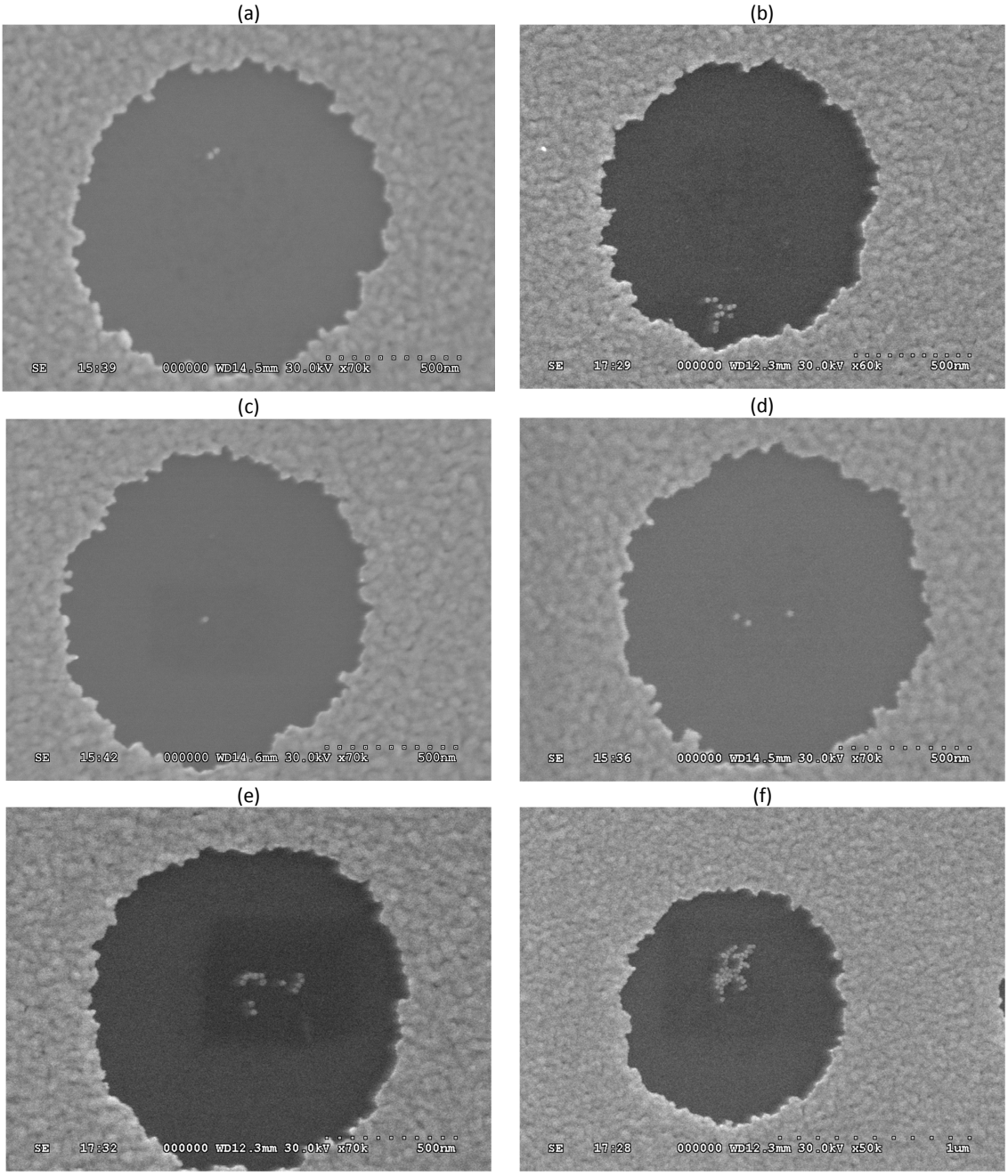

FIG. 3.10 Gate Devices after testing (2/4).

Representative SEM images of *Gate* devices after 1 minute of deposition with a driving voltage of 1 V. (a – f) Scans taken of individual *Gates* observed in FIG. 3.9. Some nanoparticles were deposited into these *Gates* with evidence of funnelling towards the centre, but without consistency. Many particles have agglomerated to form clusters (b, e, f).

(a)

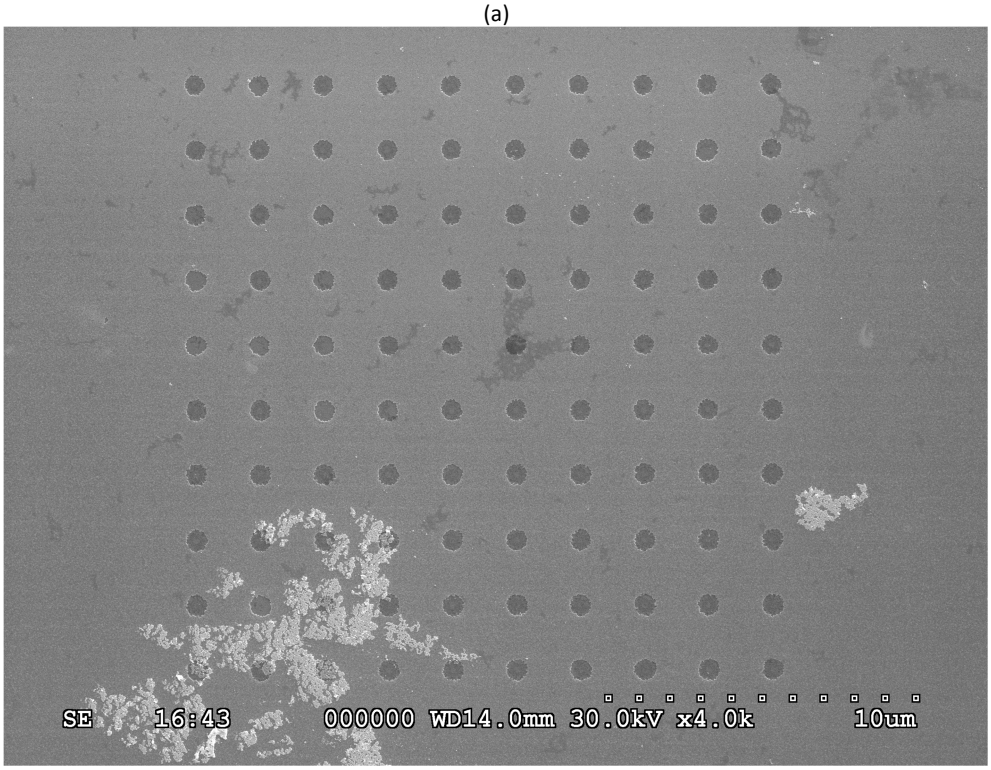

(b)

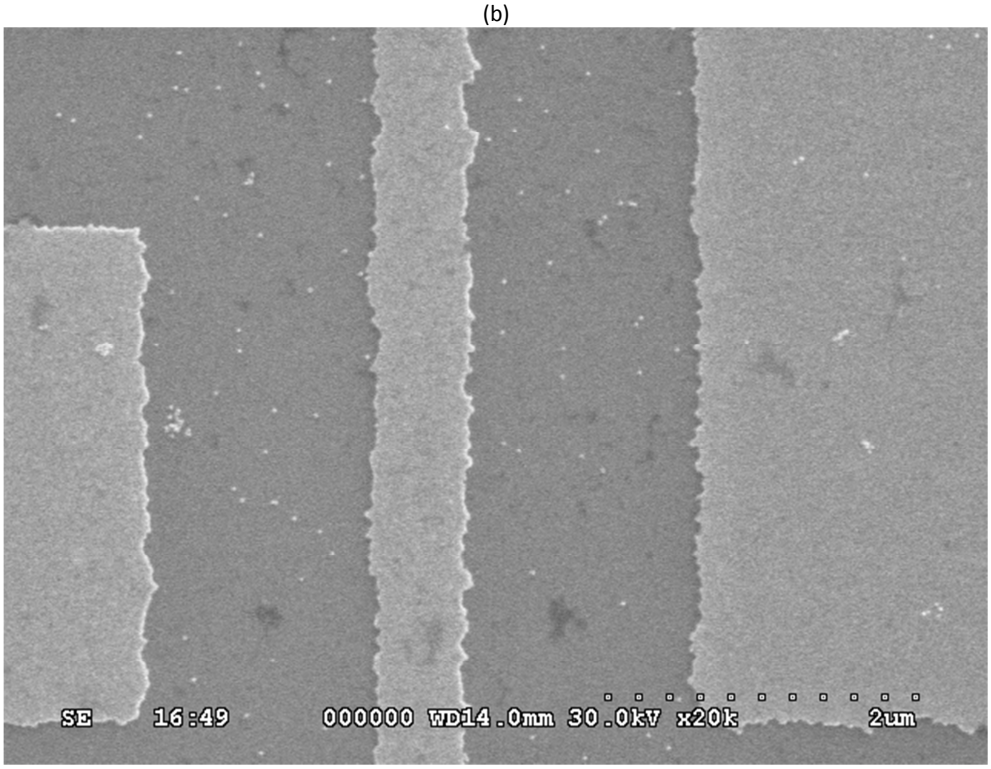

FIG. 3.11 Gate Devices after testing (3/4).

Representative SEM images of *Gate* devices after 10 minutes of deposition with a driving voltage of 3 V. Some nanoparticles were funnelled into the gates, although many still deposited on the surrounding Au and some formed clusters (a).

(a)

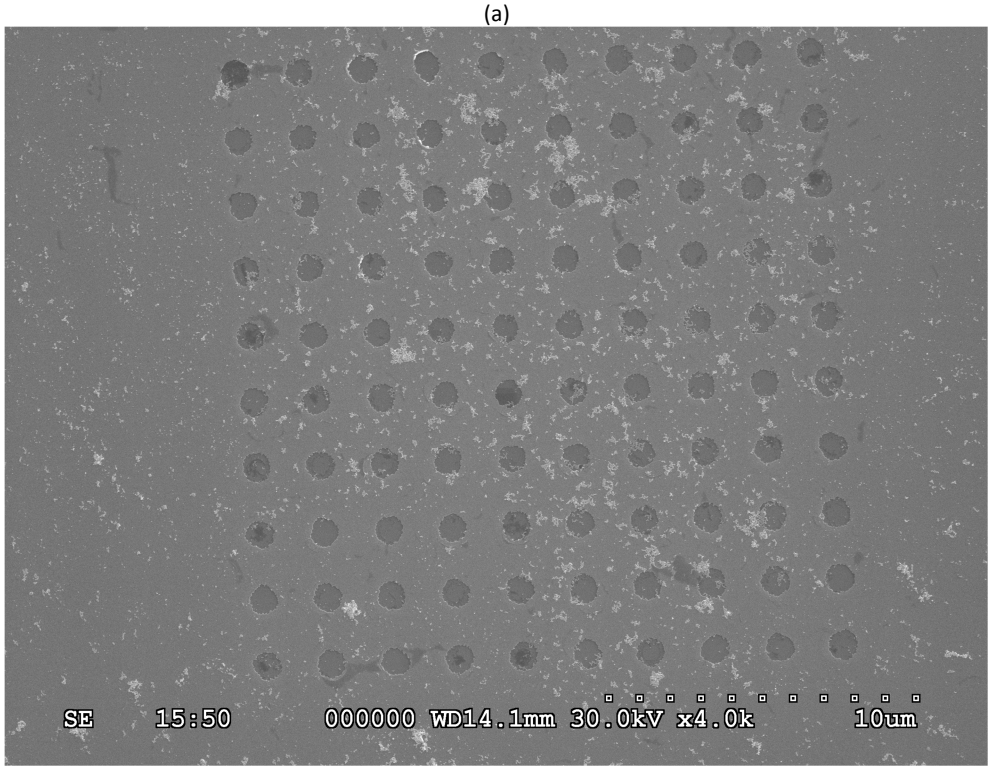

(b)

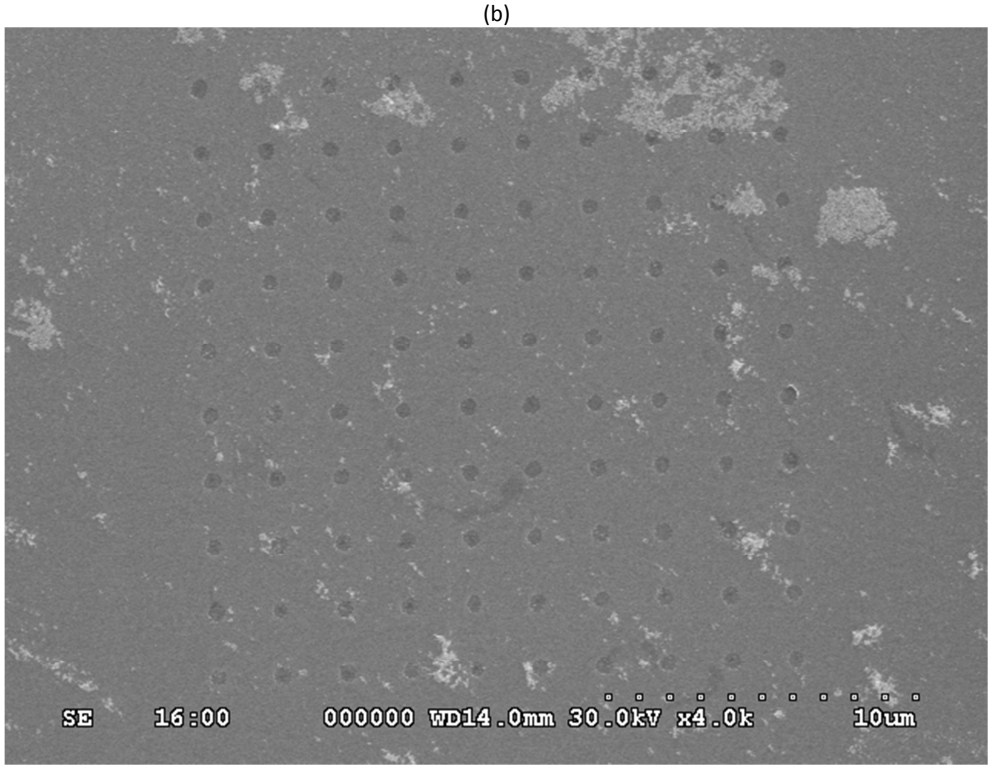

FIG. 3.12 Gate Devices after testing (4/4).

Representative SEM images of *Gate* devices after 1 hour of deposition with a driving voltage of 3 V. There is an increased presence of nanoparticles on all surfaces and the formation of clusters with increased deposition time.

3.3 Assembly in Pedestal Devices

The *Pedestal* device (section 2.3.2) operates by the same principles as the *Gate* devices, with a voltage applied to a lower electrode to funnel particles onto circular target areas of SiO_2. The primary difference is that the SiO_2 area is proud of the surrounding Au surface, to allow particles to be transferred from the top of the pedestal onto a separate substrate.

3.3.1 Pedestal Device Fabrication

The chips were designed using the same schematic that was used for the Gate devices (FIG. 3.4a), except the initial thickness of the SiO_2 was 100 nm instead of 50 nm to allow for etching. To create the pedestals, electron beam lithography patterned arrays of pillars of PMMA A4 495K resist standing on a SiO_2 coated Si substrate. The unprotected SIO_2 was then etched down with reactive ion etching, using a CHF_3 and Ar plasma at 200 W, removing approximately 55 nm of SiO_2 after 5 minutes. Subsequent thermal evaporation of 5/30 nm of Cr/Au and resist lift-off produced the intended array of 25 nm high pedestals of SiO_2 surrounded by an Au surface. Assembly of the MHA monolayer onto the Au completed the fabrication. This design proved to be particularly prone to lift-off problems, with metal areas often still capping the pedestals.

3.3.2 Pedestal Device Testing

Testing of *Pedestal* devices largely encountered the same problems as the *Gate* devices in the previous section. For example, deposition at 3 V for 60 seconds with a

(a)

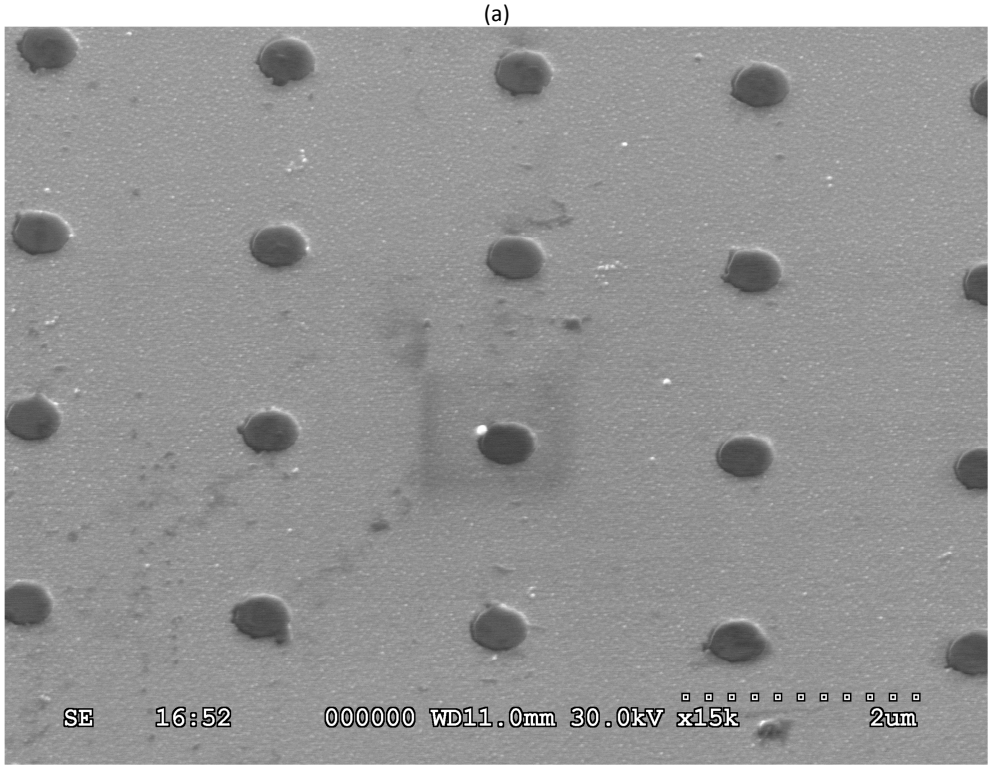

(b)

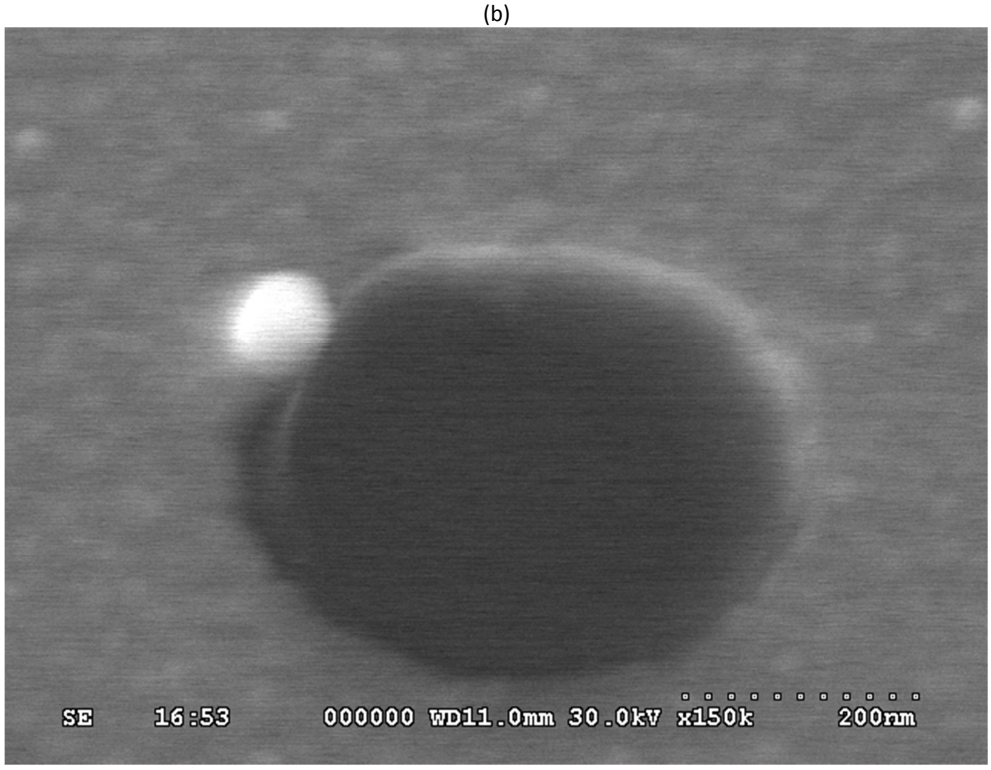

FIG. 3.13 Pedestal Devices after testing.

Representative SEM images of *Pedestal* devices after 60 s of deposition with a driving voltage of 3 V. Very few nanoparticles were visible, but the majority were dispersed randomly on both surfaces. (b) shows one nanoparticle attached to the edge of one pedestal.

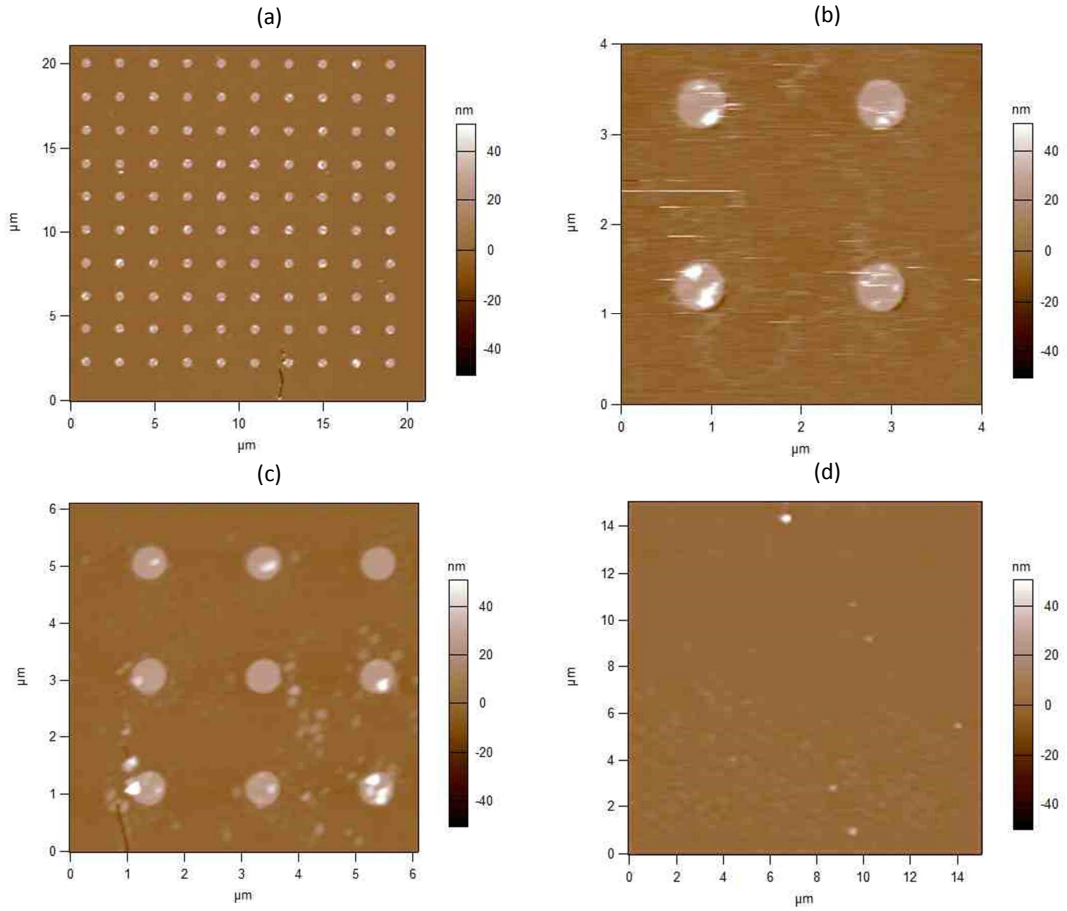

FIG. 3.14 Pedestal Devices testing with in-situ AFM imaging.

Simultaneous non-contact AFM topography images of Pedestal device Pi4 during 2 V driven deposition in a 60 nm Au colloid. Scans of pedestals (a-c) show particles present on the pedestals as desired but also on the surrounding repulsive Au-MHA surface. (d) Particles are also visible on the wider Au-MHA surface away from the target areas.

colloidal dispersion of 60 nm Au particles (FIG. 3.13) saw particles deposited randomly across both the SiO_2 and MHA-Au surfaces. FIG. 3.13b shows an unusual case where a particle had deposited onto the edge of a pedestal. For several tests there was no clear trend across the surface of higher voltages effecting deposition.

To try and examine what was occurring during placement, we setup the AFM to scan the surface during the deposition. During imaging it was possible to see objects on the MHA-Au surface around the pedestals that were probably nanoparticles from the 60

nm Au colloid. The 60 nm Au colloid was selected in order to improve the chances of successfully imaging the particles. A droplet of this colloid was deposited on the patterned area of the device, whilst the lower electrode was biased and the AFM cantilever holder was used as ground.

Topography images taken the deposition are presented in FIG. 3.14. Scans of a whole 10 x 10 array of pedestals appear to show Au nanoparticles on and around the devices, but the resolution at this scan size was too low to be certain. Subsequent smaller scans (FIG. 3.14b, c) were more conclusive, with particles apparent both on the SiO_2 and Au-MHA surfaces. Further scans of a complete Au-MHA area near the array showed particles were also present on this surface away from the attractive pedestals (FIG. 3.14d). It cannot be ruled out that the AFM probe was driving the particles towards the surface.

SEM images after the deposition (FIG. 3.15 – FIG. 3.17) revealed that the AFM imaging had indeed been affecting the nanoparticle deposition on the surface. In FIG. 3.15b nanoparticles were clearly pushed to one side during the scan of the Au-MHA area (FIG. 3.14d). The lines visible in the other images could have been modifications made to the existing MHA layer or ions deposited from the colloid; these lines were not evident where AFM scanning had been of a higher resolution (FIG. 3.16b). SEM images of other arrays saw fewer incidences of nanoparticle placement compared to the AFM imaged area. This indicates that the AFM probe was encouraging the bonding of the particles to the surface. Some particles had been deposited onto pedestals and would be suitable for attempting transfer (FIG. 3.17). Unfortunately, without any long-range order, it would be impossible to identify these particles on a transfer substrate, so it was not attempted.

(a)

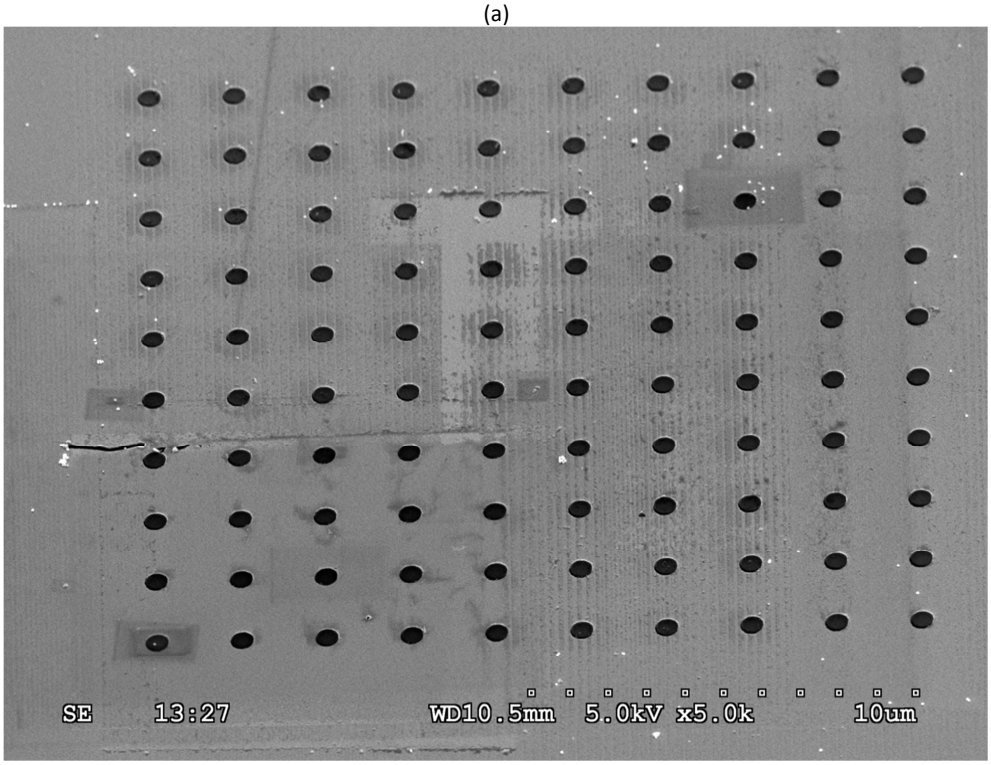

(b)

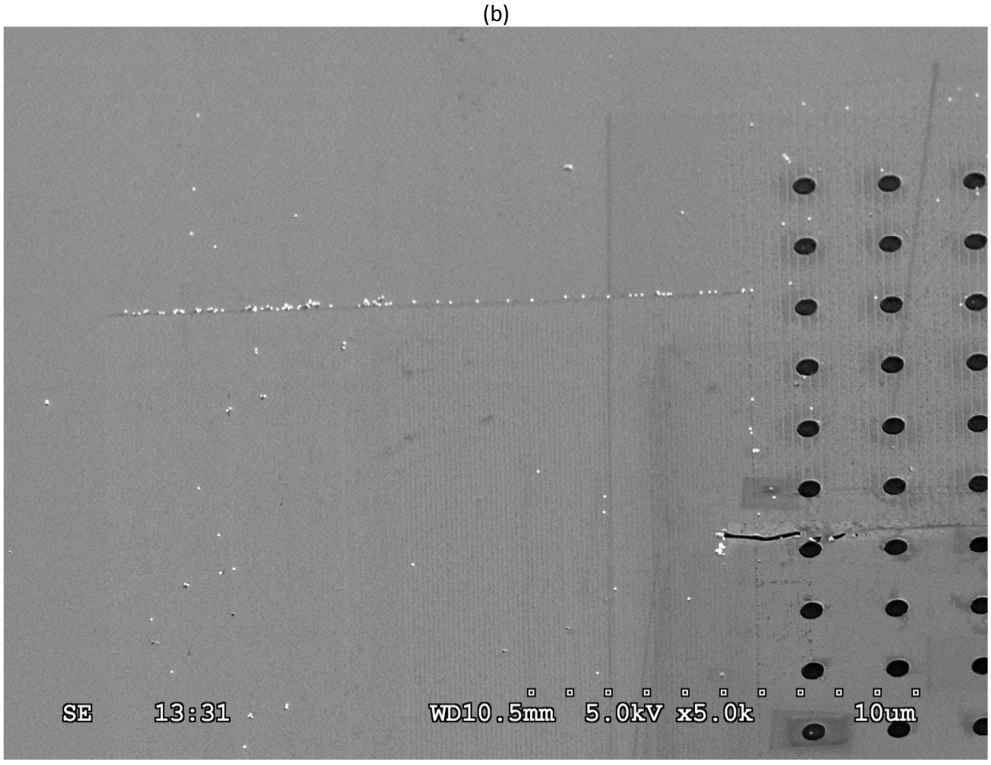

FIG. 3.15 Pedestal Devices after testing with in-situ AFM imaging (1/3).

SEM images of the region on Pedestal device Pi4 that was simultaneously imaged with AFM (FIG. 3.14) during 2 V driven deposition in a 60 nm Au colloid. The AFM probe interfered with the particle assembly: grooves are visible that align with the fast-scan axis of the AFM and a line of nanoparticles has been formed at the edge of one of the scans.

(a)

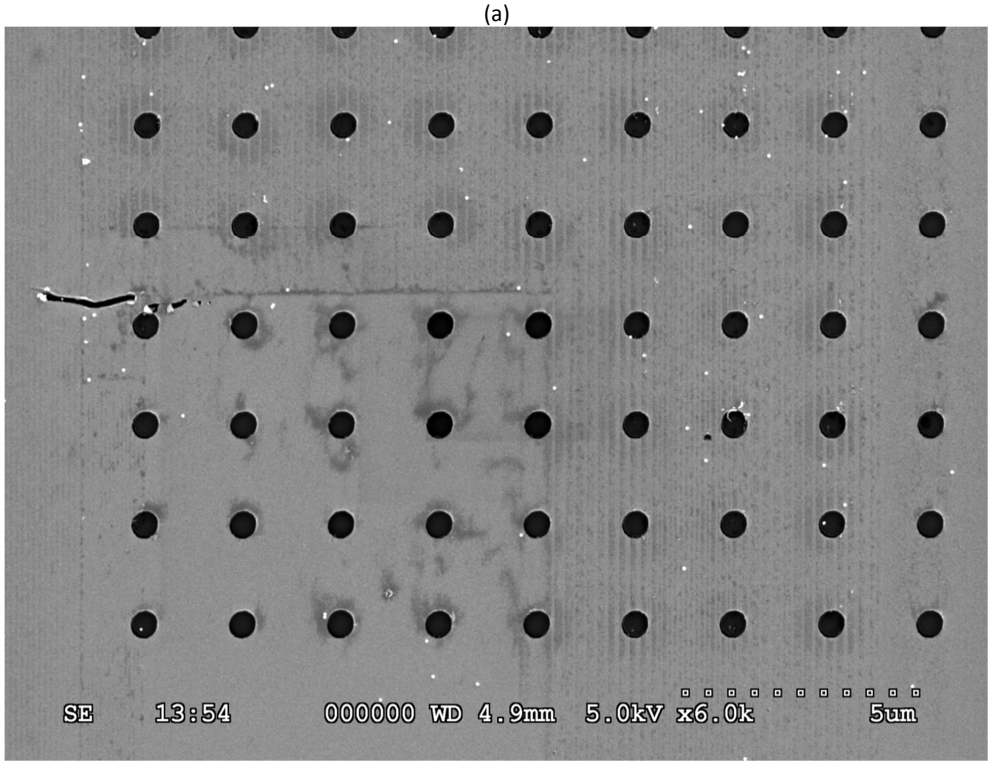

(b)

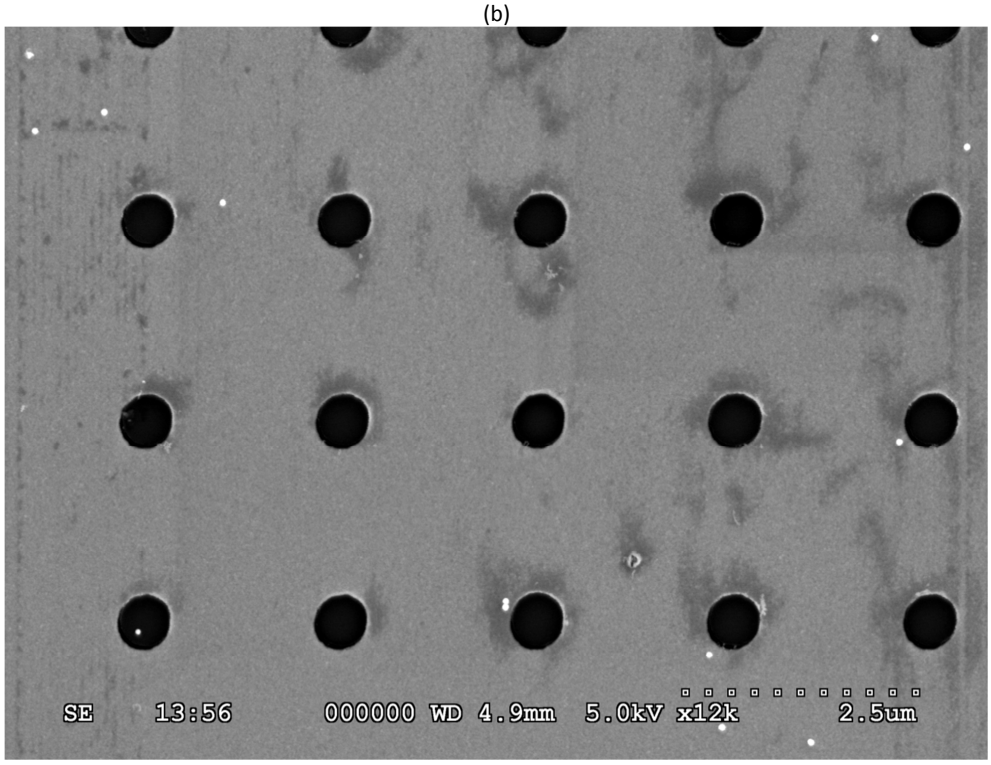

FIG. 3.16 Pedestal Device after testing with in-situ AFM imaging (2/3).

SEM images of the region on a Pedestal device that was simultaneously imaged with AFM (FIG. 3.24) during 2 V driven deposition in a 60 nm Au colloid. The AFM probe resulted in grooves appearing on the Au surface. Deposited nanoparticles followed the common response of being distributed across all surfaces.

(a)

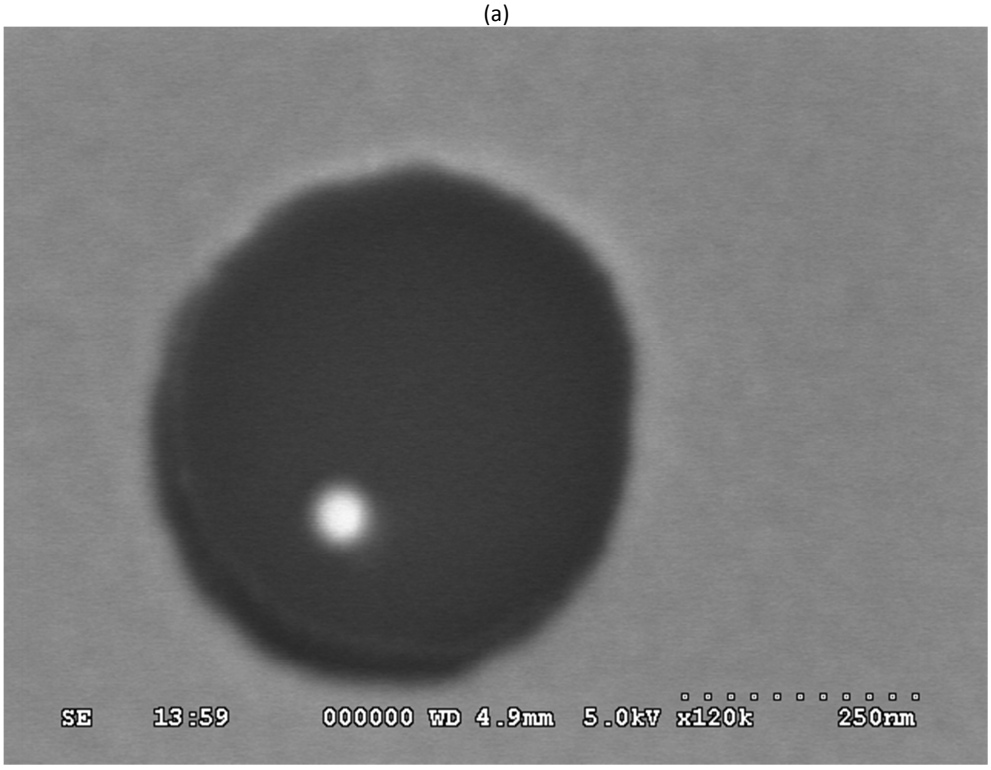

(b)

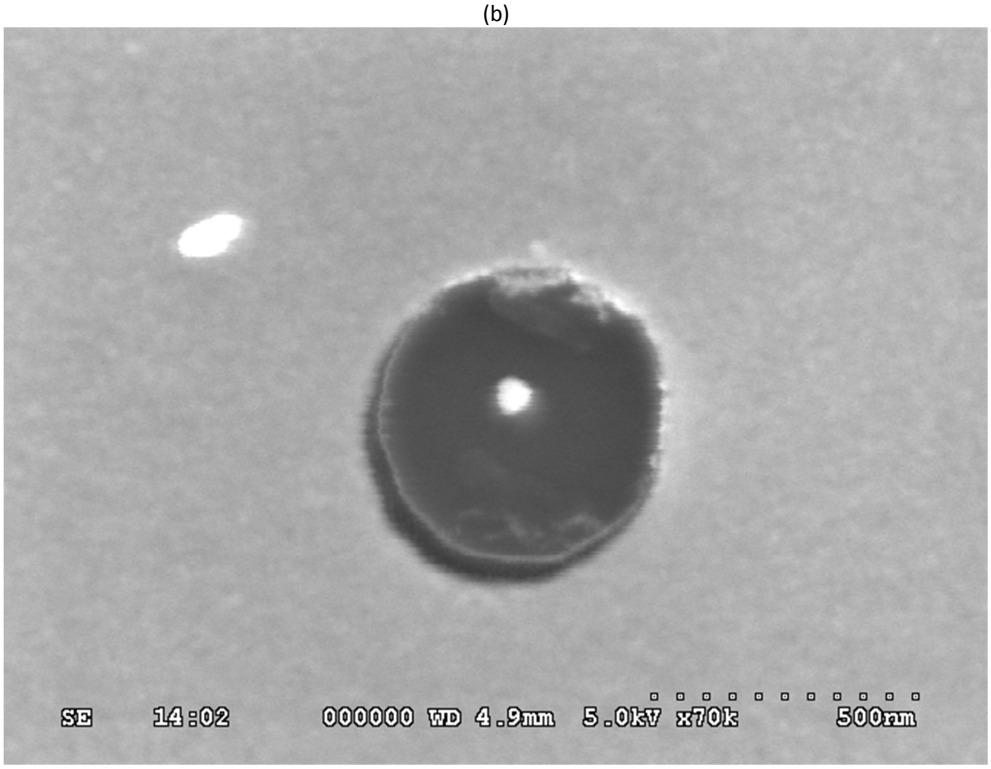

FIG. 3.17 Pedestal Device after testing with in-situ AFM imaging (3/3).

SEM images of the region on Pedestal device Pi4 that was simultaneously imaged with AFM (FIG. 3.24) during 2 V driven deposition in a 60 nm Au colloid. (a, b) examples of pedestals with nanoparticles captured on them.

3.4 Assembly in Interdigitated Electrode Devices

The *Interdigitated Electrode* design was conceived to provide an entirely voltage-driven approach to nanoparticle capture. Simulations of these devices (section 2.3.3) had indicated that the capture mechanism was capable of achieving single-particle selectivity for central electrodes with a radius of 50 nm, a 50 nm electrode gap and 50 nm of insulation. For initial tests we used a much larger central electrode with a radius of 500 nm, to establish whether the particles interacted as in these simulations.

3.4.1 Interdigitated Electrode Fabrication

The Interdigitated Electrode devices were fabricated by electron beam lithography of a PMMA A4 495K, exposing the regions of the SiO_2 surface that were to be exposed for 5/30 nm thermal evaporation of Cr/Au to form the electrodes. These devices were patterned onto chips as detailed in the schematic in FIG. 3.18a, with electrodes connected to the inner and outer electrode pads to apply a bias between the electrodes (FIG. 3.18b). These electrodes were then insulated by sputter deposition of 50 nm of SiO_2, with a shadow mask protecting the electrode pads from coverage and 5 nm of Ti as an adhesion layer. SEM features of successfully fabricated electrodes are presented in FIG. 3.18 (a, b). The surface potential above the electrodes was also measured by KPM when the electrodes were biased. When a +1 V bias was applied, the surface potential measured between the electrodes was +520 mV, whereas a -1 V bias only measured an-360 mV difference. This disparity could have been caused by cross-talk between the cantilever and the surrounding area, although the AFM was scanning from a perpendicular position to the electrodes to limit this influence.

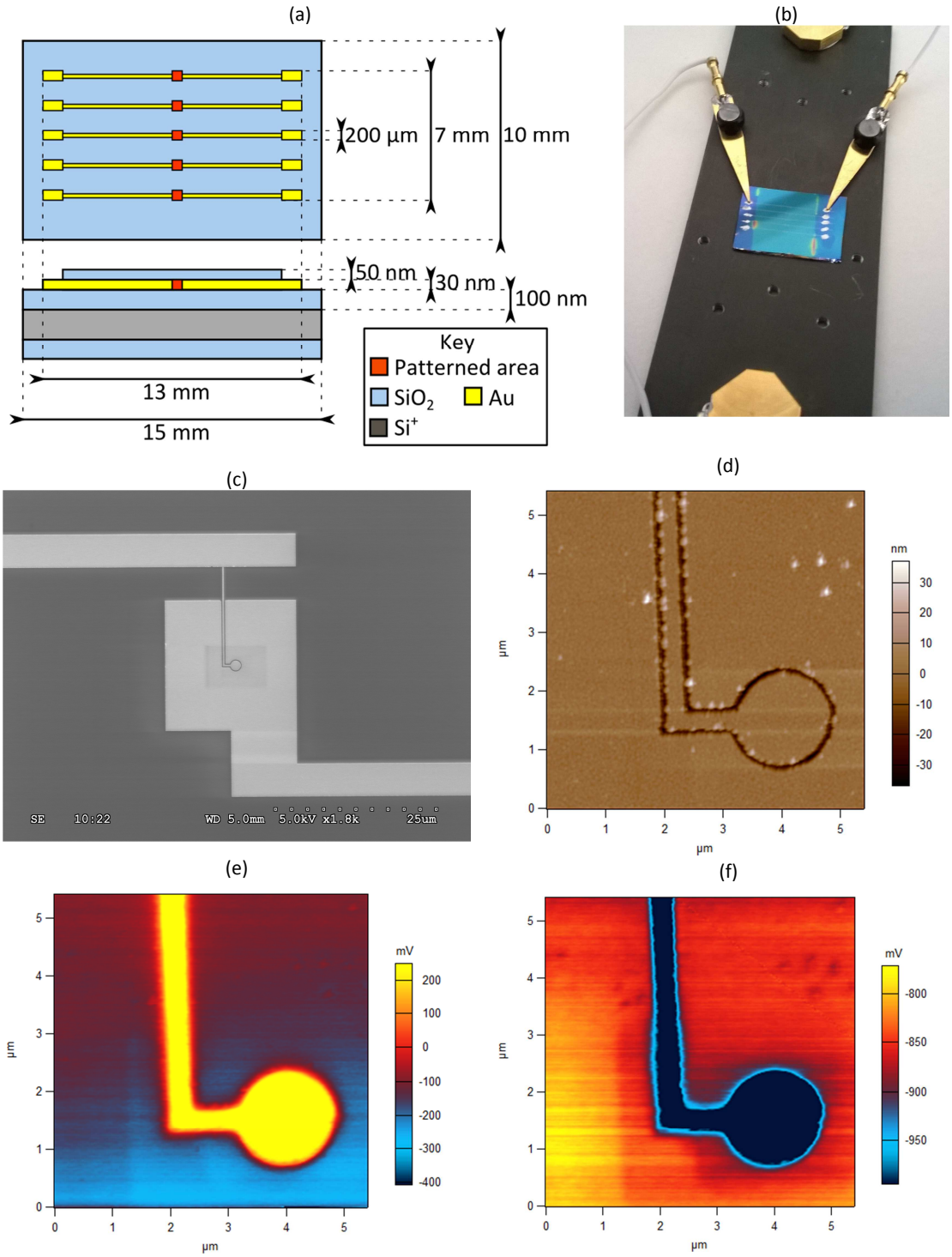

FIG. 3.18 Fabrication and KPM characterisation of Interdigitated Electrode devices.

(a) A schematic of a chip prepared for testing of Interdigitated Electrodes, with Au electrodes patterned onto a SiO_2 surface and encapsulated in sputtered SiO_2, and (b) an optical image of a chip with external electrodes contacting the inner and outer electrode contacts. Each red patterned area in (a) contain a single electrode combination, such as those imaged by (c) SEM and (d) AFM scans. (e & f) surface potential maps of an Interdigitated Electrode with (e) 1 V and (f) – 1V bias applied to the inner electrode.

(a)

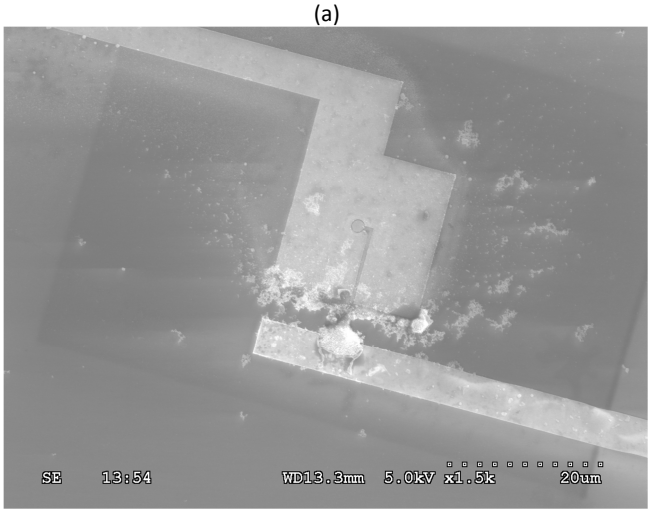

(b)

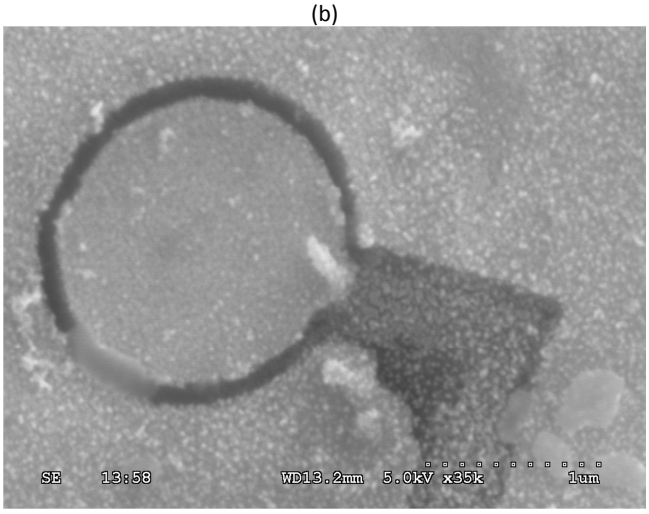

(c)

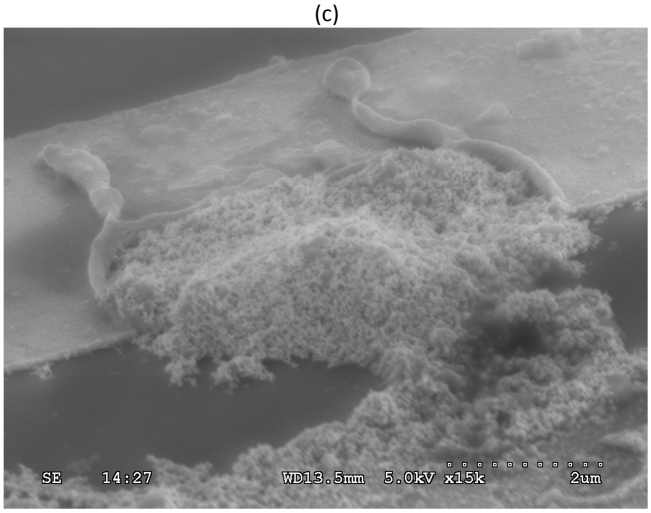

FIG. 3.19 Interdigitated Electrode Device after testing without insulation.

Assembly of 20 nm Au particles with a 1V driving bias directly onto interdigitated electrodes without the SiO_2 insulating layer. (a) The particles have completely bridged the gap between the electrodes. The main target area in (b) shows complete disorder. (c) The particles have agglomerated to form relatively large structures across the larger gap in electrodes.

3.4.2 Interdigitated Electrode Testing

Representative SEM images of the results of testing Interdigitated Electrode devices are presented in FIG. 3.19 – FIG. 3.24. Initially testing was performed using a 20 nm Au colloid as the medium for particles to be captured from. With a driving bias applied between the two electrodes, a droplet of this colloid was placed onto the region of the patterned electrodes. After an allotted amount of time, ranging from 1 to 10 minutes, the device chip would be rinsed in distilled water followed by isopropanol and finally dried with a stream of N_2 gas.

In devices where the top, insulating layer of SiO_2 was not present, the colloid would rapidly dry out following chaining of the colloidal particles between the electrodes and subsequent Joule heating. FIG. 3.19 shows SEM images of the resulting nanoparticle structures on the surface. The majority of this interaction occurred at the interface between the two electrodes with large amounts of agglomeration bridging the gap between them and short circuiting the device. When the electrodes were insulated from the 20 nm Au colloid, the majority of particles were deposited into the gap between the inner and outer electrodes (FIG. 3.20a). However, the voltage-driven deposition also appears to have destabilised the colloid around the negative, outer electrode. FIG. 3.20b presents an example where the larger particulates have been deposited on the outer/negative electrode, apparently repelled from the inner/positive electrode. There was also apparent damage to the Au electrode with the Au film peeling off. With the SiO_2 electrode this should not have been possible. The insulation appeared to be in place before testing according to AFM topography measurements.

(a)

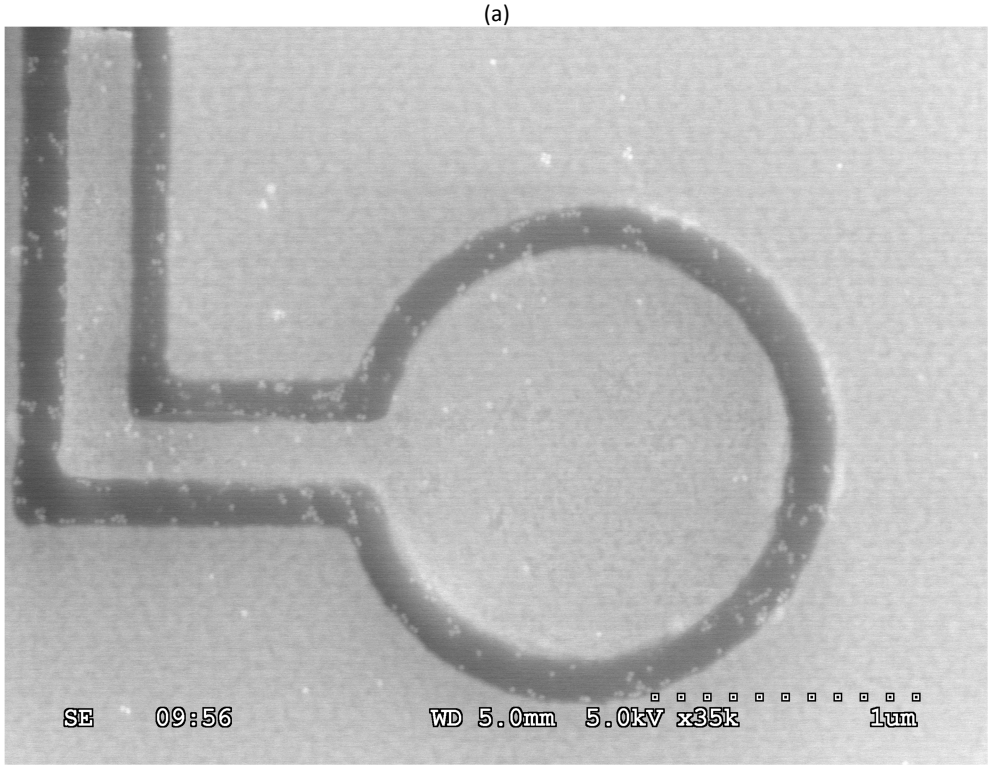

(b)

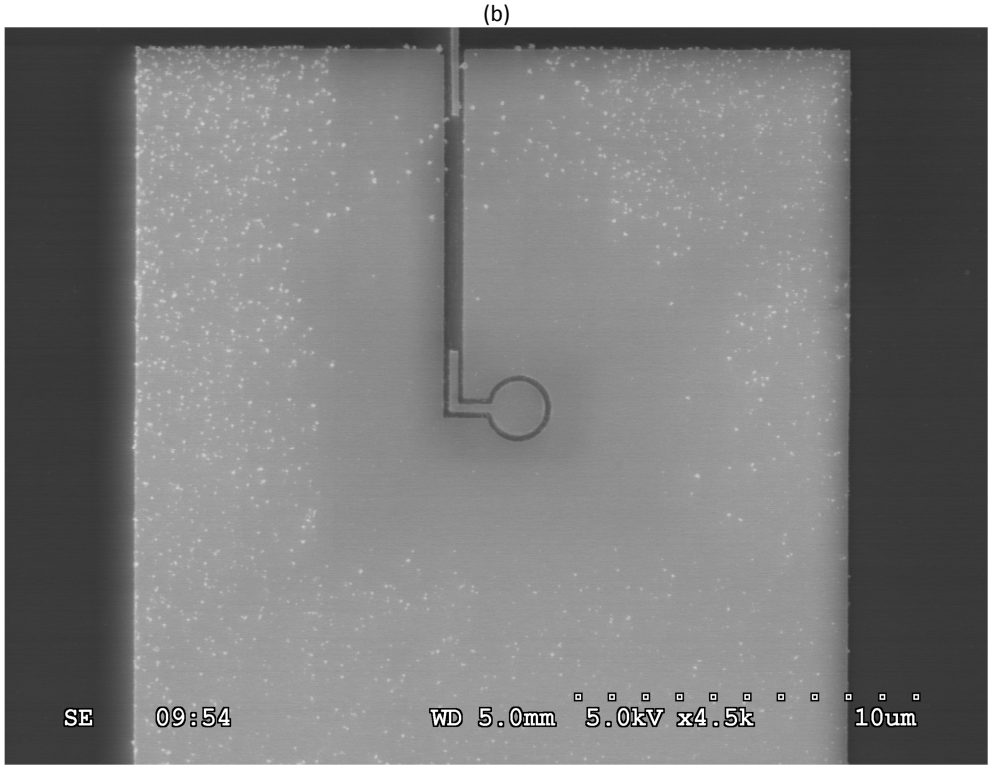

FIG. 3.20 Interdigitated electrodes after testing with a 20 nm Au colloid.

Representative SEM images after 10 minutes of deposition of 20 nm Au nanoparticles at 2.5 V directly onto a device with a 50 nm SiO_2 insulating layer. (a) 20 nm particles visible on and around the central electrode. (b) Larger particulates were deposited in regions that were attracted to the grounded electrode.

We decided to pursue further tests of the *Interdigitated Electrodes* using a larger 80 nm Au colloid, so that particle deposition could be more reliably assessed. SEM images obtained after testing with this colloid are presented in FIG. 3.23 – FIG. 3.26. Results with these devices were chaotic, with the central electrode frequently displaced from the Cr adhesion layer (FIG. 3.21) or damaged (FIG. 3.23) following testing with the colloid. The deposits of particles on the surface were frequently randomly dispersed over the electrode areas, regardless of polarity (FIG. 3.22).

Particles did appear to be more likely to accumulate at the gap between the electrodes (FIG. 3.24). To ascertain whether this was due to electric field or a geometry trap, we recessed the electrodes into the surface by adding an RIE etching step between the nanolithography and the thermal evaporation of the Cr/Au for the electrodes during fabrication. These recessed electrodes also saw particles deposit between the electrodes (FIG. 3.25, FIG. 3.26), but with no other stable trend.

Overall, the Interdigitated Electrode devices were unable to controllably manipulate the colloid with the current design. Future devices should be fabricated avoid using Au, as it is thoroughly unsuited to these types of experiments. Au deposited by sputtering was equally unstable, but stable deposition was obtained on Pt films. Unfortunately sputtering results creates greater difficulties with lift-off. Other issues that may have arisen due to the sputtered SiO_2 insulating film are yet to be investigated, due to failure of the sputtering tool.

(a)

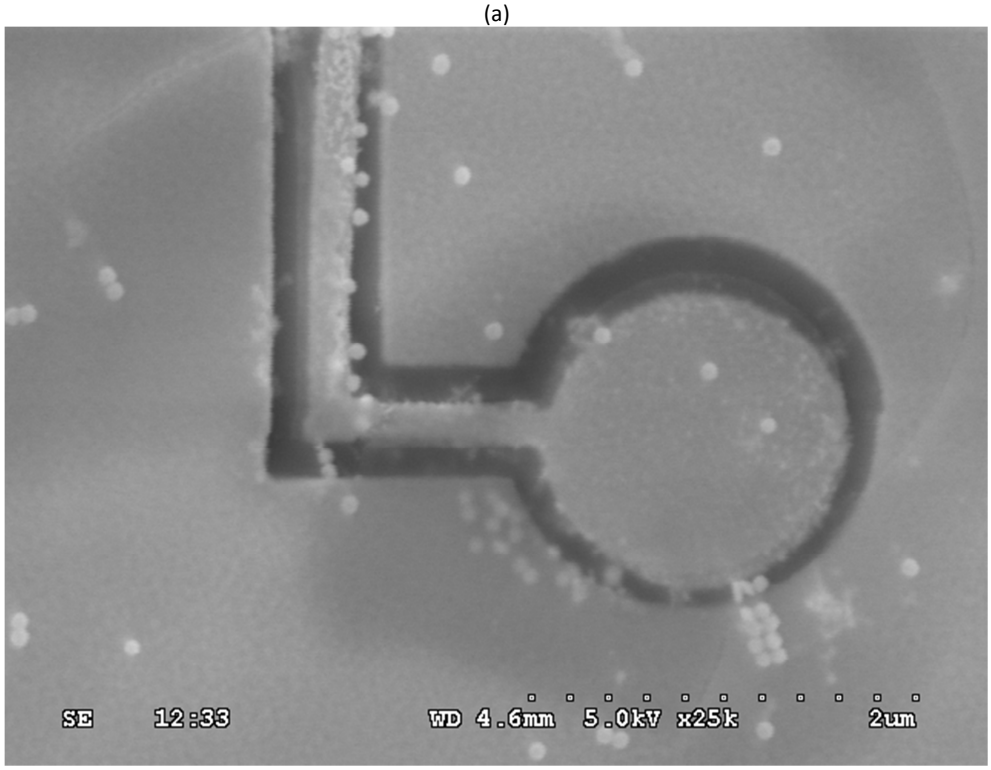

(b)

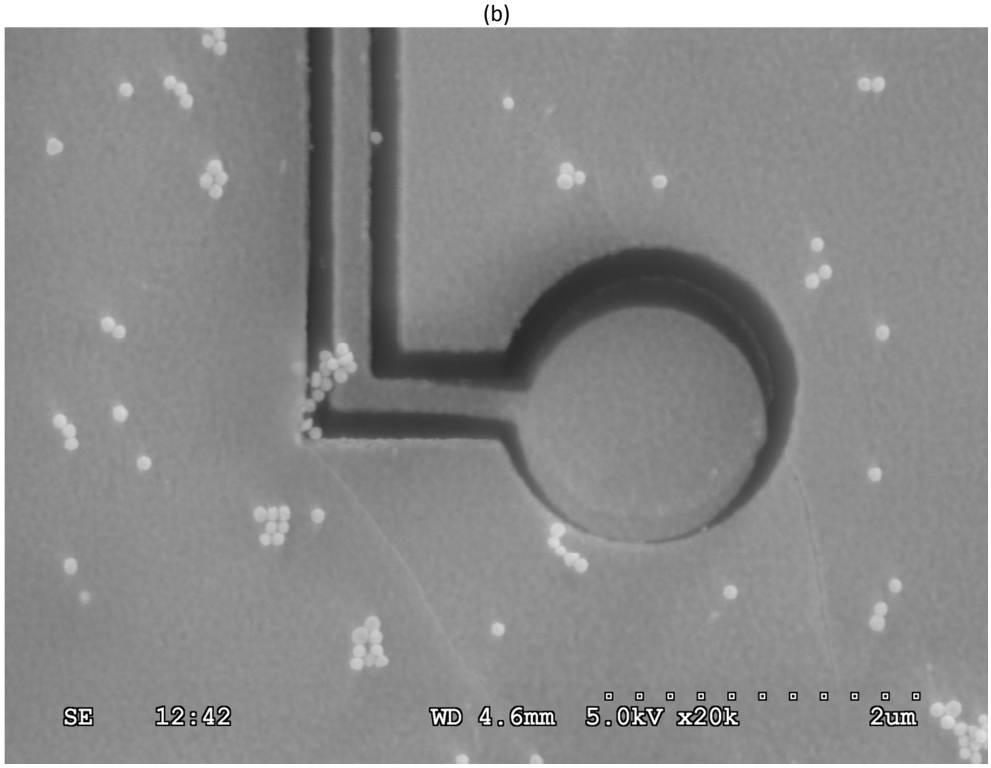

FIG. 3.21 Interdigitated electrodes after testing with an 80 nm Au colloid (1/6).

SEM images after 10 minutes of deposition of 80 nm Au nanoparticles at 1 V directly onto a device with a 50 nm SiO2 insulating layer.

(a)

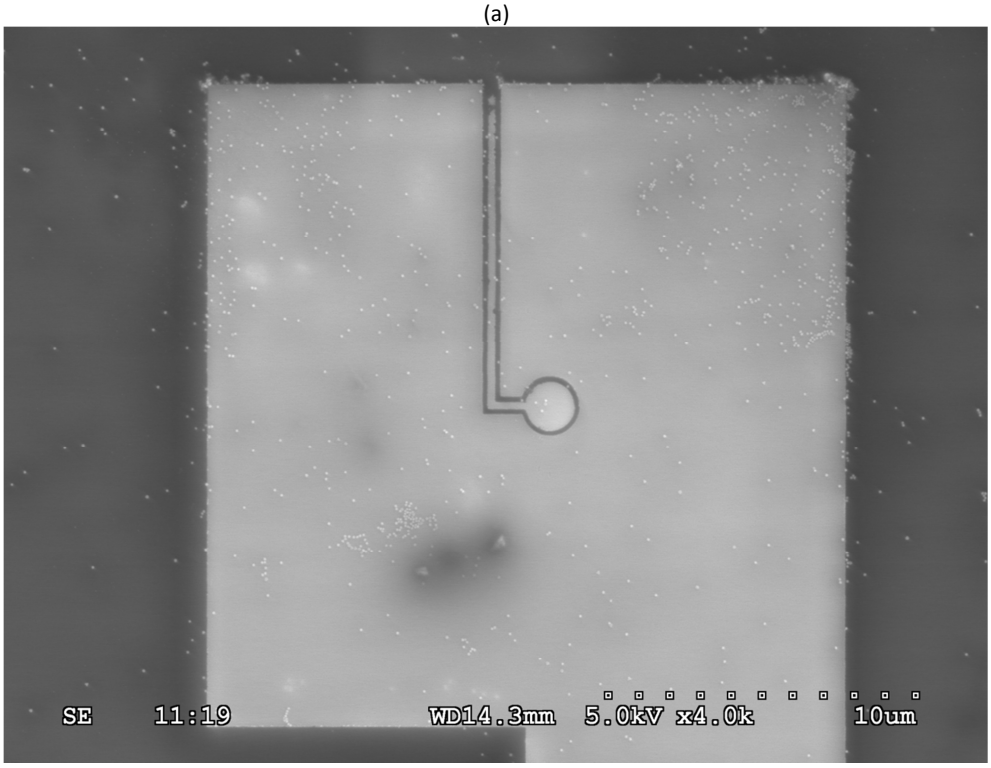

(b)

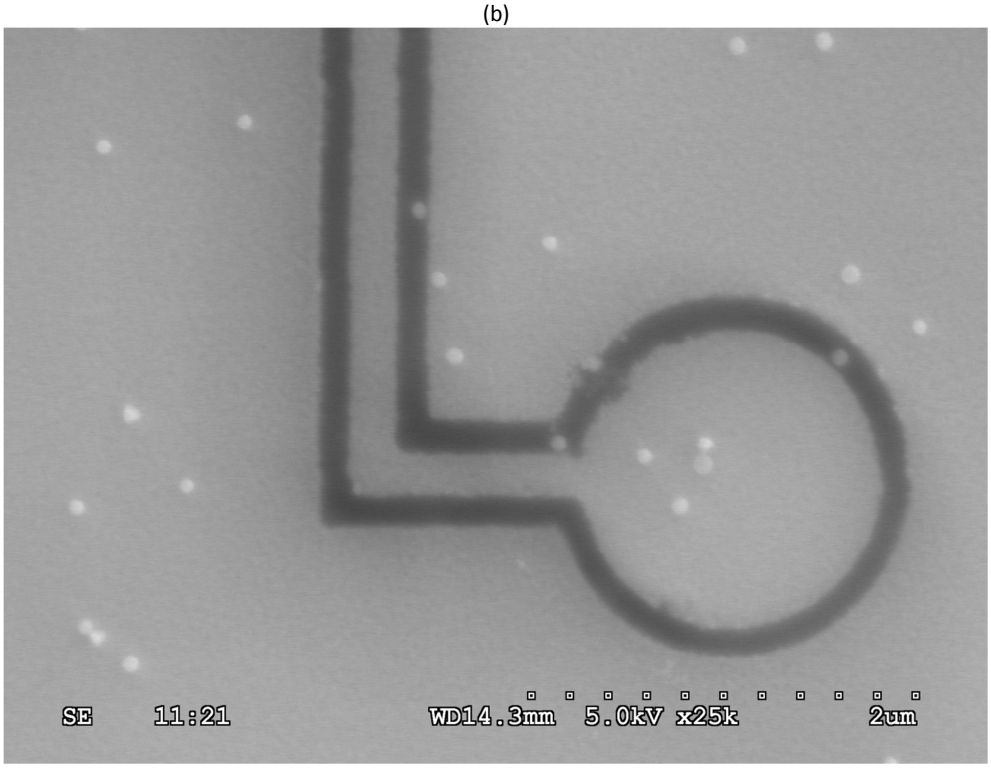

FIG. 3.22 Interdigitated electrodes after testing with an 80 nm Au colloid (2/6).

SEM images after 10 minutes of deposition of 80 nm Au nanoparticles at 2.5 V directly onto a device with a 50 nm SiO_2 insulating layer.

(a)

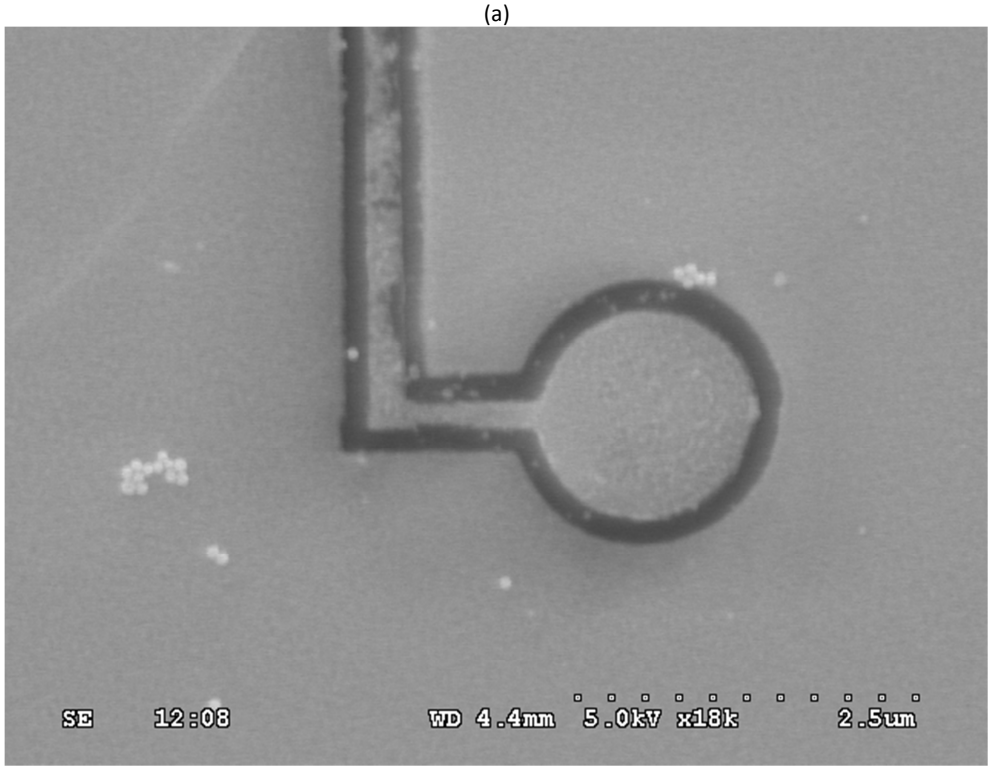

(b)

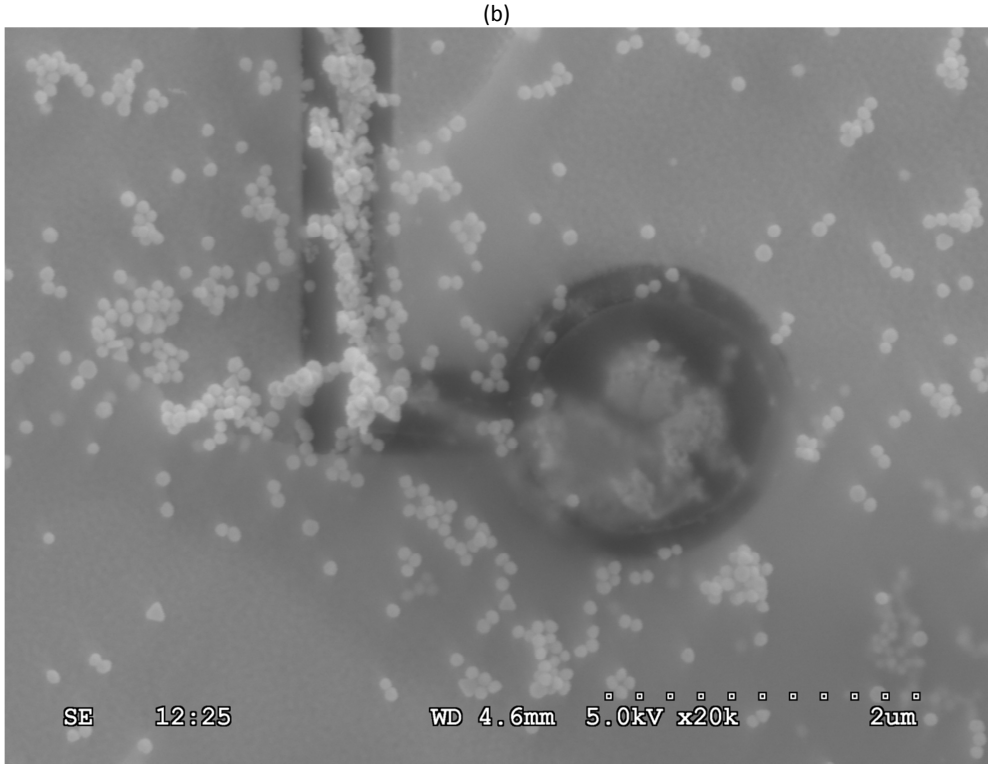

FIG. 3.23 Interdigitated electrodes after testing with an 80 nm Au colloid (3/6).

SEM images after 10 minutes of deposition of 80 nm Au nanoparticles at 4 V directly onto a device with a 50 nm SiO2 insulating layer.

(a)

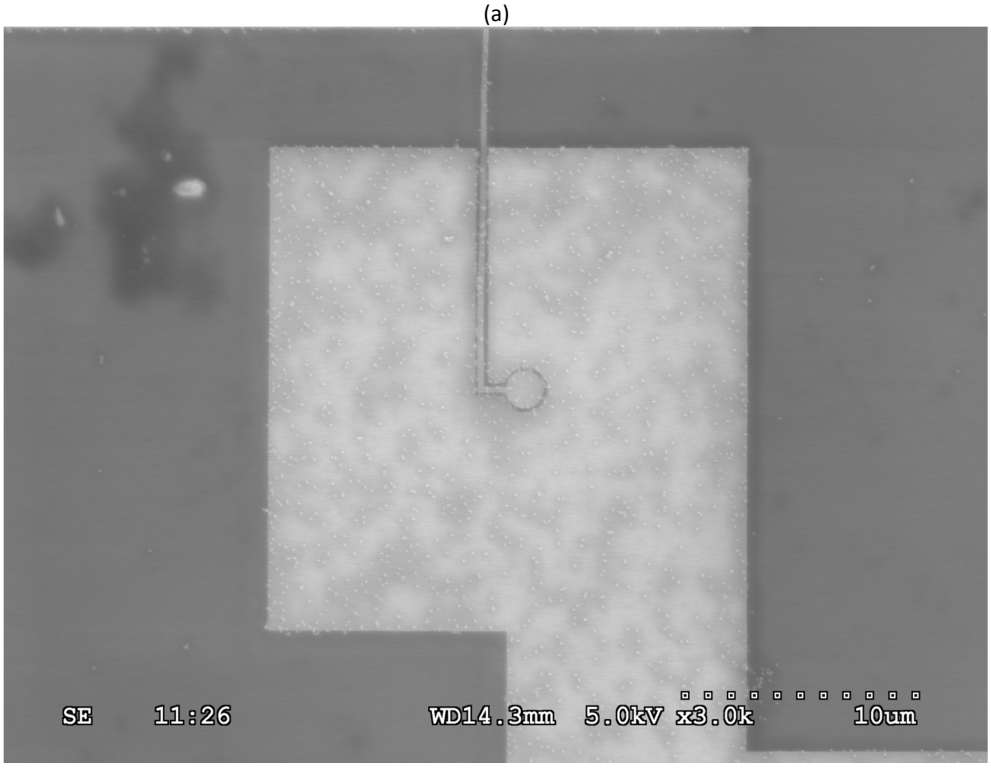

(b)

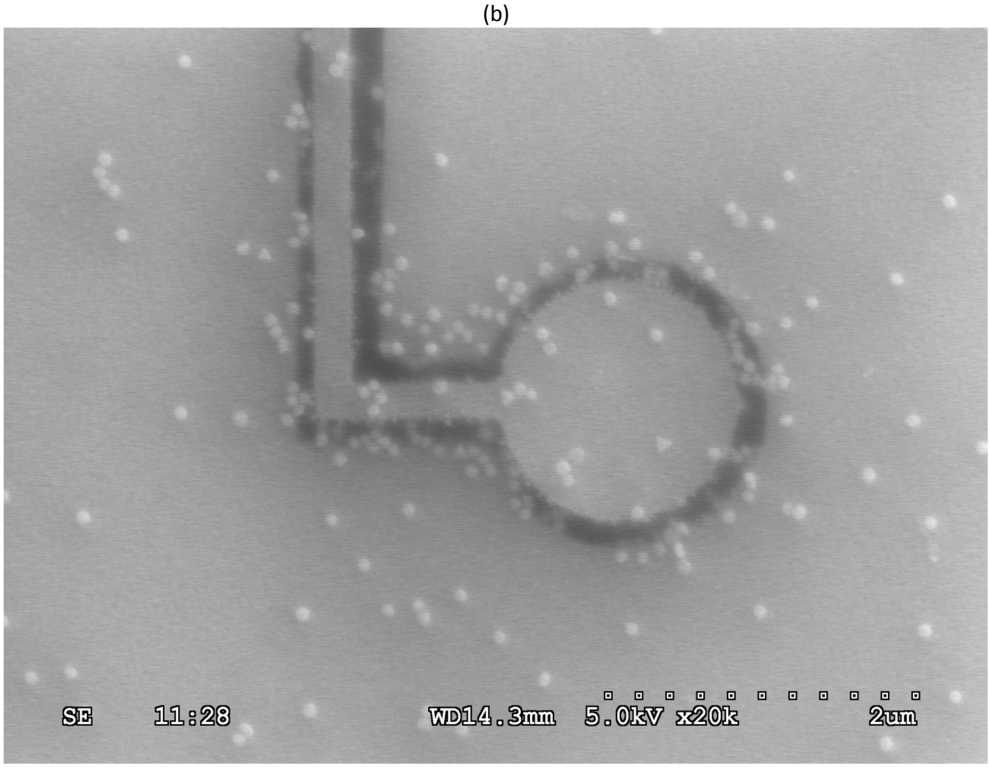

FIG. 3.24 Interdigitated electrodes after testing with an 80 nm Au colloid (4/6).

SEM images after 10 minutes of deposition of 80 nm Au nanoparticles at 4 V directly onto a device with a 50 nm SiO_2 insulating layer.

(a)

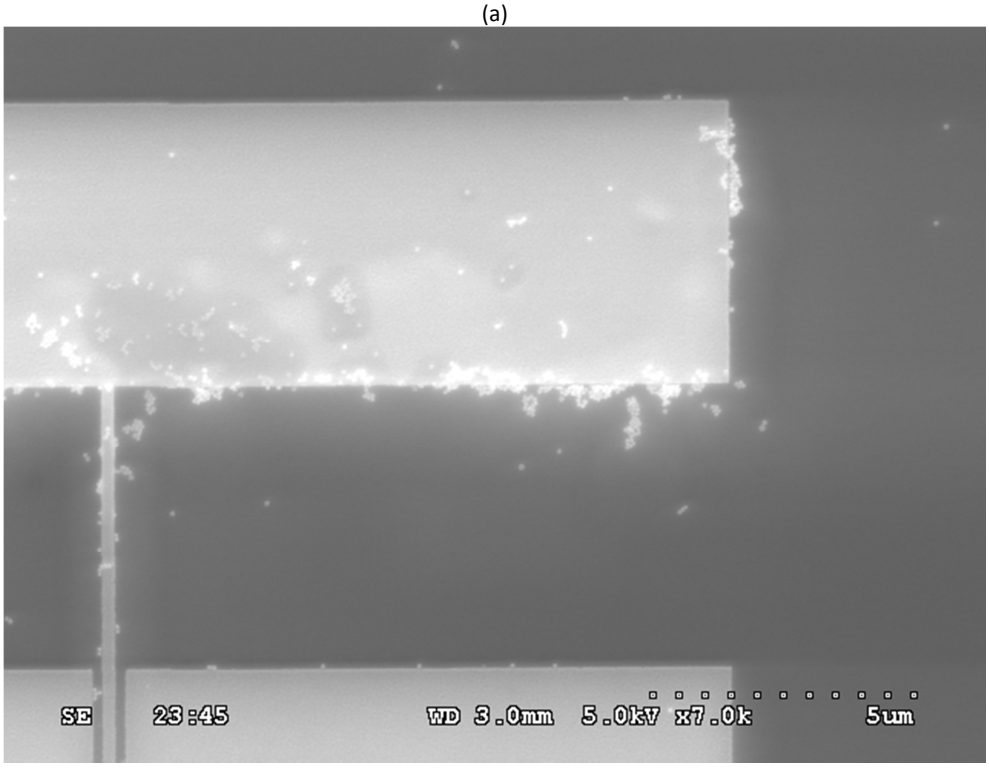

(b)

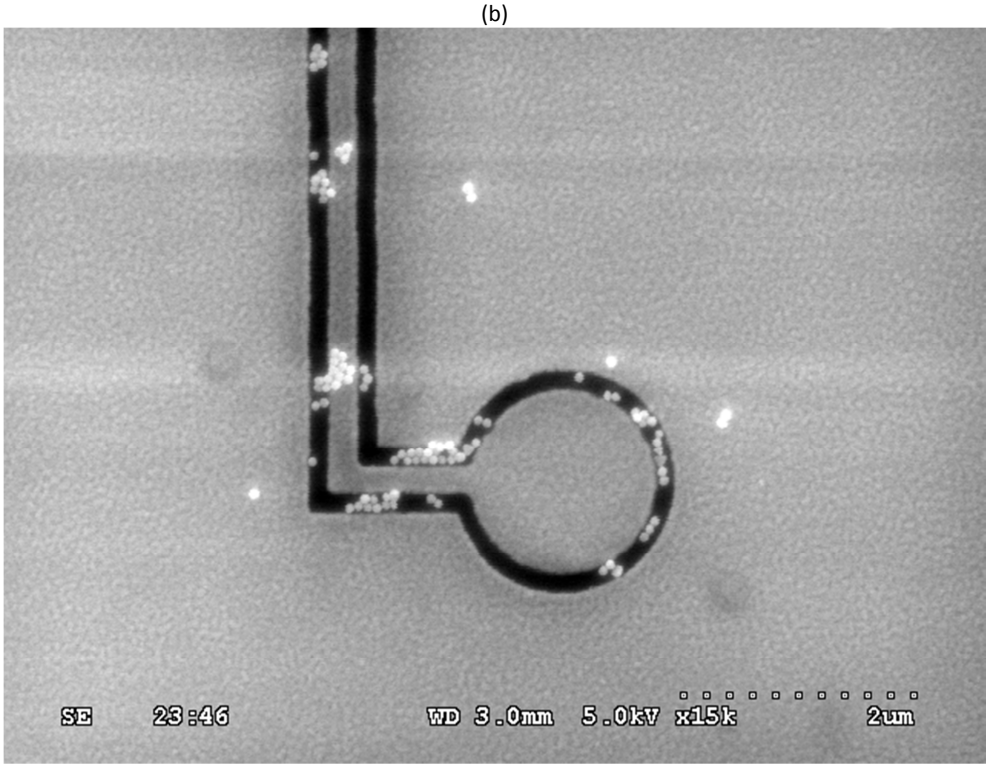

FIG. 3.25 Interdigitated electrodes after testing with an 80 nm Au colloid (5/6).

SEM images after 10 minutes of deposition of 80 nm Au nanoparticles at 4 V directly onto a recessed device with a 50 nm SiO_2 insulating layer.

(a)

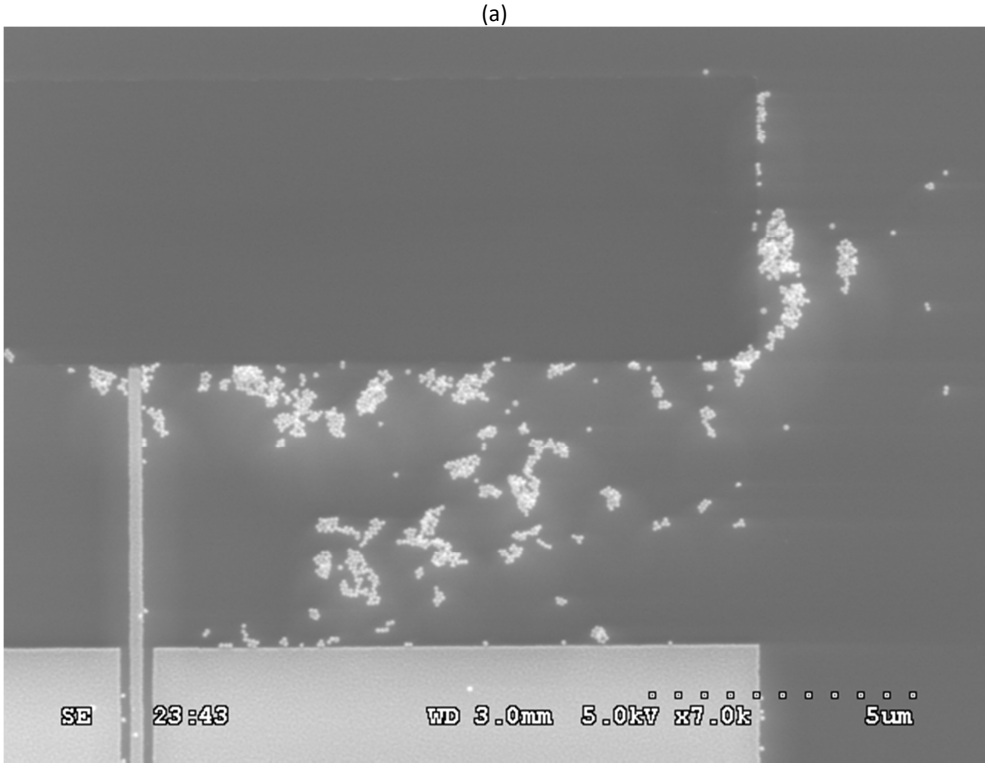

(b)

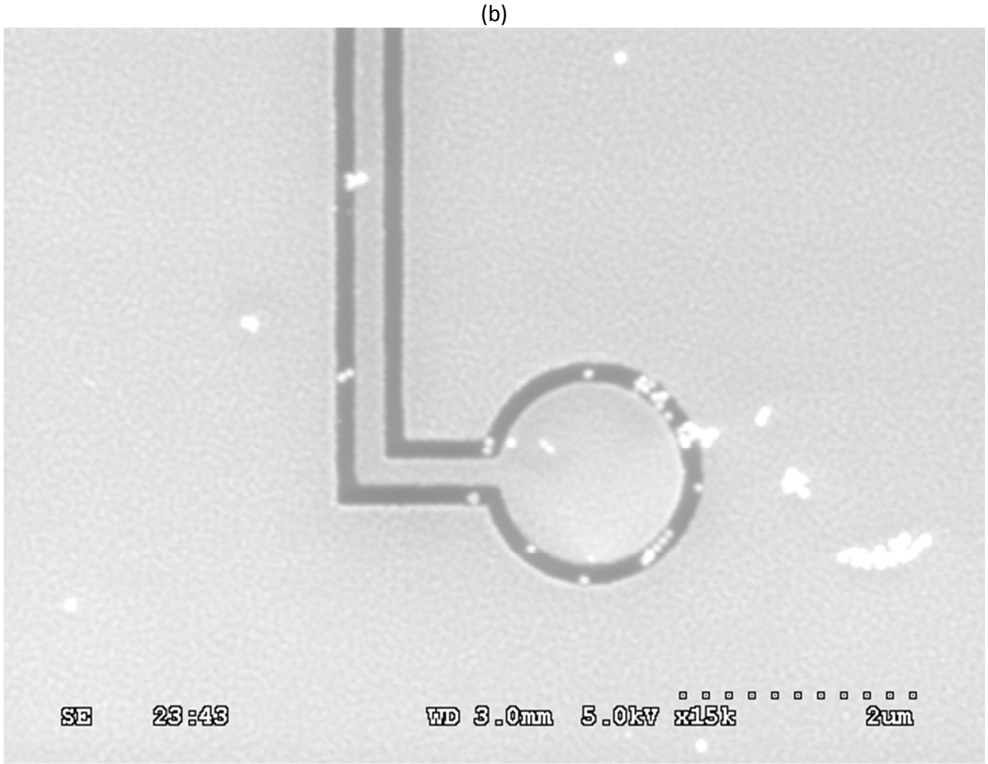

FIG. 3.26 Interdigitated electrodes after testing with an 80 nm Au colloid (6/6).

SEM images after 60 minutes of deposition of 80 nm Au nanoparticles at 4 V directly onto a recessed device with a 50 nm SiO_2 insulating layer.

3.5 Troubleshooting

To understand the mechanisms that were affecting the assembly devices tested in Chapter 3, we analysed the behaviour of the different components we had identified as potential causes of failed particle assembly. In particular, we focused on the observed instability of the colloid and the assembly of the MHA monolayers.

3.5.1 Colloid stability

During testing deposited nanoparticles were frequently aggregated on the surface, where interparticle electrostatic repulsion had failed. This called into question the stability of the gold colloids we were using in our experiments; in particular, whether the surface charge of our particles was sufficient to prevent aggregation and enable electrophoretic manipulation. To analyse their stability, we used a Malvern Zetasizer Nano ZS, which uses dynamic light scattering (DLS) to measure the diffusion of particles in the dispersion medium. Laser light deflecting off all the particles in this dispersion creates an interference pattern, which in the case of the Nano ZS is mapped as an intensity distribution using the patented non-invasive backscatter (NIBS) technique[119]. With no external electric field, the particles undergo Brownian motion that causes the intensity distribution to change over time. The rate of this change can be measured by the drop in correlation with the initial signal over time; smaller particles diffuse faster and thus the drop in correlation is also faster.

The fitting of an exponential relationship to this decay in correlation with time allows the translation diffusion coefficient, D_{dif} of particles in a dispersion to be determined; integrals of multiple decay functions can be applied to dispersions containing particles

of different sizes. The diffusion coefficient can then provide a measure of the hydrodynamic diameter, d_h of the particles via the Stokes-Einstein equation[120]:

$$d_h = \frac{k_B T}{3\pi\eta D_{dif}} \tag{4.1}$$

where η is the viscosity of the dispersion medium and k_B and T remain the Boltzmann constant and temperature. The hydrodynamic diameter of a particle is a combination of the diameter of the solid particle and the surrounding electrolyte that moves with the particle.

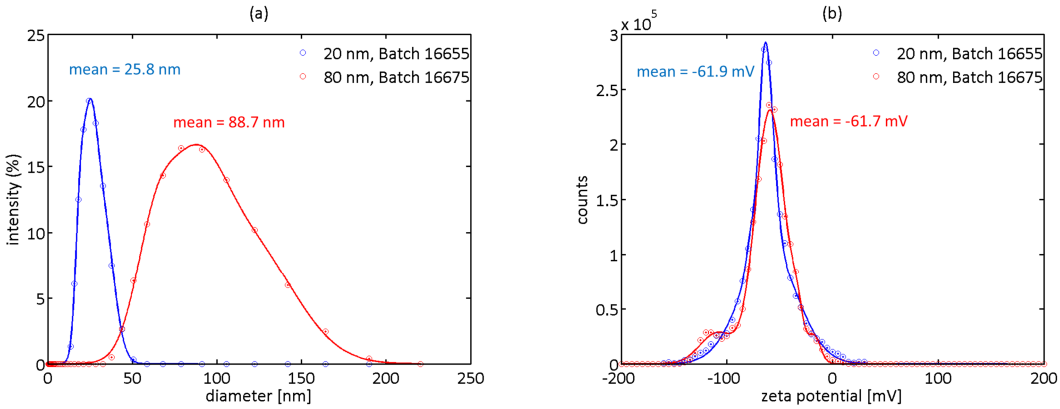

FIG 3.27 Size and zeta potential measurements of Au nanoparticles

(a) Dynamic Light Scattering (DLS) and (b) Laser Doppler Electrophoresis (LDE) measurements of 20 nm and 80 nm diameter Au nanoparticles in water. These Au nanoparticle dispersions were purchased from BBI Solutions, with the batch numbers specified in the legends. Gaussian fits have been applied to the intensity profiles of these distributions and the mean diameter and zeta potentials annotated on each graph.

The results of DLS (FIG 3.27a) showed that the 20 nm and 80 nm colloids used during testing had mean hydrodynamic diameters of 25.8 nm and 88.7 nm respectively. A wider spread of diameters was indicated for the 80 nm colloid, which may be the result of using the Turkevich method which is optimised for 20 nm particles. It is also inflated by the resolution of the measurement method and most particles corresponded well to their specifications under SEM measurement.

Laser Doppler Electrophoresis (LDE), subsequently enabled the zeta potential of the nanoparticles to be measured under an electric field. This uses the relationship between the electrophoretic mobility U_e and the zeta potential φ_Z defined by the Henry equation[121]:

$$\varphi_Z = \frac{3\eta U_e}{2\varepsilon_r f(\kappa a)} \tag{4.2}$$

where $f(\kappa a)$ is the Henry function, approximated as 1.5 for a polar medium like the Au colloid, for colloid particles with diameter a and an inverse Debye length κ. We measured similar zeta potentials for both colloids of approximately -62 mV (FIG 3.27b), which indicates that the colloids are highly stable and carry a sufficient negative surface charge to enable electrophoretic deposition of the particles.

3.5.2 Coverage of Molecular Monolayers

One particularly important requirement for the devices to operate was the molecular monolayer of MHA. This monolayer was intended to ionise in solution and provide a negative surface charge surrounding the target area of the devices, funnelling particles towards the centre and preventing particles from approaching the shielded area. To obtain more information about the composition of the MHA monolayer on the Au surface, we decided to use x-ray photoelectron spectroscopy (XPS). This allowed us to measure the characteristic binding energy of characteristic electron orbitals, identifying what elements compose the surface. Shifts in the detected peaks also allow particular atomic bonds to be identified, which aids with molecular identification.

The results for measurements taken on a gold coated wafer before and after self-assembly of are presented in FIG 3.28. The full pass covers electron binding energies up to 1300 eV, with several large peaks resulting from Au orbitals 5d (5.8 eV), 5p3

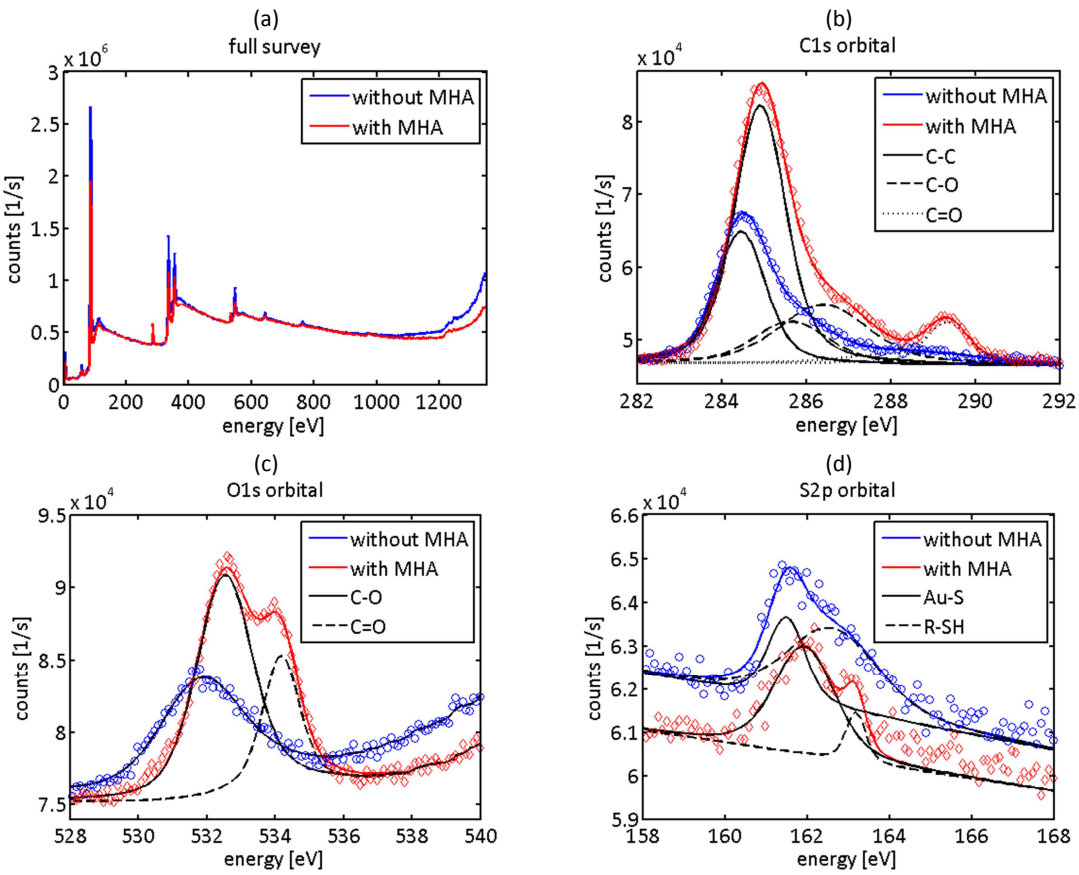

FIG 3.28 XPS identification of MHA monolayers

X-ray photoelectron spectroscopy (XPS) measurements of gold coated wafers before and after they are coated with monolayers of MHA. (a) shows the full survey scan of the surfaces and (b-d) show focused scans at the peaks at the characteristic work functions of the C1s, O1s and S2p orbitals respectively. The largest peaks in (a) resulted from the Au surface, which were suppressed by the MHA layer. MHA coatings also significantly increased the peaks for C-C and C-O bonds and creates a new C=O peak, as a result of the carboxyl terminus on the molecule. The thiol bond Au-S is present with and without MHA indicates some prior contamination.

(56.8 eV), 4f (85 eV), 4d5 (334 eV) and 4d3 (353 eV) (FIG 3.28a). All of these peaks were diminished after the MHA monolayer coated the surface, as would be expected although this does not necessarily indicate complete surface coverage.

More focused scans with 50 eV step sizes were then taken of the regions characteristic of the C1s, O1s and S2p molecular orbitals, which should identify the carboxyl and thiol elements of MHA. The C1s scan (FIG 3.28b) identified the peaks of C-C (284.8 eV),

C-O (286 eV) and C=O (288.5 eV) bonds present on the surface, with C-O (531.5 eV) and C=O (533 eV) peaks also measured in the O1s scan (FIG 3.28c). The presence of these peaks prior to MHA assembly indicates that organic contaminants were present on the surface during the measurement. Generally assembly was performed after degassing the surface by annealing on a hot plate at 120°C, but this was not done to the wafer prior to XPS measurements. After MHA assembly, all the peaks indicative of the carboxyl group become much more prominent, indicating that the MHA is on the surface.

The scan of the S2p orbital scan detected some very small peaks, characteristic of Au-S bonds (162.5 eV) and thiol bonds R-SH (164 eV), where R is an unidentified hydrocarbon (FIG 3.28d). The peak doublet fitted to the data before MHA assembly indicated an equal presence of Au-S and R-SH bonds on the surface due to an unknown contaminant. After MHA assembly the peak fitting indicated that the Au-S peak was now more prominent than the R-SH peak, the latter of which now had a higher quality factor. These results were not conclusive since the two results were very similar, but this indicated that there were more thiol molecules bound to the surface (Au-S) than unbound thiols (R-SH) after assembly. These unbound thiols were expected to be left over from the MHA self-assembly, many more of which would have been present on the surface if the sample had not been rinsed thoroughly.

The prominent presence of S atoms before assembly was a clear sign that the Au surface was contaminated, so thorough cleaning with acids was important to ensure good surface coverage. We were unable to confirm whether this contamination had occurred during the transit between the locations for MHA assembly and the XPS system. Prior cleaning of the surface with hydrochloric acid or performing the MHA

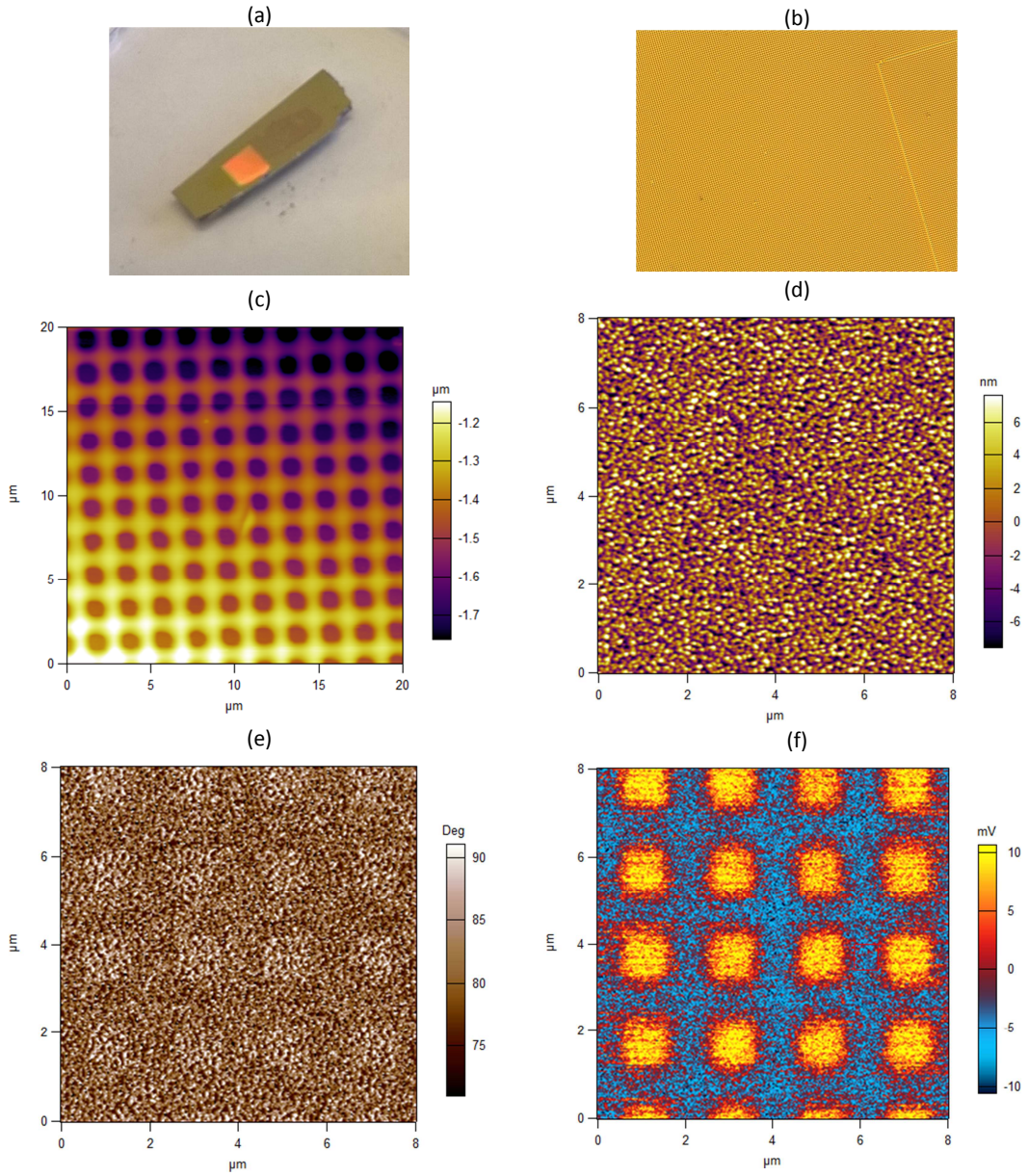

FIG 3.29 KPM of MHA monolayers.

(a) A photo, (b) optical microscope and (c) AFM image of square holes patterned into a PMMA mask by electron beam lithography. The mask intended to be square appears to be somewhat circular. AFM (d) topography and (e) phase images of a Au surface patterned with areas of MHA, which are visible as the lighter areas in the phase image. (f) KPM images of the MHA on the Au surface, where the MHA has the higher surface potential compared to the surrounding Au.

assembly process under an inert nitrogen atmosphere did not change the XPS results. The S2p peaks were expected to be suppressed by the 16-carbon chain of the MHA and correspond to results in previous studies[122]. Combined with the measurement

of the carboxyl bonds in the C1s and O1s scans and the change in contact angle of a water droplet after the MHA self-assembly process, this was strong evidence that there was MHA bonded to the gold surface.

To summarise, the presence of MHA was confirmed with XPS by the characteristic C1s, O1s and S2p peaks during XPS. To assess the surface coverage of MHA on Au, we used KPM to measure the surface potential difference between the Au and MHA regions of a sample. we made devices for these tests by patterning PMMA e-beam resist to expose arrays of 1µm x 1µm squares in the mask (FIG 3.29a-c), before using the standard MHA assembly process. Subsequent lift-off of the resist in acetone created arrays of MHA on the surface.

These MHA areas could not be discerned in the topography measurement (FIG 3.29d) due to the high surface roughness of the Au. However, the phase response of the cantilever during the topography measurement did show a contrast corresponding to the MHA coated areas (FIG 3.29e). The KPM measurements presented in FIG 3.29f shows how the monolayer has formed in the holes that were written into the resist before lift-off. These measurements indicate that MHA has grown onto the exposed Au areas evenly. If contaminants were present on the surface before lift-off as indicated in the XPS measurements in the previous section, then the MHA has displaced them.

3.6 Chapter Summary

In spite of the promising indications of the simulations in the previous chapter, the particle assembly devices that we tested did not isolate particles as they were designed. The *Gate* and *Pedestal* device designs suffered from issues of instability in the colloid as it was deposited onto the devices and the MHA monolayer that was intended to repel particles from the surface surrounding these devices was also ineffective. Measurements of Au nanoparticle colloids size distribution and zeta potential indicated that they were stable outside of testing. XPS and KPM measurements confirmed the formation of MHA monolayers on these devices. This indicates that the applied bias is inducing instability of the process and inhibiting the designed operation of these devices.

In-situ AFM scans indicated that particles were in close proximity to the surface in many cases but relatively few were found deposited on the surface after testing. This may reflect the effect of the hydrostatic barrier between each particle and the surface and the driving voltage, which the driving voltage is unable to overcome.

The *Interdigitated Electrode* devices encountered additional instability of the Au electrodes, which were frequently damaged during testing. Future tests with a Pt electrode material should be more successful, as preliminary testing has shown that it does not suffer this instability. However, instability of the colloid induced by the electrical biasing of the electrodes as observed for *Gate* and *Pedestal* devices may still affect the assembly.

Chapter 4

Nanoparticle Assembly onto Molecular Monolayers

As the approach of using an applied bias had encountered great inconsistency in results, we considered if there were ways to increase the rate of self-assembly mediated by molecular monolayer alone. In this chapter we look at the use of ionised surface ligands, innate surface charges and non-polar surfaces to achieve single-nanoparticle capture. This led to the discovery of a new, rapid method of single-nanoparticles self-assembly that should be compatible with the ultimate goal probe-based nanoparticle pick-and-place.

4.1 Self-Assembly of Nanoparticles

To confirm the validity of the reported single nanoparticle self-assembly process[48],[105] we needed to replicate the result. First we tested particle assembly on planar surfaces and then into devices designed to funnel particles into the centre of patterned holes. We had used self-assembled monolayers of MHA for gate devices; the fabrication process was discussed in Chapter 3. For the chemically-enabled self-assembly of nanoparticles, we also needed to use self-assembled monolayers of 3-(aminopropyl)triethoxysilane (APTES), a silane compound that would assemble onto oxidised surfaces of SiO_2. The APTES monolayer was made by diluting APTES (Sigma

Aldrich, ≥ 98%) to a 1 mM in toluene in an inflatable N_2 gas filled chamber. SiO_2 samples were immersed in this solution, still in the chamber, for 30 minutes. Samples were then soaked in isopropanol, removed from the chamber, and rinsed for three successive 10 minute rounds of IPA under sonication before drying by compressed air.

4.1.1 Planar surfaces

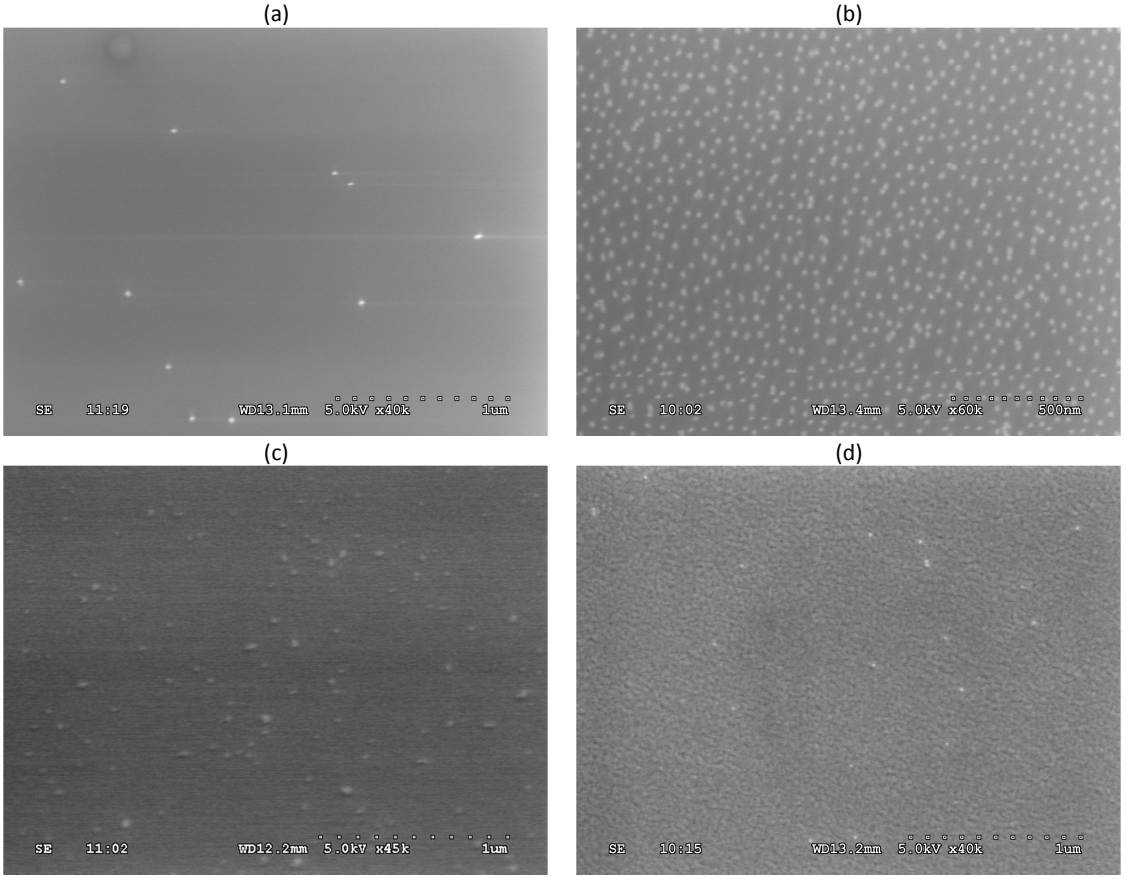

FIG 4.1 Au nanoparticle assembly on different surfaces.

SEM images of sample surfaces after immersion in a 20 nm Au colloid for 10 minutes, to compare how the particles interact with different surfaces: (a, b) silicon dioxide surface (a) without and (b) with a self-assembled monolayer of 3-(aminopropyl)triethoxysilane (APTES); (c, d) gold surface (c) without and (d) with a self-assembled monolayer of MHA.

We first tested how different surfaces and different surface ligands interacted with Au colloids to ascertain which mechanisms were compromising the devices. FIG 4.1 shows

representative SEM images of how 20 nm Au nanoparticles assembled onto SiO_2 and Au surfaces, which were immersed in the colloid for 10 minutes. When these surfaces have not been pre-coated with any kind of functional monolayer, particles appeared to distribute themselves randomly over the surface. When another SiO_2 surface was functionalised with APTES and then immersed in the colloid, the Au particles assembled into an organised layer on the surface (FIG 4.1b). The spacing between the particles was caused by their mutual electrostatic repulsion and is consistent with how the particles were expected to assemble onto a positively charged surface. When the Au surface was functionalised with MHA (FIG 4.1d), the surface appears to have become more repulsive to nanoparticles; there are several particles that still bonded to the surface, but fewer than were observed in the test with bare Au (FIG 4.1c). This reflected the repulsion that should be observed between the negatively charged MHA ligand and the nanoparticles. Many particles were able to penetrate this energy barrier, which may be reduced by manipulating the composition of the colloid itself. This could include reducing the density of particles by dilution or manipulation of the solution pH. An increase of pH should enhance negative zeta potentials, but the increase in ionic concentration will also destabilise the colloid.

4.1.2 Single-nanoparticle self-assembly mechanism

Huang et al.[48] had reported that single nanoparticles could be isolated from a colloidal dispersion onto patterned areas of APTES and MHA molecular monolayers. Electron beam lithography patterned arrays of holes into a 30 nm thin film of Au on a SiO_2 substrate. The SiO_2 surface was then functionalised with APTES followed by the functionalisation of the Au with MHA. This should drive the negatively charged Au

nanoparticles to assemble into the APTES coated SiO_2 holes selectively depending upon the diameter of the holes. We made several of these devices and then immersed them into a 20 nm Au colloid overnight. The colloid was sonicated beforehand to reduce flocculation of the particles.

The results for these devices are presented in FIG 4.2 – FIG 4.6. In FIG 4.2 the device was immersed into a 20 nm Au colloid for 12 hours. The results showed that particles were frequently captured in the larger 200 nm diameter target areas (FIG 4.2a), many particles were also deposited on the MHA coated Au surfaces that they should have been repelled from. Some particles can also be seen attached at the edge of the holes in the Au layer, which could mean that they were deposited during rinsing of the surface as with geometry based capture[56] rather than during electrostatic capture. The smaller 100 nm diameter gates (FIG 4.2b) see very few incidents of nanoparticle capture with most particles depositing on the Au-MHA surface.

Dilution of the colloid improved the results for nanoparticle capture. FIG 4.3 and FIG 4.4 show the results for another device after 12 hours immersion in a 20 nm Au colloid that was diluted in a 1:2 ratio with distilled water. This reduction in the ionic strength should increase the energy barrier between like-charged surfaces (FIG 4.3a) whilst reducing the number density of nanoparticles. The result saw many particles funnelled towards the centre of 200 nm diameter target areas (FIG 4.3), with multiple and single nanoparticle captures occurring. Smaller 100 nm diameter and width target areas FIG 4.4 reduced the number of particle captures, limiting the results to single particles in many cases, but with limited long-range consistency. Further dilution of the 20 nm Au colloid down to a 1:5 ratio with distilled water (FIG 4.5) achieved similar results to those with higher ionic and particle concentrations.

(a)

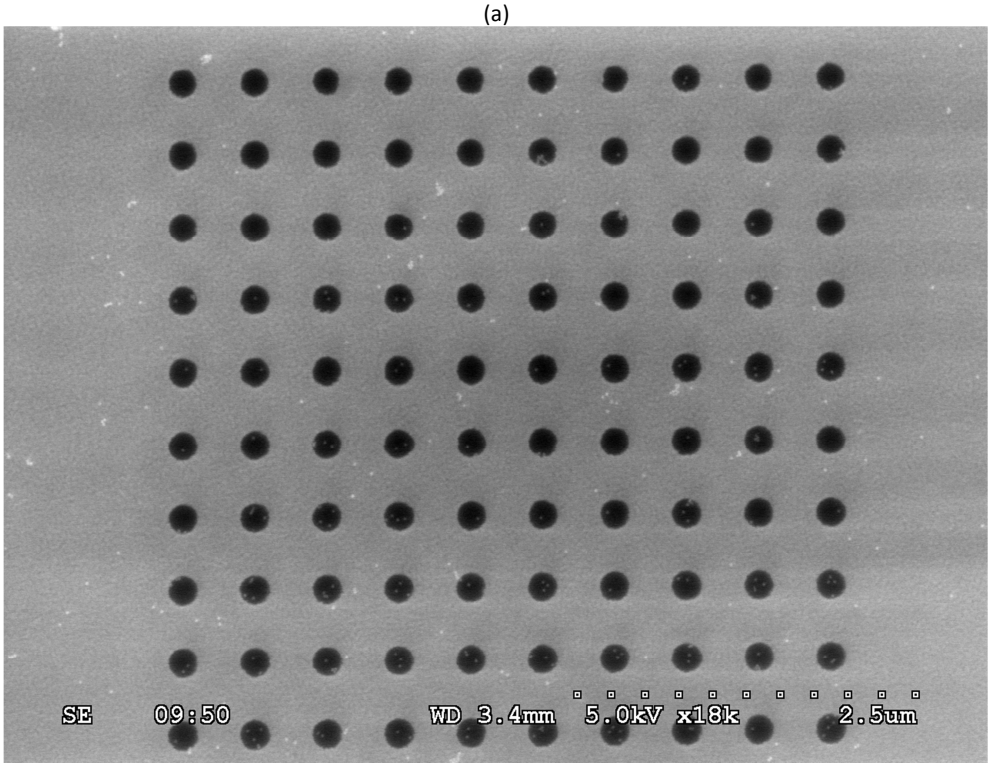

(b)

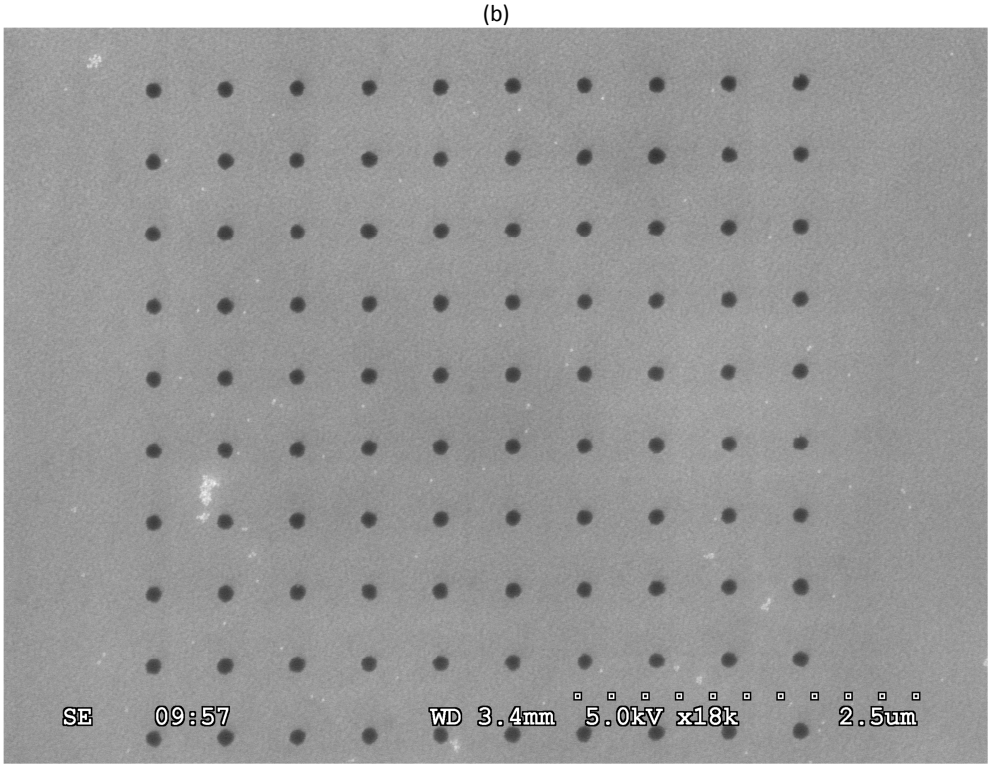

FIG 4.2 Single-nanoparticle placement driven by self-assembled monolayers (1/5).

SEM images of nanoparticles self-assembled onto devices (target areas are dark circles, with APTES coating SiO_2), after 12 hours of immersion in an undiluted 20 nm Au colloid. Many nanoparticles captured in 200 nm target areas (a), fewer particles in smaller 100 nm diameter areas. Nanoparticles also deposited on the negatively charged surface (bright).

(a)

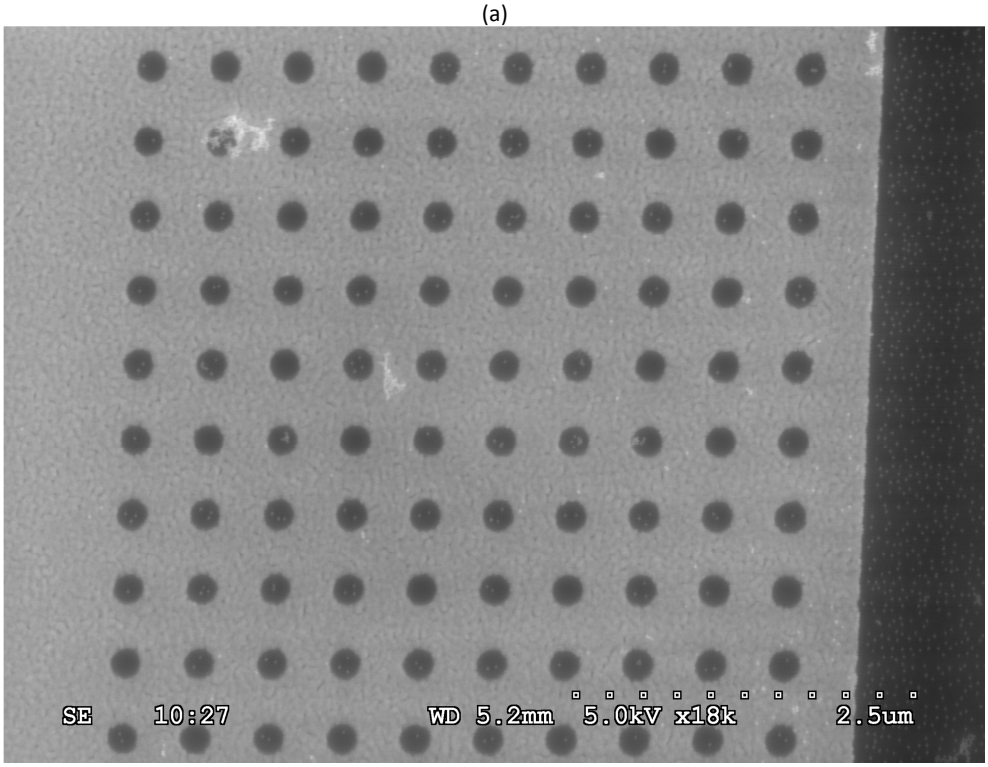

(b)

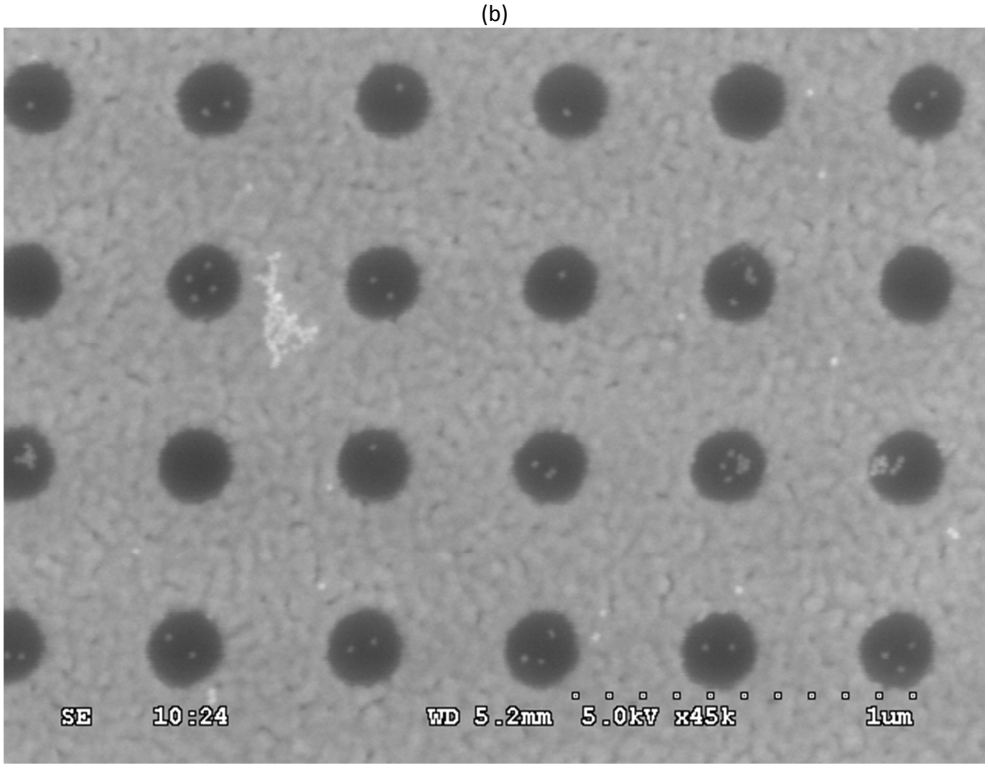

FIG 4.3 Single-nanoparticle placement driven by self-assembled monolayers (2/5).

SEM images of nanoparticles self-assembled onto gate devices, after 12 hours of immersion in a 20 nm Au colloid diluted in a 1:2 ratio with distilled water. Many nanoparticles are deposited on the 200 nm target areas but with no consistent order. Other nanoparticles have agglomerated

(a)

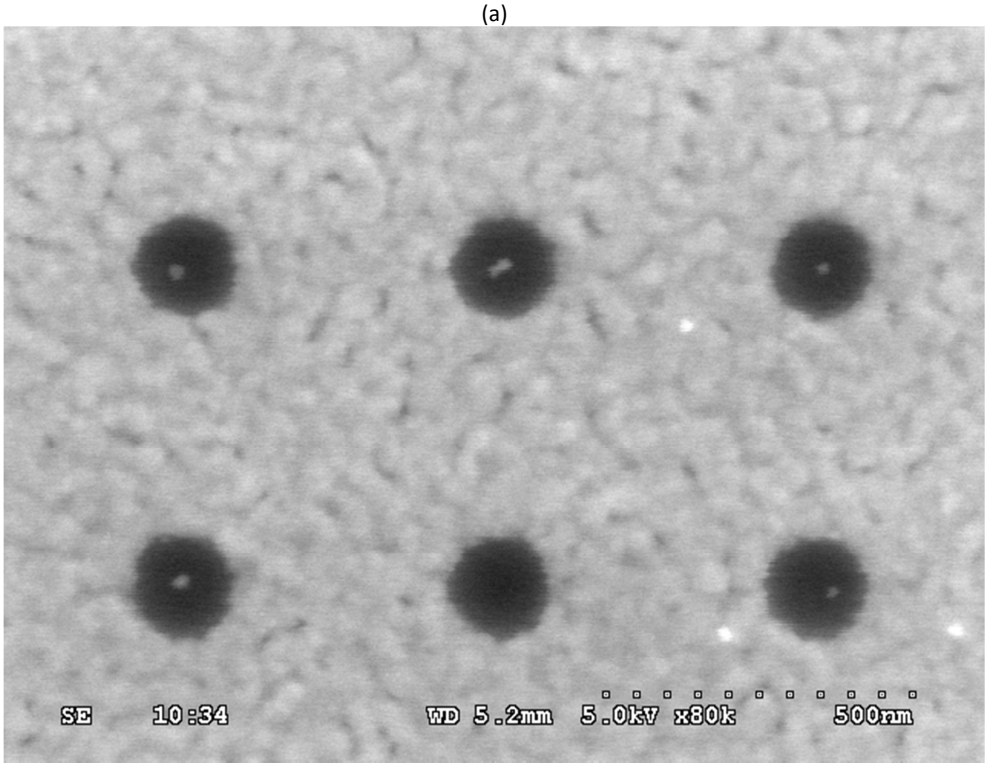

(b)

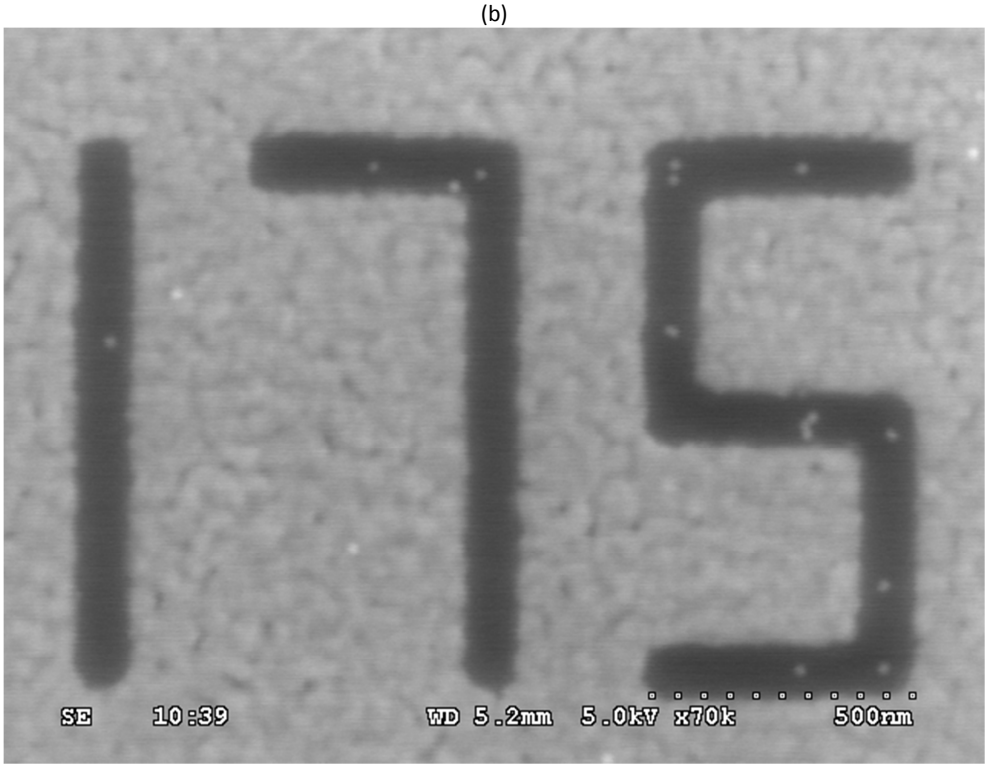

FIG 4.4 Single-nanoparticle placement driven by self-assembled monolayers (3/5).

SEM images of nanoparticles self-assembled onto gate devices, after 12 hours of immersion in a 20 nm Au colloid diluted in a 1:2 ratio with distilled water.

(a)

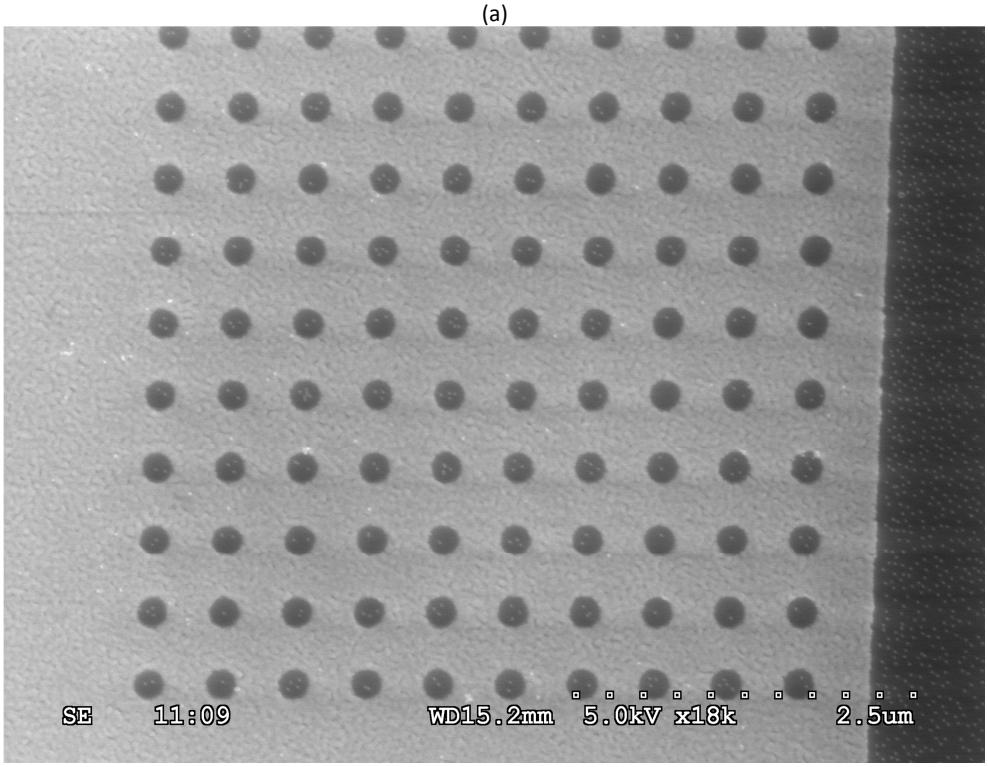

(b)



FIG 4.5 Single-nanoparticle placement driven by self-assembled monolayers (4/5).

SEM images of nanoparticles self-assembled onto gate devices, after 12 hours of immersion in a 20 nm Au colloid diluted in a 1:5 ratio with distilled water.

(a)

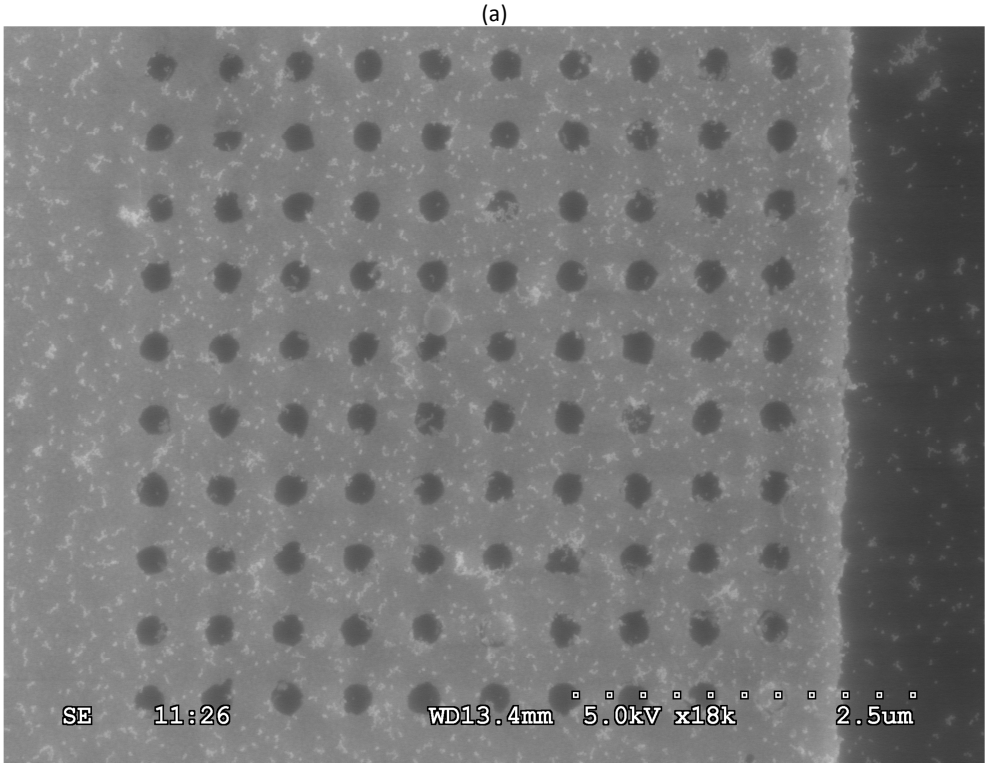

(b)

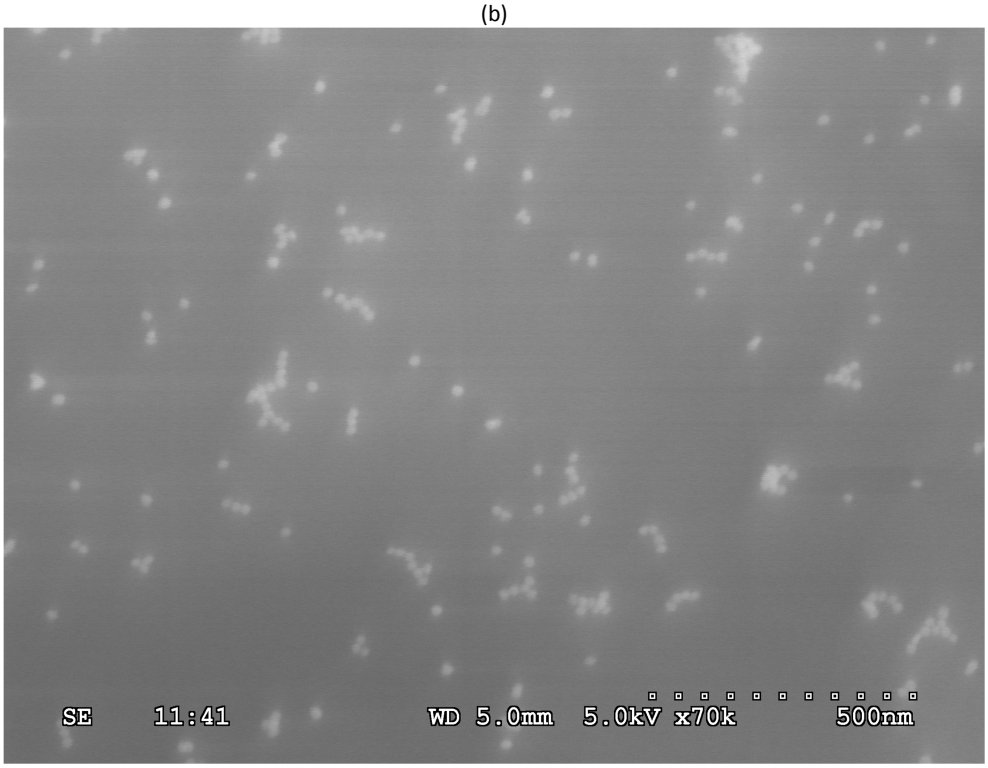

FIG 4.6 Single-nanoparticle placement driven by self-assembled monolayers (5/5).

SEM images of nanoparticles self-assembled onto gate devices, after 12 hours of immersion in an undiluted 20 nm Au colloid. The particles on this device became unstable and formed non-uniform coatings on positively and negatively charged surfaces.

With one device (FIG 4.6) the colloid became unstable and flocculation occurred and the nanoparticles formed extended chains which deposited randomly across the surface. It was not clear what triggered this unusual level of instability as the colloid had been relatively stable for other devices without dilution.

We found that the mechanism of funnelling nanoparticles by APTES/MHA self-assembly was plausible. Some devices were able to isolate individual nanoparticles into the middle of gates, such as in FIG 4.4a. The funnelling of particles towards the centre of rectangular regions in the surface (FIG 4.4b, FIG 4.5b) as was observed by Ma et al.[105]. In both cases though, these results were not very consistent, with many particles being deposited onto the surrounding MHA-coated Au. The APTES coated SiO_2 areas outside they areas were covered with a dispersed layer of Au nanoparticles, consistent with those observed with plain APTES coated samples FIG 4.1b.

4.1.3 Alternative nanoparticle self-assembly

One issue that was not taken into consideration during the initial design and testing of devices was the innate negative surface potential of the SiO_2 surface[123]. Although nanoparticles could be deposited onto a SiO_2 surface using an applied voltage through a using an insulated electrode, it was suspected this may be compromising the deposition of nanoparticles in the target area. However, we were able to use this charge to funnel the assembly of nanoparticles onto APTES surfaces, which we demonstrate in this section.

Initial SEM images of samples were able to distinguish the APTES patterned surface as a darker area compared to the uncoated surrounding SiO_2 (FIG 4.7). After 5 minutes of immersion in a 20 nm Au colloid, particles have begun to accumulate on the

(a)

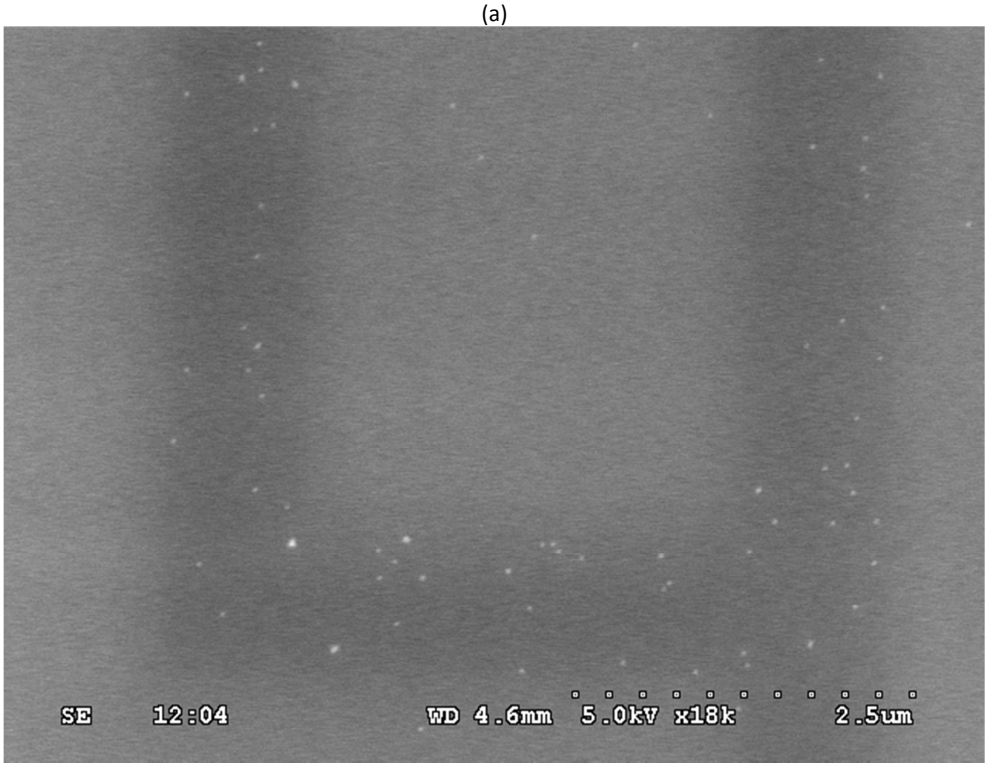

(b)

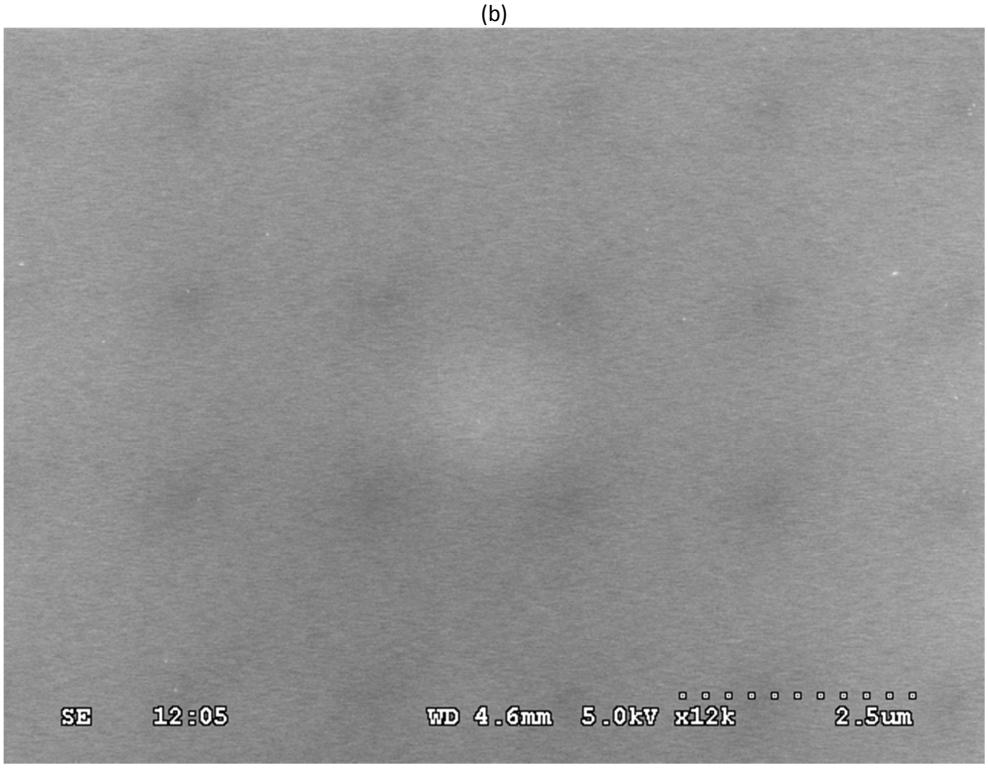

FIG 4.7 Nanoparticle Self-Assembly Funnelled by SiO_2 Surfaces (1/3).

SEM images of 20 nm Au particles self-assembled onto APTES (dark) areas, after 5 minutes of immersion in an undiluted 20 nm Au colloid. Particles deposited near to (a) 500 nm wide markers and (b) 500 nm diameter APTES circles.

(a)

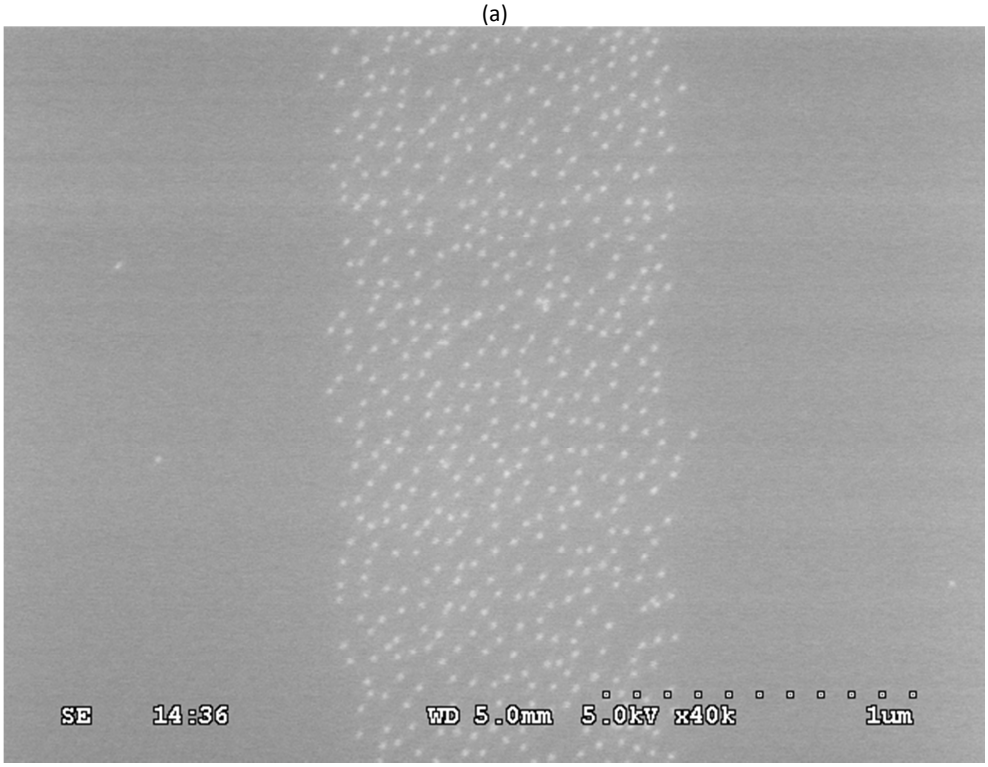

(b)

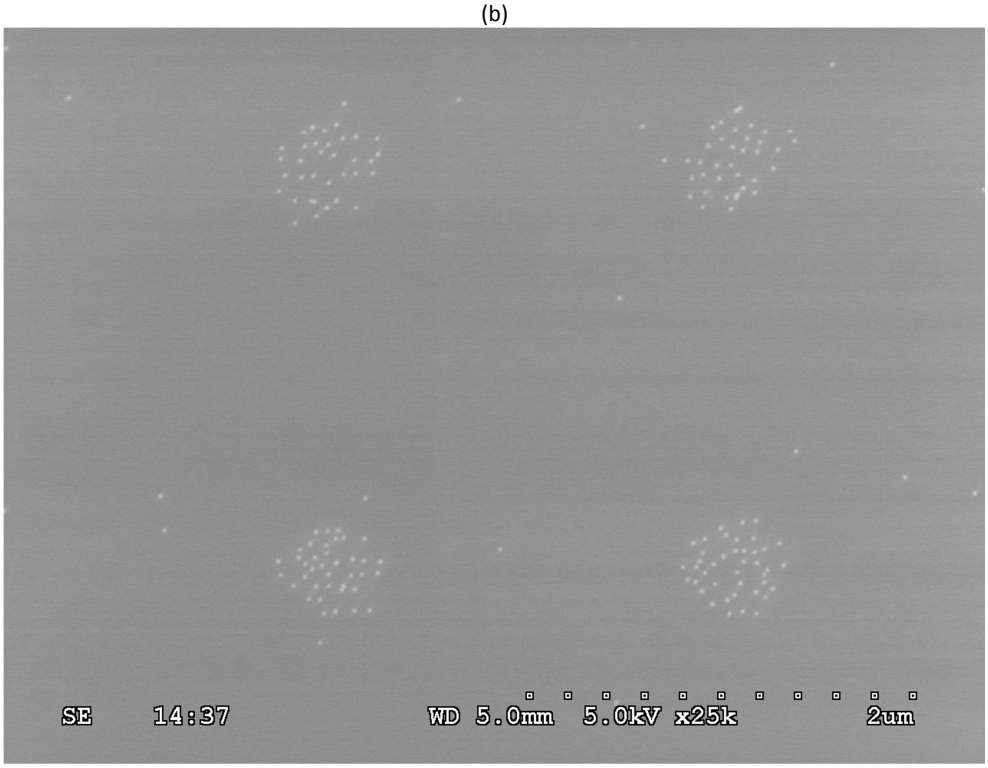

FIG 4.8 Nanoparticle Self-Assembly Funnelled by SiO_2 Surfaces (2/3).

SEM images of 20 nm Au particles self-assembled onto APTES/SiO_2, after 60 minutes of immersion in an undiluted 20 nm Au colloid. Particles assembled onto (a) 500 nm wide markers and (b) 500 nm diameter APTES circles.

(a)

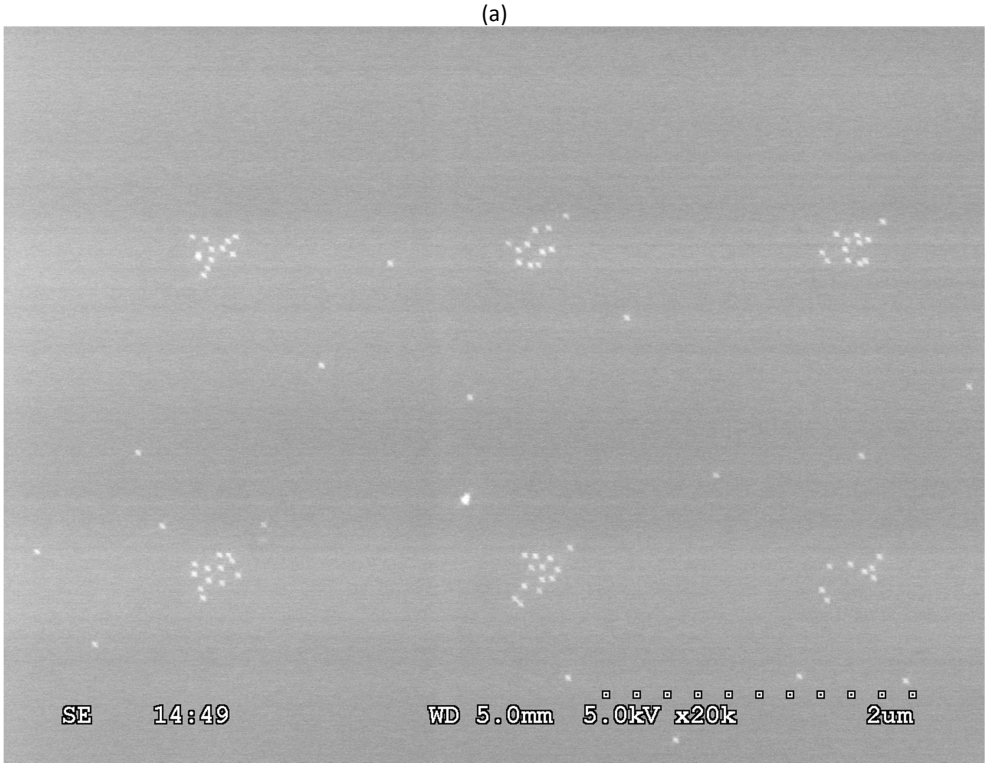

(b)

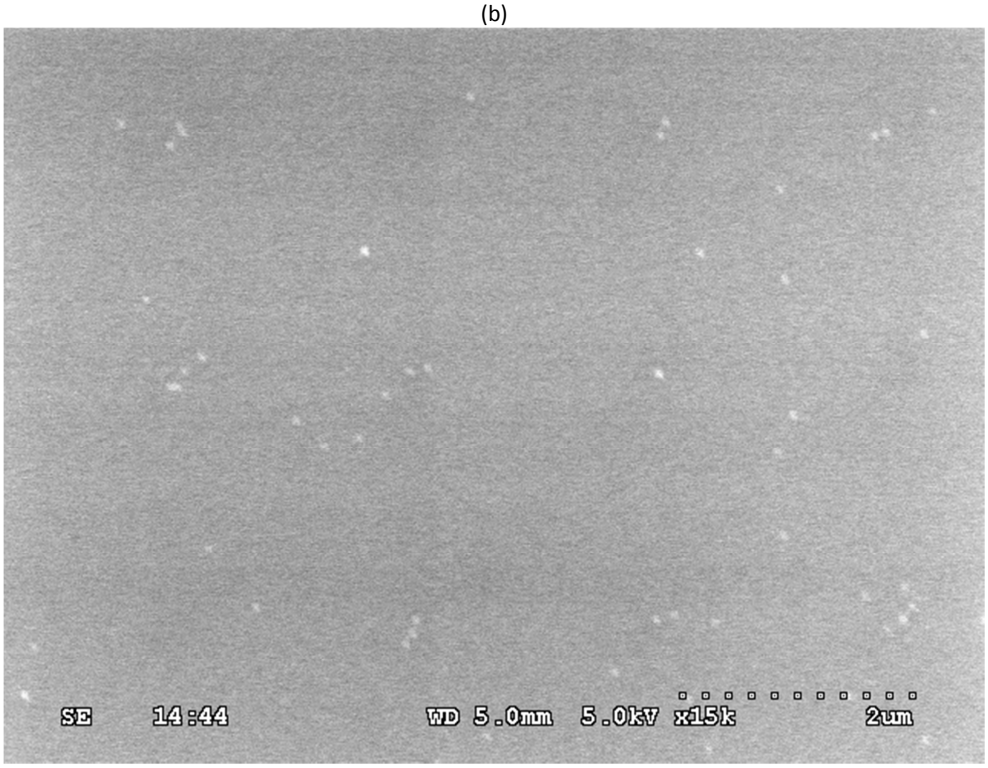

FIG 4.9 Nanoparticle Self-Assembly Funnelled by SiO_2 Surfaces (3/3).

SEM images of 20 nm Au particles self-assembled onto APTES/SiO2, after 60 minutes of immersion in an undiluted 20 nm Au colloid. Particles assembled onto (a) 300 nm and (b) 200 nm diameter APTES circles.

surfaces but there is no organisation to the layer after this amount of time (FIG 4.7). A

longer immersion time of 60 minutes resulted in nanoparticles assembling more regularly on relatively large 500 nm diameter markers and target areas (FIG 4.8). Smaller target areas of 300 nm were able to capture fewer particles (FIG 4.9a), although the deposition was less organised compared to the 500 nm diameter areas. At diameters of 200 nm incidences of single nanoparticle capture could be observed (FIG 4.9b). However, many particles had deposited onto the SiO_2 over the 60 minute timescale so it was difficult to differentiate between the captured particles and those that had penetrated the electrostatic barrier.

4.2 Devices Modified by Non-Polar Monolayers

One issue that was not taken into consideration during the initial design and testing of devices was the innate negative surface potential of the SiO2 surface. This was particularly evident in the successful funnelling on nanoparticles by SiO_2 surfaces in the previous section. Neutralising the SiO_2 surface charge may be necessary to achieve voltage-directed assembly. To do this we coated SiO_2 surfaces in a long-chain non-polar molecule of triethoxy(octadecyl)silane (TMODS), using molecular self-assembly. This was achieved by preparing a 5 mM solution of TMODS in isopropanol. 15 mm x 10 mm silicon chips covered with a 25 nm thick layer of thermally grown silicon dioxide, were patterned with a polymer mask of hole arrays (FIG. 3.2a) using electron beam lithography. These chips were immersed in the TMODS solution for 12 hours to allow a monolayer of the compound to grow, before cleaning and removing the polymer mask. These patterned TMODS-coated target areas are surrounded by SiO_2 (FIG 4.10) that provide a negative funnelling surface charge.

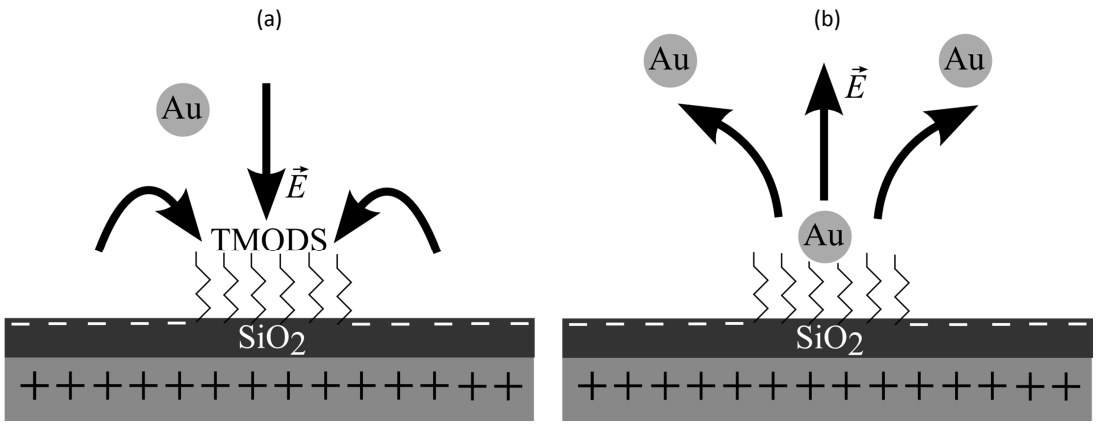

FIG 4.10 Modified Gate Device Design

A modified version of the Gate Design simulated in section 2.3.1 and tested in section 3.2. The patterned Au layer functionalised with MHA has been replaced by a clean SiO_2 surface with an innate negative surface charge to funnel nanoparticles. The target area on the SiO_2 is coated with a molecular monolayer of trimethoxy(octadecyl)silane (TMODS), to neutralise the surface charge. An electric field created by the application of a voltage through a lower Si electrode (a) attracts nanoparticles towards the target area, which (b) repel the approach of additional nanoparticles once captured.

Initial testing of the devices using a 1 V DC bias applied through the lower silicon electrode resulted in gold nanoparticles depositing in largely across both surfaces, preferentially on the TMODS. FIG 4.11 shows the result after 5 minutes of deposition. The nanoparticles appear to have deposited onto the patterned features in greater density than the silicon dioxide. However, the final result shows the particles have formed into grouped waves. We believe this to be due to poor adhesion during deposition resulting in their displacement during a rinsing step, but we cannot be certain.

Testing to see how the surface would interact when no driving voltage was used revealed that nanoparticles were still assembling onto the TMODS surface (FIG 4.12 – FIG 4.14), meaning that the voltage was not needed to drive the

(a)

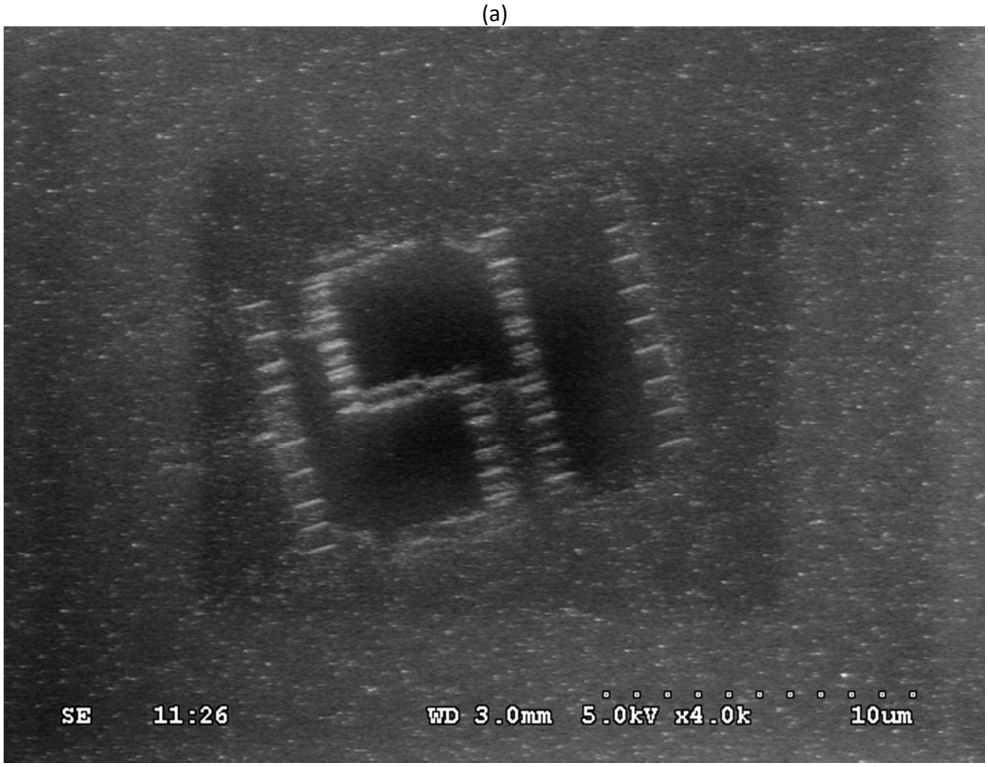

(b)

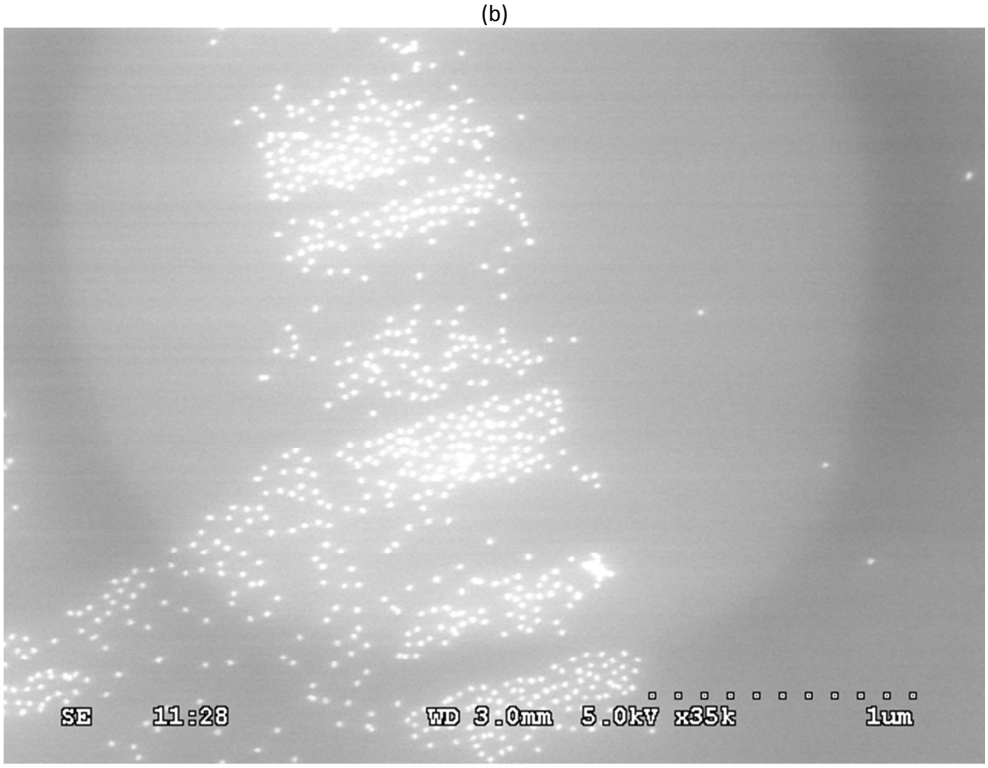

FIG 4.11 TMODS Functionalised Gate Devices (1/5).

SEM images of 20 nm Au nanoparticles after 5 minutes with 1 V bias driven assembly onto trimethoxy(octacdecyl)silane functionalised gate devices. The particles have deposited on all surfaces, preferentially on the TMODS, before subsequently detaching from the surface.

(a)

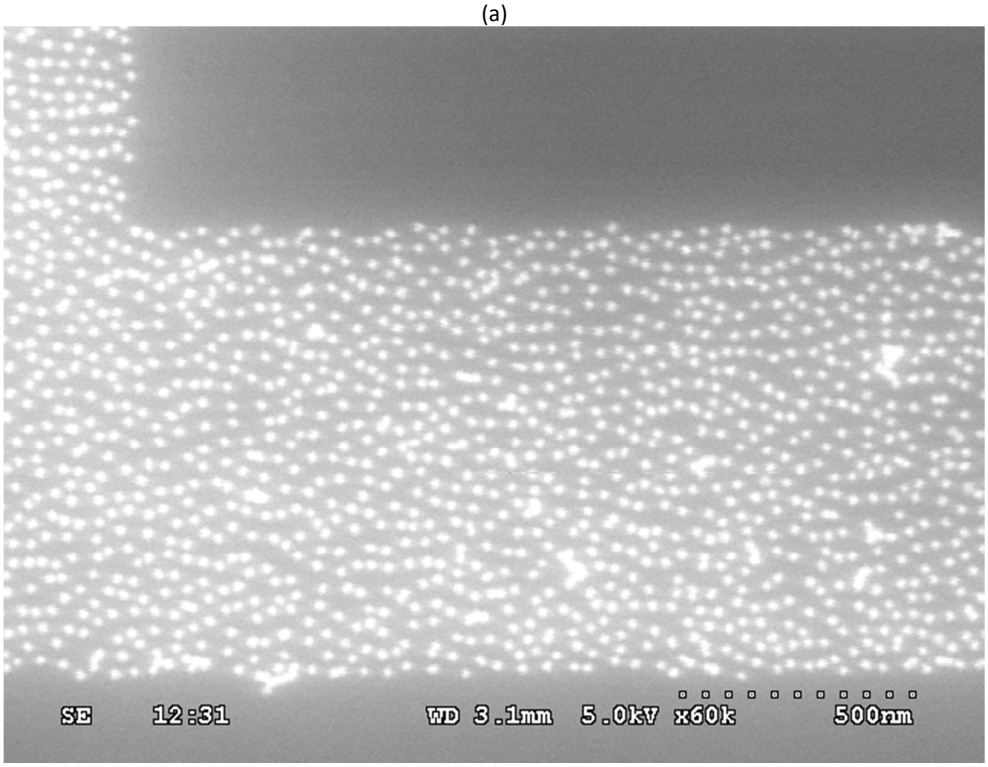

(b)

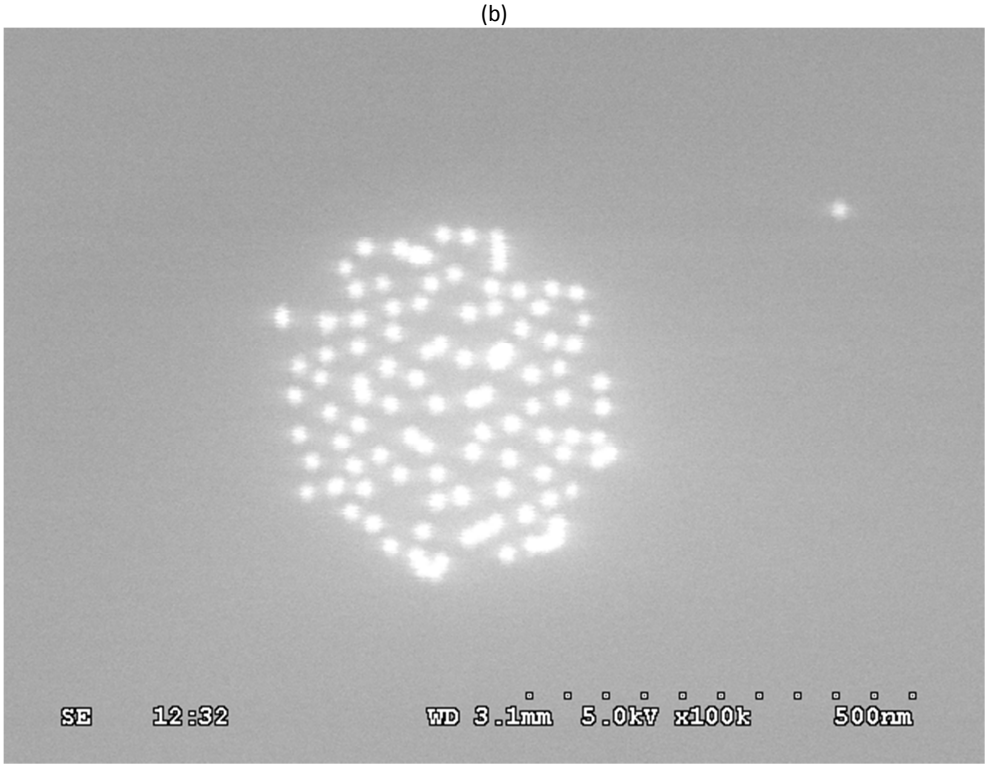

FIG 4.12 TMODS Functionalised Gate Devices (2/5).

SEM images of 20 nm Au nanoparticles after 5 minutes of self-assembly onto trimethoxy(octacdecyl)silane functionalised gate devices. Results show well-ordered assembly onto 500 nm (a) markers and (b) target areas.

(a)

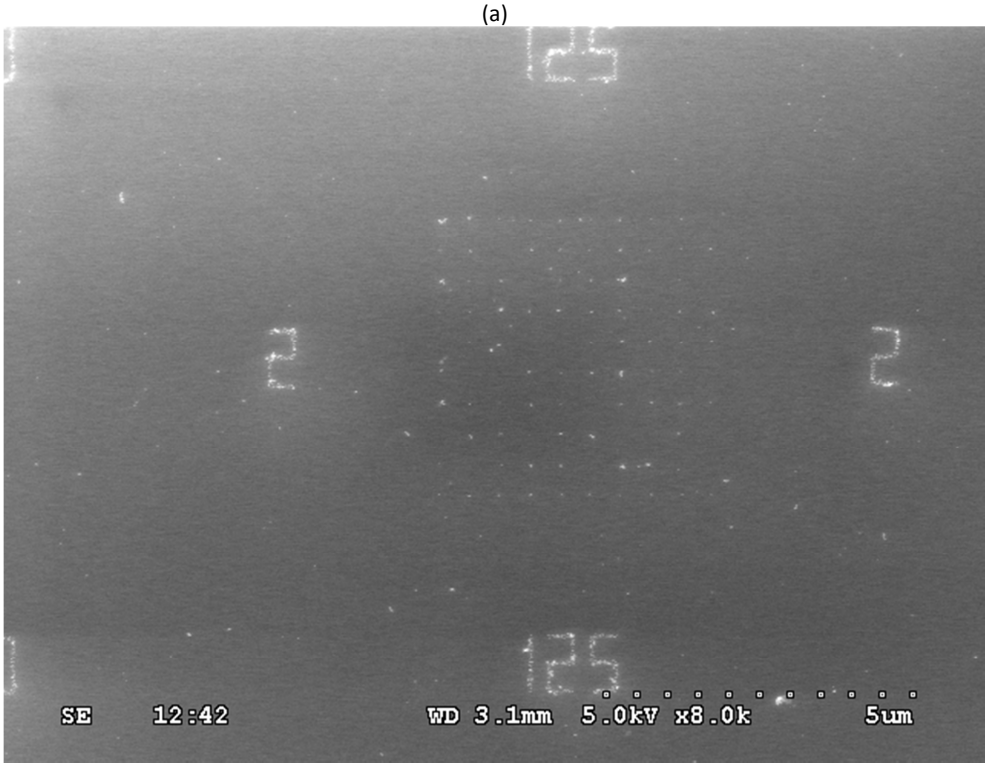

(b)

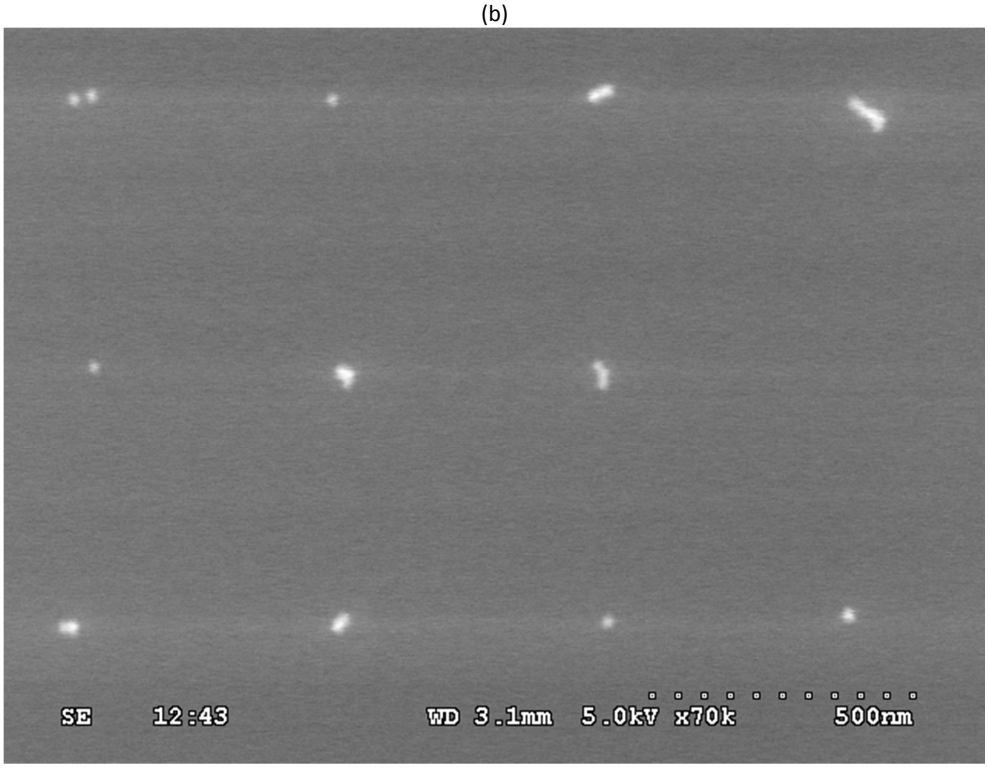

FIG 4.13 TMODS Functionalised Gate Devices (3/5).

SEM images of 20 nm Au nanoparticles after 5 minutes of self-assembly onto trimethoxy(octacdecyl)silane functionalised gate devices. 125 nm devices show multiple cases of single nanoparticle capture on target areas as well as agglomeration.

(a)

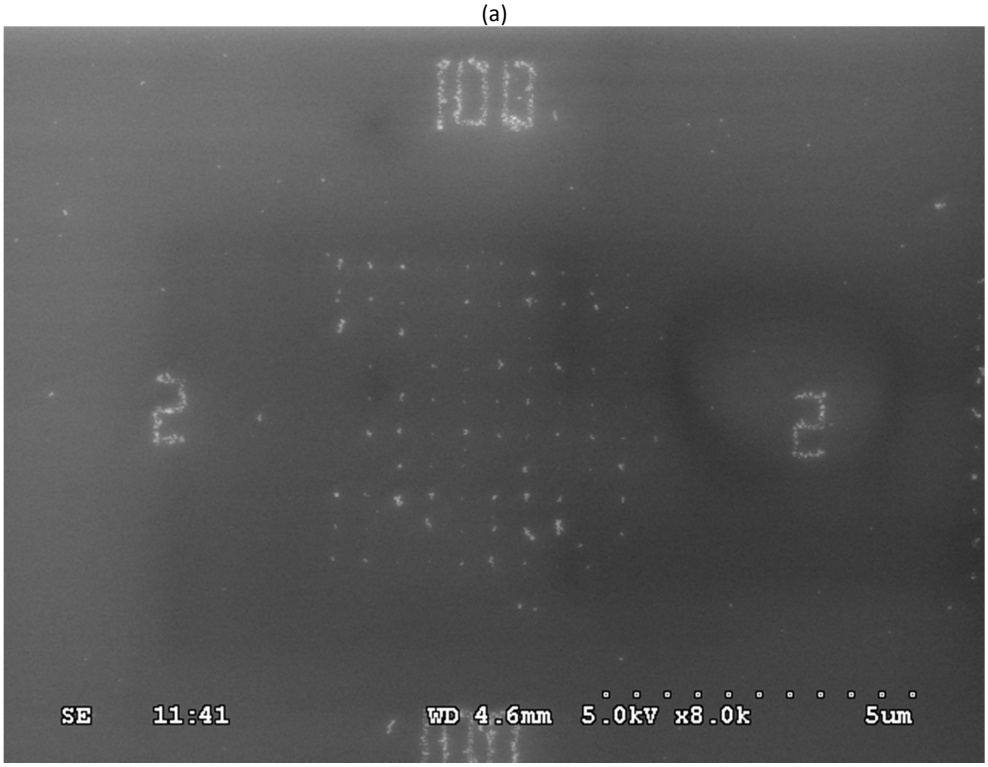

(b)

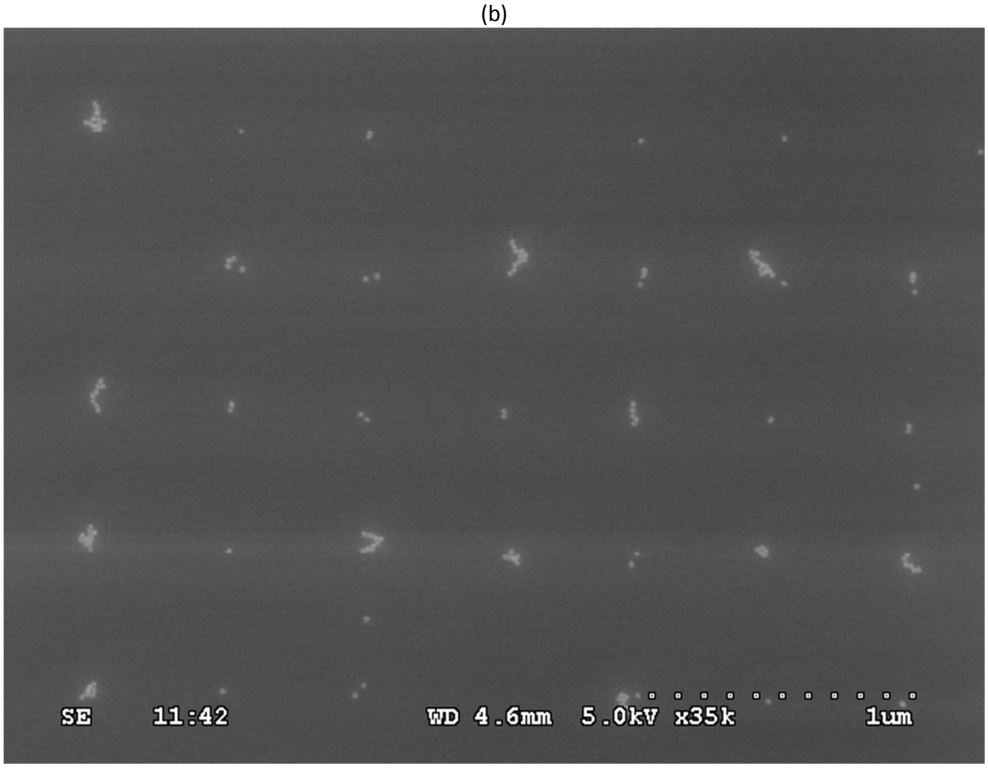

FIG 4.14 TMODS Functionalised Gate Devices (4/5).

SEM images of 20 nm Au nanoparticles after 5 minutes of self-assembly onto trimethoxy(octacdecyl)silane functionalised gate devices. 100 nm devices show multiple cases of single nanoparticle capture on target areas as well as agglomeration.

(a)

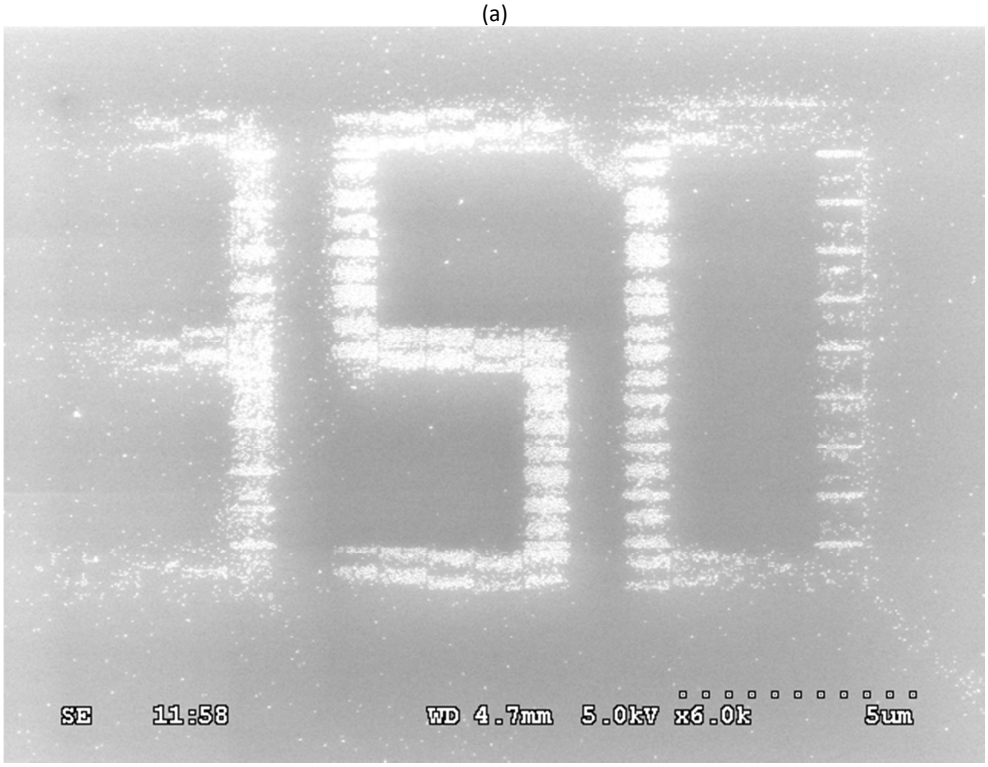

(b)

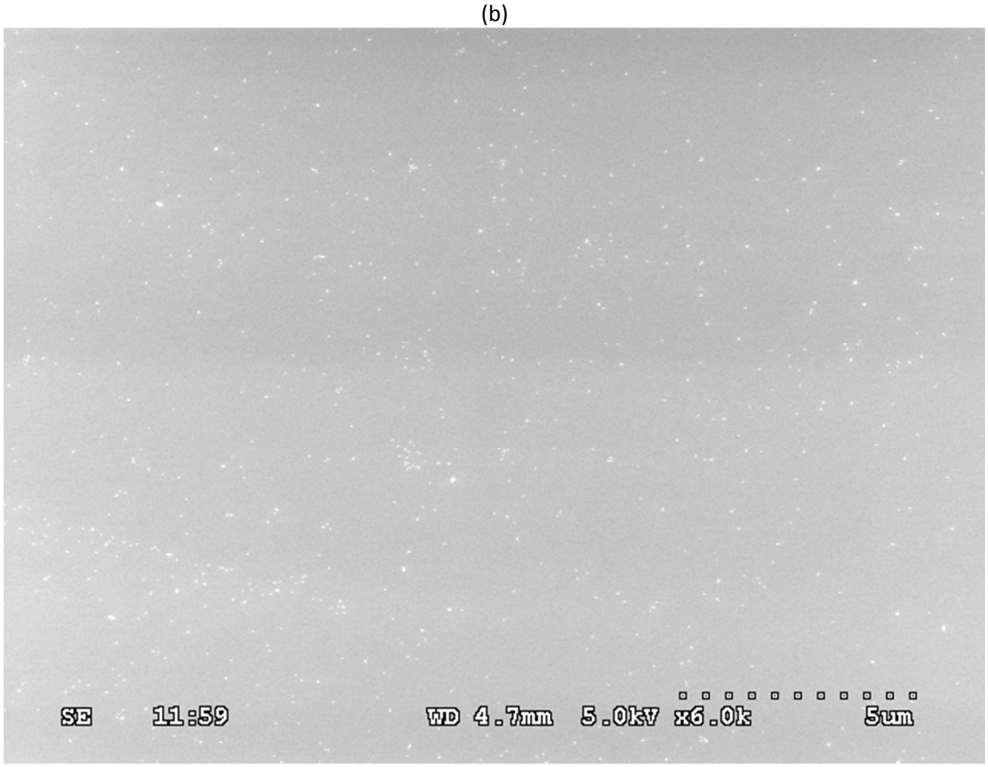

FIG 4.15 TMODS Functionalised Gate Devices (5/5).

SEM images of 20 nm Au nanoparticles after 5 minutes of self-assembly onto trimethoxy(octacdecyl)silane functionalised gate devices. In this instance the particles have destabilised on both (a) the markers and (b) in the prospective target areas.

deposition. Nanoparticles were found to assemble with long-range order over relatively short timescales – 5 minutes in the devices shown compared to several hours for the APTES surfaces used in section 4.1. Nanoparticles are shown to have assembled into a fairly monodisperse layers on markers (FIG 4.12a) and circles (FIG 4.12b), with a smaller interparticle spacing than occurred on APTES monolayers. Other smaller TMODS target areas with diameters from 100 nm to 125 nm saw incidences of single nanoparticle capture (FIG 4.13b, FIG 4.14b). The effect of particles apparently detaching from the surface during rinsing occurred with other self-assembly devices (FIG 4.15), which indicated that the applied voltage was not the underlying cause. The particles scattered from target areas do not show any similar waving effect (FIG 4.15b), which is as yet unexplained.

Innately, methyl-terminated monolayers like TMODS have been observed to possess a negative zeta potential in solution at neutral pH. However, given the balance of electronegativity between the carbon and hydrogen atoms in this ligand, the hydrogen atom would carry a slight positive charge. We think that this results in the adhesion of negatively charged ions in the Stern layer of methyl-terminated surfaces in solution. This phenomenon is known as charge inversion, which would result in the measurement of a negative zeta potential and could be reduced by lowering the ionic strength of the colloid.

The reason for the rapid assembly of nanoparticles could be explained by the hydrophobic interactions of the TMODS monolayer surface. The low interaction of the methyl ligands and water molecules prevents a hydrostatic barrier from forming on the TMODS surface, which is typical for hydrophilic charged surfaces like the amine ligands of APTES. There should still be a hydrostatic barrier on the surface of the Au

nanoparticles themselves. The reduction of this barrier would explain why the deposition time of the Au nanoparticles was much faster on the hydrophobic TMODS surface, but the absence of a strong attraction potential limits this explanation. This attraction is more completely accounted for by considering the hydrophobic interaction, where non-polar surfaces experience stronger attraction forces in water than in air[111]. This greater force arises because it is entropically unfavourable for the water molecules to remain at the interface. This causes dewetting of the surface, with the molecules moving into the bulk where mutual hydrogen bonding provides greater stability. This explanation becomes more complex when describing the TMODS-Au nanoparticle system, where both hydrophobic and hydrophilic surfaces come into close contact. Molecular dynamics simulations by other groups have demonstrated that in hydrophobic-hydrophilic interactions, the dewetting is prevented if one of the surfaces is highly hydrophilic, neutralising the hydrophobic interaction[124]. Future work could look at this TMODS-Au nanoparticle system to establish whether what threshold there might be to particle deposition, depending upon the amphiphilicity and charge of the particles.

4.3 Chapter Summary

The self-assembly process for capturing nanoparticles with APTES and MHA patterned monolayers was found to be plausible, although it was imperfect and required in excess of an hour to achieve single-particle capture. We confirmed that this process was also plausibly caused by electrostatics, by replacing the MHA-coated Au in this setup with the innate negative surface charge of SiO_2. We attempted to eliminate this surface charge in the original gate design, passivating the SiO_2 surface charge with an

alkylsilane monolayer with electrically neutral ligands and funnelled to these surfaces by the SiO_2 surface charge. However, the successful single-nanoparticle capture process achieved in these devices was found to be a self-assembly approach. This successfully occurred over a much shorter sub-5 minute timescale compared to the APTES/MHA or APTES/SiO_2 driven capture. We postulated that this efficiency is due to a hydrophobic interaction between the particles and the TMODS-coated surface, causing dewetting of the surface. This dewetting removes the hydrostatic barrier and thus causes rapid particle assembly. Future research will seek to stabilise the selectivity of this method by manipulating the composition of the colloid before applying it to a probe-based pick-and-place process.

Chapter 5

Surface Identification by Dual-Harmonic Kelvin Probe Microscopy

Any nanomanipulator that is going to achieve reliable nanoparticle pick-and-place fabrication will need to be able to identify the locations and compositions of the structures it is placing components into. These measurements must be performed on the devices whilst they are immersed in low molarity solutions that resembled the colloidal dispersions we utilise. Although AFMs are very capable at discerning objects by their size, for nanodevices integrating molecular monolayers into their structures, Kelvin probe measurements will be needed to identify the materials without contacting them. This can only work in non-polar environments. We succeeded in developing an innovative open-loop Kelvin probe technique, Dual Harmonic Kelvin Probe Microscopy, which can operate accurately in polar environments. In this chapter, we explore the technical challenges that were involved and the measurements that were used to identify nanoscale materials.

5.1 Conventional Kelvin Probe Microscopy

In the conventional closed-loop method of KPM, an AFM probe scans the surface for topographical information and then performs a second scan at a known height above the surface to measure the surface potential along this topographical line, as represented in FIG. 5.1. The first scan for topographical information uses a non-contact AFM method, where an AC voltage applied to the piezoelectric actuator the tip is mounted to causes the cantilever to oscillate close to its resonant frequency. The specifics of the topography measurement differ slightly between the different methods, for example by intermittent contact with the surface or measuring variations in the tip-sample separation. Different forces, including magnetic and acoustic, can also be used to actuate the oscillation, which helps reduce the mechanical vibration of other components, but this is less commonly used. The electrical measurement is based upon the total known electrical potential, V_{TOT}, which is acting on the tip: the total electronic potential of the proximate surface. V_S; the AC voltage applied between the tip and surface, V_{AC}; and the DC offset of the AC signal, V_{DC}[125].

$$V_{TOT} = V_S + V_{DC} + V_{AC}\sin(\omega t) \tag{5.1}$$

The AC signal causes the cantilever attached to the tip to oscillate with same angular frequency, ω. Assuming that the force acting on the tip in this situation can be modeled as a parallel plate capacitor, this potential will exert the following force on the cantilever[125]:

$$F = -\frac{1}{2}\frac{\partial C}{\partial z}V^2 \tag{5.2}$$

where $\frac{\partial C}{\partial z}$ is the capacitive gradient between the tip and the surface. In this scenario, the total electric potential is given by Eq. (5.1). Squaring this voltage results in the following relationship:

$$V_{TOT}{}^2 = (V_S + V_{DC})^2 + \frac{V_{AC}{}^2}{2} + 2V_{AC}(V_S + V_{DC})\sin(\omega t) + \frac{V_{AC}{}^2}{2}cos(2\omega t) \quad (5.3)$$

The force acting on the cantilever is then obtained by substituting Eq. (5.3) into Eq. (5.2). Three different terms for this force can be extracted by isolating the three different frequencies of the response:

DC term:
$$F_{DC} = -\frac{1}{2}\frac{\partial C}{\partial z}\left\{(V_S + V_{DC})^2 + \frac{V_{AC}{}^2}{2}\right\} \quad (5.4)$$

ω term
$$F_{\omega} = -\frac{\partial C}{\partial z}\{V_{AC}(V_S + V_{DC})\sin(\omega t)\} \quad (5.5)$$

2ω term
$$F_{2\omega} = \frac{1}{4}\frac{\partial C}{\partial z}\{V_{AC}{}^2 cos(2\omega t)\} \quad (5.6)$$

Eq. (5.5) indicates that for the cantilever response at frequency ω changes in V_S can be counteracted by an equal yet opposite change to V_{DC}. Now as an AFM tip scans over a surface with different materials on it, the surface potential changes, affecting the force that the surface exerts on the tip. The change in the DC potential applied to the drive signal to cancel out changes in surface potential is referred to as the nulling potential. With a lock-in amplifier, this DC voltage can be used to counteract changes in the surface potential in real-time as the AFM tip scans the surface, allowing a detailed map of the surface potential to be created.

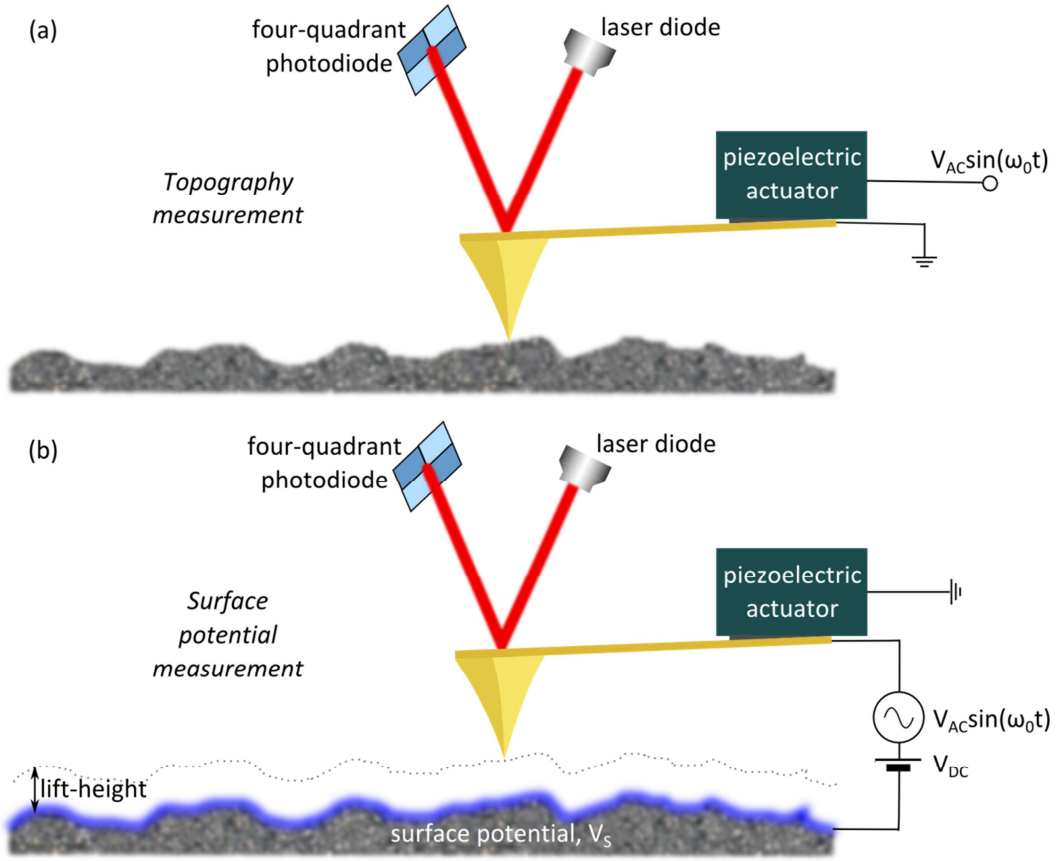

FIG. 5.1 KPM schematic.

(a) In the first pass an AFM is operated in a non-contact mode to measure the topography of a surface. To achieve this, a cantilever is oscillated at its resonant frequency ω_0 as it passes over the surface and changes in its oscillation are detected by the deflection of a laser beam reflected off the top-side of a cantilever onto a photosensitive diode. (b) Using this 2D topographical information from the first pass, the AFM is now moved to a known, constant height above the surface and the cantilever is actuated by an AC voltage, V_{AC} with a DC offset, V_{DC}, which is held between the surface and the tip. This allows a measurement of the electronic surface potential, V_S, to be achieved via the equivalency of the DC offset and the surface potential. This process is repeated sequentially for lines rastering across the surface to build up a 2D map of the topography and the surface potential.

This conventional approach to KPM can work perfectly well in a non-polar medium; we tested it in tetradecane and some research indicates this helps to limit the effect of contaminants on the measurement[126]. Unfortunately operating this mode in a polar

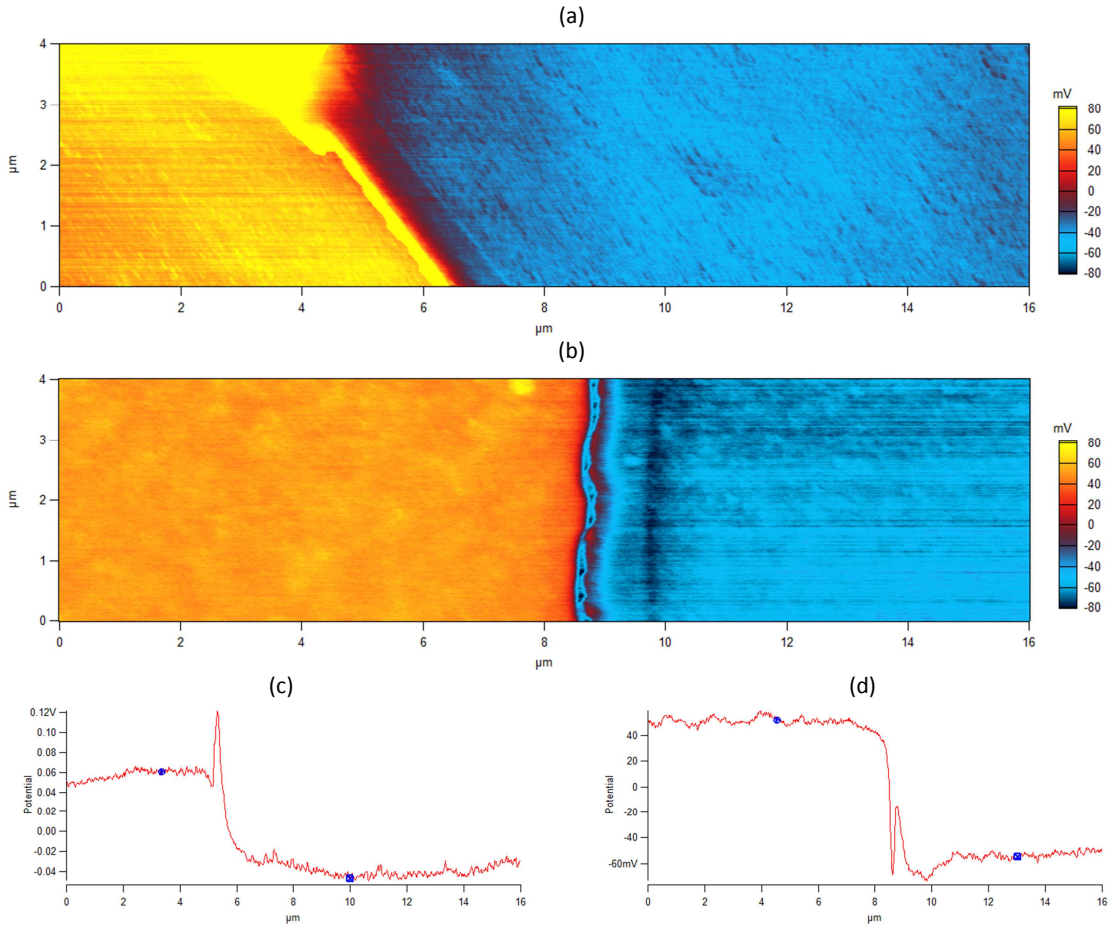

FIG. 5.2 Conventional KPM in nonpolar liquid.

Conventional KPM measurements of two adjacent titanium (left) and indium tin oxide (right) surfaces (a) in air and (b) in tetradecane. (c) and (d) show surface potential measured across the Ti-ITO step in (a) and (b). The difference in surface potential marked by the blue points (a) in air was – 106 mV and (b) in tetradecane was – 107 mV. Measurements were made with an AC drive amplitude of 3 V and 5 nm above the topography measurements. In air the drive frequency was 69.47 kHz, which dropped to 25.05 kHz in tetradecane.

liquid medium used to disperse many colloids is not possible, because both ionic species and the polar molecules of the solvent move in response to electric fields. The AC voltage that actuates the oscillation of the cantilever can still work in these conditions and in practice generates less noise than the response of a cantilever to piezo-actuation in liquid. However, the DC lock-in response at F_ω defined in Eq. (5.5) is compromised, which results in the DC voltage being increased up to the limits of the

system. Over a matter of seconds this results in electrolysis of the water and the formation of bubbles of gas around the cantilever, which result in the probe tip crashing into the surface.

5.2 Dual-Harmonic Kelvin Probe Microscopy

The open-loop DHKPM measurement is an alternative method to conventional KPM to measure the surface potential of samples that was developed by Kobayashi et al.[127],[128]. Instead of using the direct relationship between the surface voltage and the DC offset in Eq. (5.5), it obtains the surface potential by comparing the ω and 2ω components of the force response in post-processing. Removing the DC voltage component from the force response (see Eq. (5.2)) acting between an AFM tip and a surface, the total electrical potential is now defined as:

$$V_{TOT} = V_S + V_{AC}\sin(\omega t) \tag{5.7}$$

The total electronic potential, V_{TOT}, which is acting on the tip is now only dependent on the total electronic potential of the proximate surface, V_S, and the AC voltage applied between the tip and surface, V_{AC}. The three frequency dependent components of the force acting on the cantilever without the DC voltage are now defined as:

DC term:
$$F_{DC} = -\frac{1}{2}\frac{\partial C}{\partial z}\left\{{V_S}^2 + \frac{{V_{AC}}^2}{2}\right\} \tag{5.8}$$

ω term
$$F_{\omega} = -\frac{\partial C}{\partial z}\{V_{AC}V_S\sin(\omega t)\} \tag{5.9}$$

2ω term
$$F_{2\omega} = \frac{1}{4}\frac{\partial C}{\partial z}\{{V_{AC}}^2 cos(2\omega t)\} \tag{5.10}$$

By considering the amplitude of the ω and 2ω terms a new expression for the magnitude of the surface potential, Eq. (5.11), can be derived[127]:

$$|F_\omega| = G_\omega A_\omega = \left|\frac{\partial C}{\partial z} V_{AC} V_S\right|$$

$$|F_{2\omega}| = G_{2\omega} A_{2\omega} = \frac{1}{4}\left|\frac{\partial C}{\partial z} {V_{AC}}^2\right|$$

$$\frac{A_\omega}{A_{2\omega}} = 4\frac{G_{2\omega}}{G_\omega}\left|\frac{V_S}{V_{AC}}\right|$$

$$|V_S| = \frac{1}{4}\frac{A_\omega}{A_{2\omega}}\frac{G_\omega}{G_{2\omega}}|V_{AC}| \tag{5.11}$$

Here G_ω and $G_{2\omega}$ are the transfer functions for the cantilever when it is oscillating at ω and 2ω respectively, which allow for us to convert the amplitude to the force acting on the cantilever at these frequencies. For instance[127]:

$$G_\omega = \frac{1}{k\sqrt{1 - \left(\frac{\omega}{\omega_0}\right)^2 + \left(\frac{\omega}{Q\omega_0}\right)^2}} \tag{5.12}$$

is the transfer function for the force at drive frequency ω for a cantilever with a spring constant k, a natural frequency of ω_0 and a quality factor of Q under thermal excitation. In principle, this method should make it possible to measure magnitude of the surface potential in polar solvents of low ionic strength. Kobayashi et al. also stipulated that the polarity of the surface potential can be determined by analysing the polarity of the phase response of the cantilever at the drive frequency[128]:

$$V_S = sgn(\cos(\theta_\omega))\frac{1}{4}\frac{A_\omega}{A_{2\omega}}\frac{G_\omega}{G_{2\omega}}|V_{AC}| \tag{5.13}$$

where θ_ω is the phase response of the cantilever at the drive frequency. In principle this is correct, as changes in the surface potential only affect the ω response of the cantilever. In practice this proved to be fairly inconsistent, with phase frequently shifting the response between positive and negative, with the lock-in conventional KPM measurement providing a more consistent measure of the polarity.

We verified that DHKPM measurements with this setup were accurate by comparing the results of conventional KPM with the DHKPM setup (with assistance from Dr Anil Gannepalli from Asylum Research). Measurements were taken on silicon wafers with a thermally grown and polished silicon dioxide surface. These samples were then coated with lines of titanium and indium tin oxide so that the surface potential difference between these two areas could be compared by these two Kelvin probe methods. An example of the results obtained by this method is given in FIG. 5.3, where KPM (FIG. 5.3(d, f)) and DHKPM (FIG. 5.3(e, g)) measurements were taken sequentially over the same 40 μm wide area. The results showed that a similar measurement for the change in surface potential ΔV_S between the Ti and ITO was obtained: KPM measured ΔV_S = – 28.38 mV and DHKPM measured ΔV_S = – 27.16 mV. Clearly the DHKPM measurements also generated relatively more noise than the KPM method, resulting in a speckled appearance to most of the results. This was probably as a result of measuring frequencies outside of the natural frequency of the cantilever. Several sequential measurements were taken where the measuring mode was switched between conventional KPM and DHKPM.

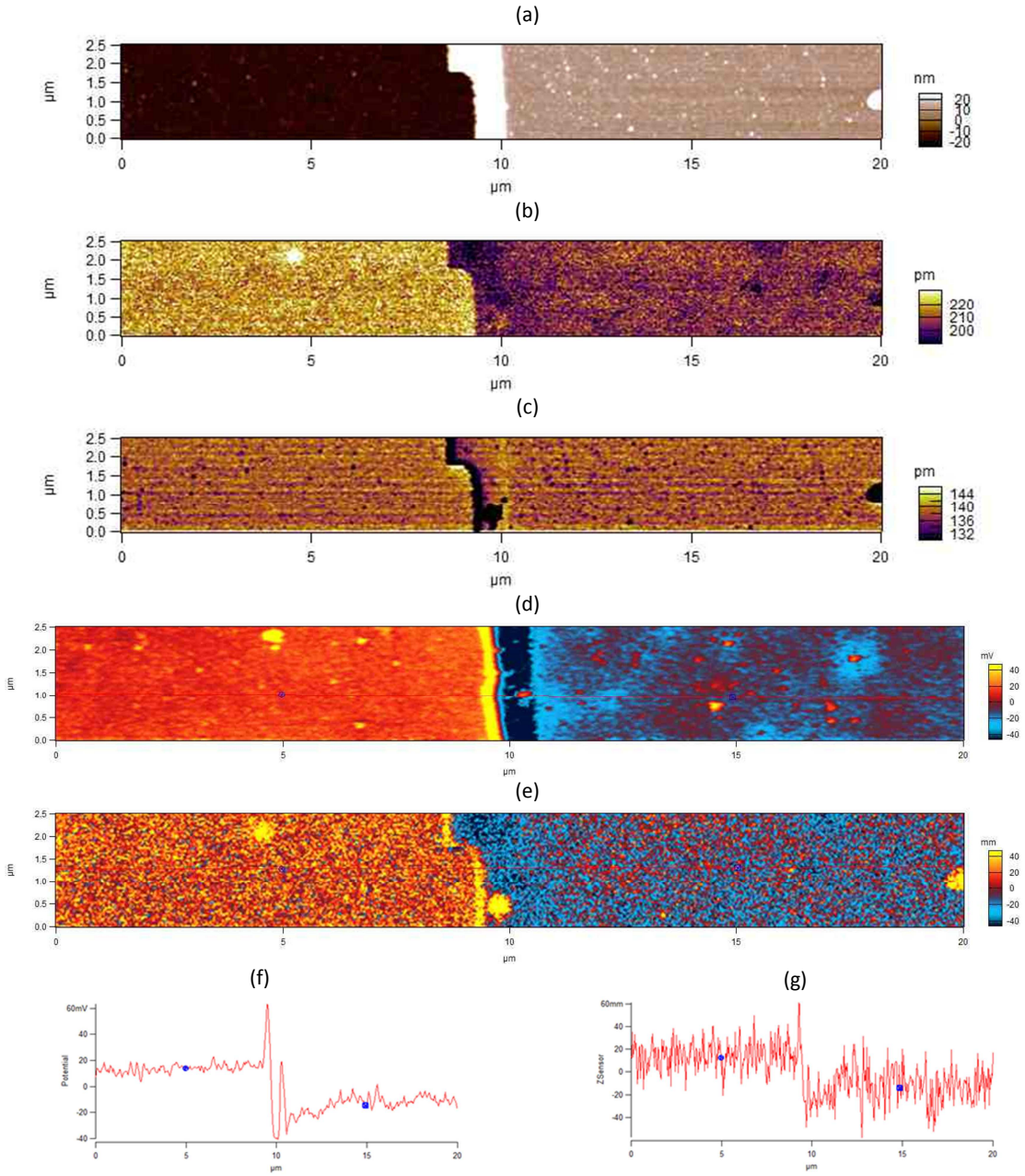

FIG. 5.3 Comparison of KPM and DHKPM on a Ti-ITO sample.

(a) Topography of adjacent titanium (left) and indium tin oxide (right) surfaces. (b, c) Amplitude deflection of the cantilever at (b) 15 kHz and (c) 30 kHz during the DHKPM measurement of this surface. (d) KPM and (e) DHKPM surface potential maps of the surface; (f) and (g) show the potential along the line indicated in each respective map. The difference in surface potential marked by the blue points in these line scans is – 28.38 mV for KPM and – 27.16 mV for DHKPM. Measurements were made with an AC drive amplitude of 3 V and 50 nm above the topography measurements. In KPM the drive frequency was 73.12 kHz and DHKPM the drive frequency was 15 kHz.

5.3 Kelvin Probe Measurements of Nanoparticles

The key relationship exploited from this is the response at the cantilever when it is electrically actuated with frequency, ω. As the AFM tip is scanned over the surface, changes to the surface potential can be cancelled out by an equivalent change in V_{DC}. A lock-in amplifier is used to nullify changes to the deflection at ω by changing V_{DC}, creating a map of the difference in surface potential between different areas of the surface the AFM tip encounters. In practice, a conventional non-contact AFM scan (amplitude or frequency modulation) is performed to form a map of the topography along a 1D line before a second pass for a KPM measurement is performed along the same line at a constant tip-sample separation. This is to limit the influence that the surface topography has on the KPM measurement. This measurement of the surface potential can then be used to calculate the work function of the surface, $\varphi_{surface}$ if the work function of the tip, φ_{tip} is known:

$$V_S = \frac{\varphi_{tip} - \varphi_{surface}}{e} \tag{5.14}$$

where e is the electronic unit charge. φ_{tip} can be calibrated by performing a KPM measurement on a surface with a well-defined work function, such as highly ordered pyrolytic graphite.

Unfortunately there are several fundamental limitations to this KPM measurement. The direct measurement of work functions only applies if the surface is entirely conductive. KPM measurements on dielectrics can still identify the contrast between different surfaces, but the DC bias applied to the tip to account for changes in the

force F_ω will also have responded to changes in the capacitance gradient $\frac{\partial C}{\partial z}$ over areas with different relative permittivity.

The necessity of taking KPM measurements far away from a surface also limits the possible lateral resolution of KPM, as features of comparable size to the separation between the tip and sample are harder to resolve against the contrast of the surrounding surface. Specialised AFM probes can improve this lateral resolution, such as coaxial probes with a conductive shell that reduce the influence of the electronic potential from the surrounding area[129]. However, as these approaches are highly specialised, the tip-sample separation is usually reduced to counter this difficulty.

There are many limitations to using the above route of analysis to correct for this effect. The capacitance gradient is highly sensitive to changes in the tip-sample separation and the tip radius. Changes to the tip radius are also very common, as material ablation frequently causes the tip to be blunted and characterising its precise radius is very difficult. It is therefore preferable to reduce the influence of $\frac{\partial C}{\partial z}$ as far as possible.

5.3.1 Influence of capacitance gradient

Consider the system of a particle on the surface and the AFM tip as two conductive spheres with radii of a and b respectively, separated by distance c between the centres of the two spheres. The capacitance between these spheres, C_{ab} can be expressed as[130],[131]:

$$C_{ab} = -4\pi\varepsilon_0 \frac{ab}{c} sinh(U) \sum_{n=1}^{\infty} \frac{1}{sinh(nU)} \tag{5.15}$$

where

$$cosh(U) = \frac{c^2 - a^2 - b^2}{2ab} \tag{5.16}$$

We had originally derived an equation for the derivative of Eq. (5.15) with respect to the separation, $\frac{\partial C_{ab}}{\partial c}$. However, this was later found to be incorrect, so we instead utilised an estimate of the capacitance gradient from Eq. (5.15) for surface particles with varying radius:

$$\frac{\partial C_{ab}(a)}{\partial c} = \frac{C_{ab}(a + \Delta a) - C_{ab}(a)}{\Delta a} \tag{5.17}$$

where Δa is the increment in particle radius. The implication we draw from these relationships is that larger particles will have a different capacitance gradient when the tip-sample separation and the size of the particles is comparable. For example, we consider the measurements of gold particles varying in size from 5 to 18 nm in diameter, which showed a trend of increasing measured work function with particle size[132]. This was attributed to redistribution of charges in the particles in response to intrinsic charges in an underlying doped Si layer. However, we consider that this measurement would also have been influenced by variations in the capacitance gradient.

KPM assumes that changes to the force, ΔF_ω are due to changes in the surface potential, ΔV_S, which leads to a change in the DC potential, ΔV_{DC}. However, if the observed changes in surface potential are due to changes in the capacitance gradient, then ΔV_{DC} will be proportional to the changes in $\frac{\partial C_{ab}}{\partial z}$. To analyse this, we calculated the capacitance gradient for the range of particle sizes measured on the surface with

Table 5.I Dependence of measured surface potential on capacitance gradient

$a\ [nm]$	$C_{ab}\ [F]$	$\frac{\partial C_{ab}}{\partial c}\ [F/m]$	K_c
2.5	-1.24E-19	-4.42E-11	0.49
3.0	-1.44E-19	-4.16E-11	0.52
3.5	-1.64E-19	-3.92E-11	0.55
4.0	-1.83E-19	-3.70E-11	0.58
4.5	-2.00E-19	-3.49E-11	0.62
5.0	-2.16E-19	-3.29E-11	0.65
5.5	-2.32E-19	-3.11E-11	0.69
6.0	-2.47E-19	-2.94E-11	0.73
6.5	-2.61E-19	-2.79E-11	0.77
7.0	-2.74E-19	-2.64E-11	0.82
7.5	-2.86E-19	-2.51E-11	0.86
8.0	-2.98E-19	-2.38E-11	0.91
8.5	-3.10E-19	-2.26E-11	0.95
9.0	-3.20E-19	-2.16E-11	1.00

an AFM tip radius of 20 nm and a tip-sample separation of 5 nm (see Table 5.I). We then calculated a ratio, K_c between the capacitance gradient for the largest particle radius and the other values for smaller particles:

$$K_c = \frac{\frac{\partial C_{ab}(a_{MAX})}{\partial z}}{\frac{\partial C_{ab}(a)}{\partial z}} \tag{5.18}$$

This represents the reduction in interaction between the tip and the sample as the particle becomes smaller, causing the apparent reduction in surface potential. Applying this correction ratio to the change in DC bias, ΔV_{DC} gives us an expression for the apparent change in surface potential. we reproduced the surface potential measurements of nanoparticles in FIG 2 of reference[132] to compare these results to. Of these measurements, we assumed that the one for the largest particle was the most accurate, so the correction ratio for each particle size was multiplied by the surface potential drop at $a = 18\ nm$ (see Table 5.I and FIG. 5.4FIG.). This data shows

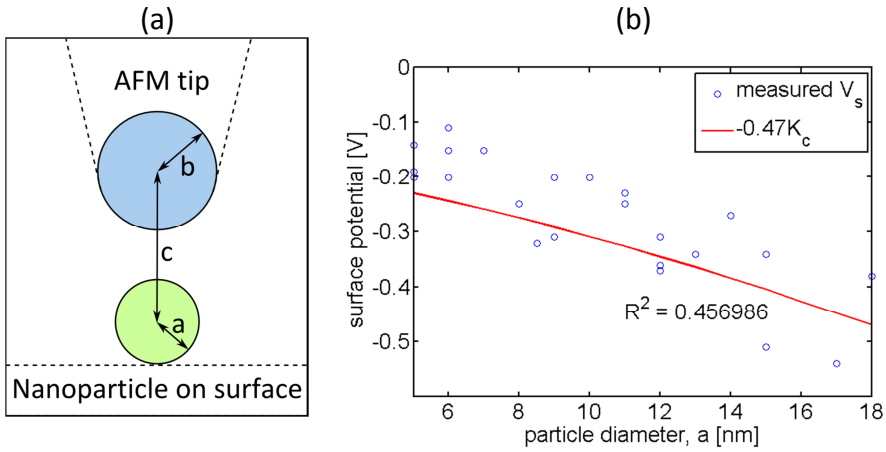

FIG. 5.4 AFM-Nanoparticle schematic and capacitance dependence of KPM.

(a) A schematic an AFM tip and a nanoparticle on a surface described as a two particle system, which is described in section 2.2 (b) Comparison of the surface potential measured on nanoparticles and calculated by an analytical solution for the capacitance gradient Eq. (5.17). The same data is described in Table 5.I.

moderate correlation between the surface potential difference measured by Zhang et al.[132] and the correction based on changes in the capacitance gradient (Eq. (5.17)). To conclude, the charge state of the nanoparticles was clearly induced by the doped-Si substrate, but variation with particle size could have been convolution of the KPM measurement instead of or as well as the change in capacitance between the Si surface and each particle. We have instead demonstrated that this relation between particle size and measured potential can be explained through variation of the capacitance gradient between the tip and the sample (Eq. (5.17)) during KPM.

5.3.2 DHKPM in air

Before introducing DHKPM to a fluid environment, we worked on taking measurements in air so that they could be compared to conventional KPM to ascertain the effectiveness of the setup. For these measurements, we prepared a Pt coated sample and coated it with Au nanoparticles from colloidal dispersions using

electrophoresis. The particles in these colloids had nominal diameters of 20, 40, 60 and 80 nm. Once immobilised on the surface, the entire surface was coated with 5 nm of Pt using RF sputter deposition, such that the work function should be equal across all the surfaces. The exact morphology of Pt on the surfaces of these particles has not been determined.

We sequentially took KPM and DHKPM measurements of the surface potential of this nanoparticle encased surface. An example of the DHKPM potential map is presented in FIG. 5.5, measured with a tip-sample separation of 5 nm. With both KPM and DHKPM measurements, we found a similar dependence of the surface potential had been observed by Zhang et al. [132] In both modes, we changed the tip-sample separation from 100 nm to 5 nm and have plotted the resulting trends for KPM and DHKPM FIG. 5.5(a) and FIG. 5.5(b) respectively. The KPM measurements were not able to resolve the difference between the particles until the lowest tip-sample separation. DHKPM on the other hand, was able to differentiate the nanoparticles from the surrounding surface from much further away. This was consistent with a reduced amount of convolution due to the capacitance gradient. A similar reduced dependence on tip-sample separation has been shown for DHKPM on flat surfaces[133], but this is the first time this effect had been observed for nanoparticles, which are much harder to measure. The increase in surface potential with particle size is apparently stronger during DHKPM, but this may be in part due to the increased resolution of nanoparticle measurement.

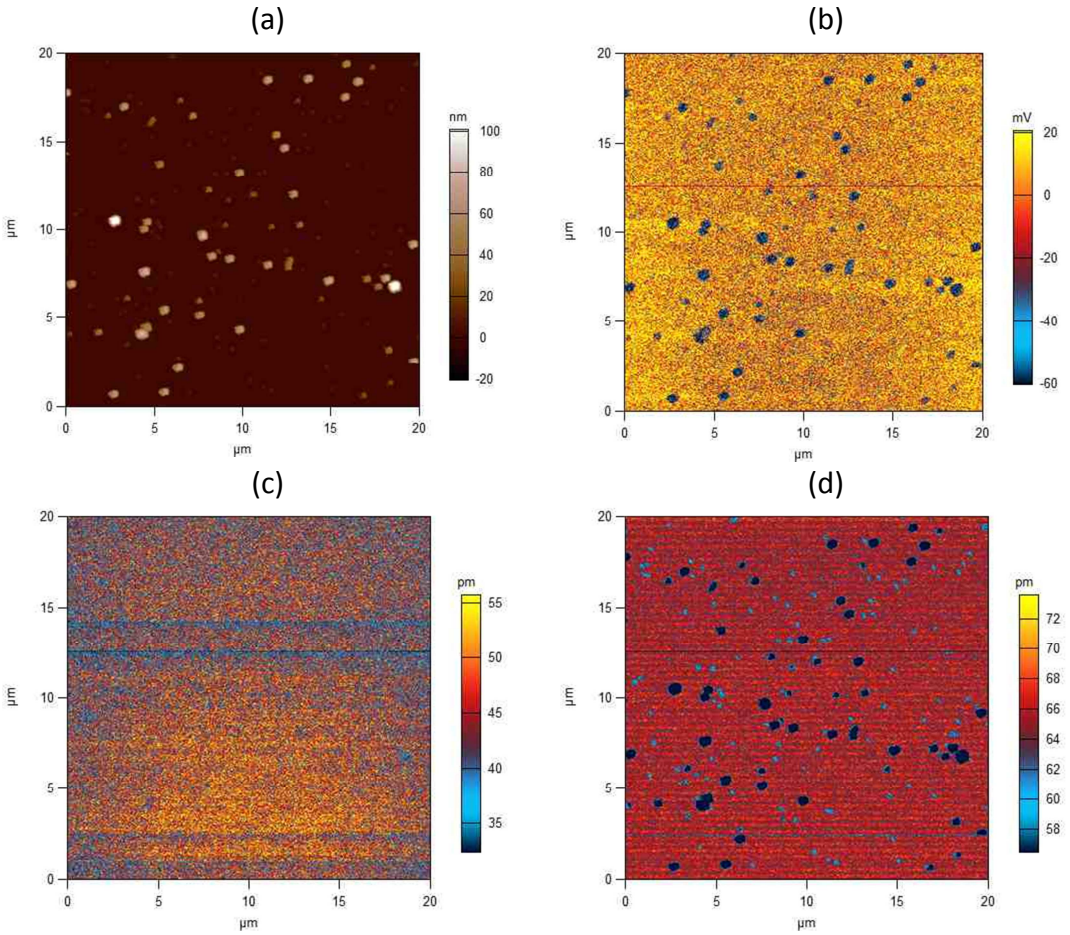

FIG. 5.5 DHKPM measurements of nanoparticles.

(a) Topography and (b) DHKPM measurements of Au nanoparticles encased in Pt on a Pt substrate. (c) and (d) show the amplitudes of the cantilever response at 15 kHz, the electric drive frequency, and 30 kHz respectively with a drive voltage of 3 V. The amplitude response to the nanoparticles is clearly much stronger at 30 kHz, indicating that the change in either the incident AC voltage on the tip or the capacitance gradient caused by the tip are the primary source of the DHKPM measurement of nanoparticles.

We applied the same model which we had used with the relative capacitance gradient between tip and sample (Eq. (5.18)) to see if our model could predict this trend FIG. 5.6(c). Up to an 80 nm particle diameter, the factor K_C was predicted to be non-linear, based on a tip radius of 20 nm. To obtain the fit, K_C was multiplied by a surface potential chosen to obtain the best coefficient of determination R^2 for the data. The coefficient was -0.152489 for the KPM trend and -0.604707 for the DHKPM trend. This

indicated a poor correlation between the measurements and the model, as the results indicated that the dependence of the surface potential would decrease with increasing

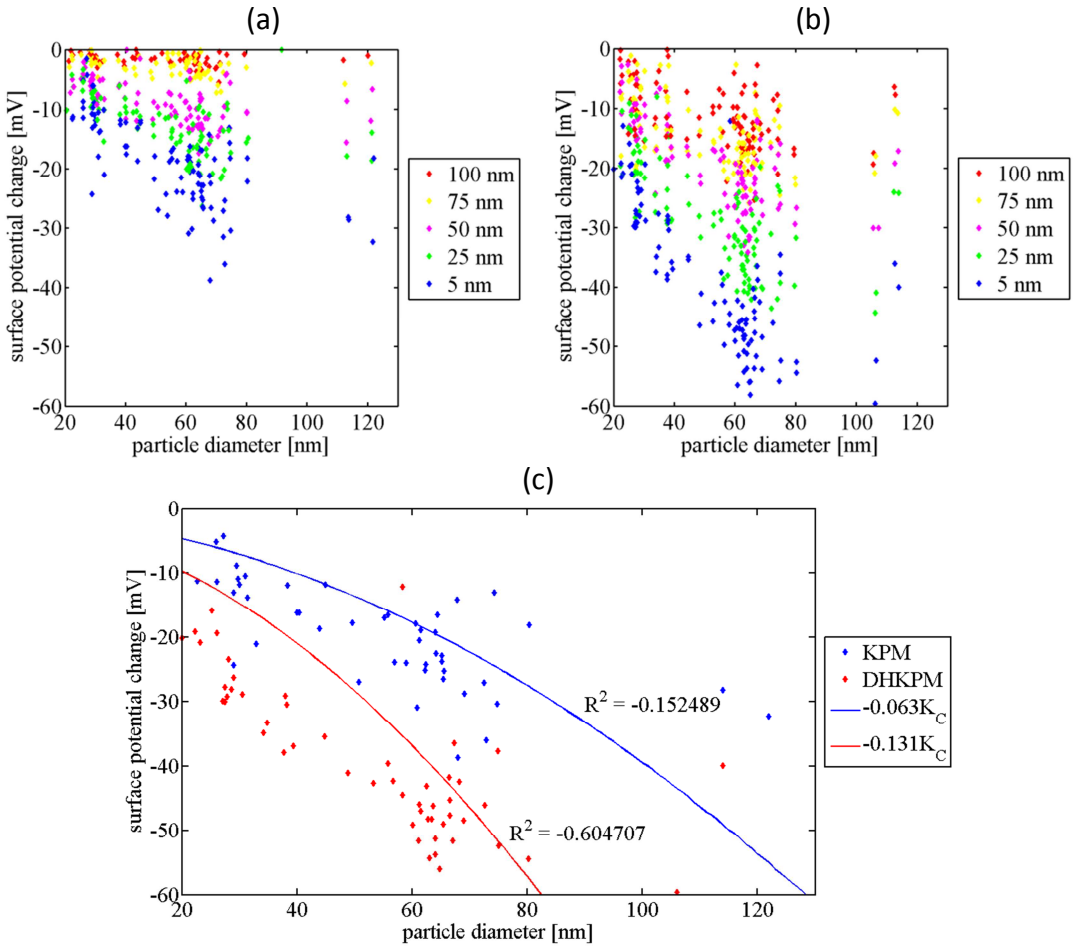

FIG. 5.6 Nanoparticle measurements with KPM vs DHKPM.

(a) Conventional KPM and (b) DHKPM surface potential measurements of different Au nanoparticles in air. In both cases the scan of the surface was lowered gradually from a tip-sample separation of 100 nm to 5 nm. (c) shows a comparison of the KPM and DHKPM measurements at 5 nm tip-sample separation with a line plot based on the change in capacitance gradient, factor K_c (Eq. (5.18)), fitting the data with a coefficient of determination R^2 printed on the plot.

particle size, whereas the model indicated the opposite trend. The surface potential was generally larger in DHKPM than KPM, indicating a higher sensitivity of DHKPM to the nanoparticles.

Thus the geometry is clearly an important factor in DHKPM measurements of nanoparticles, as it is for conventional KPM. To consider the impact of geometry on DHKPM, we compared measurements taken on these nanoparticles (FIG. 5.5) to DHKPM measurements on two adjacent flat surfaces of Ti and ITO (FIG. 5.3). In the first case, the strongest response of the cantilever was observed at 2ω (FIG. 5.5d), which according to Eq. (5.10) is only dependent on the AC drive voltage and the capacitance gradient between the tip and the surface. The poor correlation between the capacitance gradient and particle size in FIG. 5.6c wither indicates that the model of two spheres oversimplifies the system or that the variation arises from changes in the cantilever actuation from the AC drive voltage. There is a relatively small response in the cantilever amplitude at ω (FIG. 5.5c), which is indicative that there is little actual difference in surface potential between the surfaces, and the measurements are an effect of the geometry and convolution of the tip measurement. This contradicts previous claims that KPM is independent of surface geometry[125]. In comparison, when DHKPM was performed on Ti and ITO (FIG. 5.3), the cantilever amplitude at ω (FIG. 5.3b) reveals the difference between the Ti and ITO materials, as a result of its dependence on the surface potential. The response at 2ω appears to be equivalent on either side of the step, except when there is a change in the geometry. This indicates that the changes in surface potential observed in these KPM and DHKPM measurements are likely the result of changes to the capacitance gradient, which varies with particle size (Eq. (5.17)).

5.3.3 DHKPM in water

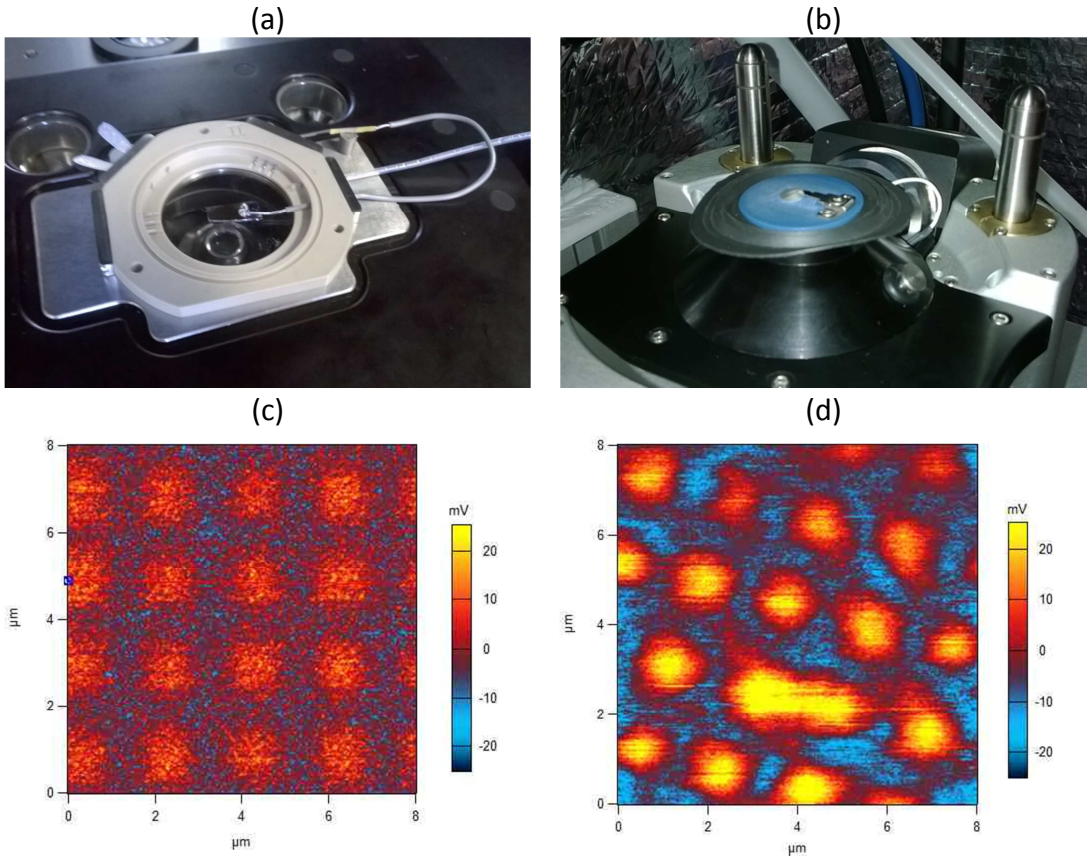

FIG. 5.7 DHKPM measurements of monolayers on a Au surface in water.

(a) The fluid cell used to immerse and isolate the sample in solution. An external electrical contact is made through one of the ports to ground the sample. (b) The AFM chip holder, fitted with a membrane to close the fluid cell. (b, c) DHKPM measurements of monolayers of MHA patterned as squares onto an Au surface. For comparison, measurements were taken (a) in air and (b) in distilled water.

As may be recalled, the goal of developing these measurements was to enable material characterisation with probes in polar media. This was identified as a key goal for a probe-based pick-and-place nanomanipulator, to identify materials in-situ and enabling accurate fabrication. Towards that goal, we were able to perform DHKPM measurements of nanoparticles and monolayers in water, which is as previously discussed not possible with conventional KPM.

Using an Au coated 360 kHz cantilever, DHKPM scans were performed in a fluid cell (FIG. 5.7) with DHKPM actuated electrically with 3 V drive amplitude, a 40 kHz frequency and a tip-sample separation of 50 nm. To image the monolayers, an Au sample patterned with square areas of MHA was used, which we previously used to assess the coverage of monolayers in section 3.5.2 (FIG 3.29). FIG. 5.7d shows that the areas patterned with MHA were successfully resolved in water. When compared to measurements taken by DHKPM in air (FIG. 5.7c), the magnitude of the measured surface potential has increased, which probably originates from ionisation of the MHA monolayer, although the polarity of this measurement is unconfirmed. It should also be a result of the increased electric field in the water environment compared to air, which may also have reduced the lateral resolution. In one case, two of the MHA squares in water appear to have overlapped, which we think is a fabrication defect. Resolution could have been improved by reducing the tip-sample separation but tip resolution was lost soon afterwards.

Imaging of nanoparticles in water was also performed in a fluid cell (FIG. 5.7a) with an Au coated cantilever, actuated with a 2 V drive amplitude, a 40 kHz frequency and a tip-sample separation of 5 nm. Topography and DHKPM potential maps of these nanoparticles are presented in FIG. 5.8(a) and FIG. 5.8(b) respectively. As in air with Pt encased Au nanoparticles, the measured surface potential difference appears to increase with particle diameter, as indicated by the plot in FIG. 5.8(c). Unfortunately, the measurement in water was very noisy. A fit based on the factor K_C (Eq. (5.18)) achieved a best R^2 value of -0.0188972 for a maximum surface potential difference of -211 mV, indicating the same poor correlation identified with measurements in air. The overall trend showed a larger measured surface potential difference compared to

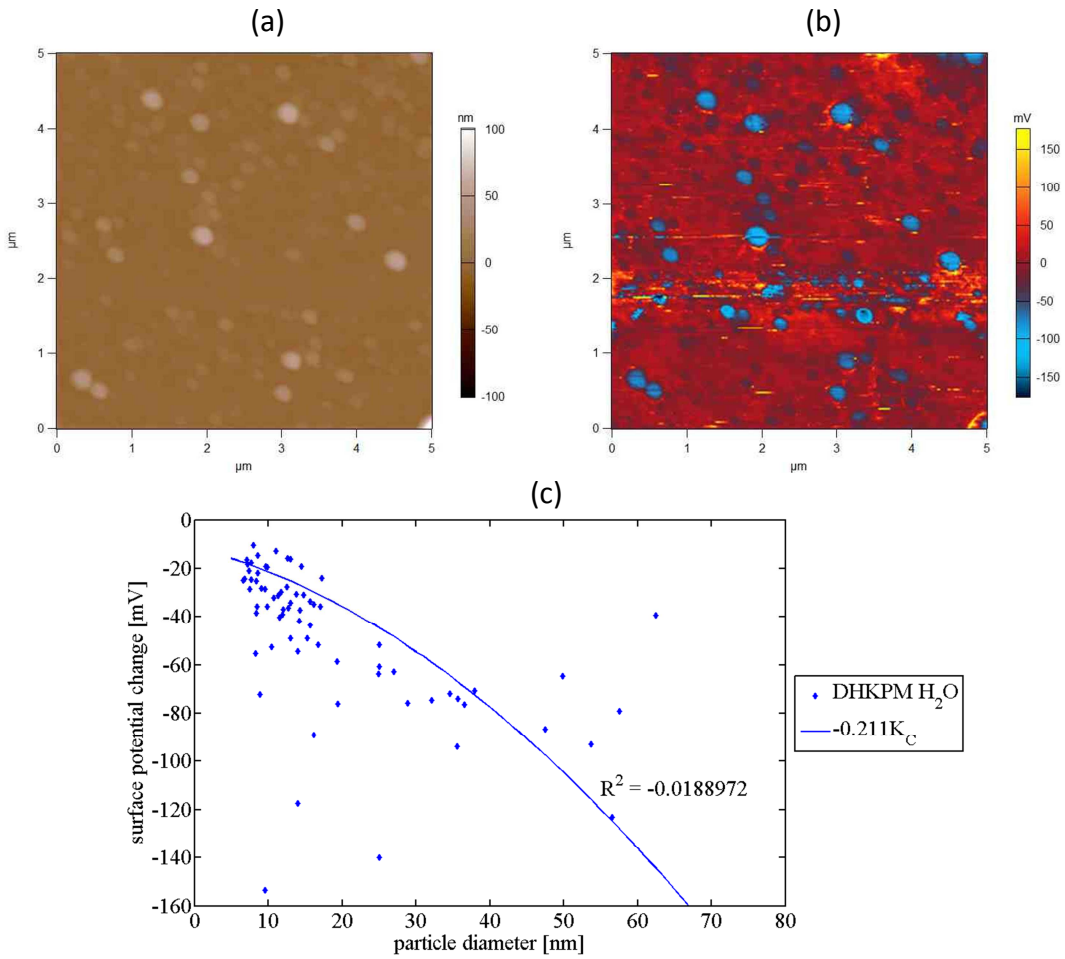

FIG. 5.8 DHKPM measurements of nanoparticles in water.

(a) Topography and (b) potential maps obtained by DHKPM measurements of Au nanoparticles immersed in distilled water. (c) a graph of the relation between the diameter of the particles and their measured surface potential, with a line plot based on the change in capacitance gradient, factor Kc (Eq. (5.20)), fitting the data with a coefficient of determination R^2 printed on the plot.

measurements in air, reflecting an increased enhanced effect in water, which was also observed for the monolayer measurements.

We attempted to improve the resolution in liquid using a silicon nitride cantilever with a lower spring constant (the above cantilever was 40 N/m) whilst maintaining a high enough natural frequency (>300 kHz) to operate well in liquid, but these were unable to resolve the topography of the nanoparticles. Future work will attempt to use longer

silicon-based cantilevers, but using the second resonant mode of the cantilever to ensure the frequency can be detected in liquid.

5.4 Chapter Summary

We have successfully developed open-loop DHKPM and demonstrated that nanoparticles can be measured and identified by this method. We have shown that this method improves the sensitivity of Kelvin probe measurements at large distances from a surface for nanometric features. This will be very important to aid the mapping of surface features for any future nanomanipulator that will need to identify such materials. It has also provided a tool to analyse the electric potential generated around these devices when they are in a colloid-like solution, which we intend to use to troubleshoot the behaviour of the voltage-driven nanoparticle assembly devices in the near future. The development of this DHKPM technique also led to some realisations about the nature of KPM measurements and how this effect can convolute the measurements of materials where no surface potential should exist. This is also important to the identification of different materials and has applications in toxicology analysis of nanoparticles[134] that is being investigated by our research group.

Chapter 6

Conclusions

The overall aim that inspired this Doctoral Research was to develop a means of rapidly and controllably assembling nano-objects from bulk suspensions. This was viewed as a means of enabling a new type of nanomanufacturing where functional components could be assembled on automotive-style assembly lines, with the method of pick-and-place being the key to unlocking this technology. From the most innovative methods available today, we decided that combining voltage-driven manipulation with chemically-mediated self-assembly of nanoparticles would be able to achieve a flexible mechanism, whilst maintaining the high precision of the self-assembly method.

Simulations of the different devices proposed to drive this particle assembly mechanism indicated that such a process would be plausible. These simulations relied upon modeling the electrochemical system of ions and particles in the colloidal suspension with the Guoy-Chapman model. This static model calculated the electric potential that was present throughout the solution to determine the effect on charged particles nearby in the suspension. Testing of these devices has shown that the situation is not as simple as proposed by these simulations. In the majority of test

nanoparticles became deposited across all the surfaces the colloidal suspension of nanoparticles was exposed to.

Troubleshooting the problems with this mechanism and investigating alternatives thus became our primary goal. The colloid that was being used was found to be fairly stable under ambient conditions, so the instability that was observed in the flocculation of nanoparticles after deposition resulted from interaction with the device. The molecular monolayer of MHA that was being used to funnel the nanoparticles away from the Au areas was also found to be intact and with good surface coverage. The MHA coverage also did not cause the absolute repulsion of nanoparticles under ambient conditions, with many nanoparticles able to break the energy barrier and bond to the Au-MHA surfaces. The selection of a new repulsive monolayer with more repulsive ligands may help this process or a change in device design to avoid this issue entirely. The instability of the Au electrodes observed in many deposition experiments, particularly the work with interdigitated electrodes, affected these experiments and may be alleviated by the choice of a more stable alternative. The unstable results for devices where applied voltages were used to instigate particle assembly, where innate surface charges saw much greater order, implies that the use of a voltage via the methods presented in this thesis is the root cause of resulting instabilities in the colloid. Alternative circuit designs may reduce these issues.

Rapid assembly of nanoparticles from colloid was proven to be achievable, instead not through applied bias but by manipulation of surface hydrophobicity. Electrostatic interactions have proven to be sufficient to funnel particles away from surface, but the hydrostatic barrier was a limiting factor to the speed of particle capture. By coating the

targeted areas with a non-polar and hydrophobic monolayer, the surface became dewetted as it was entropically favourable for the water molecules to move into the bulk. we was able to use this effect to achieve single nanoparticle-placement with TMODS patterned onto SiO_2, with 20 nm Au particles funnelled onto the TMODS surfaces with many incidences of single-particle funnelling within 5 minutes. This represents a massive improvement on current, accurate assembly times that require timescales on the order of hours. Further work can be applied to improve the selectivity of this process and the rapid assembly times should make the process practical to integrate with AFM-style probes for nanoparticle pick-and-place.

In the complementary work of this project, we also developed the means to identify the electronic potential of different materials in the polar liquids of the colloidal dispersions. The emergence of Dual-Harmonic Kelvin Probe Microscopy allowed us to identify the presence of the MHA monolayers both in air and in liquid on these devices. This also led to the identification of the dependence of both closed and open-loop Kelvin probe measurements on the nanoscale surface geometry, that may be related to the capacitance between the probe and sample.

Based on this, it is our contention that we have furthered knowledge via the following key contributions of this thesis:

1) Inventing, testing and analysing simulations and experiments with novel voltage-controllable single nanoparticle capture devices;

2) Developed a new, rapid method for single-particle assembly that combines electrostatic funnelling with hydrophobic dewetting of a non-polar monolayer, which accelerates the particle manipulation to practical timescales for applications;

3) The novel use of open-loop Dual-Harmonic Kelvin Probe Microscopy measurements to characterise the assembly of nanoparticles in solution and identifying a clear trend in the convolution of these measurements with the geometry of the surface.

Appendix A

Poisson-Nernst-Planck Model

Modeling of the solution the nanoparticles were dispersed in was performed under static conditions with the Poisson-Boltzmann equation in Chapter 2. To better model the dynamics of the system, an alternative system was considered, modeling the electrostatic potential using the Poisson-Nernst-Planck equation. This also utilises the Poisson equation for electrostatics,

$$\boldsymbol{\nabla}^2\varphi = \frac{\rho}{\varepsilon_0\varepsilon_r} = \frac{\sum_i Z_i e\, N_i}{\varepsilon_0\varepsilon_r} \tag{A.1}$$

where φ is the electronic potential, ρ is the space charge density, ε_0 and ε_r are the permittivity of free space and relative permittivity respectively, , Z_i is the valency of ionic species i, e is the electronic unit charge, N_i is the number of ionic species i per unit volume and $\boldsymbol{\nabla^2}$ is the *Laplacian* operator (Eq. 2.4). However, instead of assuming that the charges form Boltzmann distributions at charged surfaces, as the Poisson-Boltzmann equation did, we instead considered a time-dependent Nernst-Planck diffusion of ionic species in the solution, as below:

$$\frac{\partial N_i}{\partial t} = \boldsymbol{\nabla}.\left[D_i\left(\boldsymbol{\nabla}N_i + \frac{Z_i e N_i}{k_B T}\boldsymbol{\nabla}\varphi\right)\right] - u\boldsymbol{\nabla}N_i \tag{A.2}$$

where t is time, D_i is the diffusion coefficient of ionic species i, k_B is Boltzmann's constant, T is the temperature and u is the velocity of the system relative to the

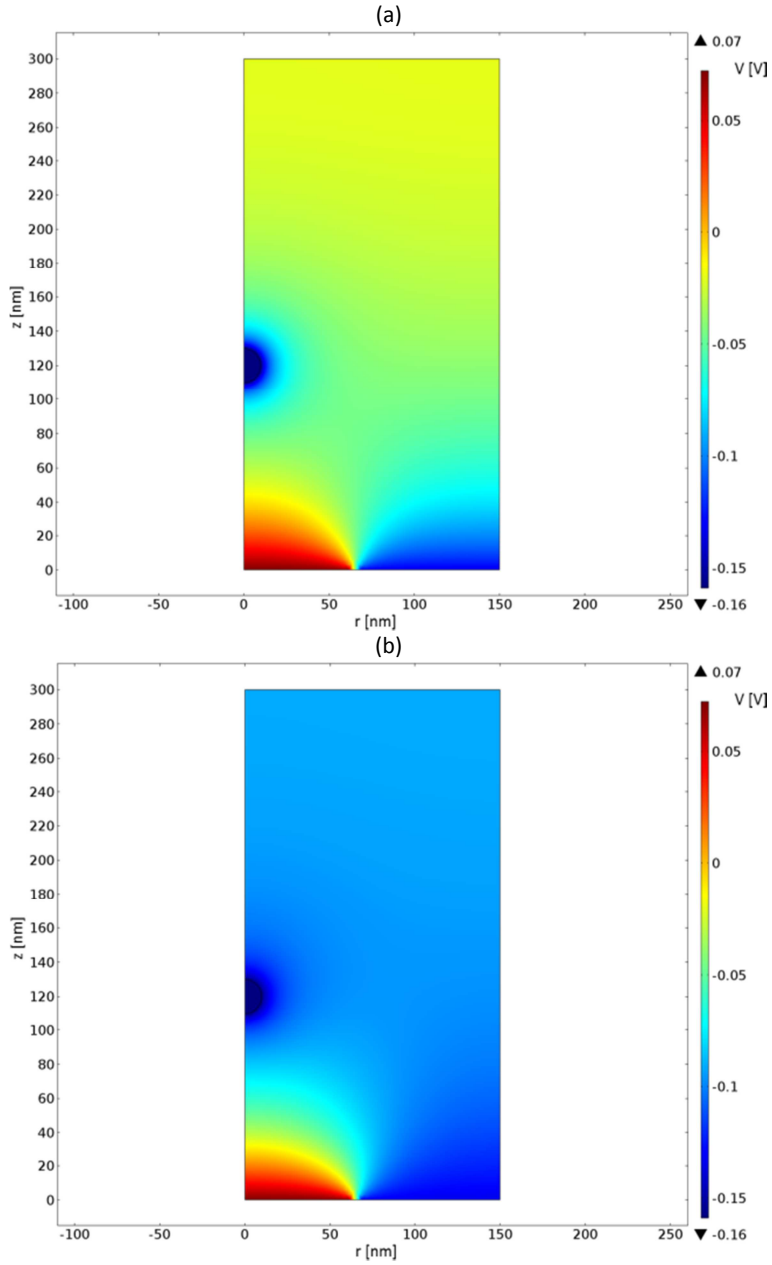

FIG. A.1 Comparison of electric potential colour maps for P-B and P-N-P systems.

The above colour maps show the electric potential map obtained by finite element modeling of two identical systems using (a) the Poisson-Boltzmann equation and (b) the Poisson-Nernst-Planck equations after 1 µs.

observer. This models the diffusion with time of the ionic species in the solution in response to charged interfaces. This differs from the Poisson-Boltzmann equation, defined in Eq. 2.5, which instead assumed that these ionic species formed exponential distributions of ions at these charged interfaces.

We decided to compare the different methods of using the Poisson-Boltzmann equation to model the electric potential, as we did in section 2.3, with this set of Poisson-Nernst-Planck equations defined above. The system modeled was a reproduction of the self-limited single-nanoparticle placement system introduced by Huang et al.[48] This relied on a 65 nm radius circular area coated with a monolayer of APTES to confer a positive surface potential of 72 mV. The surrounding surface is coated with a monolayer of MHA to confer a negative surface potential of -135 mV. This funnelling voltage is then used to model the electric potential in a surrounding electrolyte and the force acting on a 20 nm gold nanoparticle, with a surface potential of -159 mV, at a position z above this patterned surface. We used this system frequently in chapter 2 as a comparison to the voltage-directed particle assembly strategies we proposed. For this comparison, we replaced the determined concentrations of ions in the solution with a 1:1 concentration of $5x10^{-6}mol/m^3$ of monovalent ions. This was enforced as the simulation using the P-N-P equations struggled to complete its computations when additional ionic species were present in the solution. For these models, the effective result is similar regardless of the different ions involved and is strongly dependent on the order of magnitude of ions present; the valency and concentration of specific ions does not overly affect the electric potential distribution, although in reality multivalent ions do have additional effects.

The resulting electric potential distributions are presented in 2-dimensional colour plots in FIG. A.1, which is axially symmetric about the vertical axis where the radius, r = 0 nm. The resulting electric potential profiles are very similar, with a smooth decrease in electric potential moving away from charged interfaces. The most notable difference is that the bulk value of the potential, which is far away from any interface,

does not converge to the same value in the Poisson-Boltzmann (P-B) and Poisson-Nernst-Planck (P-N-P) models. These differences can be seen more clearly in FIG. A.2a and FIG. A.2b, which show line profiles of the electric potential where r = 0 nm. The electric potential profiles move from the 72 mV surface at z = 0 nm down to -159 mV either side of the gold nanoparticle 120 nm above the surface, and then back up to the respective bulk potential values as z continues to increase. The P-N-P model was calculated at different times as it developed from an initial monodispersion of ions. Although the ion concentrations were still changing during the considered 10 ns to 1 ms time frame, the electric potential was not significantly affected. Taking the definition for the zeta potential as the difference between the surface and the bulk potential, the zeta potential for the Au nanoparticle should be approximately – 70 mV. This value corresponds very well to the zeta potential of -62 mV we measured for these nanoparticles using Laser Doppler Electrophoresis (Section 3.5.1). In contrast, the P-B model for the same system results in a zeta potential of approximately -140 mV. The successful prediction of the zeta potential for the P-N-P model indicates that it is a more realistic simulation than the P-B model to predict the colloidal dispersion would work.

In spite of these differences in the electric potential profile, the P-B and P-N-P models result in very similar force profiles acting on the nanoparticle. Integrating the Maxwell Stress Tensor to determine to electric force for the nanoparticle at a range of heights above the attractive APTES surface, produced the force profiles presented in FIG. A.2c. The P-N-P model predicted a marginally more attractive force than the P-B model, and the P-N-P force is attractive over the whole range whereas the P-B

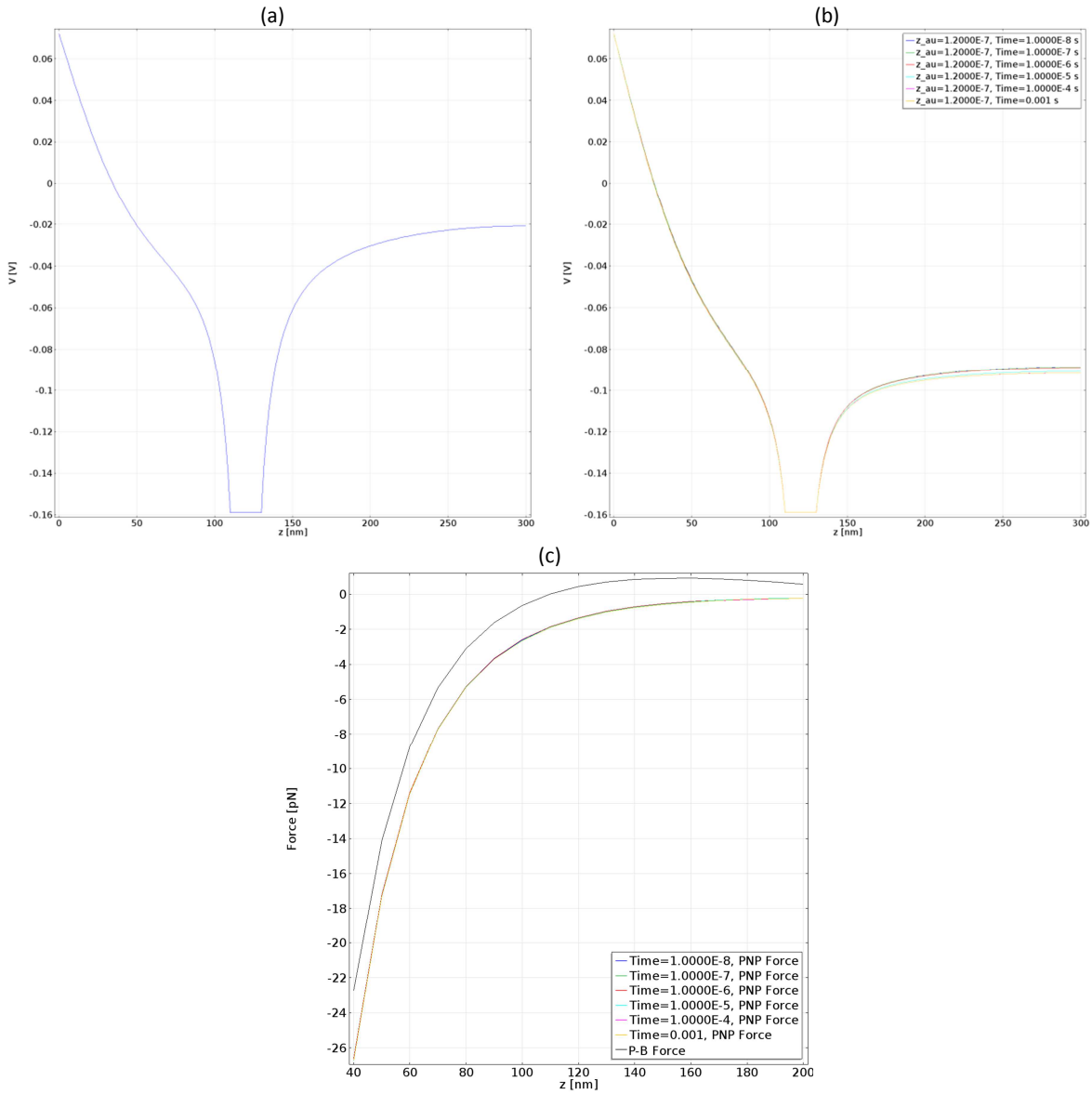

FIG. A.2 Comparison of electric potential and force profiles for P-B and P-N-P systems.

The above line profiles show the electric potential in FIG. A.1 along the line defined by r = 0 nm. These were obtained by finite element modeling of two identical systems using (a) the Poisson-Boltzmann equation and (b) the Poisson-Nernst-Planck equations. (c) shows the force profiles for the P-B and P-N-P models of the force acting on the gold nanoparticle at different heights *z* above the surface, moving along the line r = 0 nm.

force is slightly repulsive above z = 110 nm. These differences do not make a significant difference to the predicted result of the capture of a nanoparticle in this system. we also attempted to model the system with a nanoparticle blocking the

APTES surface, to compare the models when the P-B model predicted that another nanoparticle would be electrically repelled from this surface. Unfortunately the P-N-P model for this system was unable to converge to a solution for the electric potential, due to the proximity of the nanoparticle and APTES surfaces, so we was unable to compare the P-B and P-N-P models for this situation.

Ultimately due to the similarities for the force profiles acquired for simulations using the stationary Poisson-Boltzmann and time-dependent Poisson-Nernst-Planck models for electric potential, we decided that it was acceptable to use the more flexible Poisson-Boltzmann model when designing nanoparticle capture devices.

List of Tables and Figures

FIG. 1.1 Atomic manipulation with probes. 3

FIG. 1.2 Nano-object manipulation with probes. 6

FIG. 1.3 Non-contact capture of 200 nm polystyrene beads by dielectrophoretic probes. 9

FIG. 1.4 Capture of 22 nm polymer nanoparticles in a photonic crystal (PhC) resonator....11

FIG. 1.5 Manipulation of 50 nm polystyrene beads with near-field optical tweezers. 12

FIG. 1.6 Single nanoparticle printing using self-assembly. 14

FIG. 1.7 Single nanoparticle capture in an array by self-assembly....16

FIG. 1.8 Local anodic oxidation lithography of Si nanowires. 21

FIG. 1.9 Features and devices created by Direct Laser Writing. 25

FIG. 2.1 Electric potential distribution at the solid-liquid interface. 34

FIG. 2.2 DLVO potential energy barrier between two colloidal nanoparticles....38

FIG. 2.3 Dependence of colloid stability on ion concentration and surface potential....40

FIG. 2.4 Finite Element Analysis. 42

FIG. 2.5 Gate Device Concept....44

FIG. 2.6 Voltage Driven Placement: Force Vectors in Liquid. 45

FIG. 2.7 Rendering of gate device simulated electric potential. 46

FIG. 2.8 Voltage Driven Placement: Effect of Applied Voltage and Gate Diameter....47

FIG. 2.9 Voltage Driven Placement: Effect of Insulator Thickness. 48

FIG. 2.10 Voltage Driven Placement: Effect of particle surface potential. 50

FIG. 2.11 Voltage Driven Placement: Effect of Geometrical Imperfections. 51

FIG. 2.12 Pedestal Device Concept....53

FIG. 2.13 Effect of Pedestal Height and Voltage. 54

FIG. 2.14 Interdigitated Electrode Device Concept....55

FIG. 2.15 Interdigitated Electrode Placement: Effect of Voltage and Anode Radius. 56

FIG. 3.1 Electron Beam Lithography (EBL) process with positive and negative-tone resists. 61

FIG. 3.2 Schematic designs for Electron Beam Lithography of features. 64

FIG. 3.3 Fabrication of Gate devices with different electron-beam resists. 67

FIG. 3.4 Gate device testing setup. 69

FIG. 3.5 Gate devices with short-circuited insulation (1/2). 71

FIG. 3.6 Gate devices with short-circuited insulation (2/2). 72

FIG. 3.7 Gate Devices with poor MHA assembly (1/2). 74

FIG. 3.8 Gate Devices with poor MHA assembly (2/2). 75

FIG. 3.9 Gate Devices after testing (1/4). 77

FIG. 3.10 Gate Devices after testing (2/4). 78

FIG. 3.11 Gate Devices after testing (3/4). 79

FIG. 3.12 Gate Devices after testing (4/4). 80

FIG. 3.13 Pedestal Devices after testing. 82

FIG. 3.14 Pedestal Devices testing with in-situ AFM imaging. 83

FIG. 3.15 Pedestal Devices after testing with in-situ AFM imaging (1/3). 85

FIG. 3.16 Pedestal Device after testing with in-situ AFM imaging (2/3). 86

FIG. 3.17 Pedestal Device after testing with in-situ AFM imaging (3/3). 87

FIG. 3.18 Fabrication and KPM characterisation of Interdigitated Electrode devices 89

FIG. 3.19 Interdigitated Electrode Device after testing without insulation. 90

FIG. 3.20 Interdigitated electrodes after testing with a 20 nm Au colloid. 92

FIG. 3.21 Interdigitated electrodes after testing with an 80 nm Au colloid (1/6). 94

FIG. 3.22 Interdigitated electrodes after testing with an 80 nm Au colloid (2/6). 95

FIG. 3.23 Interdigitated electrodes after testing with an 80 nm Au colloid (3/6). 96

FIG. 3.24 Interdigitated electrodes after testing with an 80 nm Au colloid (4/6). 97

FIG. 3.25 Interdigitated electrodes after testing with an 80 nm Au colloid (5/6). 98

FIG. 3.26 Interdigitated electrodes after testing with an 80 nm Au colloid (6/6). 99

FIG 3.27 Size and zeta potential measurements of Au nanoparticles 101

FIG 3.28 XPS identification of MHA monolayers 103

FIG 3.29 KPM of MHA monolayers.....105

FIG 4.1 Au nanoparticle assembly on different surfaces. 108

FIG 4.2 Single-nanoparticle placement driven by self-assembled monolayers (1/5). 111

FIG 4.3 Single-nanoparticle placement driven by self-assembled monolayers (2/5). 112

FIG 4.4 Single-nanoparticle placement driven by self-assembled monolayers (3/5). 113

FIG 4.5 Single-nanoparticle placement driven by self-assembled monolayers (4/5). 114

FIG 4.6 Single-nanoparticle placement driven by self-assembled monolayers (5/5). 115

FIG 4.7 Nanoparticle Self-Assembly Funnelled by SiO_2 Surfaces (1/3).....117

FIG 4.8 Nanoparticle Self-Assembly Funnelled by SiO_2 Surfaces (2/3).....118

FIG 4.9 Nanoparticle Self-Assembly Funnelled by SiO_2 Surfaces (3/3).....119

FIG 4.10 Modified Gate Device Design.....121

FIG 4.11 TMODS Functionalised Gate Devices (1/5).....122

FIG 4.12 TMODS Functionalised Gate Devices (2/5).....123

FIG 4.13 TMODS Functionalised Gate Devices (3/5).....124

FIG 4.14 TMODS Functionalised Gate Devices (4/5).....125

FIG 4.15 TMODS Functionalised Gate Devices (5/5).....126

Table 5.I Dependence of measured surface potential on capacitance gradient 143

FIG. 5.1 KPM schematic. 134

FIG. 5.2 Conventional KPM in nonpolar liquid. 135

FIG. 5.3 Comparison of KPM and DHKPM on a Ti-ITO sample. 139

FIG. 5.4 AFM-Nanoparticle schematic and capacitance dependence of KPM. 144

FIG. 5.5 DHKPM measurements of nanoparticles. 146

FIG. 5.6 Nanoparticle measurements with KPM vs DHKPM. 147

FIG. 5.7 DHKPM measurements of monolayers on a Au surface in water. 149

FIG. 5.8 DHKPM measurements of nanoparticles in water. 151

Bibliography

1. Hornyak, G. L., Dutta, J., Tibbals, H. F. & Rao, A. K. *Introduction to Nanoscience*. (CRC Press, 2008).

2. Kane, J. *Nanoparticle necklace network arrays exhibiting room temperature single-electron switching*. (University of Nebraska-Lincoln, 2011). AT <HTTP://DIGITALCOMMONS.UNL.EDU/CHEMENGTHESES/10/>

3. Xi, N. & Li, G. *Introduction to Nanorobotic Manipulation and Assembly*. (Artech House, 2012).

4. Koh, S. J. *Strategies for controlled placement of nanoscale building blocks.* Nanoscale Res. Lett. **2,** 519–45 (2007).

5. Ariga, K. *Manipulation of Nanoscale Materials: An Introduction to Nanoarchitectonics*. (2012).

6. Eigler, D. & Schweizer, E. *Positioning single atoms with a scanning tunnelling microscope*. Nature **344,** 524–526 (1990).

7. Sugimoto, Y. *et al. Atom inlays performed at room temperature using atomic force microscopy*. Nat. Mater. **4,** 156–159 (2005).

8. Custance, O., Perez, R. & Morita, S. *Atomic force microscopy as a tool for atom manipulation.* Nat. Nanotechnol. **4,** 803–10 (2009).

9. Heucke, S., Baumann, F. & Acuna, G. *Placing individual molecules in the center of nanoapertures*. Nano Lett. **14,** 391–395 (2013).

10. Kim, S., Ratchford, D. & Li, X. *Atomic force microscope nanomanipulation with simultaneous visual guidance*. ACS Nano **3,** 2989–2994 (2009).

11. Kim, S., Shafiei, F., Ratchford, D. & Li, X. *Controlled AFM manipulation of small nanoparticles and assembly of hybrid nanostructures.* Nanotechnology **22,** 115301 (2011).

12. Sakakibara, K., Hill, J. P. & Ariga, K. *Thin-film-based nanoarchitectures for soft matter: controlled assemblies into two-dimensional worlds.* Small **7,** 1288–308 (2011).

13. Galisteo-López, J. F. *et al. Self-assembled photonic structures*. Adv. Mater. **23,** 30–69 (2011).

14. Kim, F. S., Ren, G. & Jenekhe, S. a. *One-Dimensional Nanostructures of π-Conjugated Molecular Systems: Assembly, Properties, and Applications from Photovoltaics, Sensors, and Nanophotonics to Nanoelectronics †*. Chem. Mater. **23,** 682–732 (2011).

15. Park, H. *et al. High-density integration of carbon nanotubes via chemical self-assembly.* Nat. Nanotechnol. **7,** 787–91 (2012).

16. Picco, L. M. *et al. Breaking the speed limit with atomic force microscopy*. Nanotechnology **18,** 044030 (2007).

17. Kodera, N., Yamamoto, D., Ishikawa, R. & Ando, T. *Video imaging of walking myosin V by high-speed atomic force microscopy.* Nature **468,** 72–6 (2010).

18. Tseng, A. A. *Advancements and challenges in development of atomic force microscopy for nanofabrication*. Nano Today **6,** 493–509 (2011).

19. Engstrom, D. S., Porter, B., Pacios, M. & Bhaskaran, H. *Additive nanomanufacturing – A review*. J. Mater. Res. 1–25 (2014). DOI:10.1557/JMR.2014.159

20. Gohlke, D. *et al. Atomic-scale engineering of the electrostatic landscape of semiconductor surfaces.* Nano Lett. (2013).

21. Olyanich, D. a, Kotlyar, V. G., Utas, T. V, Zotov, A. V & Saranin, A. a. *The manipulation of C(60) in molecular arrays with an STM tip in regimes below the decomposition threshold.* Nanotechnology **24,** 055302 (2013).

22. Morgenstern, K., Lorente, N. & Rieder, K.-H. *Controlled manipulation of single atoms and small molecules using the scanning tunnelling microscope*. *PHYSICA STATUS SOLIDI (B)* **250,** (2013).

23. Fuechsle, M. *et al. A single-atom transistor.* Nat. Nanotechnol. **7,** 242–6 (2012).

24. Mølhave, K., Wich, T., Kortschack, A. & Bøggild, P. *Pick-and-place nanomanipulation using microfabricated grippers.* Nanotechnology **17,** 2434–41 (2006).

25. Sardan, O. *et al. Rapid prototyping of nanotube-based devices using topology-optimized microgrippers.* Nanotechnology **19,** 495503 (2008).

26. Cagliani, A. *et al. Manipulation and in situ transmission electron microscope characterization of sub-100 nm nanostructures using a microfabricated nanogripper*. J. Micromechanics Microengineering **20,** 035009 (2010).

27. Castillo, J., Dimaki, M. & Svendsen, W. E. *Manipulation of biological samples using micro and nano techniques.* Integr. Biol. (Camb). **1,** 30–42 (2009).

28. Junno, T., Deppert, K., Montelius, L. & Samuelson, L. *Controlled manipulation of nanoparticles with an atomic force microscope*. Appl. Phys. Lett. **66,** 3627–3629 (1995).

29. Li, G., Xi, N., Yu, M. & Fung, W.-K. *Development of Augmented Reality System for AFM-Based Nanomanipulation*. IEEE Trans. Nanotechnol. **9,** 358–365 (2004).

30. Li, G., Xi, N., Chen, H., Pomeroy, C. & Prokos, M. *' Videolized ' Atomic Force Microscopy for Interactive Nanomanipulation and Nanoassembly*. IEEE Trans. Nanotechnol. **4,** 605–615 (2005).

31. Zhang, J., Member, S., Xi, N. & Chen, H. *Design , Manufacturing , and Testing of Single-Carbon-Nanotube-Based Infrared Sensors*. IEEE Trans. Nanotechnol. **8,** 245–251 (2009).

32. Qin, S., Kim, T.-H., Wang, Z. & Li, A.-P. *Nanomanipulation and nanofabrication with multi-probe scanning tunneling microscope: from individual atoms to nanowires*. Rev. Sci. Instrum. **83,** 063704 (2012).

33. Xiong, X. *et al. Large scale directed assembly of nanoparticles using nanotrench templates*. Appl. Phys. Lett. **89,** 193108 (2006).

34. Park, J.-U. *et al. Nanoscale, electrified liquid jets for high-resolution printing of charge.* Nano Lett. **10,** 584–91 (2010).

35. Kolíbal, M. *et al. Guided assembly of gold colloidal nanoparticles on silicon substrates prepatterned by charged particle beams*. ACS Nano **6,** 10098–106 (2012).

36. Zhou, Y. S. *et al. In Situ Quantitative Study of Nanoscale Triboelectrification and Patterning*. Nano Lett. AT PRESS (2013).

37. Mark, A. G., Gibbs, J. G., Lee, T.-C. & Fischer, P. *Hybrid nanocolloids with programmed three-dimensional shape and material composition.* Nat. Mater. **12,** 802–807 (2013).

38. Yilmaz, C., Kim, T.-H., Somu, S. & Busnaina, A. a. *Large-Scale Nanorods Nanomanufacturing by Electric-Field-Directed Assembly for Nanoscale Device Applications*. IEEE Trans. Nanotechnol. **9,** 653–658 (2010).

39. Wood, N. R., Wolsiefer, A. I., Cohn, R. W. & Williams, S. J. *Dielectrophoretic trapping of nanoparticles with an electrokinetic nanoprobe.* Electrophoresis **34,** 1922–30 (2013).

40. Brown, K. a & Westervelt, R. M. *Proposed triaxial atomic force microscope contact-free tweezers for nanoassembly*. Nanotechnology **20,** 385302 (2009).

41. Brown, K. a & Westervelt, R. M. *Triaxial AFM probes for noncontact trapping and manipulation*. Nano Lett. **11,** 3197–3201 (2011).

42. Jonás, A. & Zemánek, P. *Light at work: the use of optical forces for particle manipulation, sorting, and analysis.* Electrophoresis **29,** 4813–51 (2008).

43. Guffey, M. J. & Scherer, N. F. *All-optical patterning of Au nanoparticles on surfaces using optical traps.* Nano Lett. **10,** 4302–8 (2010).

44. Yan, Z. *et al. Controlling the position and orientation of single silver nanowires on a surface using structured optical fields.* ACS Nano **6,** 8144–55 (2012).

45. Yan, Z. *et al. Guiding spatial arrangements of silver nanoparticles by optical binding interactions in shaped light fields.* ACS Nano **7,** 1790–802 (2013).

46. Tong, L., Miljković, V. D. & Käll, M. *Alignment, rotation, and spinning of single plasmonic nanoparticles and nanowires using polarization dependent optical forces.* Nano Lett. **10,** 268–273 (2010).

47. Chen, Y.-F., Serey, X., Sarkar, R., Chen, P. & Erickson, D. *Controlled photonic manipulation of proteins and other nanomaterials*. Nano Lett. **12,** 1633–7 (2012).

48. Huang, H.-W., Bhadrachalam, P., Ray, V. & Koh, S. J. *Single-particle placement via self-limiting electrostatic gating*. Appl. Phys. Lett. **93,** 073110 (2008).

49. Berthelot, J. *et al. Three-dimensional manipulation with scanning near-field optical nanotweezers*. Nat. Nanotechnol. **9,** 295–299 (2014).

50. Fedoruk, M., Meixner, M., Carretero-Palacios, S., Lohmüller, T. & Feldmann, J. *Nanolithography by Plasmonic Heating and Optical Manipulation of Gold Nanoparticles*. ACS Nano AT PRESS (2013).

51. Bishop, K. J. M., Wilmer, C. E., Soh, S. & Grzybowski, B. a. *Nanoscale forces and their uses in self-assembly.* Small **5,** 1600–30 (2009).

52. Barrow, S. J., Funston, A. M., Wei, X. & Mulvaney, P. *DNA-directed self-assembly and optical properties of discrete 1D, 2D and 3D plasmonic structures*. Nano Today **8,** 138–167 (2013).

53. Gong, J., Li, G. & Tang, Z. *Self-assembly of noble metal nanocrystals: Fabrication, optical property, and application*. Nano Today **7,** 564–585 (2012).

54. Bellido, E., Domingo, N., Ojea-Jiménez, I. & Ruiz-Molina, D. *Structuration and integration of magnetic nanoparticles on surfaces and devices.* Small **8,** 1465–91 (2012).

55. Dong, B., Zhou, T., Zhang, H. & Li, C. Y. *Directed Self-Assembly of Nanoparticles for Nanomotors*. ACS Nano AT PRESS (2013). DOI:10.1021/NN400925Q

56. Kraus, T. *et al. Nanoparticle printing with single-particle resolution.* Nat. Nanotechnol. **2,** 570–6 (2007).

57. Cui, Y. *et al. Integration of Colloidal Nanocrystals into Lithographically Patterned Devices*. (2004).

58. Carlson, A., Bowen, A. M., Huang, Y., Nuzzo, R. G. & Rogers, J. a. *Transfer printing techniques for materials assembly and micro/nanodevice fabrication.* Adv. Mater. **24,** 5284–318 (2012).

59. Zheng, Y. *et al. Gutenberg-style printing of self-assembled nanoparticle arrays: electrostatic nanoparticle immobilization and DNA-mediated transfer.* Angew. Chem. Int. Ed. Engl. **50,** 4398–4402 (2011).

60. Porter, B. F., Abelmann, L. & Bhaskaran, H. *Design parameters for voltage-controllable directed assembly of single nanoparticles*. Nanotechnology **24,** (2013).

61. Gozen, B. A. & Ozdoganlar, O. B. *A Rotating-Tip-Based Mechanical Nano-Manufacturing Process: Nanomilling.* Nanoscale Res. Lett. **5,** 1403–1407 (2010).

62. Gozen, B. A. & Ozdoganlar, O. B. *Design and evaluation of a mechanical nanomanufacturing system for nanomilling*. Precis. Eng. **36,** 19–30 (2012).

63. Gozen, B. A. *Development and Analysis of a Tip-based Mechanical Nano-Manufacturing Process : Nanomilling*. (Carnegie Mellon University, 2012).

64. Cheong, L. L. *et al. Thermal Probe Maskless Lithography for 27.5 nm Half-Pitch Si Technology*. Nano Lett. **13,** 4485–4491 (2013).

65. Lee, W.-K. *et al. Nanoscale Reduction of Graphene Fluoride via Thermochemical Nanolithography*. ACS Nano (2013).

66. Szoszkiewicz, R. *et al. High-speed, sub-15 nm feature size thermochemical nanolithography.* Nano Lett. **7,** 1064–9 (2007).

67. Milner, A. a, Zhang, K. & Prior, Y. *Floating tip nanolithography.* Nano Lett. **8,** 2017–22 (2008).

68. Wang, D. *et al. Thermochemical Nanolithography of Multifunctional Nanotemplates for Assembling Nano-Objects*. Adv. Funct. Mater. **19,** 3696–3702 (2009).

69. Pires, D. *et al. Nanoscale three-dimensional patterning of molecular resists by scanning probes*. Science **328,** 732–5 (2010).

70. Fenwick, O. *et al. Thermochemical nanopatterning of organic semiconductors*. Nat. Nanotechnol. **4,** 664–8 (2009).

71. Paul, P., Knoll, a W., Holzner, F. & Duerig, U. *Field stitching in thermal probe lithography by means of surface roughness correlation.* Nanotechnology **23,** 385307 (2012).

72. Holzner, F. *et al. Directed Placement of Gold Nanorods Using a Removable Template for Guided Assembly*. 3957–3962 (2011).

73. Holzner, F. *et al. High density multi-level recording for archival data preservation*. Appl. Phys. Lett. **99,** 023110 (2011).

74. Bagri, A. *et al. Structural evolution during the reduction of chemically derived graphene oxide.* Nat. Chem. **2,** 581–7 (2010).

75. Martinez, J., Martínez, R. V & Garcia, R. *Silicon nanowire transistors with a channel width of 4 nm fabricated by atomic force microscope nanolithography.* Nano Lett. **8,** 3636–3639 (2008).

76. Martínez, R. V, Martínez, J. & Garcia, R. *Silicon nanowire circuits fabricated by AFM oxidation nanolithography.* Nanotechnology **21,** 245301 (2010).

77. Chiesa, M. *et al. Detection of the early stage of recombinational DNA repair by silicon nanowire transistors.* Nano Lett. **12,** 1275–81 (2012).

78. Masubuchi, S., Arai, M. & Machida, T. *Atomic force microscopy based tunable local anodic oxidation of graphene*. Nano Lett. **11,** 4542–6 (2011).

79. Lee, W. *et al. Chemically Isolated Graphene Nanoribbons Reversibly Formed in Fluorographene Using Polymer Nanowire Masks*. Nano Lett. **11,** 5461–5464 (2011).

80. Shin, Y., Son, J. Y., Jo, M., Shin, Y. & Jang, H. M. *High-Mobility Graphene Nanoribbons Prepared Using Polystyrene Dip-Pen Nanolithography*. J. Am. Chem. Soc. **133,** 5623–5625 (2011).

81. Shim, W. *et al. Hard-tip, soft-spring lithography.* Nature **469,** 516–520 (2011).

82. Kawata, S., Sun, H. B., Tanaka, T. & Takada, K. *Finer features for functional microdevices.* Nature **412,** 697–8 (2001).

83. Deubel, M. *et al. Direct laser writing of three-dimensional photonic-crystal templates for telecommunications.* Nat. Mater. **3,** 444–7 (2004).

84. Ergin, T., Stenger, N., Brenner, P., Pendry, J. B. & Wegener, M. *Three-dimensional invisibility cloak at optical wavelengths.* Science **328,** 337–9 (2010).

85. Fischer, J., Ergin, T. & Wegener, M. *Three-dimensional polarization-independent visible-frequency carpet invisibility cloak*. Opt. Lett. **36,** 2059–2061 (2011).

86. Röhrig, M., Thiel, M., Worgull, M. & Hölscher, H. *3D direct laser writing of nano- and microstructured hierarchical gecko-mimicking surfaces.* Small **8,** 3009–15 (2012).

87. Li, X., Cao, Y. & Gu, M. *Superresolution-focal-volume induced 3.0 Tbytes/disk capacity by focusing a radially polarized beam.* Opt. Lett. **36,** 2510–2 (2011).

88. Kabouraki, E. *et al. Redox multiphoton polymerization for 3D nanofabrication.* Nano Lett. **13,** 3831–5 (2013).

89. Cao, Y. & Gu, M. *Λ/26 Silver Nanodots Fabricated By Direct Laser Writing Through Highly Sensitive Two-Photon Photoreduction*. Appl. Phys. Lett. **103,** 213104 (2013).

90. Vasilantonakis, N. *et al. Three-dimensional metallic photonic crystals with optical bandgaps.* Adv. Mater. **24,** 1101–5 (2012).

91. Staude, I. *et al. Hybrid high-resolution three-dimensional nanofabrication for metamaterials and nanoplasmonics.* Adv. Mater. **25,** 1260–4 (2013).

92. Frölich, A., Fischer, J., Zebrowski, T., Busch, K. & Wegener, M. *Titania woodpiles with complete three-dimensional photonic bandgaps in the visible.* Adv. Mater. **25,** 3588–92 (2013).

93. Fischer, J. & Wegener, M. *Three-dimensional optical laser lithography beyond the diffraction limit*. Laser Photon. Rev. **7,** 22–44 (2013).

94. Cao, Y., Gan, Z., Jia, B., Evans, R. a & Gu, M. *High-photosensitive resin for super-resolution direct-laser-writing based on photoinhibited polymerization.* Opt. Express **19,** 19486–94 (2011).

95. Rittweger, E., Han, K. Y., Irvine, S. E., Eggeling, C. & Hell, S. W. *STED microscopy reveals crystal colour centres with nanometric resolution*. Nat. Photonics **3,** 1–4 (2009).

96. Fischer, J. & Wegener, M. *Three-dimensional direct laser writing inspired by stimulated-emission-depletion microscopy*. Opt. Mater. Express **1,** 614–624 (2011).

97. Fischer, J., von Freymann, G. & Wegener, M. *The materials challenge in diffraction-unlimited direct-laser-writing optical lithography.* Adv. Mater. **22,** 3578–82 (2010).

98. El-Kady, M. F. & Kaner, R. B. *Scalable fabrication of high-power graphene micro-supercapacitors for flexible and on-chip energy storage.* Nat. Commun. **4,** 1475 (2013).

99. Park, J. B. *et al. Fast growth of graphene patterns by laser direct writing*. Appl. Phys. Lett. **98,** 123109 (2011).

100. Kwok, K. & Chiu, W. K. S. *Growth of carbon nanotubes by open-air laser-induced chemical vapor deposition*. Carbon N. Y. **43,** 437–446 (2005).

101. Mahjouri-Samani, M. *et al. Diameter modulation by fast temperature control in laser-assisted chemical vapor deposition of single-walled carbon nanotubes.* Nanotechnology **21,** 395601 (2010).

102. Xu, B.-B. *et al. Flexible nanowiring of metal on nonplanar substrates by femtosecond-laser-induced electroless plating.* Small **6,** 1762–6 (2010).

103. Hong, S. *et al. Nonvacuum, maskless fabrication of a flexible metal grid transparent conductor by low-temperature selective laser sintering of nanoparticle ink.* ACS Nano **7,** 5024–31 (2013).

104. Tennant, D. M. *Progress and issues in e-beam and other top down nanolithography*. J. Vac. Sci. Technol. A Vacuum, Surfaces, Film. **31,** 050813 (2013).

105. Ma, L.-C. *et al. Electrostatic funneling for precise nanoparticle placement: a route to wafer-scale integration*. Nano Lett. **7,** 439–45 (2007).

106. Louis, C. & Pluchery, O. *Gold Nanoparticles for Physics, Chemistry and Biology*. (Imperial College Press, 2012).

107. Turkevich, J., Stevenson, P. C. & Hillier, J. *A study of the nucleation and growth processes in the synthesis of Colloidal Gold*. Discuss. Faraday Soc. **11,** 55–75 (1951).

108. Frens, G. *Controlled Nucleation for the Regulation of the Particle Size in Monodisperse Gold Suspensions*. Nature **241,** (1973).

109. Park, J. & Shumaker-Parry, J. S. *Strong Resistance of Citrate Anions on Metal Nanoparticles to Desorption under Thiol Functionalization*. 1665–1682 (2015).

110. Gan, P. P., Ng, S. H., Huang, Y. & Li, S. F. Y. *Green synthesis of gold nanoparticles using palm oil mill effluent (POME): A low-cost and eco-friendly viable approach*. Bioresour. Technol. **113,** 132–135 (2012).

111. Israelachvili, J. N. *Intermolecular and Surface Forces with Applications to Colloidal and Biological Systems*. (Academic Press Inc. (London) Ltd., 1985).

112. Hamann, C. H., Hamnett, A. & Vielstich, W. *Electrochemistry*. (Wiley-VCH Verlag GmbH & Co. KGaA, 2007).

113. Masliyah, J. H. & Bhattacharjee, S. *Electrokinetic and Colloid Transport Phenomena*. (John Wiley & Sons, Inc., 2006).

114. Barnes, G. & Gentle, I. R. *Interfacial Science An Introduction*. (Oxford University Press, 2005).

115. Stankovich, J. & Carnie, S. L. *Electrical Double Layer Interaction between Dissimilar Spherical Colloidal Particles and between a Sphere and a Plate : Nonlinear Poisson - Boltzmann Theory*. Langmuir **12,** 1453–1461 (1996).

116. Derjaguin, B. V. & Landau, L. *The theory of stability of highly charged lyophobic sols and coalescence of highly charged particles in electrolyte solutions*. Acta Physicochim. URSS **14,** 633–662 (1941).

117. Verwey, E. J. W. & Overbeek, J. T. G. *Theory of the Stability of Lyophobic Colloids*. (Elsevier Publishing Company Inc., 1948).

118. Elsner, H., Meyer, H. G., Voigt, a. & Grüitzner, G. *Evaluation of ma-N 2400 series DUV photoresist for electron beam exposure*. Microelectron. Eng. **46,** 389–392 (1999).

119. Mcneil-Watson, F., Connah, M. T., Jack, R. & Mcknight, D. *Light scattering measurements using simultaneous detection*. (2009). AT <HTTPS://REGISTER.EPO.ORG/APPLICATION?NUMBER=EP09702459>

120. Atkins, P. W. *Physical Chemistry*. (Oxford University Press, 1990).

121. Hunter, R. J. *Introduction to Modern Colloid Science*. (Oxford Science Publications, 1993).

122. Castner, D. G., Hinds, K. & Grainger, D. W. *X-ray photoelectron spectroscopy sulfur 2p study of organic thiol and bisulfide binding interactions with gold surfaces*. Langmuir **12,** 5083–5086 (1996).

123. Shyue, J. J. *et al. Acid-base properties and zeta potentials of self-assembled monolayers obtained via in situ transformations*. Langmuir **20,** 8693–8698 (2004).

124. Hua, L., Zangi, R. & Berne, B. J. *Hydrophobic Interactions and Dewetting between Plates with Hydrophobic and Hydrophilic Domains*. J. Phys. Chem. C **113,** 5244–5253 (2009).

125. Melitz, W., Shen, J., Kummel, A. C. & Lee, S. *Kelvin probe force microscopy and its application*. Surf. Sci. Rep. **66,** 1–27 (2011).

126. Domanski, A. L. *et al. Kelvin probe force microscopy in nonpolar liquids*. Langmuir **28,** 13892–9 (2012).

127. Kobayashi, N., Asakawa, H. & Fukuma, T. *Quantitative potential measurements of nanoparticles with different surface charges in liquid by open-loop electric potential microscopy*. J. Appl. Phys. **110,** 044315 (2011).

128. Kobayashi, N., Asakawa, H. & Fukuma, T. *Nanoscale potential measurements in liquid by frequency modulation atomic force microscopy.* Rev. Sci. Instrum. **81,** 123705 (2010).

129. Brown, K. a, Satzinger, K. J. & Westervelt, R. M. *High spatial resolution Kelvin probe force microscopy with coaxial probes.* Nanotechnology **23,** 115703 (2012).

130. Smythe, W. R. *Static and Dynamic Electricity*. (McGraw-Hill Book Company, 1968).

131. Maxwell, J. C. *A treatise on electricity and magnetism*. (Clarendon Press, 1954).

132. Zhang, Y. *et al. Sensing the Charge State of Single Gold Nanoparticles via Work Function Measurements*. Nano Lett. 51–55 (2015).

133. Lee, M., Lee, W. & Prinz, F. B. *Geometric artefact suppressed surface potential measurements*. Nanotechnology **17,** 3728–3733 (2006).

134. Fumagalli, L., Esteban-Ferrer, D., Cuervo, A., Carrascosa, J. L. & Gomila, G. *Label-free identification of single dielectric nanoparticles and viruses with ultraweak polarization forces*. Nat. Mater. **11,** 808–816 (2012).

135. Derjaguin, B. V., Rabinovich, Y. I. & Churaev, N. V. *Direct measurement of molecular forces*. Nature **272,** 313–318 (1978).